Lecture Notes in Mechanical Engineering

Tapas Kumar Roy
Basudev Bhattacharya
Chiradeep Ghosh
S. K. Ajmani *Editors*

Advanced High Strength Steel

Processing and Applications

IIM
The Indian Institute of Metals
Metallurgy Materials Engineering

Springer

Lecture Notes in Mechanical Engineering

Lecture Notes in Mechanical Engineering (LNME) publishes the latest developments in Mechanical Engineering—quickly, informally and with high quality. Original research reported in proceedings and post-proceedings represents the core of LNME. Also considered for publication are monographs, contributed volumes and lecture notes of exceptionally high quality and interest. Volumes published in LNME embrace all aspects, subfields and new challenges of mechanical engineering. Topics in the series include:

- Engineering Design
- Machinery and Machine Elements
- Mechanical Structures and Stress Analysis
- Automotive Engineering
- Engine Technology
- Aerospace Technology and Astronautics
- Nanotechnology and Microengineering
- Control, Robotics, Mechatronics
- MEMS
- Theoretical and Applied Mechanics
- Dynamical Systems, Control
- Fluid Mechanics
- Engineering Thermodynamics, Heat and Mass Transfer
- Manufacturing
- Precision Engineering, Instrumentation, Measurement
- Materials Engineering
- Tribology and Surface Technology

More information about this series at http://www.springer.com/series/11236

Tapas Kumar Roy · Basudev Bhattacharya
Chiradeep Ghosh · S. K. Ajmani
Editors

Advanced High Strength Steel

Processing and Applications

Springer

Editors
Tapas Kumar Roy
R&D Division
Tata Steel Limited
Jamshedpur, Jharkhand
India

Chiradeep Ghosh
R&D Division
Tata Steel Limited
Jamshedpur, Jharkhand
India

Basudev Bhattacharya
R&D Division
Tata Steel Limited
Jamshedpur, Jharkhand
India

S. K. Ajmani
R&D Division
Tata Steel Limited
Jamshedpur, Jharkhand
India

ISSN 2195-4356 ISSN 2195-4364 (electronic)
Lecture Notes in Mechanical Engineering
ISBN 978-981-10-7891-0 ISBN 978-981-10-7892-7 (eBook)
https://doi.org/10.1007/978-981-10-7892-7

Library of Congress Control Number: 2017963281

Printed on acid-free paper

This Springer imprint is published by Springer Nature
The registered company is Springer Nature Singapore Pte Ltd.
The registered company address is: 152 Beach Road, #21-01/04 Gateway East, Singapore 189721, Singapore

Preface

Developments in Advanced High Strength Steel, Processing and Application (AHSS 2017) is a compendium of selected papers which were presented at a two-day-long international conference held in Jamshedpur during 22–23 February 2017. This was organized by Tata Steel Limited in association with the Jamshedpur Chapter of Indian Institute of Metals.

With the increasing energy crisis and stringent environmental norms, energy saving and safety coupled with CO_2 emission have become the burning issues for many industries, particularly for automakers. Reduction in weight is turning out to be the most effective way in reducing the fuel consumption and thus subsequent emission. At this stage, the family of advanced high-strength steels (AHSS) continues to evolve and grow in different applications such as automotive industry, lifting and excavation, line pipe. New steel grades are already being used for improved performance. Looking at the market trend, it may be envisaged that the emerging steel grades will be popular day by day. Accordingly, improved steelmaking practices, inclusion engineering at different stages of steelmaking and casting as well as subsequent heat treatment and rolling practices play important roles in achieving this goal.

In recent years, India has emerged as a very strong and potential country for advanced steel research. At this juncture, it was a very unique conference where not only were the physical and mechanical metallurgy issues related to the production of AHSS discussed, but also the process metallurgy topics were covered.

The contributors of this special volume encompass national and international academic institutes, leading steel industries, steel research laboratories and technology suppliers.

Our sincere thanks to the review committee for doing a splendid job in reviewing the articles and approving them to be published in this special volume. The editors would also like to thank Springer for preparing this volume.

We sincerely hope that the present proceeding will be instrumental in expanding the horizon of our knowledge on advanced high-strength steels.

Jamshedpur, India

Dr. Tapas Kumar Roy
Dr. Basudev Bhattacharya
Dr. Chiradeep Ghosh
Dr. S. K. Ajmani

Contents

About the Editors

Dr. Tapas Kumar Roy is a Principal Scientist in the Research and Development (R&D) Division of Tata Steel Limited in Jamshedpur, India. He holds M.Tech. and Ph.D. degrees from the Indian Institute of Technology Kanpur, India. He has been associated with Tata Steel for over 20 years, and during this period, he has worked in various functions such as Scientific Services, Long Product Technology, Flat Product Technology before being moved to R&D from 2016. His areas of interest include steelmaking, secondary refining, continuous casting, inclusion engineering, ferro-alloys, defectology, mould powder, process design and improvement. He has authored more than 40 scientific research papers in national and international journals and conferences.

Dr. Basudev Bhattacharya is working as Principal Scientist in the Research and Development (R&D) Division of Tata Steel Limited in Jamshedpur, India. He holds M.Tech. and Ph.D. degrees from the Indian Institute of Technology in Kanpur, India. From 1997 to 2007, he has worked in the Cold Rolling Mill and Flat Product Technology Group in Tata Steel. From 2007 onwards, he has been in the R&D Division at Tata Steel. His areas of interest include physical metallurgy and materials science, phase transformation, designing of steel chemistry, X-ray diffraction, electron microscopy. He has been granted 4 patents, and he has authored more than 30 scientific research papers.

Dr. Chiradeep Ghosh is a Principal Researcher in the Research and Development (R&D) Division of Tata Steel Limited in Jamshedpur, India, where he has been working since 2003. He holds a M.Tech. degree from the Indian Institute of Technology Kanpur, India, and a Ph.D. degree from McGill University, Montreal, Canada. His areas of interest include thermomechanical controlled processes, phase transformation and related phenomenon, characterization of materials and electron microscopy. He has been granted 6 patents and has authored more than 35 scientific research papers and served as an editor for 2 conference proceedings. In addition,

he has also authored a book titled "The Dynamic Transformation of Deformed Austenite". He serves as a reviewer for multiple high-impact journals and is an editorial board member of Current Smart Materials.

Dr. S. K. Ajmani is Chief Researcher in the Steelmaking & Casting Research Group in Research and Development (R&D) of Tata Steel Limited in Jamshedpur, India. He holds M.Tech. and Ph.D. degrees from the Indian Institute of Technology Kanpur and Kharagpur, India, respectively. His areas of interest include steelmaking, physical and numerical modelling, continuous casting, inclusion engineering, product—process design and optimization, and mould powder development. He has worked at Tata Steel for more than 30 years and has been the chief researcher for the last 2 years. He has authored more than 100 scientific research papers in national and international journals and conferences.

Dynamic Transformation During the Torsion Simulation of Plate and Strip Rolling

John J. Jonas, Clodualdo Aranas Jr. and Samuel F. Rodrigues

Abstract Torsion simulations of plate and strip rolling were carried out on a plain C–Mn and an X70 Nb steel over the temperature range 900–1000 °C. Pass strains of 0.4 were applied at a strain rate of 1 s^{-1}. Interpass times of 0.5, 1, 1.5, 3, 10, and 20 s were employed to determine the mean flow stresses (MFSs) applicable to plate and strip rolling. By means of double differentiation, critical strains of 0.05 and 0.12 were established for the initiation of dynamic transformation and dynamic recrystallization, respectively. It is shown that the dynamic transformation of austenite to ferrite takes place above the Ae_3 temperature, resulting in significantly lower than expected MFS values. The nucleation and growth of ferrite reduces the rolling load and modifies the microstructure. Shorter interpass times produce larger decreases in MFS than longer ones because they do not permit as much retransformation to austenite as takes place during longer interpass intervals.

Keywords Strip mill simulation · Plate mill simulation · Dynamic transformation

1 Introduction

The dynamic transformation (DT) of austenite to ferrite has attracted significant interest since the work of Yada and coworkers in the 1980s [1]. They showed by means of compression tests and rolling simulations that austenite can transform into ferrite during deformation at temperatures as high as 163 °C above the Ae_3. Strip rolling simulations using interpass times of 1 s were also carried out by Yada et al. [2] in 1988 leading to similar results. In a more recent paper in 2000, they used in situ X-ray diffraction experiments to provide real-time evidence for the occurrence of dynamic transformation [3]. In this work, iron alloys were subjected to

J. J. Jonas (✉) · C. Aranas Jr. · S. F. Rodrigues
Materials Engineering, McGill University, 3610 University St,
Montreal H3A 0C5, Canada
e-mail: john.jonas@mcgill.ca

T. K. Roy et al. (eds.), *Advanced High Strength Steel*, Lecture Notes
in Mechanical Engineering, https://doi.org/10.1007/978-981-10-7892-7_1

torsion tests about 40 °C above the Ae_3 temperature. The increasing presence of $(110)_{\alpha-Fe}$ diffraction patterns revealed that ferrite was formed during deformation.

More recently, Jonas et al. [4] and the present authors reported on the results of hot torsion tests in which the characteristics of the ferrite produced dynamically during multiple successive deformations separated by short interpass times were described. Two distinct softening mechanisms were identified by using the double-differentiation method developed by Poliak and Jonas in 1996 [5]. These were shown to be dynamic transformation and dynamic recrystallization, and were determined to be initiated at critical strains of 0.05 and 0.12, respectively [4].

2 Experimental Procedure

The present steels were supplied as hot-rolled plates with thicknesses of 12.5 mm. The chemical compositions of these steels are presented in Table 1 together with their corresponding paraequilibrium and orthoequilibrium Ae_3 temperatures. The Ae_3 temperatures were calculated using the Thermo-Calc software.

The steel plates were machined into torsion specimens with diameters of 6.3 mm and gauge lengths of 22.2 mm with their cylinder axes parallel to the rolling direction.

Specially programmed torsion tests were performed for the simulation of strip rolling. The samples were heated to 1200 °C at 1 °C/s. After austenitization for 20 min, the samples were cooled at 1 °C/s down to test temperatures in the range 1000–930 °C. They were then held for 10 min, after which multiple deformations were applied while the sample was cooled at approximately 6 °C/s. The number of passes (with 1, 4, and 7 deformations) was varied so that samples could be quenched leading to quantification of the volume fraction of ferrite produced. Interpass times of 0.5, 1, 1.5, and 3 s were employed.

For the plate rolling simulations, isothermal conditions were employed, selected to represent the operation of a Steckel mill. After austenitization, the samples were cooled down to 1100 °C and held at this temperature for 60 s before a roughing pass simulation was carried out, consisting of a strain of 0.4 applied at a strain rate of 1.0 s^{-1}. The sample was then held for 90 s before being cooled to 900 °C. The samples were then held at this temperature for 7 min before the first pass of the finishing simulation was applied. Interpass times of 10 and 20 s were employed and the samples were quenched after the 7th pass to permit quantification of the volume

Table 1 Chemical compositions (mass%) and equilibrium transformation temperatures (°C)

	C	Mn	Si	Cr	Nb	Orthoequilibrium Ae_3 (°C)	Paraequilibrium Ae_3 (°C)
C–Mn	0.060	0.30	0.01	–	–	877	870
X70	0.047	1.56	–	0.21	0.092	845	810

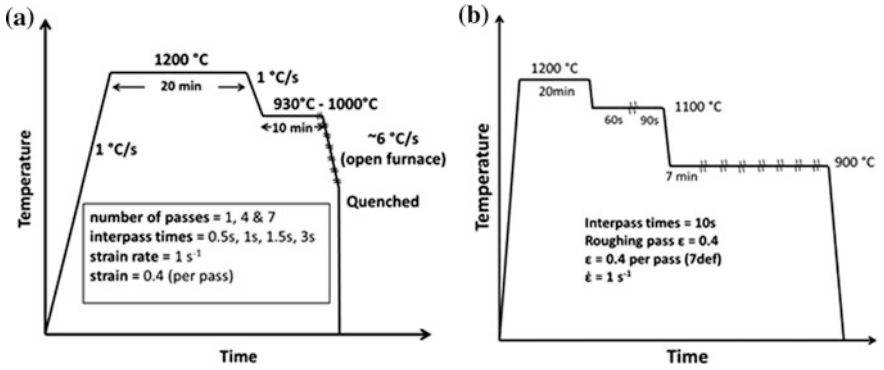

Fig. 1 Thermomechanical schedules for the torsion simulations of **a** strip and **b** plate rolling

fraction of dynamically formed ferrite. The thermomechanical schedules followed in the torsion tests are illustrated in Fig. 1. As the sample diameter increased during testing, the changes in diameter were taken into account in deriving the flow stress from the torque.

3 Results

3.1 Strip Rolling

Some typical stress–strain curves of a 7-pass strip rolling simulation (continuous cooling) with interpass pass times of 1 s are presented in Fig. 2. Although the flow curve levels are normally expected to increase due to the decreasing temperature, it is clear that the levels either display low rates of increase or even decrease during the simulations. The mean flow stresses were calculated by integration of the stress–strain curves shown in Fig. 2 and these values are plotted in the form of Boratto diagrams in Fig. 3. The Pussegoda relation [6] is also plotted here, which indicates the approximate value of the MFS for a series of first passes. Although the MFS values are expected to rise as the temperature is decreased, here there is no increase in load even though the passes are being applied at decreasing temperatures.

In torsion simulations, the applied strain increases linearly from zero along the axis to a maximum at the surface of the sample. The increase in the volume fraction of ferrite formed with distance from the axis is illustrated in Fig. 4. The martensite phase appears dark while the ferrite is light. It can be seen that only martensite is present along the axis and that the amount of ferrite increases significantly as the surface is approached. The microstructures also reveal that the volume fraction of ferrite increases progressively with pass number.

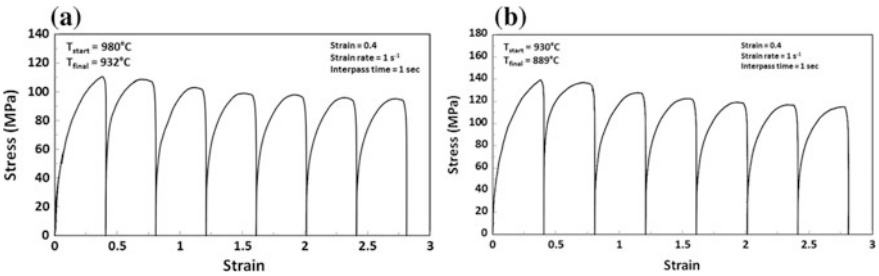

Fig. 2 Strip rolling simulations carried out on the 0.06C–0.3Mn–0.01Si steel with interpass times of 1 s and pass strains of 0.4 applied at a strain rate of 1 s^{-1}. Start and finish temperatures were **a** 980 and 932 °C, and **b** 930 and 889 °C, respectively

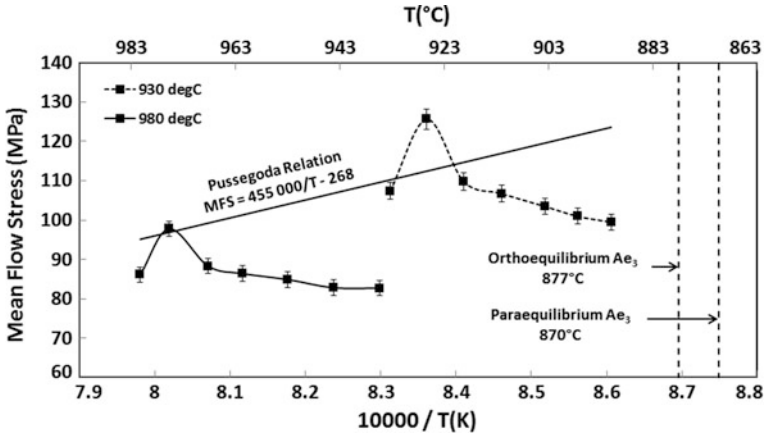

Fig. 3 The mean flow stresses associated with the flow curves in Fig. 2. The MFS increases during the second pass (due to strain accumulation) and then drops in the following passes because of the softening associated with the transformation from austenite to ferrite as well as with the occurrence of dynamic recrystallization

3.2 Plate Rolling

The isothermal flow curves determined from the 7-pass plate rolling simulations carried out on the X70 niobium steel with interpass times of 10 and 20 s are presented in Fig. 5a and b, respectively. These tests were performed at about 90 °C above the paraequilibrium Ae_3 temperature. In the absence of phase transformation, the flow stress levels should not change significantly from pass to pass. However, the peak stresses decreased from the second pass to the final pass by approximately 17% when the 10 s interpass interval was employed. On increasing the interpass time to 20 s, the load decrease was reduced to 14%.

These behaviors can be directly associated with the volume fractions of ferrite formed and retained from pass to pass. The shapes of the curves indicate that there

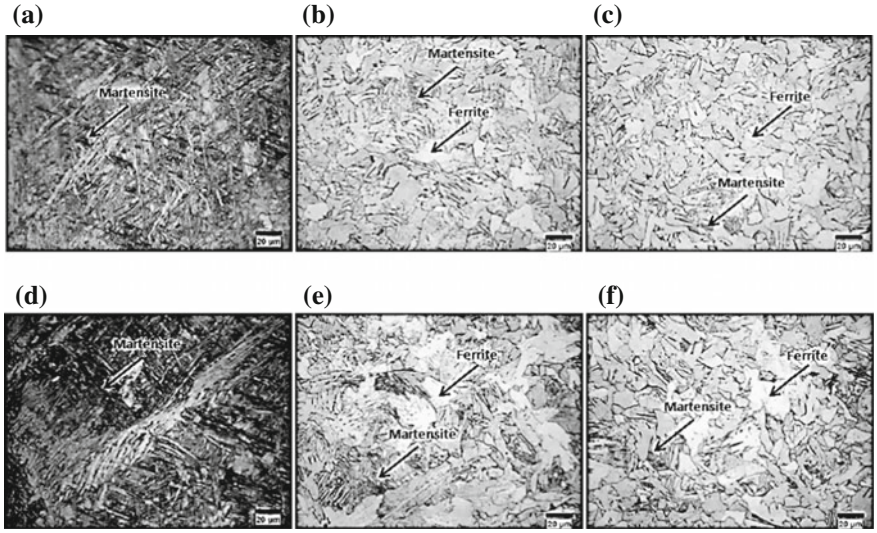

Fig. 4 Samples subjected to seven deformations beginning at 980 °C (**a**, **b**, **c**) and 930 °C (**d**, **e**, **f**). The amount of ferrite increases in moving from **a** the center to **b** 1.5 mm from the surface, and finally to **c** the surface of the sample. A similar trend can be observed in moving from **d** the center, to **e** 1.5 mm from the surface, and finally to **f** the surface of the sample

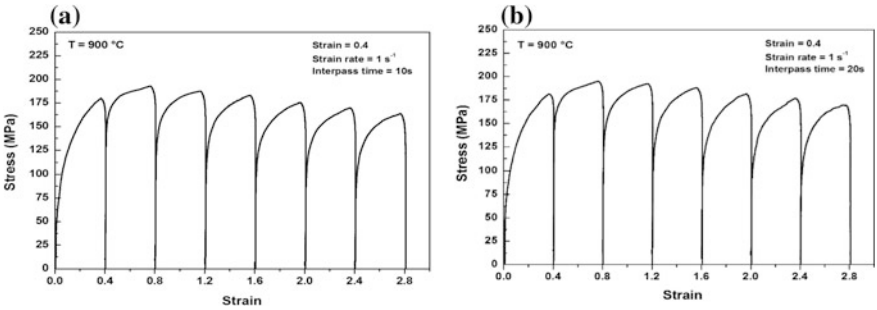

Fig. 5 Plate rolling simulations carried out on the X70 steel at 900 °C with strains of 0.4 applied at a strain rate of 1 s^{-1}. Interpass times: **a** 10 s and **b** 20 s

is slightly less static recrystallization in the first case than for the longer interpass time. The increase in stress level for the second pass is associated with strain accumulation and the gradual decrease after this pass can be attributed to the progressive formation of ferrite. MFS values illustrating this behavior are presented in Fig. 6. Here, the continuous decrease in load is readily seen.

The microstructures related to the 7-pass X70 simulation with interpass times of 10 and 20 s are illustrated in Fig. 7. The presence of significant amounts of ferrite is clearly evident: 26.3 and 21.8% for the 10 and 20 s simulations, respectively. The ferrite phase is present as both polygonal and Widmanstätten plates. These appear

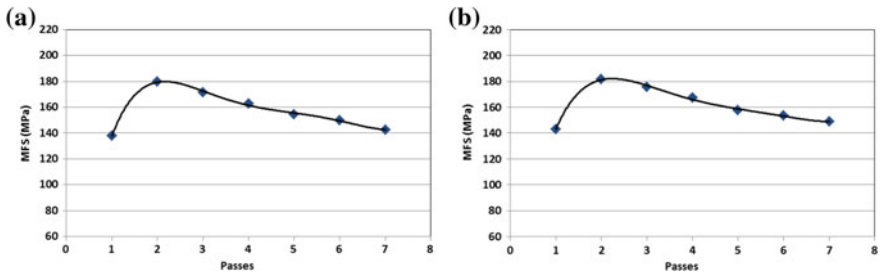

Fig. 6 The mean flow stresses associated with the flow curves in Fig. 5. The MFS increases during the second pass (due to strain accumulation) and then drops in the following passes because of the softening associated with the transformation from austenite to ferrite

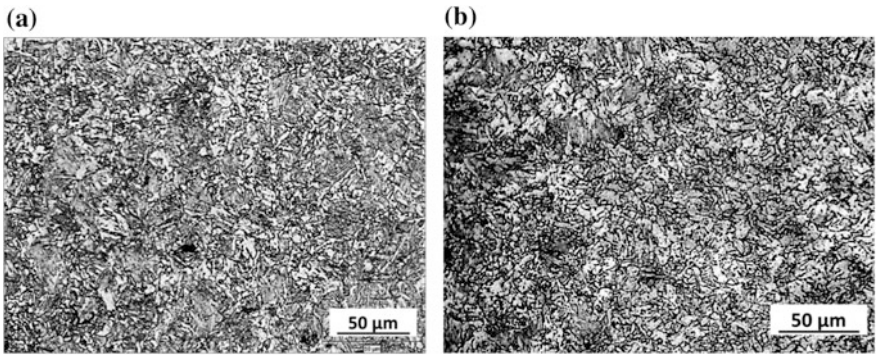

Fig. 7 Optical micrographs of X70 steel samples subjected to seven-pass deformations at 900 °C using interpass times of: **a** 10 s and **b** 20 s

to have nucleated both at grain boundaries and within the prior austenite grains. From the figure, it is evident that the 10 s ferrite grains are finer than the 20 s grains. This is an indication that more grain growth took place during the longer interpass interval. The lower ferrite volume fraction after the 20 s intervals can be attributed in turn to the greater amount of retransformation to austenite during the longer holding periods.

4 Discussion

4.1 Critical Strains

The stress levels of the flow curves in Fig. 2 (strip rolling simulation) did not increase with decreasing temperature. To investigate this unusual behavior, the double-differentiation method of analysis was applied to these curves. It was

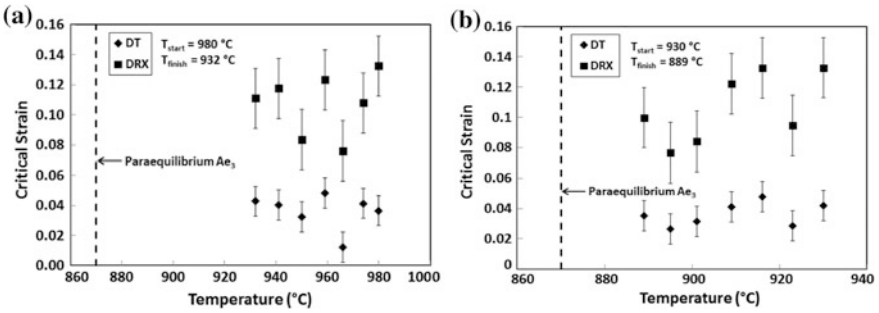

Fig. 8 Critical strains for dynamic transformation (DT) and dynamic recrystallization (DRX) in the strip rolling simulations of Fig. 2. It can be seen that DT and DRX are initiated at strains of approximately 0.05 and 0.12

verified that two distinct softening mechanisms were initiated at strains well before the peak strain. The first of these is dynamic transformation (DT), which converts some of the austenite into the softer ferrite phase, and the second is dynamic recrystallization (DRX). The critical strains required to initiate DT and DRX were determined to be around 0.05 and 0.12, respectively, as shown in Fig. 8. Several previous studies [7–10] have shown that the critical strain for DT is less than that for DRX. The transformation is reinitiated during each simulated rolling pass. Note that transformation is not continuous with increasing strain but requires the application of a series of successive critical (initiation) strains. The occurrence of this phenomenon is supported by the optical microstructures presented in the previous section, see Fig. 4.

A similar double-differentiation procedure was applied to the X70 flow curves shown in Fig. 5 (plate rolling simulations). The results obtained are presented in Fig. 9a and b for interpass times of 10 and 20 s, respectively. Here, again the DT and DRX critical strains were attained well before the peak strain. The critical strain values for the first passes are higher than for the subsequent passes. This is because

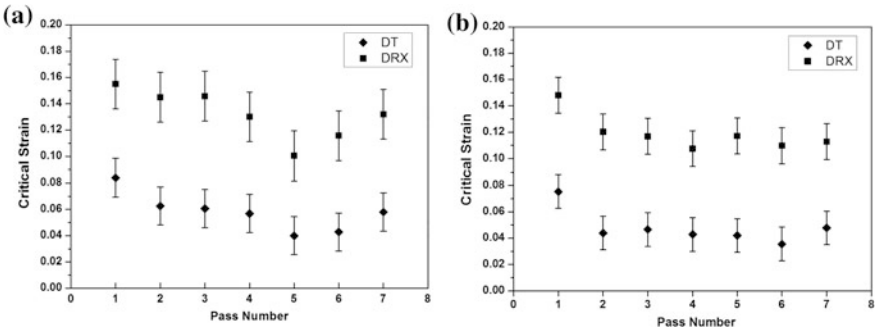

Fig. 9 Critical strains in the X70 steel subjected to interpass times of **a** 10 s and **b** 20 s. Here, the first pass always displays the highest critical strain in all the simulations

the first pass is applied to undeformed austenite, whereas there is some retained strain or work hardening present in the samples subjected to all subsequent passes. The approximate first-pass DT critical strain is 0.08 while this decreases to 0.04 in the subsequent passes, after which it remains essentially constant. Thus, the transformation is reinitiated during each simulated rolling pass.

5 Conclusions

1. Two softening mechanisms were identified as occurring in plate and strip mill simulations by applying the double-differentiation method. Dynamic transformation and dynamic recrystallization are initiated at critical strains of about 0.05 and 0.12, respectively. The dynamic transformation of austenite to ferrite above the Ae_3 temperature took place during all the simulated passes resulting in significant decreases in MFS.
2. Appreciable ferrite formed during the strip mill simulations, producing the softening. However, less ferrite was retained in the long interval simulations because the DT ferrite produced partially retransformed into austenite.
3. The volume fraction of ferrite formed during the strip mill simulations increased continuously until the last pass. This is why there was little increase in MFS as the temperature was decreased.
4. Significant amounts of ferrite formed during the plate rolling simulations, although the volume fraction of ferrite retained after the last pass decreased when the longer interpass interval was employed.
5. The DT critical strains (determined using double differentiation) were always highest in the first pass and then adopted lower values in the succeeding passes. This can be attributed to the retention of work hardening in the latter cases.

Acknowledgements The authors acknowledge with gratitude funding received from the McGill Engineering Doctoral Award (MEDA) program, the Brazilian National Council for Scientific and Technological Development (CNPq), and the Natural Sciences and Engineering Research Council of Canada.

References

1. Y. Matsumura and H. Yada, Evolution deformation of ultrafine-grained ferrite in hot successive deformation, Transactions ISIJ, 27 (1987), 492–498
2. H. Yada, T. Matsumura, and T. Senuma, Proc. Int. Conf. Physical Metallurgy of Themomechanical Processing of Steels and Other Metals, ISIJ, THERMEC, 88 (1988), 200–207
3. H. Yada, C.M. Li, and H. Yamagata, Dynamic $\gamma \rightarrow \alpha$ transformation during hot deformation in iron-nickel-carbon alloys, ISIJ international, 40 (2000), 200–206

4. J.J. Jonas, V.V. Basabe, C. Ghosh and C. Aranas, Dynamic Transformation During the Simulation of Strip Rolling, Proceedings of the 5th Baosteel Biennial Academic Conference, June (2013), C1–C6, Shanghai, China
5. E. Poliak and J.J. Jonas, A one-parameter approach to determining the critical conditions for the initiation of dynamic recrystallization, Acta Materialia, 44 (1996), 127–136
6. L.N. Pussegoda, S. Yue and J.J. Jonas, Laboratory Simulation of Seamless Tube Piercing and Rolling Using Dynamic Recrystallization Schedules, Metallurgical Transactions A, 21 (1990), 153–164
7. J.J. Jonas, C. Ghosh, X. Quelennec and V.V. Basabe, The Critical Strain for Dynamic Transformation in Hot Deformed Austenite, ISIJ International, 53 (2013), 145–151
8. C. Ghosh, V.V. Basabe and J. J. Jonas, Determination of the Critical Strains for the Initiation of Dynamic Transformation and Dynamic Recrystallization in Four Steels of Increasing Carbon Contents, Steel Research International, 84 (2013), 490–494
9. J.J. Jonas, C. Aranas, V.V. Basabe and C. Ghosh, Dynamic Transformation during the Torsion Simulation of Strip Rolling, Materials Science Forum, 783–786 (2014), 39–44
10. C. Ghosh, V.V. Basabe, J.J. Jonas, Y.M. Kim, I.H. Jung and S. Yue, The Dynamic Transformation of Deformed Austenite at Temperatures above the Ae_3, Acta Materialia, 61 (2013), 2348–2362

Microstructure Engineering of High-Performance Steels

Matthias Militzer and Thomas Garcin

Abstract Microstructure evolution during steel processing assumes a critical role in tailoring mechanical properties, e.g., the austenite–ferrite transformations are a key metallurgical tool to improve properties of advanced low-carbon steels. Microstructure engineering is a concept that links the processing parameters to the properties by accurately modeling the microstructure evolution. Systematic experimental laboratory studies provide the basis for model development and validation. Laser ultrasonics, dilatometry, and a range of microscopy techniques (including electron backscatter diffraction mapping) are used to characterize recrystallization, grain growth, phase transformations, and precipitation in high-performance steels. Based on these studies, a suite of state variable models is proposed. Examples of their applications are given for intercritical annealing of advanced automotive steel sheets and welding of high-strength line pipe grades. The extension of state variable models to the scale of the microstructure is illustrated using the phase field approach. Here, the emphasis is placed on simulating the austenite decomposition into complex ferrite–bainite microstructures. The challenges and opportunities to develop next-generation process models will be discussed.

Keywords Line pipe steel · Dual phase steel · Microstructure engineering
Phase field modeling

1 Introduction

High-performance steels with improved properties are required for a wide range of applications including automotive, construction, and energy sectors. These steels are increasingly produced as thermomechanical controlled processed (TMCP) grades where the microstructure is tailored to obtain a steel with the desired

M. Militzer (✉) · T. Garcin
Centre for Metallurgical Process Engineering, The University of British Columbia, Vancouver, BC V6T 1Z4, Canada
e-mail: Matthias.militzer@ubc.ca

T. K. Roy et al. (eds.), *Advanced High Strength Steel*, Lecture Notes in Mechanical Engineering, https://doi.org/10.1007/978-981-10-7892-7_2

mechanical properties without any additional normalization treatments. To determine, optimize, and control robust processing paths, computational tools have become an essential aspect of producing consistently high-quality TMCP grades.

Since the 1980s significant progress has been made in developing knowledge-based process models for the steel industry [1–4]. An important concept here is to predict the steel properties as a function of the operational process parameters (e.g., reduction schedule, rolling temperatures, cooling bank activities, and annealing cycle) by accurately modeling the microstructure evolution (e.g., recrystallization, grain growth, precipitation, and phase transformation) during processing. These microstructure models are combined with deformation and temperature models, and the predicted final microstructure is linked via structure–property relationships with the resulting properties. This approach has been widely used for ferrite–pearlite steels (including HSLA steels) as well as dual-phase steels with ferrite–martensite microstructures [4]. Numerous empirical parameters for these models are typically determined from time-consuming laboratory experiments and, thus, limiting these models to the investigated steel chemistries and processing conditions. It is imperative to formulate next-generation process models with predictive capabilities using a minimum of empirical parameters to also aid alloy design for advanced high-strength steels where novel alloying concepts are being explored for creating complex multiphase microstructures that are required to achieve desired property improvements. Computational materials science now offers exciting opportunities to formulate models containing fundamental information on the basic atomic mechanisms of microstructure evolution that can be implemented across different lengths and timescales [5]. For example, the phase field method [6] is a powerful tool to describe the morphological complexity of multiphase microstructures by predicting actual microstructures rather than average microstructure parameters (e.g., fraction transformed and grain size). One challenge here is that interface properties including the interaction of alloying elements with moving interfaces have to be quantified as an input for phase field simulations. While experimental studies can be used to deduce effective interface mobilities as empirical parameters, it is critical to develop more rigorous computational strategies by using atomistic simulations to provide insight into the underlying atomistic mechanisms of microstructure evolution and guidance for the selection of kinetic parameters. For example, alloying elements like Nb, Mo, and Mn affect recrystallization, grain growth, and phase transformations through their interaction with the migrating interfaces (i.e., grain boundaries and austenite–ferrite interfaces) [5]. Linking complex multiphase microstructures to properties is challenging as appropriate structure–property relationships are not yet readily available.

The present paper provides a brief review of the status of microstructure-based process models and their application to high-performance steels. Examples are provided for intercritical annealing of dual-phase steels and the heat-affected zone (HAZ) in line pipe steels.

2 Process Models

2.1 State Variable Approach

The original microstructure-based process models essentially employed a state variable approach by considering the evolution of microstructure parameters that can be measured experimentally, e.g., fraction transformed/recrystallized, grain size, precipitate size and volume fraction, and dislocation density. In a simplest scenario, only the fractions X transformed/recrystallized may be considered and this has frequently been achieved by employing the Johnson–Mehl–Avrami–Kolmogorov (JMAK) model, i.e.,

$$X = 1 - \exp(-bt^n), \tag{1}$$

where b is a rate parameter and n is the JMAK exponent that is determined from laboratory studies. Provided n is independent of temperature, the JMAK model can in combination with the additivity principle be applied to non-isothermal heat treatments that are typically employed in industrial processing. Additivity can be assumed for most transformation and recrystallization conditions of practical interest as long as they do occur not simultaneously with other microstructure changes. For example, potentially concurrently occurring ferrite recrystallization and intercritical austenite formation would require a more sophisticated model approach.

The next stage of complexity is to include grain size into the model and, if required, further microstructure features that determine the properties. Here, empirical approaches have frequently been used such as power laws for austenite grain growth and relating the ferrite grain size to the transformation start temperature during continuous cooling. In more advanced models, the actual mechanisms of microstructure evolution are explicitly incorporated. For example, austenite grain growth when pinning particles (e.g., NbC) are present can be described by

$$\frac{\mathrm{d}g}{\mathrm{d}t} = \frac{3M\sigma}{g} - P, \tag{2}$$

where g is the mean grain size, M is the grain boundary mobility, σ is the grain boundary energy, and P is the pinning pressure which is related to precipitate size and volume fraction by a Zener-type expression. Of particular interest are grain coarsening stages that are associated with dissolution of precipitates during reheating where a precipitation–dissolution/coarsening model can be coupled to the grain growth model to quantify the decrease in pinning pressure [7]. The grain boundary mobility is usually assumed to obey an Arrhenius relationship, i.e.,

$$M = M_0 \exp\left(-\frac{Q}{RT}\right), \tag{3}$$

where the pre-exponential M_0 and the effective activation energy Q are employed as fitting parameters that depend on steel chemistry.

2.2 Phase Field Modeling

The above state variable models calculate average microstructure values, i.e., an average fraction transformed or an average grain size, etc. To obtain information on the spatial distribution of microstructure constituents and their morphology modeling on the mesoscale, i.e., the scale of the microstructure, can now routinely be conducted. Here, phase field modeling (PFM) has emerged as the simulation tool of choice because it is a powerful methodology to deal with complex morphological aspects of microstructure features, e.g., formation of dendrites during solidification. PFM has also been extensively applied to describe recrystallization and phase transformations in steels [6]. In particular, the multiphase-field model originally developed by Steinbach et al. [8] has been employed here where each microstructure constituent i is defined by a unique phase field parameter φ_i. The value of φ_i is equal to 1 inside constituent i and 0 outside constituent i. Within the interface of width τ, φ_i changes continuously from 0 to 1. The phase field parameters represent the local fraction of each constituent such that the interface consists of a mixture of constituents with the constraint of $\Sigma\varphi_i = 1$. The temporal evolution of each field variable is described by the superposition of the pair-wise interaction with its neighboring constituents [8],

$$\frac{\mathrm{d}\varphi_i}{\mathrm{d}t} = \sum_{i \neq j} M_{ij} \left\{ \sigma_{ij} \left[\left(\varphi_j \nabla^2 \varphi_i - \varphi_i \nabla^2 \varphi_j \right) + \frac{\pi^2}{2\tau^2} \left(\varphi_i - \varphi_j \right) \right] + \frac{\pi}{\tau} \sqrt{\varphi_i \varphi_j} \Delta G_{ij} \right\}, \tag{4}$$

where M_{ij} is the interfacial mobility, σ_{ij} is the interfacial energy, and ΔG_{ij} is the driving pressure for interface migration which can be either the stored energy for recrystallization or the difference of chemical potentials for phase transformation. Further, the phase field model can be coupled with diffusion equations to account for long-range diffusion during phase transformation. Similarly to the state variable models, the interfacial mobility is typically employed as a fitting parameter to reproduce a set of benchmark experimental data. Further, PFM describes growth stages and has to be combined with a suitable nucleation model to ensure that proper algorithms are provided to seed nuclei in phase field simulations.

3 Results

3.1 Intercritical Annealing

Dual-phase steels for automotive applications are typically produced through intercritical annealing on continuous annealing or hot dip galvanizing lines. Here, the cold-rolled steel recrystallizes during heating and intercritical austenite forms which during the cooling stage transforms primarily into bainite and/or martensite. From a modeling perspective, one must first describe ferrite recrystallization during continuous heating to the intercritical temperature. Figure 1 shows the evolution of the ferrite fraction recrystallized during isothermal holding at three different temperatures, i.e., 650, 680, and 710 °C, in a steel with a typical dual-phase chemistry (0.06 wt%C–1.86 wt%Mn–0.15 wt%Mo). Using the JMAK approach, i.e., Eq. 1, a ferrite recrystallization model has been developed based on the metallographic observations [9]. Here, the rate parameter b is a function of temperature and n is a constant such that additivity can be applied. Further, laser ultrasonic measurements were conducted to determine the fraction recrystallized in situ by doing the heat treatments in a Gleeble 3500 thermomechanical simulator equipped with an LUMet (laser ultrasonics for metallurgy) system. The procedures of the LUMet measurements are described elsewhere [10, 11]. The LUMet measurements are in reasonable agreement with the metallographic observations even though laser ultrasonics is an indirect method, i.e., the ultrasonic velocity that changes with texture evolution during recrystallization is measured such that only those portions of recrystallization that are associated with a texture change can be recorded. The consistency of LUMet and metallographic measurements confirms the LUMet technique as an exciting experimental tool for rapid model development and validation as it reduces the need for extensive labor-intensive metallographic investigations.

Similar studies have been performed to develop a process model for intercritical annealing of a DP600 steel (0.11 wt%C–1.86 wt%Mn–0.34 wt%Cr–0.16 wt%Si) [12, 13]. Using the JMAK approach, a process model has been proposed that can be applied for sufficiently slow line speeds where ferrite recrystallization is completed before the onset of austenite formation. Increasing the line speed above a threshold

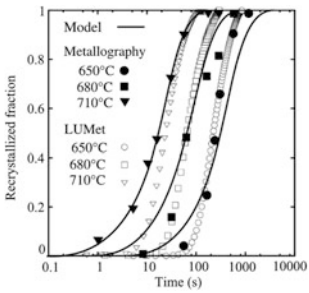

Fig. 1 Ferrite recrystallization in a 0.06 wt%C–1.86 wt%Mn–0.15 wt%Mo steel; metallography and model data taken from [9]

value, ferrite recrystallization and austenite formation occur concurrently. The simultaneous evolution of recrystallization and austenite formation can be simulated by PFM [14]. After benchmarking and validating the model with experimental data, simulations were performed by systematically varying intercritical heat treatment cycles to construct processing maps to predict the martensite fraction that is the dominant microstructure feature for the mechanical properties in dual-phase steels as a function of line speed and intercritical holding temperature [15].

3.2 *Heat-Affected Zone*

Process models have recently been developed for the HAZ in Ti–Nb microalloyed line pipe steels with complex ferrite–bainite microstructures that also include martensite/austenite (M/A) constituents [16]. The modeling approach taken is similar to that above described for intercritical annealing. For the HAZ, the microstructure features of significance include formation, grain growth, and decomposition of austenite and dissolution of NbC. Figure 2 shows austenite grain growth during continuous heating at 10 °C/s in three line pipe steels with different chemistries in terms of their C and Nb content (in wt%): 0.063C–0.034Nb, 0.028C–0.091Nb, and 0.058C–0.091Nb. LUMet grain size measurements are based on ultrasonic attenuation that can be correlated with the metallographically measured austenite grain size, here quantified as equivalent area diameter [10]. A combined austenite grain growth and NbC dissolution model has been developed adopting Eq. 2. For the 0.063C–0.034Nb steel, the model development was based on metallographic grain growth studies in combination with transmission electron microscopy investigations to quantify precipitate evolution [7]. The pre-exponential grain boundary mobility factor M_0 is the only fit parameter in the model, while Q = 350 kJ/mol is taken from the literature [17]. Adopting the same model approach and varying M_0 austenite grain size evolution is described in the two other steels based on the LUMet measurements. The values of M_0 are summarized in Table 1 indicating a decreasing effective grain boundary mobility with increased alloying content, in particular Nb microalloying.

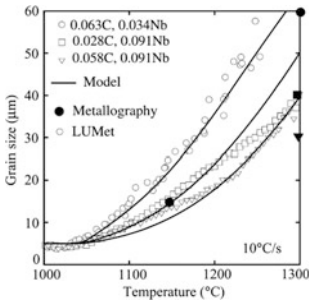

Fig. 2 Austenite grain growth during continuous heating at 10 °C/s in line pipe steels

Table 1 Grain boundary mobility parameter for line pipe steels

Steel	M_0 (m^4/Js)
0.063C–0.034Nb	280
0.028C–0.091Nb	100
0.058C–0.091Nb	50

Figure 3 provides examples of austenite decomposition during continuous cooling in the 0.063C–0.034Nb steel. In addition to the austenite grain size, the amount of Nb in solution strongly affects the transformation behavior. Both the austenite grain size and the amount of Nb in solution increase with reheating temperature. For a given cooling rate, here 30 °C/s, the transformation temperatures decrease with increasing austenite grain size and amount of Nb in solution. The continuous cooling transformation behavior can be described with the JMAK approach adopting additivity when the rate parameter b is taken as a function of temperature, austenite grain size, and Nb in solution [16].

Alternatively, PFM can be combined with the NbC dissolution model to describe austenite grain growth and decomposition, by taking the grain boundary and interface mobilities as functions of both temperature and Nb in solution [18]. Further, simulation of bainite formation requires to introduce anisotropy factors into the mobility to replicate the morphological complexity of bainite sheaves, as discussed elsewhere in detail [18]. An advantage of the PFM approach is that it can be used to seamlessly describe the microstructure gradient in the HAZ as a function of distance from the fusion line. PFM simulations predict the gradual transition from a coarse bainite microstructure near the fusion line to a predominantly ferrite microstructure further away from the fusion line [18], as illustrated in Fig. 4 for the 0.063C–0.034Nb steel and Gleeble-simulated HAZ thermal cycles with peak temperatures of 1000 and 1350 °C, respectively. To evaluate the integrity of weld joints, it is critical to determine and predict the fracture toughness of the HAZ which will also require a detailed description and analysis of the bainite substructure. Appropriate models for the substructure evolution and its correlation with mechanical properties have yet to be established.

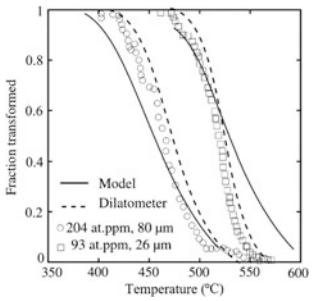

Fig. 3 Austenite decomposition in the 0.063C–0.034Nb steel cooled at 30 °C/s from different austenite grain sizes and Nb contents in solution; symbols indicate LUMet measurements

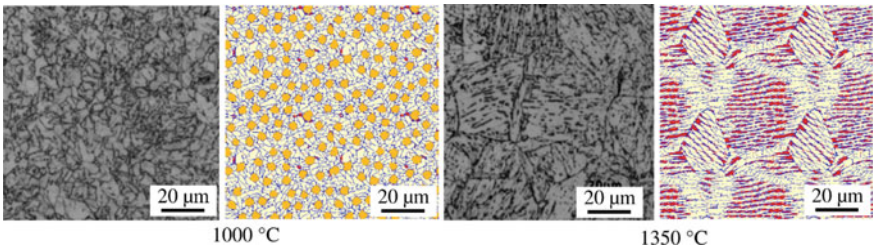

Fig. 4 Comparison of microstructures obtained in the 0.063C–0.034Nb steel for Gleeble-simulated HAZ thermal cycles with peak temperatures of 1000 °C (left) and 1350 °C (right) and microstructures predicted by PFM (ferrite: yellow, bainite: white, M/A: red)

4 Conclusions

Microstructure process models have been developed for advanced steels with ferrite–bainite–martensite microstructures using the conventional microstructure engineering state variable approach. To increase the predictive capability of these models, PFM enables to also describe spatial and morphological aspects of these complex microstructures. A critical aspect of future work is the development of reliable structure–property relationships for steels with multiphase microstructures. Further, to aid steel chemistry design, a multiscale approach may be considered for next-generation process models where the effects of alloying elements on the atomistic mechanisms of microstructure evolution are rigorously incorporated.

References

1. T. Senuma, M. Suehiro and H. Yada, ISIJ International, 32 (1992), 423–432
2. Y.J. Lan, D.Z. Li, X.C. Sha and Y.Y. Li, Steel Research International, 75 (2004), 462–467
3. A. Perlade, D. Grandemange and T. Iung, Ironmaking Steelmaking, 32 (2005), 299–302
4. M. Militzer, ISIJ International, 47 (2007), 1–15
5. M. Militzer, J.J. Hoyt, N. Provatas, J. Rottler, C.W. Sinclair and H. Zurob, JOM, 66 (2014), 740–746
6. M. Militzer, Current Opinion in Solid State and Materials Science, 15 (2011), 106–115
7. K. Banerjee, M. Militzer, M. Perez and X. Wang, Metallurgical and Materials Transactions, 41A (2010), 3161–3172
8. I. Steinbach, F. Pezzola, B. Nestler, M. Seeßelberg, R. Prieler, G.J. Schmitz and J.L.L. Rezende, Physica D, 94 (1996),135–147
9. J. Huang, W.J. Poole and M. Militzer, Metallurgical and Materials Transactions, 35A (2004), 3363–3375
10. M. Militzer, T. Garcin, M. Kulakov and W.J. Poole, The Fifth Baosteel Biennial Academic Conference, (2013), Shanghai, China
11. M. Maalekian, R. Radis, M. Militzer, A. Moreau and W.J. Poole, Acta Materialia, 60 (2012), 1015–1026
12. M. Kulakov, W.J. Poole and M. Militzer, Metallurgical and Materials Transactions, 44A (2013), 3564–3576

13. M. Kulakov, W.J. Poole and M. Militzer, ISIJ International, 54 (2014), 2627–2636
14. B. Zhu and M. Militzer, Metallurgical and Materials Transactions, 46A (2015), 1073–1084
15. B. Zhu and M. Militzer, HSLA Steels, Microalloying & Offshore Engineering Steels 2015, (2015), 387–393
16. T. Garcin, W.J. Poole, M. Militzer and L. Collins, Materials Science and Technology, 32 (2016), 708–721
17. J. Moon, J. Lee and C. Lee, Materials Science and Engineering A, 459 (2007), 40–46
18. M. Toloui, PhD Thesis, The University of British Columbia, (2015)

Recent Topics on Development of Automotive High-Strength Sheet Steels

Naoki Yoshinaga, Hiroyuki Kawata and Kazuo Hikida

Abstract In order to contribute to weight reduction of car body, advanced high-strength sheet steels have been intensively investigated. A cold-rolled sheet steel of 1180 MPa grade with superior press formability and sheet steel for hot stamping with 1800 MPa of tensile strength have been developed typically. The microstructure control for those materials and some other practical properties, such as crashworthiness, antihydrogen embrittlement, and so on, will be discussed.

Keywords Automotive steel · Stretchability · Hot stamping

1 Introduction

Advanced high-strength sheet steels have been highly demanded in order to reduce the weight of car body. Low-carbon 980 MPa cold-rolled sheet steels with or without zinc coating have been already developed and widely applied to automotive body [1–3]. As shown in Fig. 1, three different types can be supplied depending on the customer demand for press forming. Among these, Type II with good bending is mostly used. Sufficient press formability as well as crash worthiness, weldability, and antihydrogen embrittlement property is required for such high-strength sheet steels.

The higher strength level is of course very much demanded for more weight reduction. New type high-strength sheet steel with 1180 MPa of tensile strength has been developed and applied for automobiles [4]. This steel has good properties above mentioned, which will be described in the present paper in some more details. Moreover, 1800 MPa grade hot stamping material has also been developed and industrially produced [5–7]. The characteristics of this steel will be also mentioned.

N. Yoshinaga (✉) · H. Kawata · K. Hikida
Steel Research Laboratories, Nippon Steel & Sumitomo Metal Corporation, 20-1 Shintomi, Futtsu-City, Chiba 293-8511, Japan
e-mail: yoshinaga.6yr.naoki@jp.nssmc.com

T. K. Roy et al. (eds.), *Advanced High Strength Steel*, Lecture Notes in Mechanical Engineering, https://doi.org/10.1007/978-981-10-7892-7_3

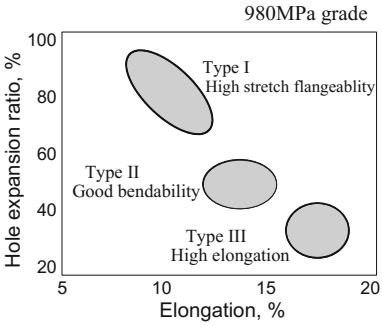

Fig. 1 Typical mechanical properties of 980 MPa low-carbon sheet steels

2 Development of 1180 MPa Grade Cold-Rolled Sheet Steel with Good Practical Performance

The typical microstructure of the developed steel is shown in Fig. 2, which is consist of martensite and bainite together with small amount of ferrite and retained austenite. The chemical compositions, especially of C, Si, and Mn, were carefully determined to have this microstructure and superior performances.

The tensile properties examined using JIS No.5 specimen and hole expansion ratio (λ) of the developed steel together with conventional high-strength DP-type steels are demonstrated in Table 1. It is obvious that the developed 1180 MPa grade has prominent elongation and λ balance with sufficient YS level, which is important for crashworthiness.

Stretchability was evaluated by means of measuring limit of dome height (LDH). The experimental procedure is described in Fig. 3. Specimen length is 200 mm and the width was changed from 115 to 130 mm to achieve near plain strain mode. It is clear from Fig. 3 that the stretchability of the developed material is as good as that of 980DP grade, because of its superior work hardenability and resulting high elongation.

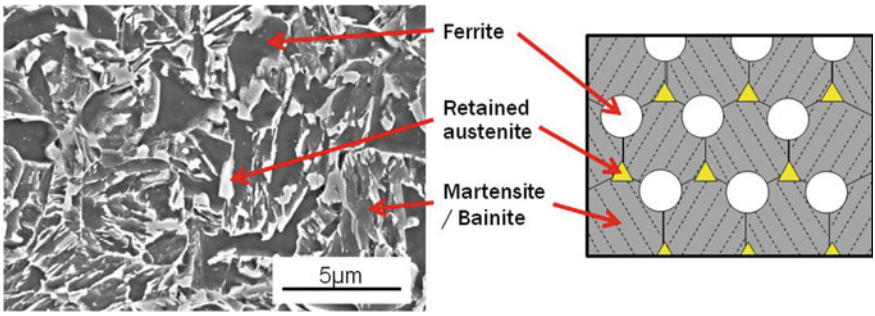

Fig. 2 SEM image of developed 1180 MPa sheet steel which consists of ferrite, martensite, bainite, and retained austenite

Table 1 Mechanical properties of steels (t = 1.2 mm)

Steel	*YS*/MPa	*TS*/MPa	*El* (%)	λ (%)
Developed	895	1199	17	48
1180DP	1063	1286	8	57
980DP	691	1015	15	30
780DP	491	822	21	27

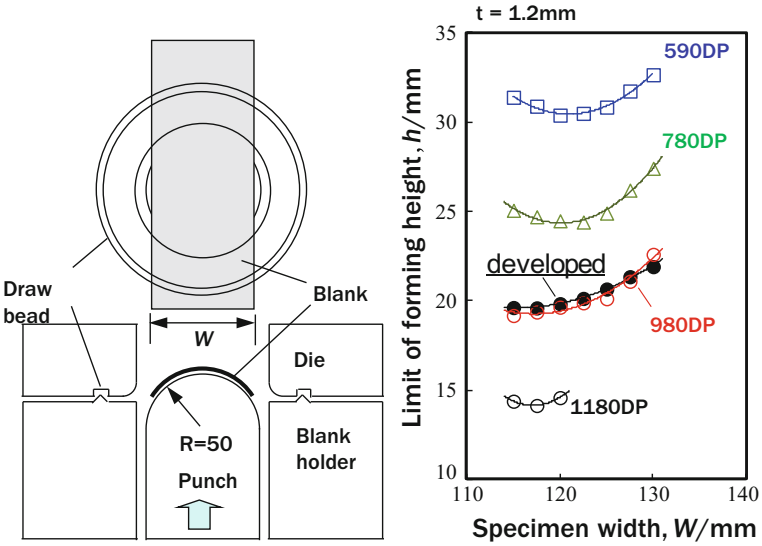

Fig. 3 Limit of dome height (LDH) derived from hemispherical punch stretching test

The influence on the weight reduction of this material was evaluated from the point of view of crashworthiness. FEM simulation for high-speed three-point bending test as described in Fig. 4 was carried out. The length of the frame is 900 mm and the cross section was hat-type closed structure. Swift type equation for stress–strain curve was employed, and the strain rate dependence was taken into account using Cowper–Symonds equation based on the experiments changing the strain rate from 10^{-3}/s to 10^{3}/s using high-speed tensile test equipment. Absorption energy was calculated at the stroke of 50 mm. The results obtained are represented in Fig. 4. It is suggested that 590 MPa DP steel with 1.6 mm in thickness can be substituted by the developed 1180 MPa grade with 1.2 mm, which corresponds to 25% weight reduction. It should be noted that this material has good property against hydrogen embrittlement.

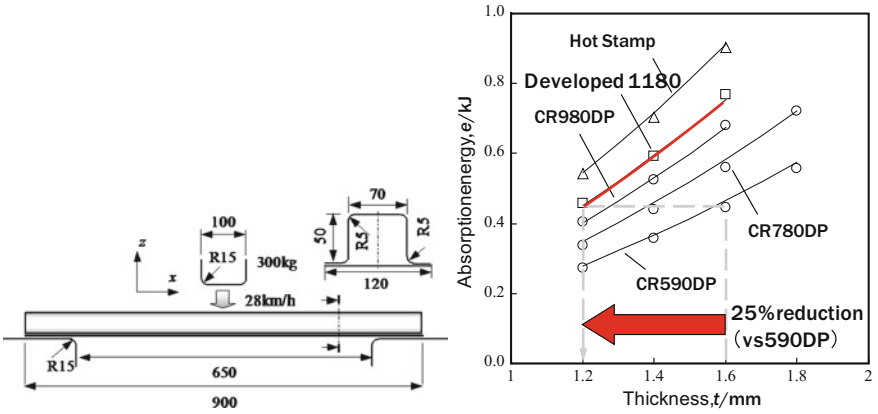

Fig. 4 Absorption energy of developed steel in comparison with some conventional high-strength steels calculated FEM simulation

3 Development of 1800 MPa Grade for Hot Stamping

The representative tensile properties of the developed material after quenching are listed in Table 2 [5, 7]. The elongation of the developed steel is almost same as that of conventional 1500 MPa grade.

As shown in Fig. 5, lath martensite microstructure is observed just after quenching in both conventional and developed steels. The critical cooling rate to have full martensite microstructure is approximately 20 °C/s according to the dilatometric experiment [6], which can be sufficiently achieved in the conventional production line of automobile parts. The prior austenite grain size is apparently refined in the developed 1800 MPa grade steel, which can contribute to have the low-temperature toughness better. The fracture surface after tensile test exhibits ductile structure in both cases. It is found in addition that the much finer dimples can be observed in the developed material.

In order to evaluate the crashworthiness of the developed steel, dynamic three-point bending test was examined. The peak force increased about 26% in the developed 1800 MPa compared to that of the conventional 1500 MPa grade, which can give rise to thickness reduction, e.g., from 1.6 to 1.4 mm.

Table 2 Tensile properties of developed steel sheet with 1800 MPa of TS after quenching

Steel grade (MPa)	YS (MPa)	TS (MPa)	El (%)	Remarks
1500	1162	1545	8.0	Conventional
1800	1267	1882	7.8	Developed

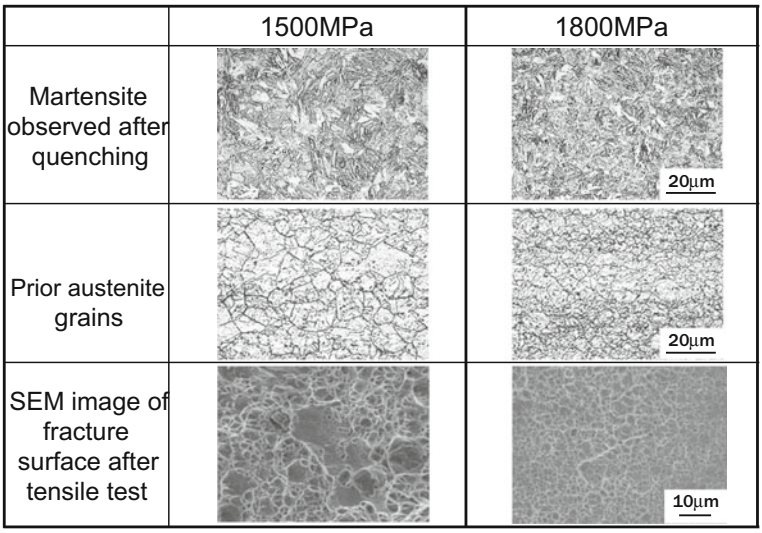

Fig. 5 Comparison of microstructures between conventional 1500 MPa and developed 1800 MPa grade

Since the cooling rate of each position depends on how contact between die and material is strong, there has been a difficulty in having aiming hardness homogeneously in whole quenched area of an automobile part. Therefore, the original quenching die has been tried to developed [8]. Water supplying nozzle is introduced in this new die so that the water quenching becomes possible, which results in the homogeneous hardness (Figs. 6 and 7).

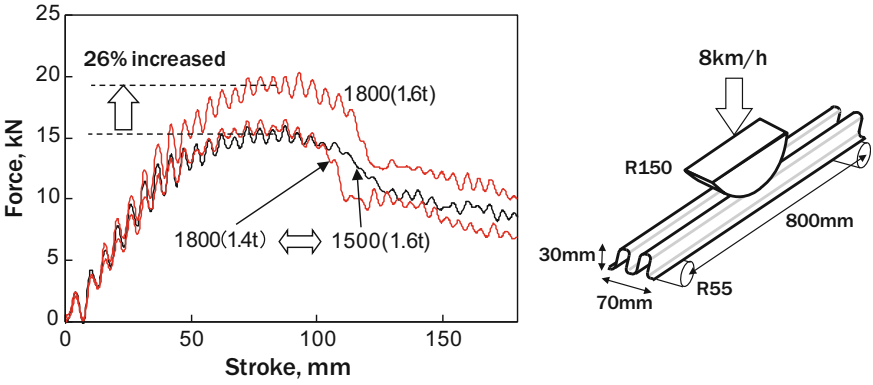

Fig. 6 Comparison of crashworthiness between developed 1800 MPa and conventional 1500 MPa grade, evaluated by dynamic three-point bending test

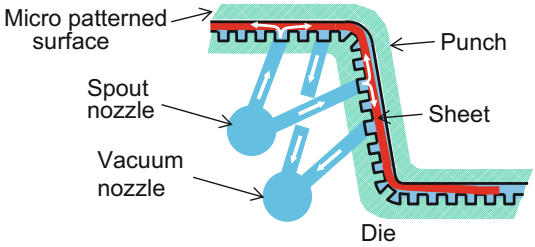

Fig. 7 Schematic illustration of direct water quenching die for hot stamping

4 Summary

High-strength sheet steels become more and more important. On the other hand, there are several obstacles needed to overcome, such as press formability, weldability, crashworthiness, hydrogen embrittlement, and so on. It is considered that the emphasis should be placed on to investigate more from fundamental and substantial aspects in the future.

References

1. N. Yoshinaga, Y. Sakuma, S. Hiwatashi, K. Shiozaki and K. Takagi, Collected abstracts of JSAE Congress (Autumn), 20045745 (2004), Society of Automotive Engineers of Japan
2. K. Takakura, K. Takagi and N. Yoshinaga, SAE International, 2006011586, (2006)
3. T. Nonaka, N. Fujita, T. Tomokiyo, K. Matsumura and T. Miyagi, Proceedings of World Automotive Congress FISITA2008, Munich Germany, F2008-04-023, (2008)
4. H. Kawata, N. Maruyama, S. Yonemura, A. Murasato, K. Honda, C. Wakabayashi and H. Hamatani, Collected abstracts of JSAE Congress (Spring), 20145314, (2014), Society of Automotive Engineers of Japan
5. T. Nishibata, N. Kojima, T. Ozawa and K. Nakashima, CAMP-ISIJ, 21 (2008), 597
6. T. Nishibata and N. Kojima, Tetsu-to-Hagané, 96 (2010), 378
7. K. Hikida, T. Nishibata, H. Kikuchi, T. Suzuki and N. Nakayama, Materia Japan, JIM, 52–2 (2013), 68
8. N. Nomura, H. Fukuchi and A. Seto, Proceedings of 5th International Conference on Hot Sheet Metal Forming of High-Performance Steel CHS^2, (2015), 549, Toronto, Canada

An Overview on Structure–Property Relationship of TRIP-Aided Steel

Ravi Ranjan, Tanmay Bhattacharyya and Shiv Brat Singh

Abstract Retained austenite in microstructure of TRIP-aided steel plays an important role and governs its performance. In the present paper, the microstructure and mechanical properties of some experimental TRIP-aided steels have been discussed. Prediction of the amount of retained austenite in the final microstructure has been done using mathematical models based on (a) artificial neural network (ANN) technique and (b) the theory of bainite transformation. The microstructure and mechanical properties of the experimental TRIP-aided steels have been studied and an attempt has been made to establish a correlation between the two. Promising results on microstructure and strength–ductility combinations along with reasonably enhanced coatability were obtained on laboratory samples.

Keywords TRIP aided steel · Artificial neural network · Retained austenite Bainite

1 Introduction

Steels are known to offer wide range of properties through minor changes in the composition and/or processing parameters. This flexibility of steel has made it one of the most widely used materials for various applications. The selection of steel composition and processing parameters is mainly dominated by the choice of the application. For example, the material for automotive applications requires it to offer high strength combined with adequate formability. This requirement with respect to the properties comes from the necessity to (a) manufacture the components with complex shapes and (b) reduce the weight of the vehicle, enhancing the fuel efficiency and reducing the greenhouse gas (GHG) emission, without compromising the safety.

R. Ranjan · S. B. Singh (✉)
Indian Institute of Technology Kharagpur, Kharagpur, West Bengal, India
e-mail: sbs22@metal.iitkgp.ernet.in

T. Bhattacharyya
TATA Steel Ltd, Jamshedpur, India

T. K. Roy et al. (eds.), *Advanced High Strength Steel*, Lecture Notes in Mechanical Engineering, https://doi.org/10.1007/978-981-10-7892-7_4

Accordingly, various steels belonging to AHSS (advanced high-strength steels) genre have been developed in the recent years. The AHSS genre in general includes steels like, Dual Phase (DP), Complex Phase (CP), Transformation Induced Plasticity (TRIP), Twinning Induced Plasticity (TWIP), etc. Among these steels, TRIP-aided Steels and TWIP steels give superior combination of strength and formability. The properties of a steel depend on its microstructure where the contributions from the conventional strengthening mechanisms (e.g., solid solution strengthening, precipitation hardening, grain refinement, etc.) determine its strength, ductility, etc. Among these strengthening mechanisms, grain refinement is perhaps the only way to achieve simultaneous improvement in the strength and formability. TRIP and TWIP steels offer additional mechanism attributed to the characteristic strain hardening behavior, which results in superior strength—formability combination. In general, a gradual strain hardening behavior of the material, extending to higher strain range, reflects better combination of strength and formability.

TWIP steels are single phase, austenitic, steels. In these steels, the application of strain results in the continuous development of deformation twins with progress of deformation. These deformation twins present additional barriers, along with the grain boundaries, to the dislocation movement and thereby enhance the strain hardening behavior in TWIP steels. The formation of deformation twin is ensured through optimum design of the composition so that its SFE (stacking fault energy) value falls in the specific range of 20–30 mJ/m^2 [1, 2]. These specific requirements of TWIP steels with respect to the microstructure and SFE value necessitate high concentration of alloying elements (25–30 wt% Mn for example) that causes problems during production. TRIP-aided steels, on the other hand, are low-alloy steels with typical total alloying addition of ≤ 5 wt% and retained austenite in the range of 5–20% [3]. The presence of a small amount of retained austenite ensures that onset of necking is delayed during the tensile test through its deformation induced transformation to martensite. The transformation of austenite to martensite, under the influence of strain, leading to enhancement in the strength—formability combination, identified first by Zackay et al. [4], is known as the TRIP (transformation-induced plasticity) effect. Other advantages of the presence of retained austenite include an improvement in the fatigue properties and crashworthiness due to the crack tip blunting effect [5–7].

In low-alloy steels (e.g., TRIP-aided Steels), austenite is stable only above a specific temperature, called the A_{C_1} temperature (austenite start temperature during heating). Therefore, the austenite in these steel has a tendency to decompose when cooled to the ambient temperature. Decomposition of austenite to phases or phase mixtures, such as, ferrite, pearlite, etc., requires long-range diffusion of solutes and therefore can be avoided by employing fast cooling rate. However, the austenite to martensite transformation cannot be avoided because of its thermal and diffusion-less nature. The only way to stabilize the austenite to ambient temperature is to lower its martensite start temperature below the ambient temperature. The martensite start temperature of austenite depends primarily on the composition. In

this aspect, carbon is the most effective element [4]. Therefore, generally a two-step thermal treatment is employed in low-alloy steel. This results in the retention of a fraction of austenite in the final microstructure [8–11]. The first step in the two-step thermal treatment, called the intercritical transformation (IT) treatment, consists of a treatment in the two-phase ferrite + austenite region. This treatment results in a local increase in the hardenability of austenite and lowering of its martensite start temperature. However, the carbon enrichment of austenite after the IT treatment is generally insufficient to lower its martensite start temperature below the ambient temperature. Therefore, a treatment is given in the bainite transformation range in the second stage, called the IBT (isothermal bainite transformation) treatment, which ensures sufficient carbon enrichment of austenite to push its martensite start temperature below the ambient temperature.

The thermal treatment philosophy suggests that the carbon enrichment of austenite during different stages of the transformation, especially during the IBT treatment, is the most important aspect. Therefore, alloying elements, such as, Si and/or Al, are added to the steel in sufficient quantity to restrict carbide precipitation. However, addition of Si in higher amounts has been reported to lead to the formation of a very strong oxide layer during high-temperature processing [12, 13]. This deteriorates the surface finish, coatability, and other surface-related properties. Therefore, Al is often selected to partially or completely replace Si taking into account its solid solution strengthening effect and its ability to inhibit carbide precipitation [14]. Phosphorous (P) is also often considered in the composition design mainly to account for the loss of solid solution strengthening on the reduction of the Si content. Moreover, *P* addition in small amounts, typically <0.1 wt%, has been reported to increase the retained austenite fraction without a noteworthy deterioration in the formability related properties, such as, strength, ductility, etc. [15].

The two-step thermal treatment can be employed via a cold rolling route or hot rolling route. However, incorporation of the two-step thermal treatment in cold rolling (conventional processing route) requires an extra step (IT treatment). This extra step adds to the cost and therefore the production of the material with the desired microstructure directly after hot rolling would save cost. In addition, hot rolling route presents an opportunity to form a TRIP-aided microstructure consisting of bainite and retained austenite, called the TRIP-aided bainitic steels. The increase in the fraction of bainite is expected to enhance the strength level achieved through conventional processing route.

Accordingly, different approaches which enable one to calculate optimum hot rolling parameters to obtain TRIP-aided microstructure are presented in the present work. In addition, results of some simulated thermo-mechanical treatments are discussed with special emphasis on the role of retained austenite on the strain hardening behavior and subsequent effect on the strength–ductility balance.

2 Thermal Treatment Design

Based on the discussion presented in the previous section, the composition and processing parameters of TRIP-aided steels are designed to achieve maximum fraction of retained austenite fraction with optimum stability. The term "optimum stable retained austenite" denotes that it is metastable at the ambient temperature so that it undergoes gradual transformation to martensite during deformation that helps maintain strain hardening in the higher strain range through the TRIP effect. The retained austenite stability is mainly influenced by the parameters selected for IT and IBT treatment with the latter being more critical. Therefore, two mathematical models have been developed to predict the amount of retained austenite as a function of the processing parameters. The first model is based on the empirical artificial neural network (ANN), while the other is based on the phase calculation following the displacive theory of bainite transformation.

2.1 Prediction of Microstructure Through Artificial Neural Network (ANN) Model

A very complex relationship between an arbitrary number of "input" variables and "output" variables is established through artificial neural network (ANN) models. These are empirical models where the relationship between "input" and "output" variables is not predetermined unlike conventional regression models [16]. The relationship between the "input" variables and "output" variables is established through training and testing the model over the experimental data [17]. Multilayer perceptron (MLP) models have been widely used in metallurgy of steel due to its widespread ability for pattern recognition and function approximation [18, 19].

An ANN model was developed in the present work to predict the amount of retained austenite ($V_{\gamma_{ret}}$, the "output" variable) as a function of composition and processing parameters, viz., intercritical annealing (IA) and isothermal bainitic transformation (IBT) temperatures ("input" variables). Data were compiled from published literature for training and testing the model. Some representative relationships of "input" and "output" variables are illustrated in Fig. 1. The relationships are reasonably consistent with the theory of transformation [20].

2.2 Phase Calculation

The conventional two-step thermal treatment is schematically presented in Fig. 2. In addition, a portion of the Fe–C phase diagram along with the T_0 curve is superimposed in Fig. 2. The T_0 curve is defined as the locus of the points where the free energies of austenite and ferrite of the same composition are equal and

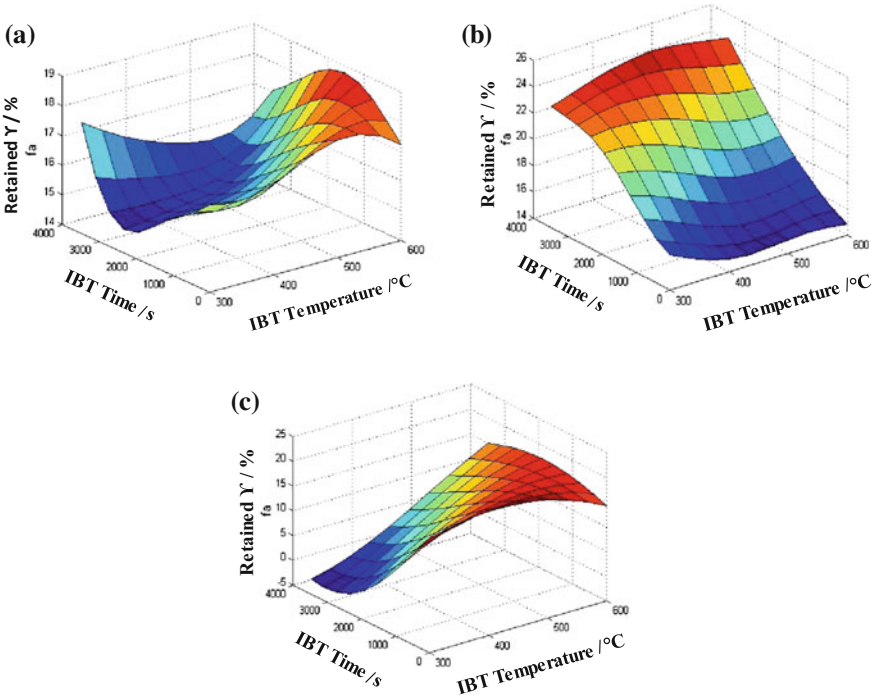

Fig. 1 Prediction of retained austenite for different IBT parameters for some experimental steels, **a** steel 1, IA 830 °C/600 s, **b** steel 2, IA 820 °C/600 s, and **c** steel 3, IA 770 °C/600 s

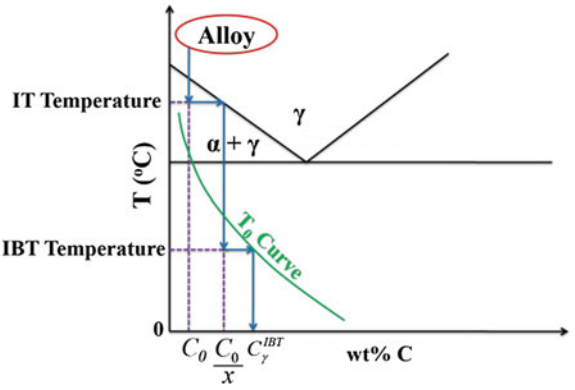

Fig. 2 Schematic diagram showing the T_0 curve superimposed on Fe–C phase diagram

represent the upper limit above which the bainite transformation is thermodynamically impossible [16, 21, 22].

The phase diagram and T_0 curve for a given composition can be calculated using a thermodynamic based software such as Thermo-Calc. This allows to obtain the

termination point of the austenite decomposition to ferrite and bainite at the respective treatment temperatures, i.e., IT and IBT respectively, as shown in Fig. 2. The fraction of ferrite, bainite, and remaining austenite after the IBT treatment can be calculated through mass balance at the two stages of transformation. The carbon enrichment of austenite after the IBT treatment, given by $C_{\gamma}^{\mathrm{IBT}}$, determines the amount of martensite that can form on cooling due to the ambient temperature (T) and the amount of austenite retained in the final microstructure. This athermal austenite to martensite transformation is generally described by the equation proposed by Koistinen and Marburger (KM) [23]. Hence, application of mass balance at the two stages of transformation in combination with the KM equation allows one to establish the correlation among the steel composition, the IT and IBT temperatures and the phase distribution. The distribution of phases is therefore given by Eq. 1 [24]. The inherent assumptions used to develop Eq. 1 are: (a) the paraequilibrium condition is maintained during the IT treatment (only carbon is partitioned from ferrite to austenite), (b) the carbon concentration in ferrite and bainitic ferrite is negligible, and (c) all the transformation reaches their cessation points. It should be noted that the bainite transformation at the IBT temperature stops when the carbon content of the untransformed austenite reaches the T_0 limit at the IBT temperature [16, 21, 22]. Thus, the carbon content of the retained austenite $\left(C_{\gamma_{\mathrm{ret}}}\right)$ and martensite (if any) in the final microstructure is the same as the carbon content of the austenite left untransformed after the IBT treatment $\left(C_{\gamma}^{\mathrm{IBT}}\right)$, i.e., $C_{\gamma_{\mathrm{ret}}} = C_{\gamma}^{\mathrm{IBT}}$.

$$\left.\begin{aligned} f_{\alpha} &= 1 - f_{\gamma};\ f_{\alpha_b} = f_{\gamma} - \left(\frac{C_0}{C_{\gamma}^{\mathrm{IBT}}}\right) \\ f_{\gamma_{\mathrm{ret}}} &= \left(C_0/C_{\gamma}^{\mathrm{IBT}}\right) \times \left(1 - f_{\alpha'}^{\mathrm{KM}}\right) \\ f_{\alpha'} &= \left(C_0/C_{\gamma}^{\mathrm{IBT}}\right) \times \left(f_{\alpha'}^{\mathrm{KM}}\right) \end{aligned}\right\} \tag{1}$$

Here, $f_{\alpha'}^{\mathrm{KM}} = \mathrm{KM\ Equation} = 1 - \exp\{-0.011(M_s - T)\}$.

An example of the calculation using Eq. 1 for an experimental C–Mn–Si–Al steel is shown in Fig. 3 [24]. It should be noted here that Fig. 3 is valid for any concentration of carbon in the alloy steel. The main role of carbon here is to affect the lowest temperature at which the bainite transformation is possible. The necessary data, such as, phase diagram, T_0 curve, were obtained using Thermo-Calc. The selection of 50% ferrite for the calculation is based on the experimental observations of different workers that indicate optimum result [25, 26].

Figure 3 indicates that the amount of retained austenite is maximum at an intermediate IBT temperature (critical temperature) when its carbon concentration is 1.16 wt%. An increase in the IBT temperature beyond this critical temperature results in a decrease in the retained austenite amount. This decrease is attributed to the increase in the fraction of martensite transformed from the remaining austenite, due to its lower carbon concentration, after the IBT treatment. Similarly, the decrease in retained austenite fraction on decrease in IBT temperature below the

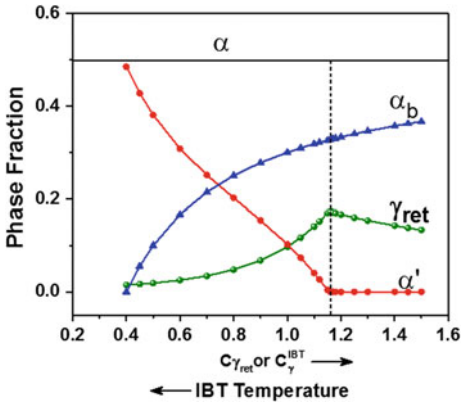

Fig. 3 Effect of austenite carbon enrichment at the IBT temperature on phase evolution. The vertical dotted line indicates the $C_{\gamma_{ret}}$ or C_γ^{IBT} value that pushes the Ms temperature of the austenite remaining untransformed at the IBT temperature to less than the quenching temperature so that no martensite forms. Since T_0 line has a negative slope, an increase in $C_{\gamma_{ret}}$ (or C_γ^{IBT}) corresponds to a decrease in the IBT temperature. The change in IBT temperature indicated here is qualitative; the exact correlation between IBT temperature and $C_{\gamma_{ret}}$ or C_γ^{IBT} would depend on the composition of the steel [24]

critical temperature is mainly associated with the continuous increase in the amount of bainite on lowering of the IBT temperature.

In spite of several simplifying assumptions, the proposed method has been observed to give a reasonably good estimation of the distribution of the phases in the final microstructure as a function of the intercritical treatment (IT) temperature and the IBT temperature [24].

3 Role of Retained Austenite on the Mechanical Behavior

As pointed earlier, the retained austenite is present in TRIP-aided Steels as a minor phase that typically falls in the range of 5–20%. Accordingly, the basic characteristic features of austenite, i.e., small volume fraction, low hardness, alone do not justify its significant impact on the strength–formability combination in TRIP-aided Steels. It has been suggested that the role of retained austenite becomes significant when it transforms to martensite during the course of straining (TRIP effect). However, the TRIP has to be triggered at an appropriate, preferably at high, strain level and should be gradual for an optimum contribution. The basic understanding of the strain hardening behavior is developed generally by a detailed analysis of the tensile stress–strain curve. Different parameters, such as average strain hardening exponent (n_{av}), incremental change in strain hardening exponent (n_{incr}), uniform elongation (e_u), etc., are used as reference.

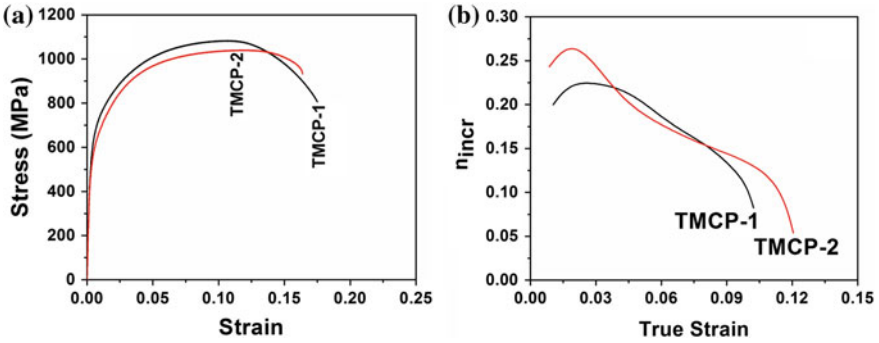

Fig. 4 **a** Engineering stress–engineering strain curves of an experimental Si–Al TRIP-aided steel processed through different TMCP schedules; **b** Strain hardening behavior of the TMCP processed steels [24]

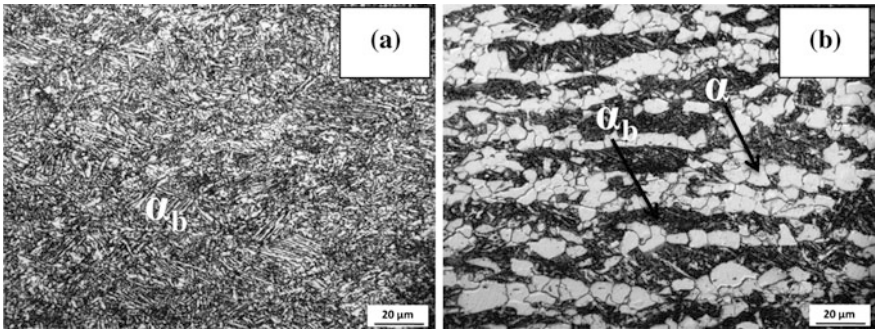

Fig. 5 Optical micrographs of Si–Al TRIP-aided steel processed through: **a** TMCP-1; and **b** TMCP-2; Etchant: Nital (2%). Here, α: ferrite; α_b: bainite [24]

A typical stress–strain curve along with corresponding incremental change in the strain hardening curve (n_{incr} vs. true strain) for an experimental Si–Al-based TRIP-aided Steel subjected to different thermo-mechanical treatments, i.e., TMCP-1 and TMCP-2, is shown in Fig. 4 [24]. The optical microstructures of the samples subjected to these thermo-mechanical treatments are given in Fig. 5 [24]. The relevant mechanical properties and measured phase distribution are given in Table 1 [24].

In general, the samples subjected to different thermo-mechanical treatment yielded excellent combination of mechanical properties (Fig. 4a and Table 1) with TMCP-1 being the best. The best combination of properties offered by the sample subjected to TMCP-1 is attributed to various factors, such as increase in the fraction of bainite (Fig. 5, finer than the conventional ferrite with higher dislocation density), a much gradual behavior of the strain hardening curve that has extended to higher strain range, etc. [24]. To analyze the role of retained austenite further, the

Table 1 Relevant mechanical properties and Phase distribution after different TMCP

Schedule	Ferrite (%)	Retained austenite		0.2% Y.S (MPa)	UTS (MPa)	e_u (%)	e_t (%)	n_{av}
		$V_{\gamma_{ret}}$	$C_{\gamma_{ret}}$ (wt%)					
TMCP-1	–	11.5	1.03 ± 0.08	621 ± 15	1076 ± 6.5	11 ± 0.10	18 ± 0.50	0.21
TMCP-2	45 ± 1.0	6.8	0.69 ± 0.01	564 ± 13	1042 ± 2.5	12 ± 0.20	16 ± 0.10	0.21

$V_{\gamma_{ret}}$: volume percentage of retained austenite $\left(=100 f_{\gamma_{ret}}\right)$; $C_{\gamma_{ret}}$: carbon content in retained austenite; *Y.S* Yield strength; *UTS* Ultimate tensile strength; e_u uniform elongation; e_t: total elongation; n_{av}: average strain hardening exponent

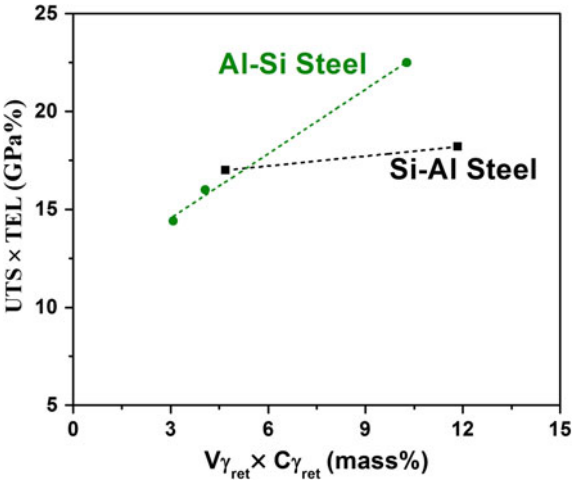

Fig. 6 Effect of retained austenite fraction and its carbon content on the strength–ductility balance [24]

mathematical product of the tensile strength (UTS) and total elongation (TEL) that defines the strength–ductility balance [27, 28] is plotted as a function of the product of the retained austenite volume fraction and its carbon concentration for the two steel composition (Si–Al Steel and Al–Si Steel [24]) (Fig. 6). This product value is effectively equal to the total concentration in the retained austenite and thus reflects its stability. The data shown in Fig. 6 clearly emphasize the enhancement in the strength–ductility balance with increase in the total carbon content of retained austenite. This presents experimental evidence of the positive contribution of the small amount of austenite retained in the microstructure on the mechanical properties of the material.

4 Coatability of TRIP-Aided Steel

Coatability of TRIP-aided steel is always a big challenge [29]. A comparative study between a conventional TRIP-aided steel (with Si content around 1.5 wt%) against steels with lower Si (with Si content around 0.6 wt%; silicon partially replaced by aluminum) has shown the following:

(a) Partial replacement of Si by Al and higher dew points during annealing significantly improved the wettability during hot dip galvanizing leading to reasonably improved coating with enhanced adherence property.
(b) The coatability improved in lower Si steel at higher dew point because of restriction in the formation of complex Si–Mn oxide.

5 Summary of the Work

Optimization of the amount of retained austenite and its stability during different mechanical and thermal conditions are important features of TRIP-aided steel. The current work is focused on the prediction of the amount of retained austenite in microstructure and its carbon content through two different methods: (a) artificial neural network (ANN) method and (b) the displacive theory of bainite transformation. A reasonably good prediction has been made by these methodologies and the outcome has been efficiently employed to develop TRIP-aided steels that offered promising structure property combinations with improved coatability. The studies on these relationships for experimental steels established an enhancement in the strength–ductility balance with an increase in the amount of the retained austenite and its carbon content.

References

1. B.C. De Cooman, K. Chin and J. Kim, New Trends and Development in Automotive System Engineering (M. Chiaberge), INTECH Open Access Publisher, (2011), 101
2. M.Y. Demeri, Advanced High-Strength Steels: Science, Technology, and Applications, ASM International, (2013)
3. G. Cole, A. Glove, R. Jeryan and G. Davies, Steel World, 2 (1997), 75
4. V.F. Zackay, E.R. Parker and E.R. Parker, ASM Trans, 60 (1967), 252
5. G.B. Olson, R. Chait, M. Azrin and R.A. Gagne, Metallurgical and Materials Transactions A, 11 (1980), 1069
6. K.-i. Sugimoto, D. Fiji, and N. Yoshikawa, Procedia Engineering, 2 (2012), 359
7. J. Danzeisen, M. Merklein and K. Roll, International Journal of Material Forming, 1 (2008), 221–224
8. A.K. Srivastava, G. Jha, N. Gope and S.B. Singh, Materials Characterization, 57 (2006), 127
9. P. Jacques, X. Cornet, Ph. Harlet, J. Ladriere and F. Delannay, Metallurgical and Materials Transactions A, 29 (1998), 2383
10. T. De Cock, J.P. Ferrer, C. Capdevila, F.G. Caballero, V. López and C.G. de Andrés, Scripta Materiallia, 55 (2006), 441
11. D.W. Suh, S.J. Park, T.H. Lee, C.S. Oh and S.J. Kim, Metallurgical and Materials Transactions A, 41 (2010), 397
12. M. De Meyer, D. Vanderschueren and B.C. De Cooman, ISIJ International, 39 (1999), 813
13. A. Pichler, P. Stiaszny, R. Potzinger, R. Tikal and E. Werner, Proc. 40th MWSP Conf., ISS, Warrendale, 1998, 259
14. B.C. De Cooman, Current Opinion in Solid State and Material Science, 8 (2004), 285
15. H.C. Chen, H. Era and M. Shimizu, Metallurgical and Materials Transactions A, 20 (1989), 437
16. H.K.D.H. Bhadeshia and R.W.K. Honeycombe, Steels Microstructure and Properties, 3rd Edition, Elsevier Ltd. (2006)
17. J. Hertz, A. Krogh and R.G. Palmer, Introduction to the Theory of Neural Computing, Addison-Wesley Publishing Company (1991)
18. S. Mandal, P.V. Sivaprasad, P. Barat and B. Raj, Materials and Manufacturing Processes, 24 (2009), 219
19. S. Datta, M.K. Banerjee, Scandinavian Journal of Metallurgy, 33 (2004), 310

20. T. Bhattacharyya, S.B. Singh, S.S. Dey, S. Bhattacharyya, W. Bleck, and D. Bhattacharjee, Materials Science & Engineering A, 565 (2013), 148
21. H.K.D.H. Bhadeshia, Bainite in Steel, 2nd Edition, Maney Materials Science, (2001)
22. S.B. Singh, Phase transformation, in Steels (E. Pereloma and D.V. Edmonds), Woodhead Publishing, (2012)
23. D.P. Koistinen and R.E. Marburger, Acta Metallurgica, 7 (1959), 59
24. R. Ranjan, H. Beladi, S.B. Singh and P.D. Hodgson, Metallurgical and Materials Transactions A, 46 (2015), 3232
25. S.J. Kim, G.C. Lee, I. Choi and S. Lee, Metallurgical and Materials Transactions A, 32 (2001), 505
26. M.F. Gallagher, J.G. Speer, D.K. Matlock and M.N. Fonstein, Proceedings of the 44th Mechanical Working and Steel Processing Conference, Iron and Steel Society, Orlando (2002), 53
27. M. Soliman and H. Palkowaski, Metallurgical and Materials Transactions A, 39 (2008), 2513
28. S. Hashimoto, S. Ikeda, K. Sugimoto and S. Miyake, ISIJ International, 44 (2004), 1590
29. T. Bhattacharyya, S.B. Singh, S. Bhattacharyya, R.K. Ray, W. Bleck and D. Bhattacharjee, Surface & Coatings Technology, 235 (2013), 226

Mechanical Properties and Applications of a New Stainless TWIP Steel

P. E. Di Nunzio, F. Ruffini and R. Guerra

Abstract A new austenitic stainless steel, Fe–18Cr–Mn–Ni–Cu deforming by mechanical twinning, has been developed to improve the mechanical properties of low-Ni stainless steels of the series 200. The steel is intended to be produced by a conventional industrial route as cold-rolled sheets. Its chemical composition has been designed by considering all the relevant issues for industrial manufacturing (i.e., residual delta ferrite content, typical amount of tramp elements), while keeping the stacking fault energy within the range for achieving the TWIP effect. Tensile tests have shown $R_{p02} > 300$ MPa, $R_m > 1000$ MPa, and El > 80% in annealed conditions. Its good resistance to delayed cracking makes it suitable for deep drawing applications as an alternative to AISI 304 in mild environment and high-Mn TWIP steels in the automotive industry.

Keywords Stacking fault energy · TWIP · Austenitic stainless steel
Mechanical twin · Annealing twin

1 Introduction

Plastic deformation in metals can be obtained by two competitive mechanisms: dislocation glide and mechanical twinning. The metallurgical parameter controlling which one prevails is the stacking fault energy (SFE). In metals with fcc lattice and small SFE, ordinary dislocations can dissociate into two components, the so-called Shockley partials. The lattice region between a couple of partial dislocations contains a stacking sequence of (111) planes which is that of an hcp lattice instead of

P. E. Di Nunzio (✉)
RINA Consulting - Centro Sviluppo Materiali, Via di Castel Romano, 100, 00128 Rome, RM, Italy
e-mail: p.dinunzio@c-s-m.it

F. Ruffini · R. Guerra
RINA Consulting - Centro Sviluppo Materiali S.p.A., Viale B. Brin, 218, 05100 Terni, TR, Italy

T. K. Roy et al. (eds.), *Advanced High Strength Steel*, Lecture Notes in Mechanical Engineering, https://doi.org/10.1007/978-981-10-7892-7_5

fcc. The mobility of these dislocations, as well as the possibility of undergoing a cross slip, is greatly reduced by the dissociation. Consequently, steels deforming by a prevailing twinning-induced plasticity (TWIP) are characterized by a high work hardening because the twins act as obstacles to the motion of ordinary dislocations (dynamic Hall–Petch effect [1, 2]).

Austenitic stainless steels have, in general, a low SFE. Therefore, the TWIP effect can be activated through an appropriate design of their chemical composition to obtain an interesting combination of properties. These can be exploited, for example, in the automotive industry or, in general, for all the applications where good mechanical properties are associated to an excellent resistance to corrosion.

The steel Fe–18Cr–Mn–Ni–Cu here developed confirms that the TWIP effect significantly improves the mechanical properties of austenitic stainless steels. In addition, since Ni is replaced by Mn, Cu, C, and N to stabilize the austenite structure and to reduce the SFE at the desired level, it is also less expensive compared to other steels of the series 300.

According to the literature [3, 4], the TWIP effect can be activated within a well-defined range of the stacking fault energy. For SFE values below about 20 mJ/m^2, the steel exhibits a TRIP behavior. The Transformation-Induced Plasticity implies the formation of ε martensite, with hcp lattice, and α' martensite with bcc lattice. Similarly, above a certain value of the SFE, the deformation mechanism by dislocation glide prevails. Thus, within the range SFE_{min}–SFE_{max}, both mechanical twinning and dislocation glide contribute to the deformation.

Therefore, the design of the new chemical composition has been aimed at finding the optimum value of the SFE which favors such a mixed deformation mechanism while preventing the formation of the undesired martensite at room temperature.

The chemical composition of an AISI 204 steel (SFE = 26 mJ/m^2) exhibiting a TRIP behavior at room temperature has been used as starting point. Thermodynamic calculations by the Thermo-Calc commercial software have been used to predict the stability of austenite and empirical models, such as that of Pickering, Schramm & Reed, and Rhodes & Thompson have been employed to estimate the SFE [5–7] aiming at a value in the range from 34 to 36 mJ/m^2. The necessary stabilization of austenite to prevent the TRIP effect has been also exploited to keep the amount of δ-ferrite as low as possible in order to ensure a good deformability during hot rolling.

The results here presented have been collected from previous works where additional details on the deformation mechanisms can be found [8, 9].

2 Materials

The steel used in the characterization has been produced in the laboratory with the following chemical composition (in mass percent): 0.07C, 10Mn, 10Cr, 2Cu, and 0.2N. It has been cast under vacuum as an 80 kg ingot, hot rolled down to a thickness of 3 mm starting at 1200 °C and finishing at 900 °C and subsequently

annealed at 1100 °C for 60 s. Finally, it has been cold rolled down to 1 mm thickness (66% deformation) and annealed at 1100 °C for 60 s to recrystallize the structure.

3 Results and Discussion

3.1 Microstructure After Cold Rolling

The microstructure after cold rolling is composed of elongated austenite grains with a high density of deformation bands arranged according one or more slip systems, as illustrated in Fig. 1a. An X-ray diffraction analysis has shown that neither ε nor α' martensite is formed during the deformation at room temperature. After annealing, the fully recrystallized microstructure is equiaxed with an average grain size of 35 µm and few annealing twins (Fig. 1b).

3.2 Evolution of the Microstructure with Cold Deformation

The evolution of the microstructure with increasing the strain from 0.05 up to 0.36 at room temperature has been investigated by optical microscopy, SEM and EBSD.

At the lowest strain level ($\varepsilon = 0.05$), no mechanical twins are observed (Fig. 2a) and deformation proceeds by dislocation glide. At $\varepsilon = 0.095$, very thin mechanical twins formed on a single slip system appear in few grains (Fig. 2b). This indicates that, similarly to the high-Mn steels, the TWIP mechanism requires a minimum level of deformation, between 5 and 10%, to be activated. With increasing the deformation in the range from 0.18 to 0.26, the volume fraction of the austenite with mechanical twins increases until eventually two slip systems, primary and

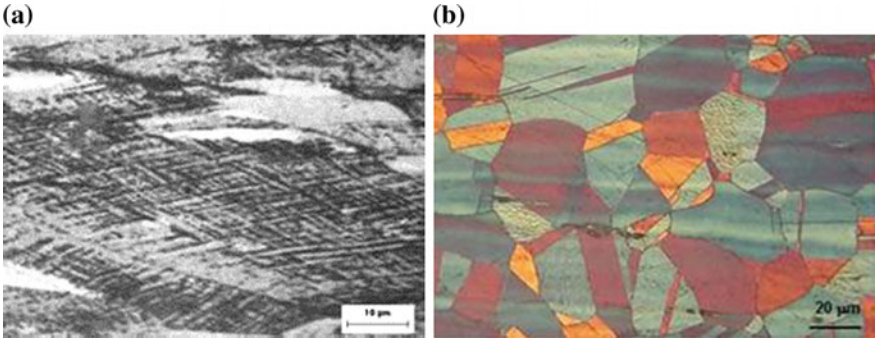

Fig. 1 Microstructures: **a** after 66% cold rolling (electrolytic etching HNO_3 + HCl); **b** after recrystallization annealing (Beraha color etching)

secondary, develop, as shown in Fig. 2c, d. A similar result is apparent from the EBSD maps reported in Fig. 3.

In general, it is observed that grains where twinning is activated have a high Taylor factor, especially during the early stages of deformation. This is in agreement with the hypothesis that for such grains dislocation glide is more difficult [10, 11]. Moreover, as deformation increases, both the fraction of grains with active twinning systems and the density of twins increase.

The material deformed at a true strain of 0.36 has been observed by TEM to evaluate the structure of mechanical twins and to check for the presence of martensite. The initial thickness of mechanical twins has been found to be about 10 nm just after the nucleation. Then, it increases with increasing the deformation up to few micrometers. Also twin bundles, composed by the further nucleation of microtwins on those previously formed, have been observed. In this specimen, the fraction of mechanical twins has been estimated around 0.16. An example of the crystallographic characterization of the twins is shown in Fig. 4. The electron diffraction pattern obtained in the twinned region within a single austenite grain exhibits the typical feature of overlapping of two crystal lattices related to each other by a common (111) reflection plane.

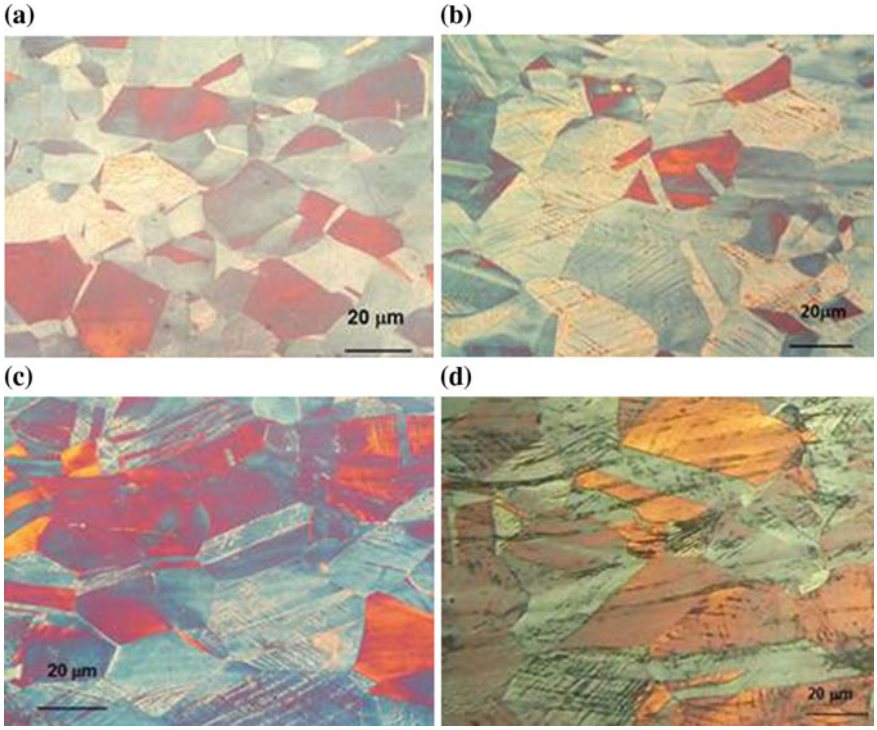

Fig. 2 Microstructure evolution after different deformations at room temperature: **a** $\varepsilon = 0.05$; **b** $\varepsilon = 0.095$; **c** $\varepsilon = 0.18$; **d** $\varepsilon = 0.26$

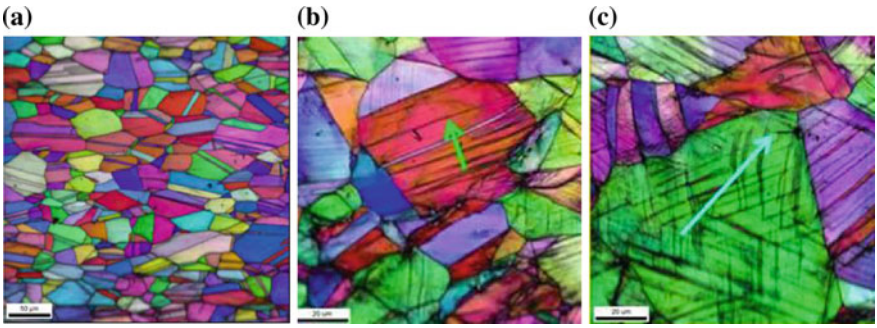

Fig. 3 EBSD maps (inverse pole figure + image quality index) of specimens deformed at room temperature: **a** $\varepsilon = 0.05$; **b** $\varepsilon = 0.095$; **c** $\varepsilon = 0.26$. Arrows indicate mechanical twins

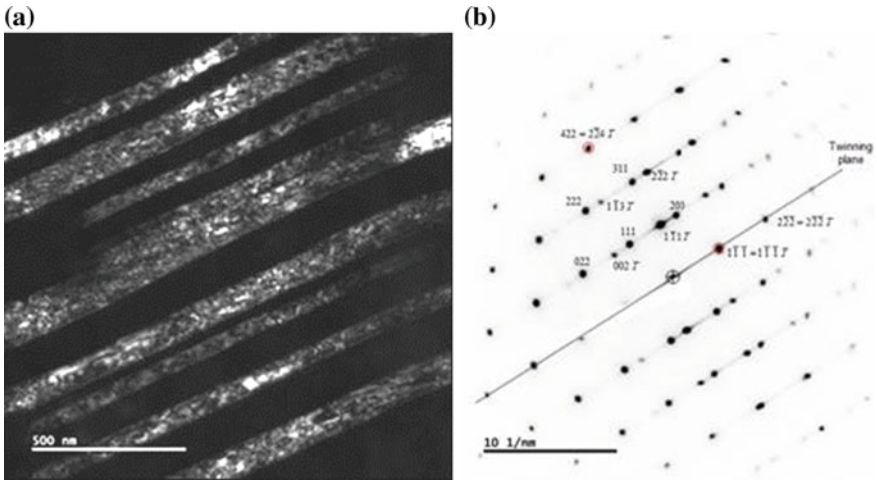

Fig. 4 TEM images of a cold deformed specimen: **a** Dark field image of mechanical twins within an austenite grain; **b** Electron diffraction pattern from the same region

3.3 Microstructure of Specimens Deformed at Low Temperature

A parameter commonly used to estimate the tendency of a stainless steel to form strain-induced martensite when deformed is the M_{d30}, i.e., the temperature at which 50% of martensite is formed after 30% deformation. This has been determined by 30% cold deforming the steel at 0, −20, and −50 °C and by measuring the fraction of strain-induced martensite by a ferritoscope obtaining 5, 20, and 45%, respectively. These results permit to estimate an M_{d30} of about −50 °C, i.e., well below the room temperature, thus explaining why strain-induced martensite is not found after cold rolling at room temperature. By comparison, the Angel's empirical

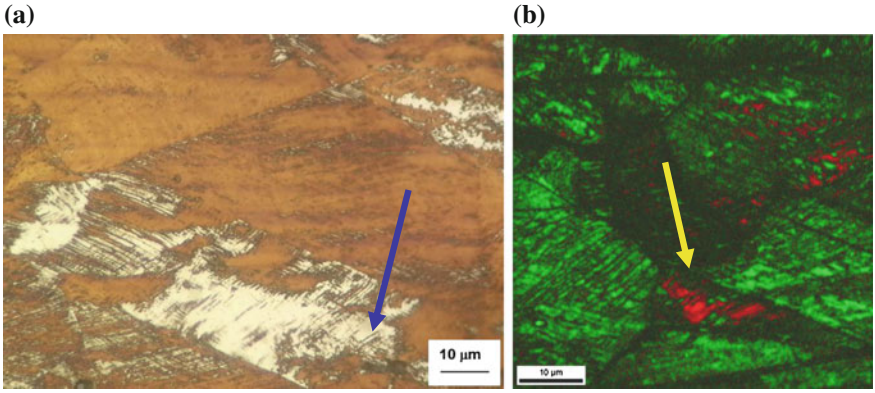

Fig. 5 Arrows show martensite in a specimen deformed at −50 °C with $\varepsilon = 0.26$: **a** Optical microscope image; **b** EBSD map (phase distribution + image quality index)

equation [12] yields −21 °C. The deformation-induced martensitic transformation has also been studied by EBSD. An example is illustrated in Fig. 5.

3.4 Determination of the Stacking Fault Energy

The experimental determination of the SFE of the newly developed steel permits to define its relative position compared to the reference material AISI 304 (SFE = 26 mJ/m^2) and to predict its evolution with temperature according to the Ericsson equation [13, 14]. Measurements by TEM have been carried out on thin foils of the annealed steel subjected to a small deformation (around 3–4%) to introduce a controlled dislocation density by observing the extended nodes. The SFE is calculated by the equation of Ruff and Ives [15] which uses the radius W of the circle inscribed in the node

$$\mathrm{SFE} = k \cdot \, G b^2 / W, \tag{1}$$

where G is the shear modulus, b the modulus of the Burgers vector, and k a constant of the order of unity. By measuring about 10 nodes in the best geometric conditions, a SFE of 35.7 ± 1.2 mJ/m^2 has been determined.

3.5 Tensile Properties as a Function of Temperature

Tensile properties of the new TWIP steel have been determined on the cold-rolled and annealed material in the temperature range from −50 to +100 °C by tensile tests

with constant strain rate of 2.5×10^{-4} s^{-1} up to 20 °C and 7.0×10^{-5} s^{-1} above 60 °C. True stress versus true strain curves are reported in Fig. 6a. Similar curves of the steels AISI 304 and AISI 204 at room temperature are also shown for comparison. Curves of the calculated strain hardening rate ($d\sigma/d\varepsilon$) are reported in Fig. 6b.

It can be observed that at room temperature, the new steel has a better performance compared to AISI 204 and AISI 304 grades since it exhibits a higher ultimate tensile strength (about 1100 MPa) together with an excellent ductility (total elongation is close to 80%). The strain hardening rate at room temperature is higher than that of AISI 304 steel. Its behavior with temperature is typical of the austenitic stainless steels. As temperature is decreased, both yield strength and ultimate tensile strength increase while the total elongation remains high. At the

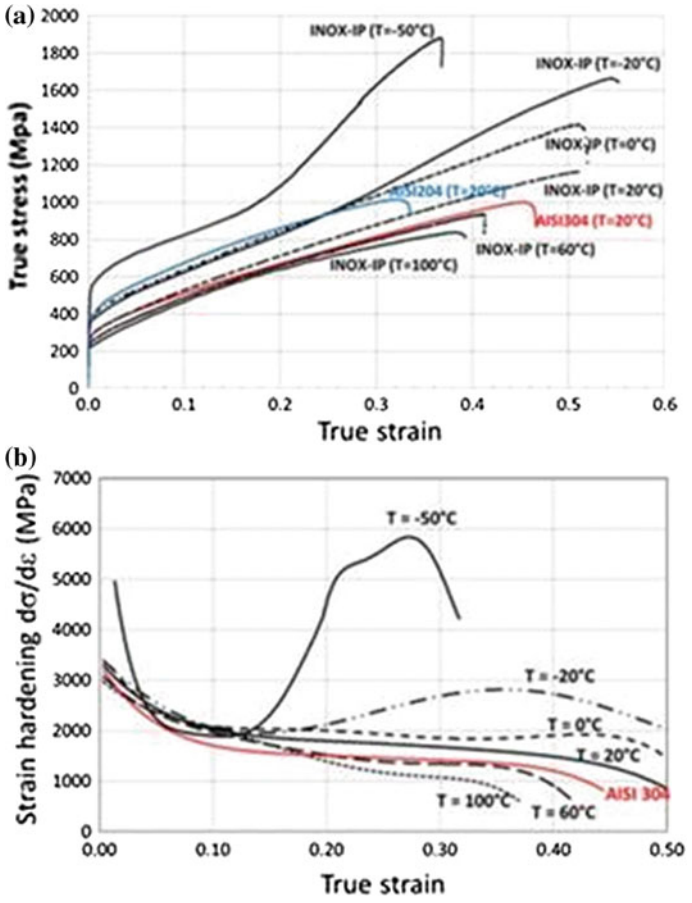

Fig. 6 Tensile properties as a function of temperature: **a** True stress versus true strain; **b** Strain hardening rate

lowest temperatures, −20 and −50 °C, close to the M_{d30}, the TRIP behavior, implying the formation of α' martensite, is activated and the strain hardening rate increases noticeably.

4 Discussion and Conclusions

A new austenitic stainless steel, Fe–18Cr–Mn–Ni–Cu deforming by mechanical twinning, has been developed to improve the mechanical properties of low-Ni stainless steels of the series 200. The microstructural and mechanical investigations here presented have confirmed that by an accurate design of its chemical composition, the TWIP effect can be exploited from room temperature up to about 100 °C without inducing any martensitic transformation and achieving a very interesting combination of mechanical properties. In fact, it exhibits a high ultimate tensile strength of about 1000 MPa and an excellent ductility with a total elongation up to 80%.

Additional tests not reported here have demonstrated that it also possesses an excellent deep drawability, comparable with that of AISI 304 steel and that it does not suffer from delayed cracking. From the viewpoint of corrosion resistance, it is more similar to steels of the series 200 rather than to AISI 304, but nevertheless it has an intrinsic advantage if compared to high-Mn TWIP steels with similar tensile properties.

Since the steel is intended to be produced by a conventional industrial route as cold-rolled sheets, the design of its chemical composition has taken into account the unavoidable presence of trace elements that are typical of an EAF-based production route. Regarding its future industrialization, a further advantage that deserves to be mentioned is that the production cost has been estimated 30% lower compared to that of AISI 304.

To conclude, all these characteristics make the new steel very attractive for deep drawing applications as an alternative to AISI 304 in mild environment and high-Mn TWIP steels, for example, in the automotive industry where a high resistance to impact is required.

References

1. A. Chateau and O. Bouaziz, Materials Science and Engineering: A, 387–389 (2004), 143–147
2. I. Gutierrez-Urrutia and D. Raabe, Acta Materialia, 59 (2011), 6449
3. C. Scott, S. Allain, M. Faral and N. Guelton, Metallurgical Research & Technology, 103 (2006), 293–302
4. M.A. Meyers and O. Vohringer, Acta Materialia, 49 (2001), 4025–4039
5. F.B. Pickering and G.L. Dunlop (Eds.), Stainless Steels 84. Chalmers University of Technology, Göteborg, 3–4 September, 1984, The Institute of Metals, (1985), p. 12, London

6. R.E. Schramm and R.P. Reed, Metallurgical and Materials Transactions A, 6 (1975), 1345–1355
7. C.G. Rhodes and A.W. Thompson, Metallurgical and Materials Transactions A, 8 (1977), 1901–1911
8. A. Ferraiuolo, S. Cicalé and A. Costa, New stainless TWIP steel Fe-17Cr-MnNiCu: mechanical properties characterization and microstructure evolution during deformation, Proc. TMP 2016 Conference, 26–28 October 2016 Milano, Italy
9. A. Ferraiuolo, New stainless TWIP steel characterized by excellent plasticity and suitable for light-weighting steel components for automotive applications, Proc. 2nd International Conference on High Manganese Steels 2014 (HMnS2), August 31–September 4, (2014), Aachen, Germany
10. I. Gutierrez-Urrutia, S. Zaefferer and D. Raabe, Materials Science and Engineering: A, 527 (2010), 3552–3560
11. D. Xianfeng, D. Wanga, K. Wanga and F. Han, Philosophical Magazine Letters, 93 (2013), 316–321
12. T. Angel, Journal of the Iron and Steel Institute, 177 (1954), 165–174
13. T. Ericsson, Acta Materialia, 14 (1966), 853–863
14. L. Remy, Acta Metallurgica, 25 (1977), 173–179
15. A.W. Ruff and L. K. Ives, Acta Metallurgica, 15 (1967), 189–198

Evolution of Texture in Some Mn Steel

Rajib Kalsar and Satyam Suwas

Abstract Deformation texture, microstructure, and tensile properties have been studied in a high Al containing TWIP steel with a composition Fe–12Mn–0.6C–5.5Al. Alloy was cold rolled to a large reduction in thickness ($\varepsilon_t \approx 3$). The deformed microstructure has been characterized by X-ray diffraction and electron backscatter diffraction. Bulk X-ray texture reveals the development of Bs-type texture with deformation. Microstructural features indicate the occurrence of different deformation mechanisms at different reduction levels. At very early stage of deformation, dislocation slip is the dominant mechanism, at intermediate stage, deformation takes place by twinning, and at large strains, the deformation is governed by shear banding. Significant improvement of yield strength is observed by the addition of Al.

Keywords Structure · Texture · Microstructure · Yield strength

1 Introduction

For the past few decades, twinning-induced plasticity in steels is a subject of great interest for both academic and industrial research due to their excellent mechanical properties such as high strength and good ductility [1–4]. Banana diagram in Fig. 1 shows the existence of TWIP steels in all kinds of automobile materials [5]. These steels primarily contain Mn and C in addition to Fe. Fe–Mn–C-based steels exhibit very high strain hardening rate due to the formation of very high fraction of deformation twins [6]. This can lead to dynamic Hall–Petch effect in TWIP steels [7, 8].

R. Kalsar · S. Suwas (✉)
Department of Materials Engineering, Indian Institute of Science, Bangalore 560012, India
e-mail: satyamsuwas@materials.iisc.ernet.in

T. K. Roy et al. (eds.), *Advanced High Strength Steel*, Lecture Notes in Mechanical Engineering, https://doi.org/10.1007/978-981-10-7892-7_6

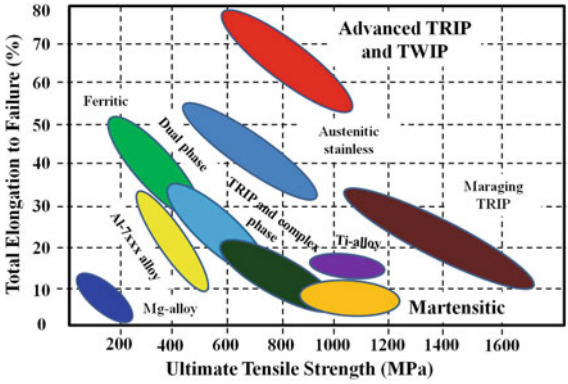

Fig. 1 Schematic illustration of strength–elongation properties of structural materials (ferrous and nonferrous) generally used in automobile applications [5]

In this effect, original grain is progressively subdivided by lamellar twins during plastic deformation, which in turn leads to reduction in the mean free path of dislocations resulting in higher strain hardening rate. Some authors also attribute very high strain hardening rate to dynamic strain aging (DSA) [9–12]. The deformation mechanisms in TWIP steels strongly depend on stacking fault energy (SFE) [13, 14], hence is a strong function of composition and temperature [15, 16]. It is reported that addition of Al and C generally increases the SFE [17]. Addition of manganese, on the other hand, stabilizes the austenite phase by lowering down the transformation temperature. For alloys with SFE in the range of 20–50 mJ m^{-2}, deformation takes place by mechanical twinning whereas for materials with SFE below 15 mJ m^{-2} , deformation is governed by martensitic transformation [18, 19]. The critical value of SFE for the transition from strain-induced phase transformation to mechanical twinning has been reported by Remy and Pineau [14] is SFE > 9 mJ m^{-2}, and the maximum value of SFE for the formation of ε- martensite is 12 mJ m^{-2}.

It is well known that FCC materials develop characteristic textures on deformation, which depends on the SFE. Materials with higher SFE (i.e., Al, Ni, and Cu) do not deform by twinning and develop a strong Cu-type texture, while the materials with low SFE (i.e., Ni60Co, Cu-30Zn, and Ag) generally deform by twinning and develop Bs-type texture [20–22]. Recently, Madhavan et al. [23–25] reported Cu-type to Bs-type texture transition in Ni–Co alloy, materials with SFE in the same range as TWIP steel at very large rolling strains.

The present investigation deals with evolution of texture, microstructure, and mechanical properties in an Al-modified medium Mn TWIP steel, namely with a composition, Fe–12Mn–0.6C–5.5Al. The material has been cold rolled to very large strains ($\varepsilon_t \approx 3$). The structural changes as well as the evolution of texture and microtexture have been studied using X-ray diffraction, X-ray texture measurement, and EBSD, respectively, with rolling strain. The mechanical properties have been evaluated for this steel using tensile test.

2 Experimental

2.1 Material and Processing

The TWIP steel with composition Fe–12Mn–0.6C–5.5Al was melted in a tungsten arc melting furnace under an Ar atmosphere. Nearly 25 gm charge was melted several times to get homogeneous composition. As-melted button-shaped sample was homogenized in a furnace at 1100 °C for 5 h under high vacuum ($<10^{-5}$ mbar). The homogenized button was cross rolled up to 50% reduction in thickness and then annealed at 830 °C for 30 min. An equiaxed microstructure with average grain size ~50 μm was obtained after this treatment. The so-obtained plate was treated as the starting material. The plate was rolled to thickness reductions 40, 70, 90, and 95%.

2.2 Characterizations

Structural characterization of the material at different stages was carried out by X-ray diffraction. Bulk crystallographic textures were measured for starting as well as cold-rolled samples using a Bruker D8 discover diffractometer based on the Schultz reflection geometry, equipped with a four-circle goniometer employing Cok_{α} (λ = 0.1791 nm) target. Four incomplete pole figures (111), (200), (220), and (311) were measured. Measurement was performed at the mid-section parallel to the rolling plane. All the measurements were carried out in the range phi = 0°–360° and chi = 0°–75° with a step size 5° and exposure time 5 s. The orientation distribution functions (ODFs) were calculated from the four measured pole figures using MTex$^{(R)}$, a MATLAB-based texture analysis tool [26]. Microstructural characterization was performed in a FEI ESEM-Quanta scanning electron microscope (SEM), equipped with electron backscatter diffraction (EBSD) system. EBSD scans were recorded on the transverse (TD) plane. The TD plane of the rolled samples was polished metallographically followed by electropolishing. Struers ElectroPol-5 electropolishing system was used for EBSD sample preparation. The analysis of the EBSD scans was done using TSL-OIM software. The mechanical properties were evaluated by carrying out tensile tests on annealed strips. For tensile tests, dog-bone-shaped samples with 6 mm gauge length, 2 mm width, and 0.7 mm thickness were used. Tensile tests were carried out in a Servo-hydraulic UTS machine at room temperature with strain rate of 6×10^{-3}/sec. All the tests were carried out up to fracture.

3 Results and Discussion

3.1 Structural Characterization by X-Ray Diffraction

Figure 2 shows the X-ray diffraction patterns of the starting materials and the cold-rolled samples. The patterns indicate the stability of austenite phase up to a very large strain ($\varepsilon_t \approx 3.0$). Traces of strain-induced α'-martensite (BCC) phase are observed at very high rolling strain. No ε-martensite (HCP) has been observed at any deformation level. Since, the peak intensity of martensite phase is very less, it can be assumed that deformation mainly takes place purely by deformation-based mechanisms (e.g., slip, partial slip, or twinning) rather than transformation-based mechanisms like deformation-induced martensitic transformation.

3.2 Evolution of Bulk Texture

The $\Phi_2 = 0°$, 45°, and 65° sections for the orientation distribution function (ODF) plots for the deformed samples are shown in Fig. 3. The ODF sections show a brass (Bs) type texture in all the cold-rolled samples. The highest volume of $f(g)$ has been observed at Goss ($\{110\}\langle 001\rangle$) position and small intensities at Cu ($\{112\}\langle 111\rangle$) and S ($\{123\}\langle 634\rangle$) locations. Many authors have reported Bs-type texture evolution during rolling in high Mn TWIP steels [27–29]. These authors also examined the texture evolution using viscoplastic self-consistent (VPSC) modeling for further understanding of the contributions of slip and twinning to texture evolution and have reported that twinning plays a predominant role in the formation of Bs-type texture. In the ODFs, weak γ-fiber ($\{111\}\|$ND) is also observed ($\Phi_2 = 45°$). The γ-fiber intensity remains the same throughout the

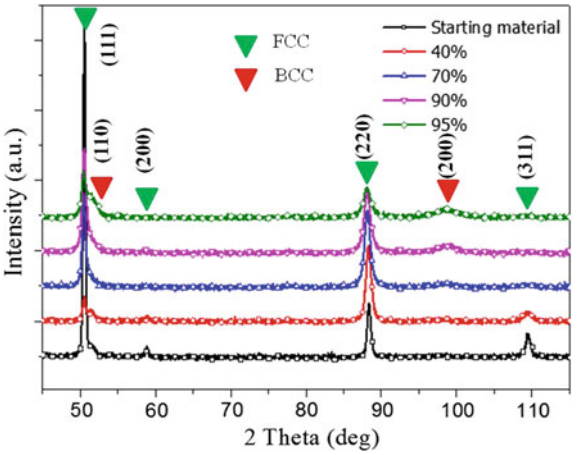

Fig. 2 X-ray diffraction patterns recorded from the starting material and after cold rolling to 40, 70, 90, and 95% reduction

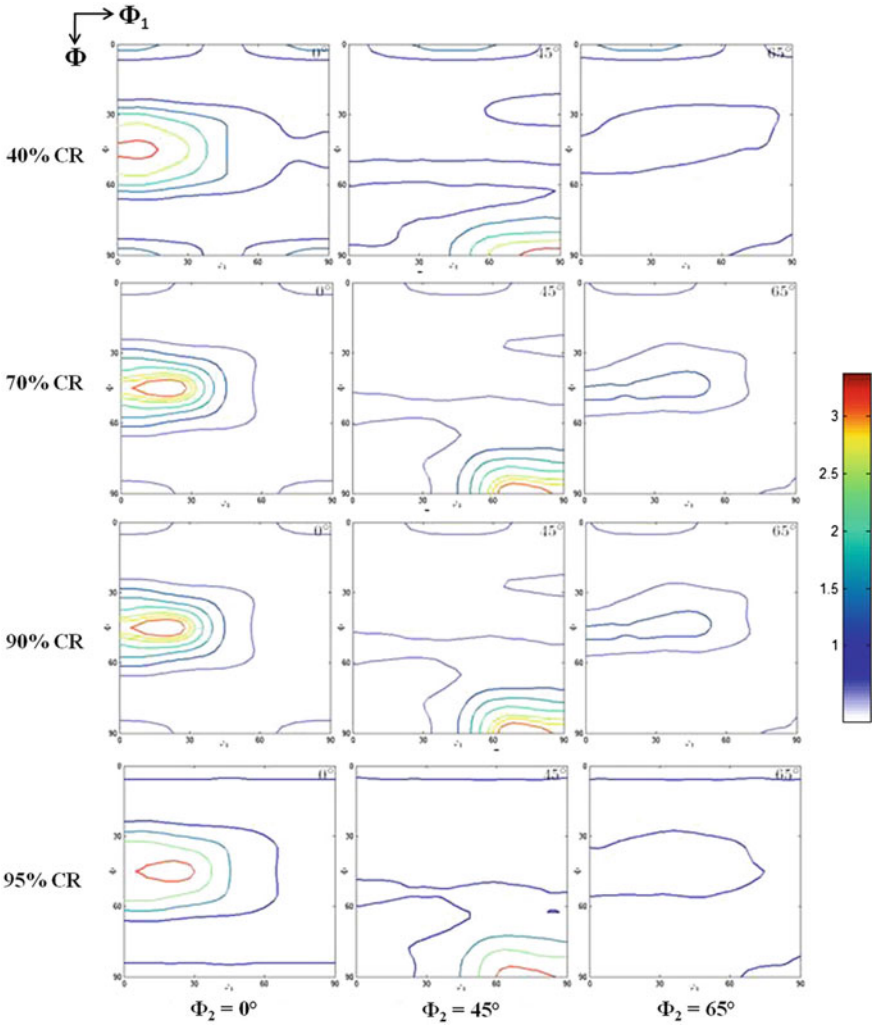

Fig. 3 Φ_2 = 0°, 45°, and 65° ODF sections of 40 to 95% cold-rolled TWIP steel

deformation. The development of such a weak γ-fiber is reported by many authors earlier for TWIP steels [27, 30] and other low-SFE materials [23–25, 31].

In order to depict the texture changes more clearly, texture fibers have been plotted. These plots show the relative texture intensity change, $f(g)$ with deformation corresponding to different texture components. Figure 4 shows the α-fiber (⟨110⟩||ND) and β-fiber (⟨110⟩||ND tilted 60° from ND toward TD). The α-fiber comprises Goss and Bs components, whereas β-fiber connects Cu, S and Bs ({110} ⟨112⟩) components. It can be seen that up to 90% thickness reduction, the intensity of Goss component along the α-fiber increases. However, at higher reduction levels,

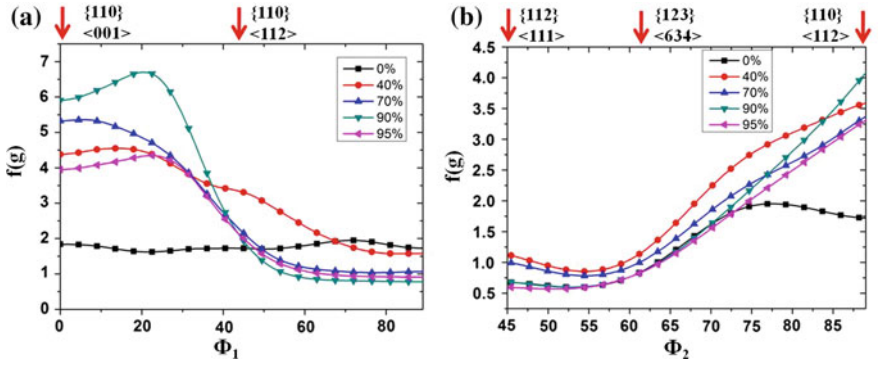

Fig. 4 Variation of intensity of texture components in terms of $f(g)$ along **a** α-fiber, and **b** β-fiber

the intensity of Goss component decreases (Fig. 4a). On the contrary, the intensities of Cu and S components along β-fiber remain the same throughout the deformation level howsoever weak (Fig. 4b).

3.3 Microtexture Evolution

Figure 5 shows the EBSD generated inverse pole figure (IPF) maps of the deformed samples. Figures 5a and b reveal the presence of deformation twins in many grains as well as very large deformation gradients inside the grains in the 40% rolled sample. However, the observed twin fraction is lesser compared to that reported in TWIP steels with the compositions of 16–30 wt% Mn [17, 32, 33]. This indicates that the addition of Al reduces the extent of deformation twinning in TWIP steels. It is well known that the critical stress for deformation twinning is inversely proportional to SFE of FCC materials [34]. It has been reported that the addition of 1wt% of Al increases the SFE by 7.8 mJ/m^2 in Fe–18Mn–0.6C TWIP steels [17]. The present alloy contains 5.5 wt% Al, therefore, it is expected to have higher SFE than the Al-free TWIP steels reported in literature. This could be the possible reason for lesser fractions of deformation twins in the microstructures. The prominent feature of the orientation is the presence of very large orientation gradients inside the grains. Such a feature is the characteristic of slip-based deformation. This suggests that in the material under present investigation, deformation takes place primarily by slip. Figures 5c and d display the microstructures of 50 and 70% deformed samples, respectively. Both the microstructures exhibit heavy shear banding at these deformation levels. The shear-banded regions are heavily deformed and could not get indexed in EBSD. Hence, the unindexed regions are considered as shear bands, which mainly form at 35°–45° angle with respect to the rolling direction (RD).

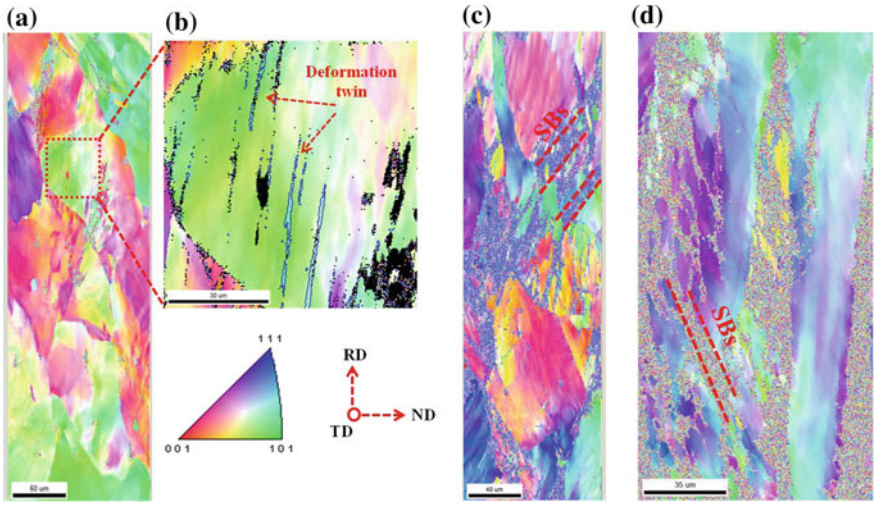

Fig. 5 EBSD microstructures: **a** inverse pole figure (IPF) of 40% rolled, **b** enlarged portion of **a**. **c** IPF of 50% rolled sample. **d** IPF of 70% rolled sample

These shear bands are also known as brass-type shear bands. Formation of Bs-type shear bands in low-SFE materials is reported by many authors at large strain [13, 23, 25, 28, 35].

3.4 Mechanical Properties

The tensile stress–strain curve of the experimental alloy Fe–12Mn–0.6C–5.5Al is shown in Fig. 6. The engineering stress–strain plot shows an excellent combination of mechanical properties with a yield strength (YS) ~750 MPa, ultimate tensile strength (UTS) ~ 1100 MPa, and ductility ~55%. Although TWIP steels exhibit very high ultimate tensile strength and uniform elongation, it has poor yield strength which imposes a limit to the designs for different components. Even though Al addition increases the SFE and decreases the twin probability in TWIP steels, it has a strong positive effect on yield strength. The probable mechanism for enhancement of yield strength in TWIP steels by the addition of Al could be solid solution strengthening [17]. Figure 6b shows the reported yield strength of various TWIP steels along with the present material, that is, Fe–12Mn–0.6C–5.5Al. It clearly shows a significant increase in yield strength due to the addition of Al to the TWIP steel Fe–12Mn–0.6C.

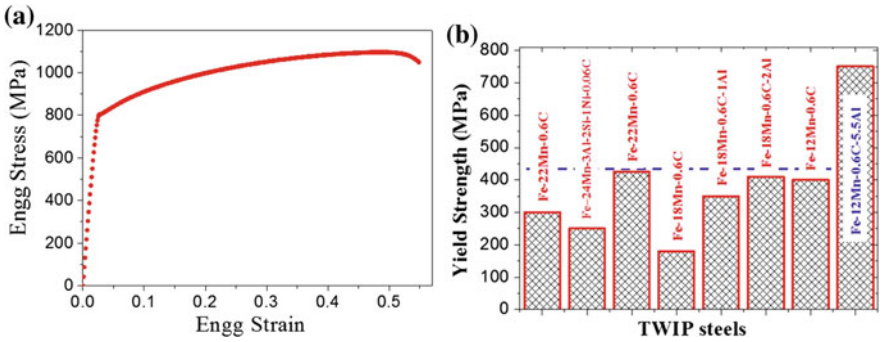

Fig. 6 **a** Tensile stress–strain curve of Fe–12Mn–0.6C–5.5Al TWIP steel. **b** Comparative yield strength (MPa), plotted with Fe–12Mn–0.6C–5.5Al TWIP steel and data available in literature [17, 27, 32, 36, 37]

4 Conclusions

Based on the structural characterization as well as macro- and microtextures and mechanical characterization of a Fe–12Mn–0.6C–5.5Al TWIP steel, the following conclusions can be drawn:

1. The composition Fe–12Mn–0.6C–5.5Al is very stable on deformation. Very small or negligible fraction of strain-induced martensite forms at very large rolling strains.
2. The texture of as-rolled materials is primarily Bs-type throughout the deformation level. Very week Cu and S components are observed at very early and intermediate stages of deformation. The evolution of a weaker fiber is noticed since early stages of deformation, which remains unchanged up to very large strains ($\varepsilon_t \approx 3.0$).
3. Three micromechanisms of deformation have been noticed depending on the amount of deformation, namely, large deformation gradient, twinning, and shear bands. The sequence of mechanisms is as follows. For lower deformation, micromechanism operative is normal slip, then for intermediate deformation, it is deformation twinning and at large strains, deformation is governed by shear banding.
4. A significant increase in yield strength has been observed in the Al-added TWIP steel, which is almost twice the yield strength of Al-free TWIP steel corresponding to this composition.

Acknowledgements This work was inspired by a grant from R & D Division, Tata Steel India Ltd. The authors are grateful to Drs. S. Chandra and S. Kundu for many useful discussions. The extensive use of microscopes at the Advanced Facility of Microscopy and Microanalysis (AFMM) facility and XRD at the Institute X-ray facility, Indian Institute of Science, Bangalore is also acknowledged.

References

1. O. Bouaziz, S. Allain, C.P. Scott, P. Cugy and D. Barbier, Current Opinion in Solid State & Materials Science, 15 (2011), 141–168
2. B.C. DeCooman, O. Kwon and K. Chin, Materials Science and Technology, 28 (2012), 513–527
3. Neu, R., Mater Perform Charact, 2 (2013), 244–284
4. O. Grässel, L. Krüger, G. Frommeyer and L.W. Meyer, International Journal of Plasticity, 16 (2000), 1391–1409
5. C. Herrera, D. Ponge and D. Raabe, Acta Materialia, 59 (2011), 4653–4664
6. O. Bouaziz, S. Allain and C. Scott, Scripta Materialia, 58 (2008), 484–487
7. L. Remy, Acta Materialia, 26 (1978), 443–451
8. I. Karaman, H. Sehitoglu, A.J. Beaudoin, Y.I. Chumlyakov, H.J. Maier and C.N. Tomé, Acta Materialia, 48 (2000), 2031–2047
9. K. Renard, S. Ryelandt and P. Jacques, Materials Science and Engineering: A, 527 (2010), 2969–2977
10. L. Bracke, J. Penning and N. Akdut, Metallurgical and Materials Transactions A, 38 (2007), 520–528
11. S. Lee, J. Kim, S.-J. Lee and B.C. DeCooman, Scripta Materialia, 65 (2011), 528–531
12. L. Chen, H.-S. Kim, S.-K. Kim and B.C. DeCooman, ISIJ International, 47 (2007), 1804–1812
13. L. Bracke, K. Verbeken, L. Kestens and J. Penning, Acta Materialia, 57 (2009), 1512–1524
14. L. Remy, and A. Pineau, Materials Science and Engineering, 28 (1977), 99–107
15. T.-H. Lee, E. Shin, C.-S. Oh, H.-Y. Ha and S.-J. Kim, Acta Materialia, 58 (2010), 3173–3186
16. S. Curtze, V.-T. Kuokkala, A. Oikari, J. Talonen and H. Hänninen, Acta Materialia, 59 (2011), 1068–1076
17. J.-E. Jin and Y.-K. Lee, Acta Materialia, 60 (2012), 1680–1688
18. G. Olson, and M. Cohen, J. Less-Common Met., 28 (1972), 107–118
19. S. Allain, J.-P. Chateau, O. Bouaziz, S. Migot and N. Guelton, Materials Science and Engineering: A, 387 (2004), 158–162
20. J. Hirsch and K. Lücke, Acta Metallurgica, 36 (1988), 2883–2904
21. T. Leffers and R. Ray, Progress in Materials Science, 54 (2009), 351–396
22. R. Smallman and D. Green, Acta Metallurgica, 12 (1964), 145–154
23. R. Madhavan, R. Ray and S. Suwas, Acta Materialia, 74 (2014), 151–164
24. R. Madhavan, R. Ray and S. Suwas, Acta Materialia, 78 (2014), 222–235
25. R. Madhavan and S. Suwas, Philosophical Magazine Letters, 94 (2014), 548–555
26. F. Bachmann, R. Hielscher and H. Schaeben. Texture analysis with MTEX–free and open source software toolbox. in Solid State Phenomena. (2010). Trans Tech Publ
27. A.A. Saleh, C. Haase, E.V. Pereloma, D.A. Molodov and A.A. Gazder, Acta Materialia, 70 (2014), 259–271
28. N.P. Gurao, P. Kumar, B. Bhattacharya, A. Haldar and S. Suwas, Metallurgical and Materials Transactions A, 43 (2012), 5193–5201
29. C. Haase, S.G. Chowdhury, L.A. Barrales-Mora, D.A. Molodov and G. Gottstein, Metallurgical and Materials Transactions A, 44 (2013), 911–922
30. S. Vercammen, B. Blanpain, B.C. DeCooman and P. Wollants, Acta Materialia, 52 (2004), 2005–2012
31. J. Hirsch and K. Lücke, Acta Metallurgica, 36 (1988), 2863–2882
32. J.-E. Jin and Y.-K. Lee, Materials Science and Engineering: A, 527 (2009), 157–161
33. I. Gutierrez-Urrutia and D. Raabe, Acta Materialia, 59 (2011), 6449–6462
34. T. Byun, Acta Materialia, 51(2003), 3063–3071

35. R. Garg, S. Ranganathan and S. Suwas, Materials Science and Engineering: A, 527 (2010), 4582–4592
36. D. Barbier, N. Gey, S. Allain, N. Bozzolo and M. Humbert, Materials Science and Engineering: A, 500 (2009), 196–206
37. S. Lee, Y. Estrin and B.C. DeCooman, Metallurgical and Materials Transactions A, 45 (2014), 717–730

Development of Advanced High-Strength Steel for Lifting and Excavation Sector at Essar Steel

Akshay Shingweker, Nitin Amte, Sirshendu Chattopadhyay and Deepak Gupta

Abstract Earthmoving and lifting equipment are born tough—some of the industrially produced very high strength steels are used in these equipments. Two types of high-strength steel are generally used: (1) High-strength steel for wear resistance and, (2) High-strength steels for fatigue resistance used in load bearing members. The wear resistant steels generally have hardness in the range of 400–600 BHN and yield strength in the range of 1000–1200 MPa. The high-strength steels with high fatigue resistance have yield strength in the range of 550–980 MPa. These steels were earlier imported from few European and Japanese mills. The paper outlines the journey of development of these two categories of steel for Lifting and Excavation Sector at Essar Steel India Ltd. Metallurgical design considerations and process control issues for industrial manufacturing have been briefly outlined in this paper.

Keywords Lifting and excavation · Abrasion resistance steel · TMCP

1 Introduction

Lifting and excavating is a diverse industry with a range of subsectors like earthmoving equipment, material handling equipment, and cranes and mining machinery. With the increasing impetus to construction sector by the Government of India, the construction industry is gathering momentum. It is projected that construction

A. Shingweker (✉) · N. Amte · S. Chattopadhyay (✉) · D. Gupta
Research and Development, Essar Steel India Limited,
Hazira, Surat 394 270, India
e-mail: akshay.shingweker@essarsteel.co.in

S. Chattopadhyay
e-mail: Sirshendu.Chattopadhyay@essarsteeil.co.in

N. Amte
e-mail: Nitin.Amte@essarsteel.co.in

T. K. Roy et al. (eds.), *Advanced High Strength Steel*, Lecture Notes
in Mechanical Engineering, https://doi.org/10.1007/978-981-10-7892-7_7

equipment sale will grow at a CAGR of 6.18%, in volume terms, and reach to 96,700 units by FY18 from 50,000 in FY07 [1].

Parallel to this growth, there is a demand to optimize the cost of production in mines, quarries, and construction through greater haulage capacity of the earth-moving equipment and better fuel efficiency. Machines such as cranes, heavy duty dumpers, excavators, and earth movers are growing in size and are being deployed in increasingly severe environments. High-strength steels are being increasingly used in load bearing members like crane booms, chassis of hauling equipment, etc. It has been reported that use of high-strength steel has resulted in 20% higher payload capacity in world's largest dump truck BelAZ 75710 [2].

In addition, certain components of earthmoving equipment are subjected to severe abrasive wear and impact load. To increase the life of these components, a class of steel with very high abrasion resistance and impact toughness has been developed over the last two decades. Typically, such steels have hardness levels 400–600 BHN along with good impact toughness and weldability. To cater to these markets, Essar Steel has developed a series of abrasion resistance steel with different hardness from 400–500 BHN which are marketed under the brand name ROCKSTAR. In addition, high-strength steel plates having yield strength level of 700–1000 MPa with excellent toughness branded as TUFMAX, BOOMOR were also developed for load bearing structural components of the earthmoving equipment.

2 Characteristics of Steels for Earth Moving Equipment

BOOMOR and ROCKSTAR family of steels is generally manufactured through quenching and tempering route. TUFMAX steels are processed through thermo-mechanically controlled rolling, followed by acclerated cooling. Table 1 shows the target mechanical properties for wear resistant and for high-strength steels used in load bearing members. Other required properties in these grades are good weldability, flatness, and good fatigue resistance.

3 Alloy Design Concept

The alloy design concepts of ROCKSTAR, TUFMAX, and BOOMOR are different, as their final properties and processing routes are different. However, there is one common requirement in all these three family of grades, i.e., high strength or hardness combined with good toughness, weldability, and bend properties. Very careful balancing of the alloying elements and microstructural engineering is required to achieve optimum combination of strength, hardness, impact toughness, and weldability. The alloy design and processing concept of ROCKSTAR, TUFMAX, and BOOMOR high-performance steel plate series are shown in Fig. 1.

Table 1 Targeted product characteristics

Grade	Thick (in mm)	Tensile Properties[a]			Hardness (in BHN)	Charpy impact (min)[a]	Bend properties (bend radius and bend angle)
		YS, MPa (min)	TS, MPa (min)	%El (in 2″) (min)			
ROCKSTAR 400	6.00–80	1000	1250	12	360–430	40 J @ −30° C	3 × T (180°)
ROCKSTAR 450	6.00–80	1150	1350	12	425–475	30 J @ −20° C	3 × T (90°)
ROCKSTAR 500	6.00–50	1250	1500	8	470–540	27 J @ 20° C	5 × T (90°)
TUFMAX 700	3.00–12.0	690	750	12	–	27 J @ −20° C	1.50 × T (180°)
BOOMOR 900	6.00–50.0	890	940	11	–	30 J @ −40° C	3.00 × T (180°)

[a]Test sample orientation: transverse to rolling direction for tensile and bend test and longitudinal to rolling direction for Charpy impact test

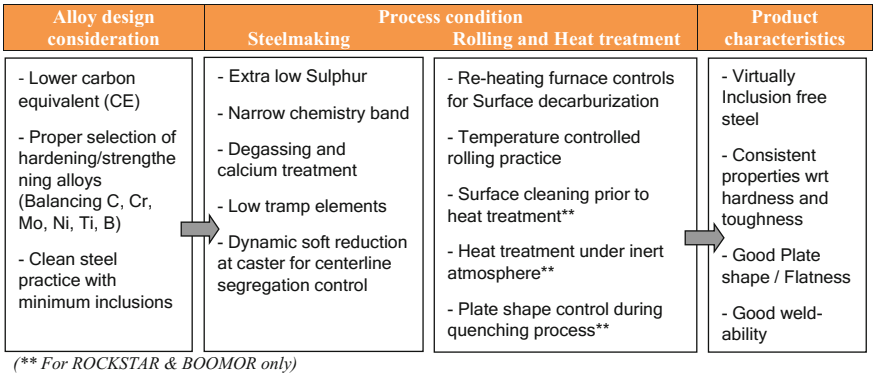

Fig. 1 Alloy design concept of abrasion resistant and high-strength steel plate series

4 Abrasion Resistant Steel: ROCKSTAR

There are no international standards for this family of steel. Different steel manufacturers have adopted different alloying philosophies to achieve the desired results, and are marketing these grades under different brand names.

Abrasion resistance is a function of hardness (Fig. 2a), and this is also dependent on the hardness of phases in the steel microstructure (Fig. 2b) [3, 4]. Most manufacturers use a combination of alloying elements like boron, chromium, and molybdenum along with micro-alloys like niobium to achieve the desired properties. The choice and proportion of alloying elements depend upon the equipment configuration and process capability of the manufacturer. Typical chemical composition of ROCKSTAR steel is listed in Table 2.

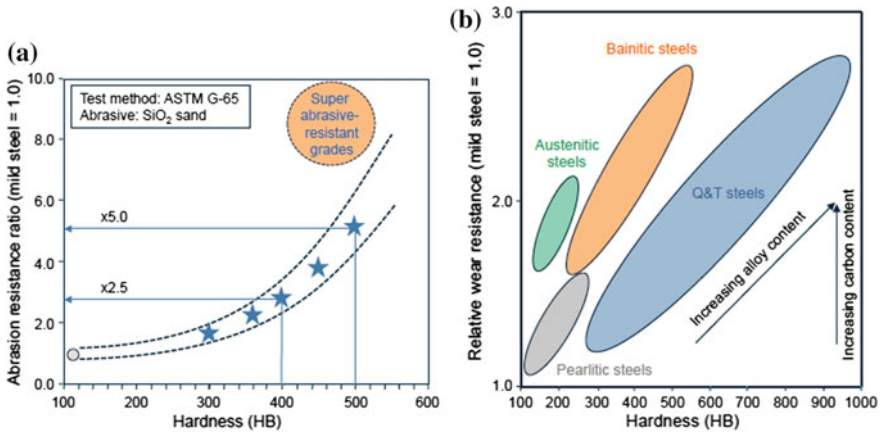

Fig. 2 **a** Relation of hardness with abrasion resistance **b** relation of steel microstructure

One of the key challenges in production of wear resistant steel grades is maintaining the hardness across the thickness of the plates. During quenching process, the surface layers are cooled at a faster rate than the core. Hence, the steel tends to develop a hardness gradient across the thickness. Such gradient is not desired by end users. This phenomenon is more prominent in thicker plates. Hence, alloying elements like Mo, Cr, and Ni in combination with high cooling rates are required to achieve a high hardness value in the core of thickness with a homogeneous martensitic microstructure. In addition, special care is required during reheating of slabs before hot rolling and austenitizing of plates before quenching to ensure that carbon does not get depleted from the surface creating a decarburized layer leading to low surface hardness. Figure 3 shows the uniformity of the product characteristics with respect to hardness across the thickness. This indicates the homogeneous microstructure all along the thickness. Figure 4 shows the typical tempered martensitic microstructure of ROCKSTAR 400 grade.

Another consideration during usage of high-strength steel is maintaining the flatness of steel plates, as it is very difficult to straighten the high-strength plates during fabrication. The steel should not only have good flatness but also free from residual stress which makes the steel wavy after plate cutting. During quenching, if the cooling is uneven through the cooling zone, the plate will inevitably be deformed. The factors causing steel warpage are phase transition, nonuniform yield stress, and thermal conductivity. Among these, the phase transition expansion is an important factor [5]. At Essar, the optimum recipe for quenching was obtained through a set of controlled trials coupled with statistical data analysis, so that flatness of less than 1/4th of ASTM A6 standard tolerances could be regularly supplied to the customers.

Table 2 Typical chemical composition of ROCKSTAR grades

Steel grade	%C	%Si	%Mn	%P	%S	%Cr	%B	%Ni	%Mo	CE
ROCKSTAR 400	≤ 0.25	≤ 0.60	≤ 1.50	≤ 0.02	≤ 0.01	≤ 1.00	≤ 0.0035	≤ 1.00	≤ 0.50	0.45–0.65
ROCKSTAR 450	≤ 0.27	≤ 0.60	≤ 1.50	≤ 0.02	≤ 0.01	≤ 1.00	≤ 0.0035	≤ 1.00	≤ 0.60	0.52–0.65
ROCKSTAR 500	≤ 0.35	≤ 0.60	≤ 1.50	≤ 0.02	≤ 0.01	≤ 1.20	≤ 0.0035	≤ 1.00	≤ 0.70	0.60–0.75

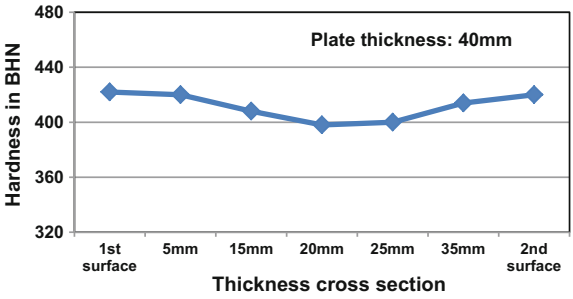

Fig. 3 Typical through thickness hardness distribution of ROCKSTAR 400 plate (40 mm Thick)

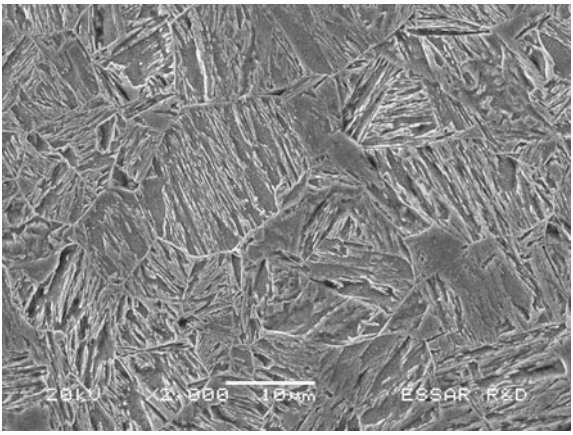

Fig. 4 Microstructure of ROCKSTAR 400 showing Tempered Martensite

5 High-Strength Thermo-Mechanically Controlled Rolled Plates

This product is characterized by very high strength with superior fatigue life and finds applications in crane booms and other heavy load bearing structures. These grades generally conform to international standards EN10149-2 550 MC, 650 MC, and 700 MC. These are marketed at Essar under the brand name of TUFMAX.

The carbon content was kept low (<0.08%) with addition of Mn and Si, the strengthening from grain refinement was achieved through addition of Nb and Ti. Thermo-mechanical rolling demands high deformation below the no-recrystallization temperature. This translates to very high rolling loads during finishing passes of hot rolling for high-strength steel. Hence, care was taken to balance the different strengthening mechanisms compatible with the equipment conditions. Further strengthening was achieved using precipitation strengthening or dislocation hardening (bainitic transformation) or a combination of both. Optimum processing parameters ensured that fine precipitates were uniformly distributed and added to the strength. Typically such precipitations happen during

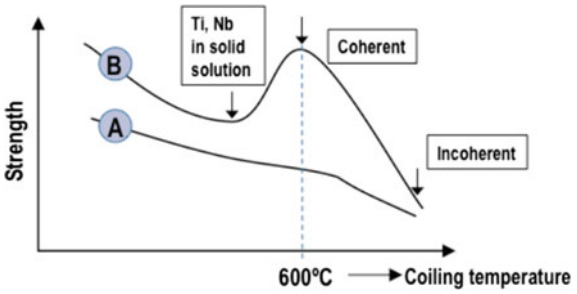

Fig. 5 Influence of coiling conditions on strengthening mechanism. **a** No carbide formers available, **b** Carbide formers in solid solution after austenite processing)

austenite-to-ferrite transformation since the solubility of carbide formers like Ti and Nb is much lower in ferrite. The coiling temperature plays an important role. The effect of coiling temperature on strength through precipitation strengthening is shown in Fig. 5 [6]. Typical chemistry adopted at Essar is given in Table 3.

The typical product mechanical properties are listed in Table 4. Yield strength of about 720–760 MPa, tensile strength of about 780–840 MPa, and yield ratio of 0.90 resulted in good elongation. Strain hardening index was ~0.10, which lead to good work hardening ability. The impact energy at −20 °C was 75–100 J. The fracture morphology was ductile fracture with hole expansion of 70%. The close bend of the product was without any crack formation on the bend portion.

Figures 6a and b show the typical microstructure of TUFMAX steel which constitutes fine ferrite–bainite structure with precipitation inside the ferrite grains. Other than normal TiN precipitations which are typically cubic and few hundred nanometers in size, the structure also reveals ultrafine precipitates. These precipitates were typically 20–40 nm in size which had contributed to strength through precipitation strengthening.

As discussed earlier, the development of strength in this type of steel is dependent on the processing parameters like temperatures before and after rolling, during coiling as well as amount of deformation. In industrial scenario, the

Table 3 Chemical composition of TUFMAX 700

Steel grade	%C	%Si	%Mn	%P	%S	%Al	%Nb + Ti + Mo	CE
TUFMAX 700	0.040–0.080	0.10–0.40	1.40–1.80	0.015 max	0.005 max	0.020–0.040	0.25–0.40	0.40–0.45

Table 4 Mechanical properties achieved in hot-rolled plates

TUFMAX 700	Mechanical properties			Bend 180°	Impact energy @ −20 °C
	YS, MPa	UTS, MPa	%El (GL: 2″)		
Target values	700 min	750 min	12 min	1.50 × T	27 J min
Typical achieved values for 10 mm	730–760	800–840	18–20	Satisfactory	75–100 J

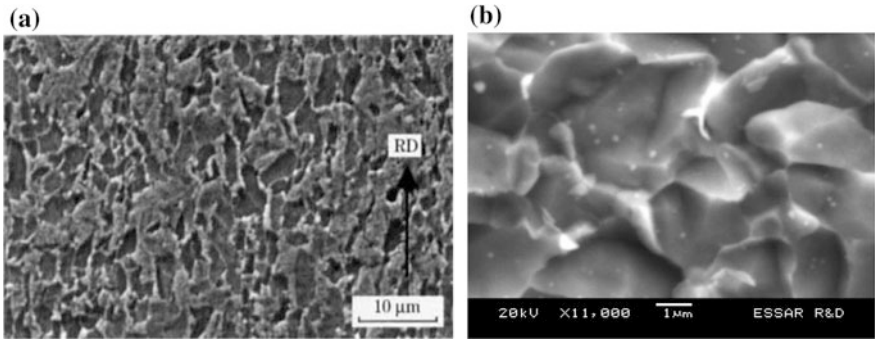

Fig. 6 **a** SEM micrograph showing fine ferrite–bainite microstructure (2% Nital), **b** SEM micrograph showing fine precipitates in ferrite matrix (2% Nital)

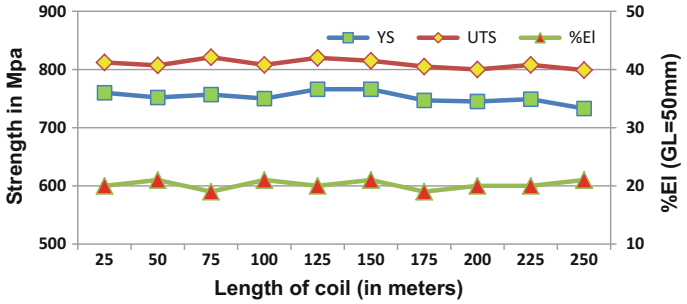

Fig. 7 Tensile properties along the length of a coil

temperatures tend to vary across the length of the steel strip/plate. Hence, the process control needs to be very stringent for this type of steel to achieve uniformity of properties along the length of the strip. Figure 7 shows the properties along the length of a coil produced.

6 High-Strength Quenched and Tempered Plates: BOOMOR 900

There is a demand for very high strength steel (YS > 700 MPa) for structural components in earthmoving equipment. These steels require a combination of very high strength, good impact toughness, and weldability due to severe operating condition. To cater to this requirement, Essar developed the BOOMOR family of products through quench and tempered route generally conforming to international specifications EN10025-6-S 890QL. The chemical composition of the developed

Table 5 Typical chemistry of BOOMOR 900

Steel grade	%C	%Si	%Mn	%P	%S	%Al	Others %(Nb + Ti + Mo + V + Cr)	CE
BOOMOR 900	0.18 max	0.30 max	1.30 min	0.015 max	0.005 max	0.030 max	1.30 max	~0.60

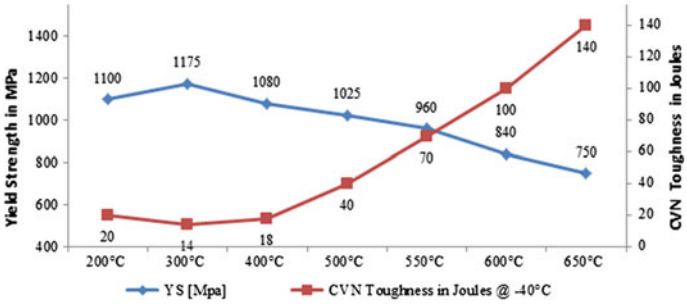

Fig. 8 Material characteristics at different tempering parameters for BOOMOR 900

Table 6 Typical properties of BOOMOR 900

Steel grade	Mechanical properties			Bend 180°	Impact energy @ −40 °C
BOOMOR 900	YS, Mpa	UTS, Mpa	%El (GL: 2″)		
Target value	890 min	940 min	11 min	3.00 X T	27 J min
Typical achieved values 50 mm	940–960	990–1020	15–18	Satisfactory	80–100 J

BOOMOR 900 steel is shown in Table 5. The carbon content and carbon equivalent of this class steel are below 0.18 and 0.60%, respectively. The plate thickness for manufacturing ranged from 5.0 to 50.0 mm.

The controlled rolling process was adopted for proper working of austenite and achieving the finer grain size. The plates after rolling were heat treated with quenching and tempering process. The plates were austenitized for sufficient time for homogenization followed by water quenching in roller press quenching machine. A series of simulation experiments were carried out to arrive at optimum tempering temperature. Figure 8 shows that the optimum tempering temperature lies around 550 °C to achieve the required strength and toughness. Based on the simulation studies, the plates were processed for tempering. Table 6 shows typical mechanical properties of the plates.

7 Conclusions

With the development of ROCKSTAR, TUFMAX, and BOOMOR, Essar Steel has expanded its product range of steel plates to cater to almost all of the flat steel requirements for lifting and excavation sector. Essar Steel has been successful, to a high degree, in import substitution of flat steels used in lifting, excavation, and mining sector.

References

1. India brand equity website http://www.ibef.org/industry/infrastructure-presentation.
2. https://www.worldsteel.org/media-centre/Steel-news/High-strength-steel–Creating-stronger–lighter–sustainable-products.html
3. K.-H.Z. Gahr, Microstructure and Wear of Materials, (1987), 132–292, Elsevier Science Publishers, Amsterdam, Netherlands
4. JFE Technical Report No. 11, June (2008), 26–28
5. D. Zhu, S. Zhang, G. Liu, Applied Mechanics and Materials, 52–54 (2011), 595–600, Trans Tech Publications, Switzerland.
6. V. Leory and J. Herman, ECSC Report EUR 15748 FR, Contract No. 7210-MA/201, (1996)

High-Strength Linepipe Steels and Physical Simulation of Production Processes

Fulvio Siciliano

Abstract Linepipe steels have evolved into very sophisticated engineering materials with double the strength of the original 1950s thermomechanically processed API Grade X-52 linepipe. The high demand for linepipe steels resulted in a revolution in rolling practices and steelmaking technologies. Additionally, steel and alloying price fluctuations brought the challenge to produce cost-effective linepipe steel to meet modern specifications. Physical simulation of steel fabrication processes plays an important role in optimizing parameters such as casting, reheating, rolling, and accelerated cooling conditions among others, meeting stringent specifications frequently required in recent pipeline projects. The use of physical simulation has been shown to be an important tool to develop new linepipe steels allowing production cost savings and improved performance.

Keywords Steels · Pipeline · Hot rolling · Physical modeling

1 Introduction

High-Strength Low-Alloy (HSLA) steel was first introduced in ship plate, beams, bridge steels, reinforcing bar, and heat-treated forgings, and was not introduced into linepipe steels until 1959 [1]. However, the escalating technological demands of high-pressure pipeline systems can be credited with the rapid evolution of HSLA technology since then. Today's pipeline designs consider all aspects of a steel's performance, including strength, toughness, weldability, fatigue, collapse resistance, and strain tolerance, as well as environmental degradation such as stress corrosion cracking and resistance to sour hydrocarbons containing H_2S and CO_2, in which combination of properties must be achieved at competitive prices. In the ensuing years (1968–1975), the strengthening mechanisms operating in microalloyed steels became better understood and quantified [2, 3] and optimized

F. Siciliano (✉)
DSI-Dynamic Systems Inc., Poestenkill, NY 12140, USA
e-mail: fulvio@gleeble.com

T. K. Roy et al. (eds.), *Advanced High Strength Steel*, Lecture Notes in Mechanical Engineering, https://doi.org/10.1007/978-981-10-7892-7_8

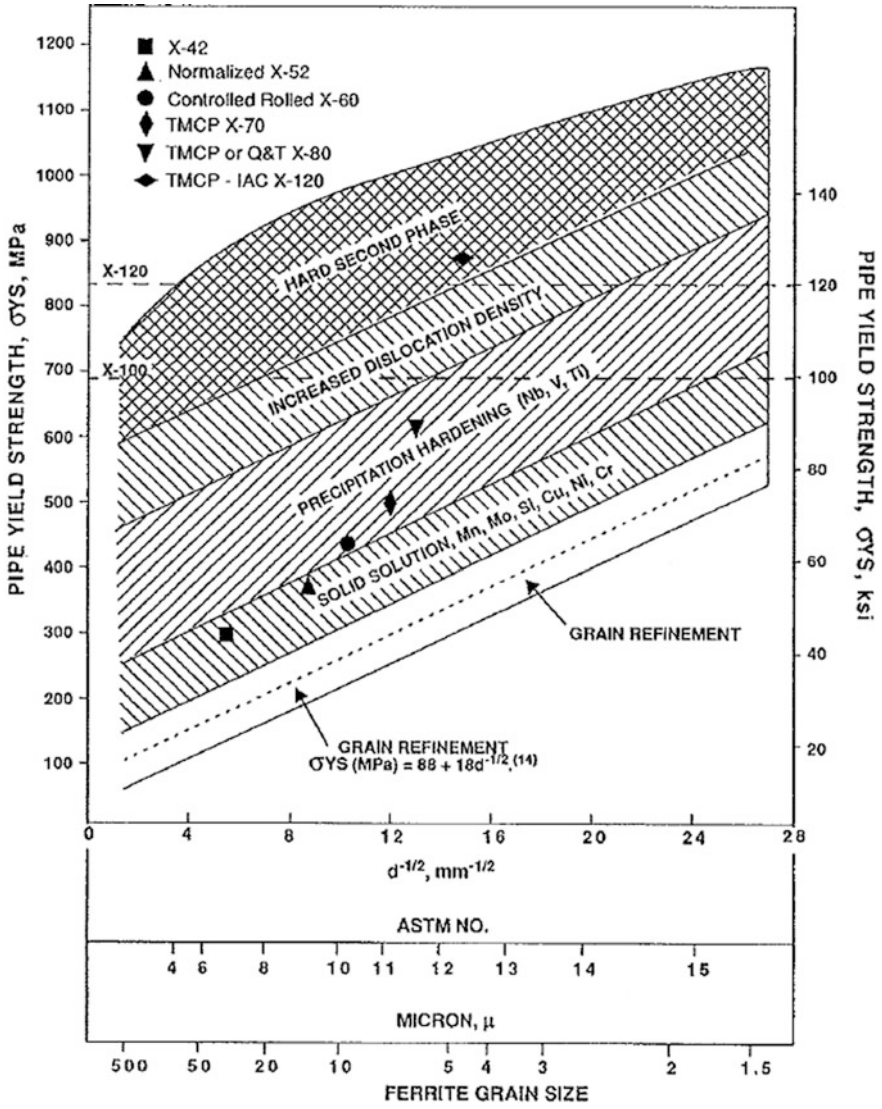

Fig. 1 Required combination of strengthening components for hot-rolled plate and skelp [4]

compositional and processing regimes were established. The available strengthening mechanisms used today can be depicted as simple incremental building blocks as illustrated in Fig. 1. These strengthening components are all utilized to varying degrees in modern high-strength linepipe.

2 The Role of Physical Modeling on Linepipe Steel Developments

During evolution of linepipe steels, physical simulation can play an important role in the development processes. Industrial processing conditions can be simulated in a laboratory scale, at a negligible cost as compared to an industrial trial. In the following sections, four examples of linepipe steel process simulations will be shown as well as the benefits of physical modeling to linepipe steel production.

2.1 Continuous Casting

In-situ casting followed by tension testing is a useful procedure to simulate continuous casting and evaluate the hot ductility. This subject is of great importance in linepipe steel since some alloying elements can drastically decrease the hot ductility after casting, especially in the range of 750–850 °C.

Low hot ductility can cause a series of cracking problems during continuous casting, the most common being transversal cracks during unbending the slab. The temperature at corners of the slab can be considerably lower as compared to the central portions leading to low ductility spots. The in-situ melt followed by tension has been shown to be an efficient method to simulate the industrial continuous casting conditions. First, a cylindrical tension specimen is melted inside a quartz crucible and later solidified by decreasing the temperature below the melting point. Figure 2 shows the experimental apparatus used to perform such simulation.

In this way, an as-cast microstructure is produced, and thermal and mechanical simulations of any location of the slab can be duplicated. The critical locations, where low temperatures/tension stresses are found, should be evaluated by means of physical simulation. Figure 3 displays the reduction in cross-sectional area versus

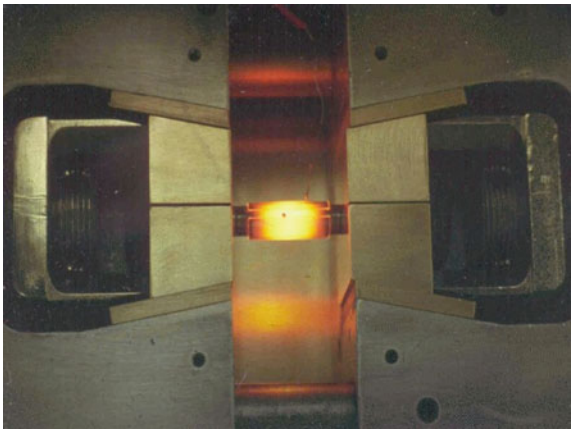

Fig. 2 Gleeble system during in-situ melting of a steel specimen inside a quartz crucible

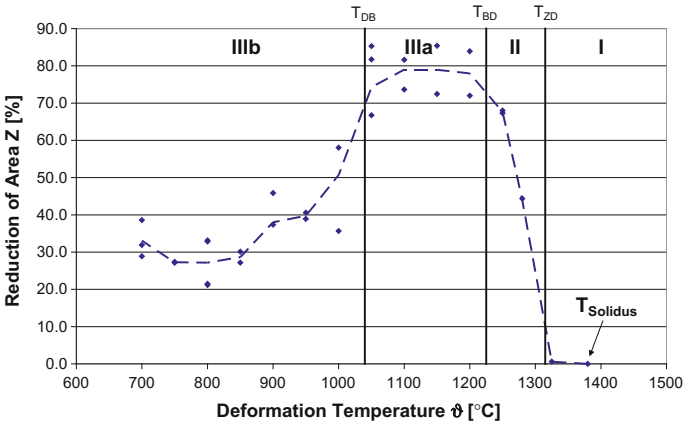

Fig. 3 Typical curve for hot ductility of as-cast steel. T_{ZD}: zero ductility temperature; T_{BD}: brittle–ductile transition temperature; T_{DB}: ductile–brittle transition temperature [5]

temperature, and the curve obtained points out the low ductility trough. In linepipe steels, due to additions of some alloying/microalloying elements, the reduction in cross-sectional area can be as low as about 30%, which is a level where slab cracks are prone to occur.

2.2 *Hot Rolling*

Roll force prediction is of utmost importance during industrial-scale hot rolling processes, especially linepipe steels where loads are usually in the upper levels due to the higher hot deformation resistance. In this way, the analysis of the mean flow stress (MFS) curve generated in physical modeling gives important information about the loads developed in each pass during rolling. Inaccurate predictions of roll force can lead to mill operational instability, shape defects, and thickness issues not to mention the potential for costly mill damage. Figure 4 shows the MFS evolution during hot rolling in hot strip mill (HSM), thin-slab casting direct rolling (TSCDR), and plate mill (PM). By using simple processing parameters such as temperatures, strains, and strain rates, the MFS evolution curves can be predicted with excellent accuracy [6].

The high-temperature multi-pass deformation under industrial conditions can be simulated by means of torsion or plane strain compression. Both methods have been shown to be reliable options to study hot rolling schedules [6, 8, 9]. Due to the massive amounts of deformation applied in most linepipe steel processing routes during hot rolling, torsion and plane strain compression have become popular simulation methods, capable of applying large strains per pass, at high strain rates with short interpass times, similar to industrial processing conditions. When

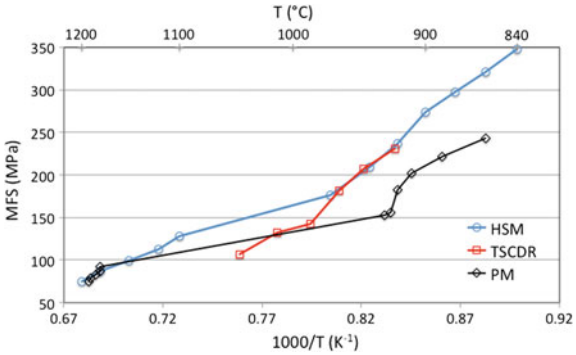

Fig. 4 MFS behavior during rolling by three different routes: TSCDR, plate mill, and hot strip mill [7]

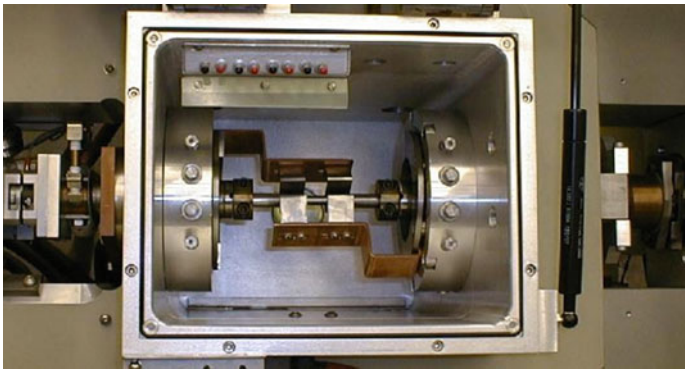

Fig. 5 View of a Gleeble torsion system used for tests shown in this work

comparing rolling, plane strain compression, and torsion, all are forms of plane strain (strain increments happen in two directions). In this way, there are only minor geometrical differences between the processes. Figure 5 shows an example of a torsion simulation system capable of applying multiple deformations at high strain rates with maximum torque of 100 Nm and maximum rotational speed of 1500 RPM. One example of a torsion specimen is displayed in Fig. 6. The testing gauge length is 20 mm and the gauge diameter is 10 mm which allows maximum strain rates of about 70 s^{-1}. Increasing the specimen diameter and reducing the gauge length will allow testing at strain rates of over 250 s^{-1}.

Torsion simulation produces torque and angle which are converted to true stress and true strain. The resulting stress–strain curves of torsion hot deformation schedules are exemplified in Fig. 7, where an MFS diagram with excellent fit between torsion simulation and industrial rolling can be observed.

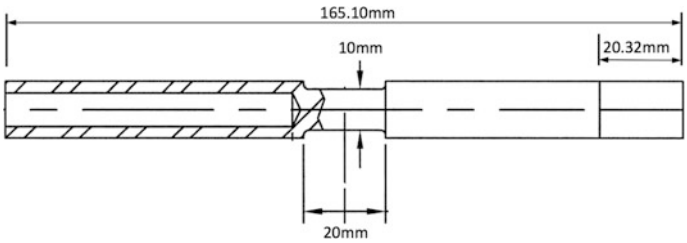

Fig. 6 Torsion specimen critical dimensions

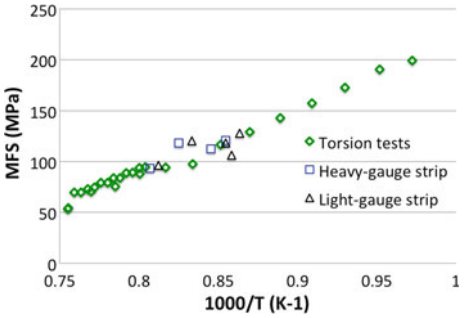

Fig. 7 MFS behavior of different hot torsion simulation schedules compared to industrial strip rolling schedules [6]

Rolling schedules of linepipe steels are designed to produce fine and uniform grain size along the thickness and width of the strip or plate. Final grain sizes can be predicted by simulation, both physical and numerical. In the below case, low values of toughness were initially observed in the final product, an X-70 plate. Simulation of the rolling schedule was carried out resulting in a final grain size of 37 μm. An improved schedule was designed and tested, producing average grain size of 22 μm, 40% smaller than the resulting grain size produced by the original schedule. In this development case, numerical modeling was used to calculate the grain size evolution and later the final grain size was confirmed by physical simulation. These results are presented in Fig. 8. The improved rolling schedule was then applied into production and toughness values required in the specification were met.

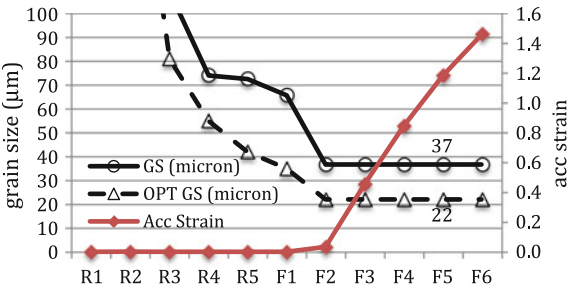

Fig. 8 Evolution of grain size and accumulated strains during rolling under conventional (GS) and optimized (OPT GS) hot rolling schedules

2.3 Cooling After Hot Rolling

Microstructure produced during accelerated cooling process performed in plate, hot strip, or thin-slab casting mills can be easily predicted by means of physical modeling. Simulation of quenching after multi-pass deformation is very reliable and can be safely extrapolated to full-scale accelerated cooling in linepipe steel production. The resulting microstructure as well as its uniformity across thickness will dictate the final mechanical properties of the steel. Figure 9 shows different microstructures originating from two different cooling rates in a typical X-70 steel composition: a lower cooling rate (e.g., 30°C/s to 600°C) producing ferrite+pearlite microstructure and a higher cooling rate (e.g., 12°C/s to 600°C) producing a ferrite +acicular ferrite microstructure. The transition to acicular ferrite microstructure leads to higher strengths.

Finally, from an economical point of view, physical modeling experiments can significantly reduce the required number of full-scale rolling trials from, for example, from five to three trial slabs. In a plate mill, this reduction can result in savings in the order of USD 80,000 for just one phase of the development process. In hot strip mills, equivalent savings can easily reach USD 200,000. In addition, streamlining the chemical composition can also be performed with physical simulation. Optimized chemical compositions can be designed to allow the reduction of alloying additions and tested before the industrial trial at negligible costs, leading to higher profit margin to the steel producer.

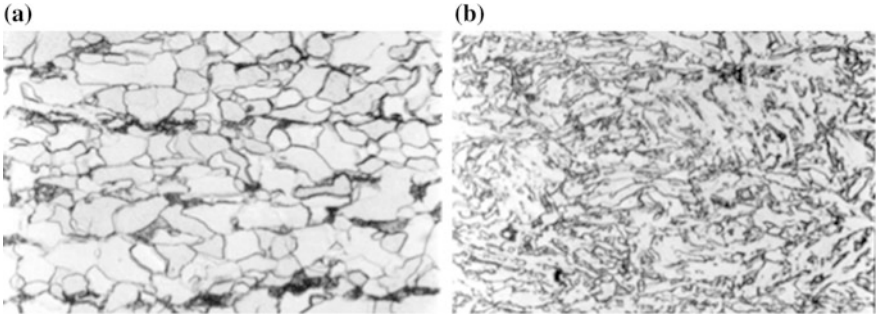

Fig. 9 Examples of microstructures in a X-70 steel after rolling and cooling **a** ferrite+pearlite after lower cooling rate, **b** ferrite+acicular ferrite after faster cooling rate (500X)

3 Summary

Cost-effective production of special and high value-added steels such as linepipe and advanced high-strength steels can greatly benefit from small-scale physical simulation. Physical simulation will play a major role in the optimization of production steps such as continuous casting, hot rolling, and accelerated cooling as well as other extremely important aspects such as heat treatment response and weldability. Physical simulation provides not only the metallurgical understanding but also considerable savings in production and alloy addition costs.

Acknowledgements I would like to express my sincere thanks to Dr. Brian Allen, Mr. Todd Bonesteel, and Mr. James Papa from DSI for the great support during preparation of this work.

References

1. A.G. Barkow, Columbium Steel in High-Pressure Line Pipe Service, AISI Regional Technical Meeting No. 59, Buffalo, N.Y., (1960)
2. F.B. Pickering and T. Gladman, An Investigation into Some Factors which Control the Strength of Carbon Steels, Metallurgical Developments in Carbon Steels. Harrogate, U.K., ISI Special Report 81, May (1963)
3. R.B.G. Yeo, A.G. Melville, P.E. Repas and J.M. Gray. Properties and Control of Hot-Rolled Steel, Journal of Metals, 20 (1968), 33–43
4. F. Siciliano and J.M. Gray, High Strength Microalloyed Linepipe: Half a Century of Evolution. Pipeline Technology Conference, October 12–14 (2009) Ostend, Belgium.
5. W. Jungnickel, Determination of the deformability behavior of continuous casting shells. MEFORM 2011, (2011), Freiberg, Germany
6. F. Siciliano, B. Allen and D. Ferguson, Hot torsion tests - a reliable rolling simulation method for C-Mn steels. Thermec'16-International Conference on Processing & Manufacturing of Advanced Materials, May/June (2016), Graz, Austria
7. F. Siciliano, Mathematical Modeling of Hot Rolling: A practical Tool to Improve Rolling Schedules and Steel Properties– (*Keynote paper)* - Proceedings of the 7th International Conference on Physical and Numerical Simulation of Materials Processing, June (2013), University of Oulu, Finland
8. F. Siciliano, Torsion Simulation Method applied to Hot Rolling of Steels. SIMPRO 2016-Thermomechanical Simulation and Processing of Steels Conference, RDCIS-SAIL, (2016), Ranchi, India
9. F. Siciliano, Physical simulation ofhot rolling of C-Mn steels by different deformation methods. ICPNS '16 Seattle, (2016), USA

Recent Advances in Welding of High-Strength Bainitic Steel for Automotive Applications

V. S. M. Ramakrishna R, Jai Prakash Gautam, G. Madhusudhan Reddy and K. Bhanu Sankara Rao

Abstract Bead-on-Plate Friction Stir Welding (FSW) joints were produced on 3-mm thick Ultra-fine Bainitic Steel using polycrystalline cubic boron nitride (PcBN) tool. The rotational speeds employed include 80, 100, 150, and 200 rpm. All the weld joints were prepared at a traverse speed of 35 mm/min. The noncontact online thermography has been used to measure interface temperature between the top surface of plate and bottom of the tool shoulder bottom. This measurement enabled to determine the peak temperature reached in the stir zone (SZ) during FSW. The interface temperatures at all rotational speeds are ∼below 673 K. The microstructure in the base metal (BM) is composed of carbide-free bainite and retained austenite. After FSW, the weld joint revealed BM, stir zone (SZ), and thermomechanically affected zone (TMAZ). The retained austenite decreased with increasing rotational speed in SZ and there has been a gradual transition of microstructure in the TMAZ. Stir zone exhibited higher hardness compared to BM. Maximum hardness in SZ occurred at 150 rpm.

Keywords Friction Stir Welding · Bainite · Retained austenite

V. S. M. Ramakrishna R
Mahatma Gandhi Institute of Technology, Gandipet, Hyderabad 500075, India

V. S. M. Ramakrishna R · J. P. Gautam
School of Engineering Sciences and Technology, University of Hyderabad, Hyderabad 500046, India

G. Madhusudhan Reddy
Defence Metallurgical Research Laboratory, Hyderabad 500058, India

K. Bhanu Sankara Rao (✉)
MGIT, Hyderabad 500075, India
e-mail: kota.bhanu@gmail.com

T. K. Roy et al. (eds.), *Advanced High Strength Steel*, Lecture Notes in Mechanical Engineering, https://doi.org/10.1007/978-981-10-7892-7_9

1 Introduction

The carbide-free bainitic steels are being considered as excellent candidate materials in automobile applications due to their favorable combination of tensile strength and ductility. It is being considered that these steels do not require either complex heat treatments or thermomechanical processes to achieve higher strength. The strength is mainly achieved by means of the very fine bainitic ferrite plates, where a soft retained austenite phase imbibed will control the levels of ductility achieved. The mechanical stability of retained austenite plays an important role in obtaining the elongation by TRIP effect. TATA Steel Research and Development Group at Ijmuiden, Netherlands has developed continuously cooled ultra-fine bainitic steel with excellent combination of strength (UTS: 1370 MPa) and ductility (21% elongation) [1]. The process route employed to produce strip is hot rolling followed accelerated cooling on the runout table and subsequent coiling. The transformation of austenite occurred during the cooling of the coil at temperatures lower than 673 K.

During manufacturing of automotive components, welding is unavoidable. Bainitic steels require welding methods that will not destroy the much needed bainitic structure and at the same time shall not produce wider heat affected zones. Friction Stir Welding (FSW) appears to be a suitable method for welding high-strength bainitic steel. In FSW process, a rotating tool containing the shoulder and pin is plunged into the joint between the two flat plates which generate heat due to friction and plastic deformation. The work piece is softened around the tool and material is transported from advancing side to retreating side [1]. In FSW, welding occurs in solid state and therefore weld metal will not contain any defects associated with melting and distortion resulting from thermal contraction that occurs on subsequent solidification. In recent years, the usage of FSW has been explored in the fabrication of various steels [2, 3]. This study is aimed at establishing the feasibility of FSW of ultra-fine bainite steel plate of 3 mm thickness, (i) demonstrating the usage of in-line thermography to monitor the temperature changes resulting from the variation in rotational speed of tool and (ii) evaluating of the effect of rotational speed on the development of microstructure and hardness in various zones.

2 Experimental Details

Bead-on-plate FSW joints were produced on 3 mm thick Ultra-fine Bainitic Steel using polycrystalline cubic boron nitride (PcBN) tool. The rotational speeds employed include 80, 100, 150, and 200 rpm. All the weld joints were prepared at a traverse speed of 35 mm/min. Tools were tilted by 2° from plate normal. Argon gas shielding was employed to prevent the oxidation of the surface during FSW. The sound bead-on-plate FSW weld obtained at 80 rpm is shown in Fig. 1.

The samples for metallography are polished with emery papers with increasing fineness followed by polishing with 0.6 and 0.1 μm diamond pastes. The samples were etched with LePera reagent to reveal the microstructure. The finer details of microstructure are obtained by observing the etched samples under a Field Emission Gun Scanning electron microscope operating at 40 kV setting.

Fig. 1 Bead-on-plate FSW weld at 80 rpm

3 Results and Discussion

The composition of bainitic steel is shown in Table 1. This steel possessed ultimate tensile strength of 1370 MPa and 21% total elongation. The steel owes these properties due to the occurrence of ultra-fine bainite plates (∼100–130 nm) and from the high density of dislocations derived from the bainitic transformation. The actual microstructure of base metal is composed of carbon-free bainite and carbon-enriched retained austenite of ∼21%. It is believed that the presence of retained austenite in the final microstructure contributes to the outstanding ductility values of the steel. In BM, there was sufficiently wide window between the B_s and M_s temperatures. This facilitated the bainitic transformation with suppression of transformation to martensite [1]. It may be noted that martensite exhibits less ductility and imparts brittleness to the steel.

As shown in Fig. 2, the transverse cross section of the weld joint at all rotational speeds revealed base metal, stir zone (SZ), and thermomechanically affected zone (TMAZ). Typical microstructures obtained by SEM and pertaining to BM, SZ, and TMAZ in 150 rpm joint are illustrated in Fig. 4. Base metal microstructure showed bainitic plates and bright particles pertaining to retained austenite on lath boundaries. The retained austenite content decreased in SZ with increasing rotational speed and probably appears to have transformed to lower bainite/martensite. In the TMAZ, the retained austenite phase was higher than in SZ. The decrease of the retained austenite in SZ can be attributed to the disintegration of austenite due to intense plastic deformation occurring in this zone.

Table 1 Chemical composition of ultra-fine bainitic steel

Element	C	Mn	Si	Cr	Al	Ti
Weight %	0.34	1.80	1.51	0.92	0.015	0.032

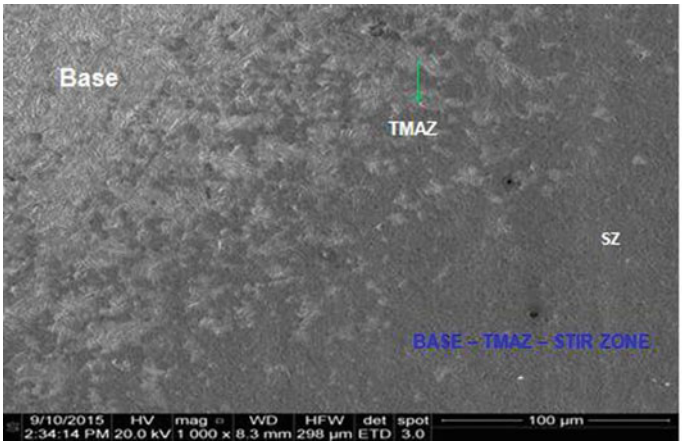

Fig. 2 Microstructure of transverse cross section of the weld joint at rotational speed of 80 rpm revealing base metal, stir zone (SZ), and thermomechanically affected zone (TMAZ)

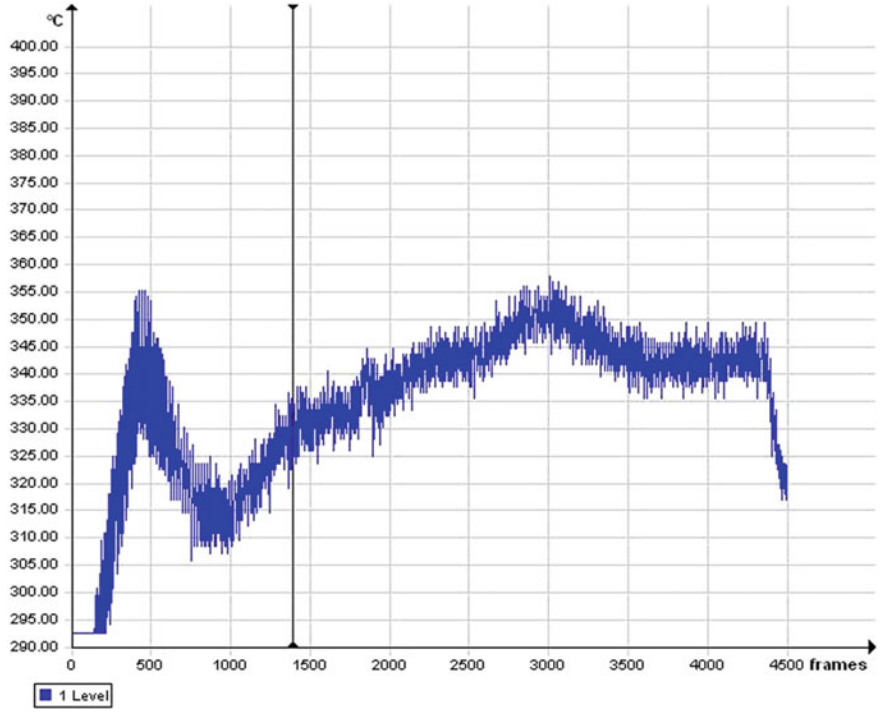

Fig. 3 Thermal profile obtained from the tool at 80 rpm

Table 2 Thermography analysis for temperature changes at various stir speeds

S. No.	Stir speed (rpm)	Feed rate (mm/min)	Tool temp. (°C)	Interface temp. (°C)	0.01 mm below interface (°C)
1	200	35	825–830	430–440	396–403
2	150	35	795–800	424–431	391–396
3	100	35	765–770	435–441	394–397
4	80	35	745–750	407–411	371–376

The thermal image obtained for 80 rpm condition is shown in Fig. 3. The thermography analysis conducted on tool, interface, and 0.01 mm below interface from thermal images recorded at various rotational speeds is shown in Table 2. The temperatures reported at 0.01 mm below the surface reflect the temperatures prevailing in stir zone at various rotational speeds. At all rotational speeds, the SZ is

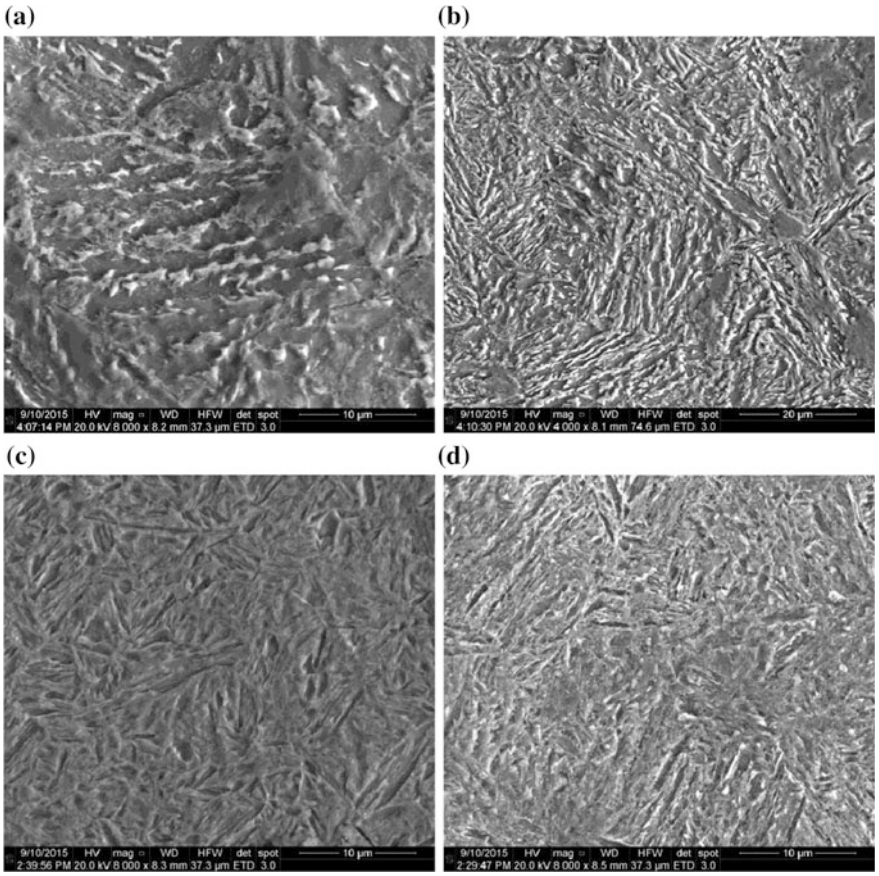

Fig. 4 **a**, **b** Microstructure of BM depicting bainite and retained austenite, **c** bainite laths in SZ and **d** bainite and disintegrated retained austenite in TMAZ at 150 rpm

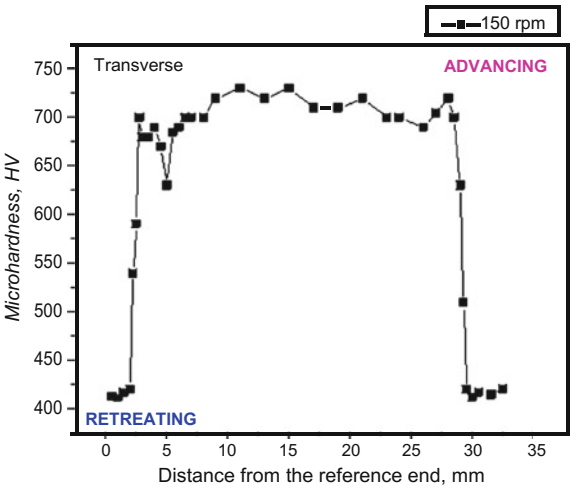

Fig. 5 Microhardness profile across weld joint. Stir zone shows very high hardness

below the down coiling temperature of ~673 K (Table 2) and hence the basic microstructure in SZ shall be bainite. Some amount of deformation-induced martensite could be expected due to raise in the M_d temperature during intense plastic deformation in SZ by transforming the retained austenite. Such type of transformation in actual practise shall contribute to the elongation through TRIP effect (Fig. 4).

The Vickers hardness profile obtained on the transverse cross section of welds in the mid-thickness zone for 150 rpm is depicted in Fig. 5. Hardness of the BM is about ~425 Hv. At all the rotational speeds, the SZ revealed very high hardness. At 80 rpm, the peak hardness in SZ is ~650 Hv. Hardness in SZ increased with rotational speed and displayed maximum at 150 rpm. At 150 rpm, the peak hardness is ~725 Hv. Very high hardness in SZ is in qualitative agreement with the results obtained on ferritic-martensitic steels [2]. A rapid decrease in the hardness in TMAZ was seen as the distance from the stir zone increased and ultimately attained values shown by the unaffected BM. On retreating side, a small dip in hardness was observed at the interface of SZ and TMAZ. The very high hardness in SZs could be associated with the strengthening effects associated with the transformation products of retained austenite, high dislocation density, and residual stresses. Appropriate post weld heat treatments are necessary to reduce the hardness of SZ. The post-weld heat treatment temperatures shall be less than those adopted for down coiling.

4 Conclusions

Recently developed ultra-fine bainitic steel has been subjected to FSW employing rotational speeds of 80, 100, 150, and 200 rpm with a tool speed of 35 mm/min. Defect-free bead-on-plate welds are successfully produced using polycrystalline

cubic boron nitride tool. The FSW weld joint is composed of BM, SZ, and TMAZ. The microstructure and hardness in SZ varied as a function of rotational speed. The very high hardness in SZs has been attributed to the strengthening effects associated with the transformation products of retained austenite, high dislocation density, and residual stresses.

References

1. S. Das and A. Haldar, Continuously cooled Ultrafine Bainitic Steel with Excellent Strength-Elongation Combination, Metallurgical and Materials Transactions A, 45A (2014), 1844–1854
2. V.L. Manugula, K.V. Rajulapati, G.M. Reddy, R, Mythili and K.B.S. Rao, A critical assessment of the microstructure and mechanical properties of friction stir welded reduced activation ferritic-martensitic steel, Material and Design, 92 (2016), 200–212
3. Z. Feng, D. Hoelzer, M.A. Sokolov and L.T. Tan, Friction stir welding of ODS Steels and Advanced Ferritic Martensitic Steels Oak Ridge National Laboratory Fusion Reactor Materials Program, June 30, (2013), DEC/ ER-0313/54-Vol. 54

Mechanical Properties of Copper-Added Ultra-fine Bainitic Steel

Malay Kundu, Shubhabrata Datta, Sven Curtze, V.-T. Kuokkala and Partha Protim Chattopadhyay

Abstract Addition of copper in high-carbon bainitic steel has resulted in attractive elongation. Heterogeneous copper precipitation in the course of bainitic transformation, at low homologous temperature, has resulted into attractive strength–ductility combination despite the limited dislocation controlled plasticity of nanoscale bainite. Early yielding of bainite facilitates strain partitioning between the blocky austenite and bainitic sheaves, leading to the continuous work hardening. In contrast to the tensile fracture strain, the compressive fracture strain has been found to be less dependent on the austenite volume fraction. The nanoindentation results indicated limited work hardening of the bainite sheaves.

Keywords Bainitic steels · Nanostructure · Work hardening · Strength–ductility combination

1 Introduction

Recently, a class of high-carbon ultra-fine/nanostructured bainitic steels have emerged with the ability to offer the combination of high strength (~2000 MPa) and high level of fracture strain (~20%) [1–5]. Microstructure of such steels essentially comprises blocky austenite and bainitic sheaves containing ultra-thin bainitic ferrite (<100 nm), separated by the austenite films. The steels exhibited the yield ratio close to one limiting the formability. The underlying micro-mechanism

M. Kundu · P. P. Chattopadhyay (✉)
Indian Institute of Engineering Science and Technology, Shibpur, Howrah 711103, India
e-mail: director.nifft@gov.in

S. Datta
SRM University, Chennai 603203, Tamil Nadu, India

S. Curtze · V.-T. Kuokkala
Department of Materials Science, Tampere University of Technology, POB 589, 33101 Tampere, Finland

T. K. Roy et al. (eds.), *Advanced High Strength Steel*, Lecture Notes in Mechanical Engineering, https://doi.org/10.1007/978-981-10-7892-7_10

of such plasticity behaviour is yet to be established unambiguously. It has been proposed that if the grain size (separation between the boundaries of coherent domains at least in one direction) is reduced below the bowing length of a Frank–Reed source or the spacing between the dislocation in a pile-up, a more energetically favourable mechanism like grain confinement and/or elastic strain accommodation may operate as the microscopic deformation mechanism at higher level of yield strength [6, 7].

In the present effort of developing Cu-added high-strength steel, it is envisaged that heterogeneous precipitation of Cu in the finer bainite sheave is favourable for interface-controlled plasticity of the bainite sheave. Here, an attempt has been made to investigate the aforesaid hypothesis in a high-strength hypo-eutectoid bainitic steel containing about 1.0 wt% Cu. Selected results of corresponding C–Mn–Si–Co–Al steel have also been appended for comparison and to understand the underlying mechanism.

2 Experimental Procedure

The alloys were prepared in a laboratory-scale air induction melting furnace as 5 kg melts. Table 1 presents the results of the spectroscopic analysis obtained by using an Optical Emission Spectrometer. The 50 mm × 50 mm × 200 mm cast ingots were subsequently hot forged into the bars of 18 mm × 18 mm section. The forged bars were soaked at 1200 °C for 45 min and hot rolled down to a thickness of approximately 6 mm in five passes to attain the finish rolling temperatures (FRT) of 900 °C followed by air cooling. The air-cooled samples after austenitisation at 900 °C were quenched in oil bath maintained at the isothermal holding temperature of 300 °C and held for different times. To study the microstructures, the metallographic samples were etched using 2% nital solution and were examined under a scanning electron microscope (SEM) operated at 15 kV. Transmission electron microscopy of the selected sample was performed using a microscope at an operating voltage of 200 kV.

Room temperature tensile test was carried out using a computer-controlled universal testing equipment with an extensometer at a strain rate of 3.3×10^{-3} s^{-1}. The test specimen was prepared as per ASTM Standard (ASTM: Vol. 01.02: E8M—00). Compression tests were performed on Split Hopkins Pressure Bar at a strain rate of 1900 s^{-1}.

Table 1 Concentration of alloying elements in the steel samples (in wt%)

Sample	%C	%Si	%Mn	%Mo	%Cr	%V	%Ti	%Al	%Co	%Cu
Steel-A	0.64	1.63	1.62	0.36	1.29	0.08	0.04	1.15	1.63	1.03
Steel-B	0.63	1.59	1.59	0.39	1.37	0.07	–	1.21	1.46	–

3 Results and Discussions

Figure 1a–d shows the SEM micrograph of Steel-A isothermally treated for 5 and 30 h and of Steel-B isothermally treated for 5 and 30 h at 300 °C, respectively. The SEM micrograph exhibits significant amount of bainitic transformation in both the steels even after 5 h of holding. The bainite volume fraction increases significantly due to increase in holding time from 5 to 30 h.

The TEM micrographs obtained from Steel-A after isothermal holding for 30 h are shown in Fig. 2. Figure 2a reveals the ferritic plates of nanoscale dimension. Figure 5b shows the formation of Cu precipitates. The diffraction rings in the SAEDP image appended in Fig. 2b evidence the formation of nanoscale Cu precipitates. Figure 2b also reveals that the Cu precipitates are preferably formed near the boundary of ferrite plate than within the plates. It is reasonable to postulate that in the case of ultra-fine bainitic sample, abundance of the α–γ interfaces and very short diffusion distance within the ferrite favour heterogeneous precipitation of Cu at ferrite plate boundaries.

Figure 3 presents the true stress versus true strain curves for Cu-added steel (Steel-A) for different holding times. The similar curves for Al–Co-added steel (Steel-B), isothermally held for 30 h, are also appended for comparison. It is interesting to note that in the case of Steel-A, despite the difference in bainite volume fraction for different holding time, the samples exhibit comparable yield

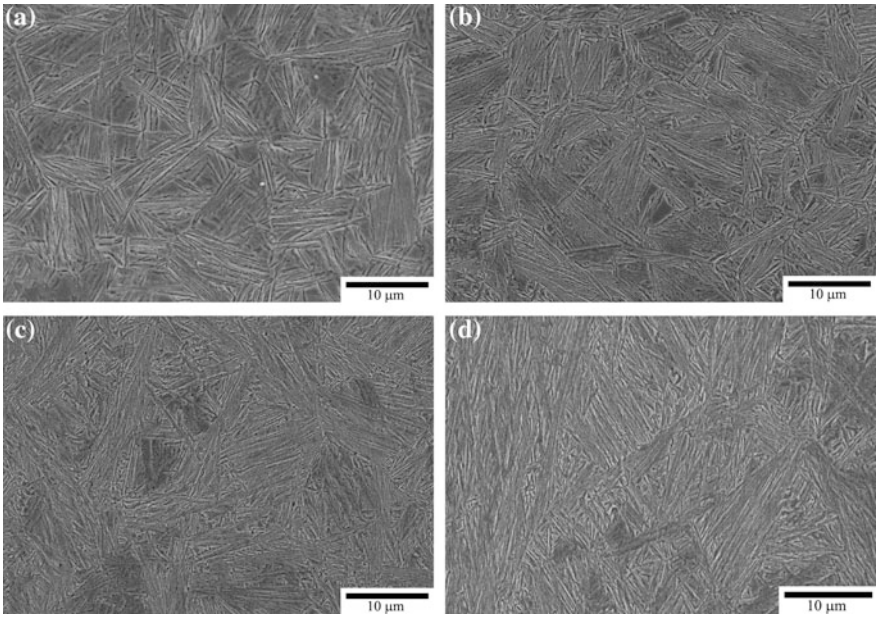

Fig. 1 SEM micrograph of Steel-A isothermally treated for **a** 5 h and **b** 30 h and of Steel-B isothermally treated for **c** 5 h and **d** 30 h at 300 °C

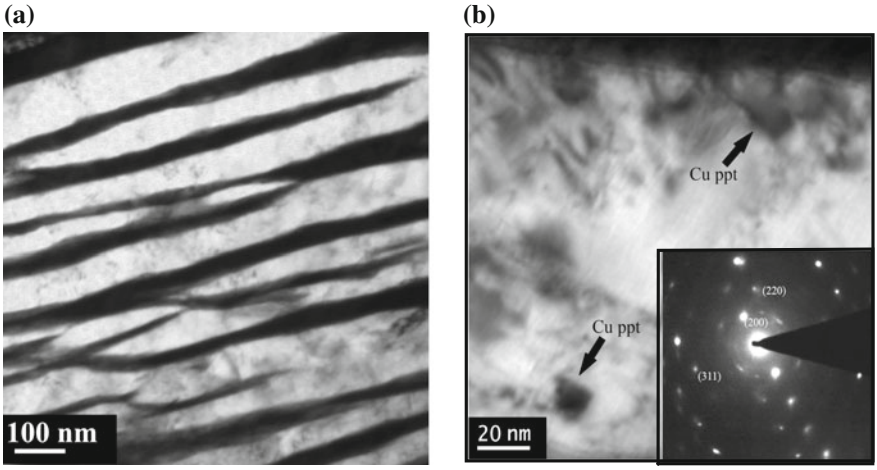

Fig. 2 TEM micrographs obtained from Steel-A isothermally held for 30 h **a** bainite sheave with ferritic plates of nanoscale dimension and **b** Cu precipitates at the edge of bainite plate

strength and the slope of the tensile curves. It is also apparent that the yield strength of Steel-A, isothermally treated for 30 h, is evidently lower than the corresponding sample of Steel-B. Moreover, the tensile plot of Steel-A shows continuous work hardening in contrast to the weaker work hardening observed in the case of Steel-B at the early stage of straining.

Figure 4 compares the work hardening behaviour of Steel-A and Steel-B, isothermally treated for 30 h. In the case of Steel-B, the work hardening capacity is clearly exhausted only after initial straining. On the other hand, appreciable work hardening is observed in the case of Steel-A with two different slopes. While the initial work hardening is presumably due to the deformation of bainite sheave, the second stage may be attributed to the result of deformation-induced transformation of austenite.

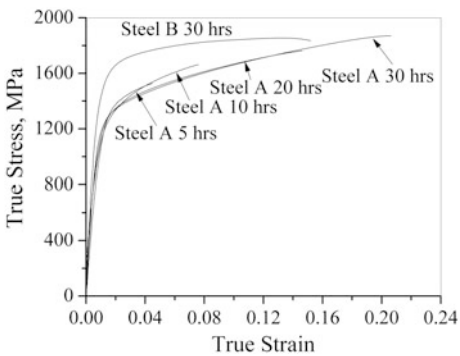

Fig. 3 True stress versus true strain curves for Cu-added steel (Steel-A) for different holding times. The stress–strain curves for Al–Co-added steel (Steel-B) isothermally held for 30 h are appended for comparison

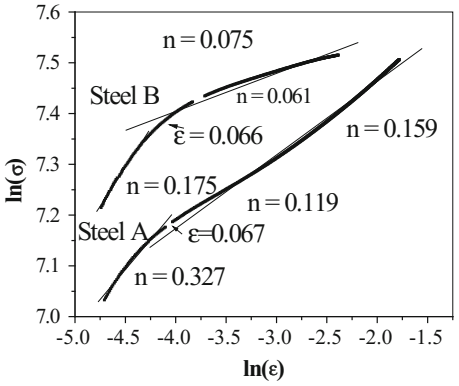

Fig. 4 Hollomon curves for the steels isothermally treated for 30 h

Figure 5a, b shows the SEM and micrograph obtained from the samples, isothermally treated for 30 h, close to and 2 mm away from the fractured end in tensile direction. The micrograph shown in Fig. 5a evidences the deformation of bainite sheaves and Fig. 5b exhibits cooperative sliding of the ferrite plates in the bainite sheaves along the direction of strain.

It may be mentioned here that in the case of the ultra-fine bainitic microstructure containing bainite plates with less than 100 nm thickness, dislocation controlled plasticity is limited as the bainite plate thickness is lower or comparable to the bowing length of a Frank-Reed source or the spacing between the dislocation in a pile-up. Such a condition of straining results in limited work hardening [6]. However, heterogeneous precipitation of Cu at the interfaces of ultra-fine bainite sheave results into early sliding of the interface and consequent yielding. With increase in strain, the deformation stress increases due to deformation of Cu particles and increase in friction at the interfaces leading to the work hardening of the bainite sheave, particularly in the paucity of dislocation controlled plasticity. At higher level of strain work hardening is governed by the strain partitioning between the blocky austenite and the bainite sheave depending on the available volume fraction of blocky austenite. This is indicative of the fact that the percolation

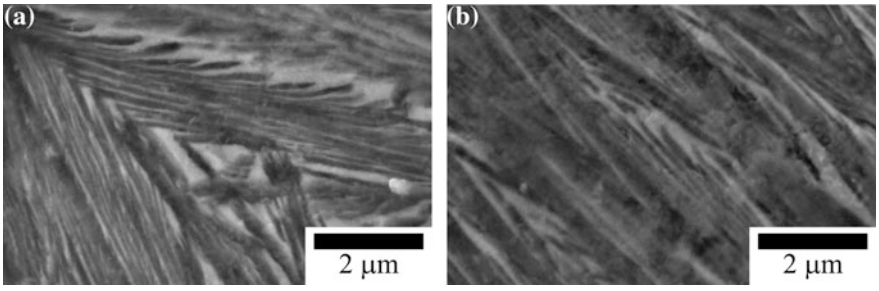

Fig. 5 SEM micrograph obtained from the fractured tensile sample isothermally treated for 30 h **a** close to and **b** 2 mm away from the fractured end in tensile direction

threshold value [8] is attained at different levels of strain for different initial volume fractions of austenite, leading to the different fracture strains for different samples of Steel-A. Therefore, it is evident that Steel-A sample, isothermally treated for 30 h, results in better yield ratio, work hardening and elongation than the corresponding sample of Steel-B as the manifestation of two-stage work hardening behaviour.

Figure 6 shows the results of compressive properties for Cu-added steels (Steel-A) isothermally treated for different durations at 300 °C. Similar result for Steel-B, isothermally treated for 30 h, is also appended for comparison. It is evident that in the case of Steel-A, the samples treated for different duration exhibit comparable fracture strain in contrast to the corresponding tensile results. The observation indicates that variation in the volume fraction of blocky austenite plays less significant role in determining the fracture strain in the case of compression test unlike the tensile test. In this context, it is imperative to mention that each of the 24

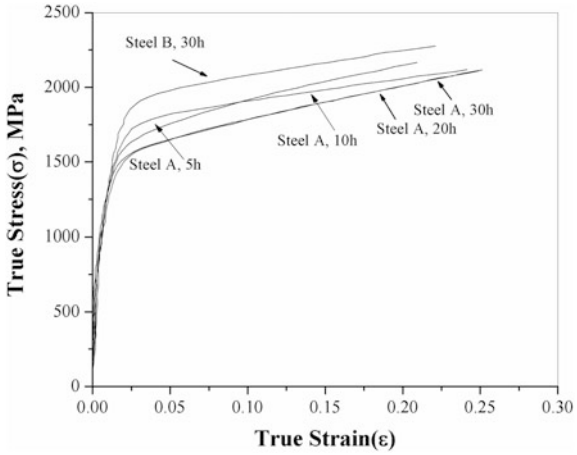

Fig. 6 Compression curves for isothermally treated Steel-A sample for different durations and Steel-B for 30 h of holding

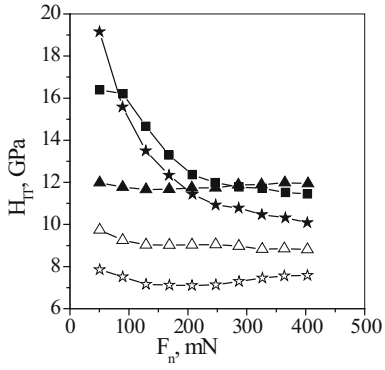

Fig. 7 Hardness versus indentation load of Cu-added alloy after isothermal holding at 300 °C for 30 h

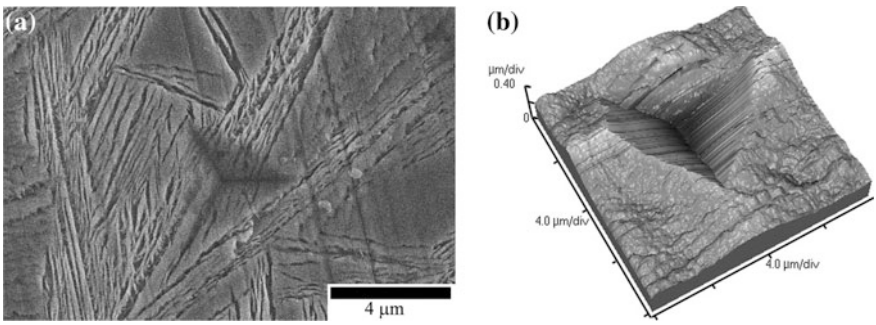

Fig. 8 Indentation marks obtained from **a** SEM images **b** AFM image of bainitic region

Kurdjumov-Sachs variant has one compressive axis and two tensile axes for the martensitic transformation Therefore, under compression, smaller number of variants result in the negative value of the mechanical interaction energy obtained as the product of transformation strain and externally applied stress for the given specimen coordinate.

It may also be recorded that Steel-B exhibits higher level of yield and ultimate strength than the same for Steel-A with comparable elongation values. Thus, the results of the compression test also substantiate that heterogeneous Cu precipitation within the bainite sheave exerts the softening effect in a similar manner to that observed in the case of tensile test.

Figure 7 shows two different bands of values in the nanohardness (H_{IT}) versus indentation force (F_n) curves obtained from Steel-A, treated for 30 h. The solid and the open symbols exhibit the hardness values obtained from the bainite sheave and blocky austenite regions, respectively. Despite the observed scatter in the measurement (2–8%), the bainite sheaves yielded much higher hardness values than the blocky austenite regions.

Figure 8a shows the indentation spot on the bainite sheave. The indentation is evidently sharp and accommodates the straining of bainite without much distortion of the sheave morphology even within the indented area. The austenite films clearly bend along the edges of the indentation profile down to deeper regions of indentation. Figure 8b shows the three-dimensional AFM images of the indentation profile. Indentation in the bainitic regions shows sharp edges with predominantly sink in profile. Pile-up effect is the feature of indentation in the cases of nonwork hardening or sufficiently work hardened materials. In such materials, propagation of plastic strain within the material volume underneath the indenter is constrained. As a result, with the progress of indentation, the material piles up along the edges of the indentation to give way to the indentation.

4 Summary

In summary, Cu addition has resulted in significant lowering of yield strength in the ultra-fine hypo-eutectoid bainitic steel, without deteriorating the ultimate tensile strength and elongation. This may be attributed to the precipitation of Cu at the ferrite–austenite boundary in the bainitic sheave. Due to heterogeneous precipitation of Cu, grain boundary controlled deformation initiated at lower stress. With increase in strain, deformation of Cu originated frictional effect at the interfaces leading to work hardening. Concomitant accumulation of strain at the austenite resulted in deformation-induced transformation of austenite to martensite leading to the onset of fracture beyond the percolation threshold value for given volume fraction of austenite. In contrast to the results of tensile deformation, variation of austenite volume fraction has not exhibited significant variation in fracture strain for compression test.

References

1. F.G. Caballero and H.K.D.H. Bhadeshia, Current Opinion in Solid State & Materials Science, 8 (2004), 251
2. A.S. Podder and H.K.D.H. Bhadeshia, Materials Science and Engineering: A, 527 (2010), 2121
3. C. García-Mateo, F.G. Caballero and H.K.D.H. Bhadeshia, ISIJ International, 43 (2003), 1238
4. M. Peet, S.S. Babu, M.K. Miller and H.K.D.H. Bhadeshia, Scripta Materialia, 50 (2004), 1277
5. C. García-Mateo, F.G. Caballero and H.K.D.H. Bhadeshia, Materials Transactions, 46 (2005), 1216
6. C.C. Koch, T.D. Shen, in: C. Suryanarayana, J. Singh and F.H. Froes (Eds.), P.A. TMS, Warrendale, (1996), 333–354
7. H.K.D.H. Bhadeshia, Proceedings of the Royal Society of London A, 466 (2010), 3–18
8. H.K.D.H. Bhadeshia, The Nature, Mechanism and Properties of Strong Bainite, in Proceedings of the 1st International Symposium on Steel Science (IS3–2007), The Iron and Steel Institute of Japan, (2007)

Microstructure-Based Deformation Modeling of Dual-Phase Steels

Danish Khan and B. P. Gautham

Abstract Dual-phase steels contain complex composite microstructure of ferrite and martensite phases that govern their mechanical behavior. Traditional analytical approaches of modeling the flow curve of composite microstructures of simplistic morphologies are therefore not able to capture the exact physics of deformation in totality. Therefore in order to model the flow behavior of such complex microstructures accurately, it is important to make the actual representation of microstructure to be a part of the model. The current work focusses on modeling the flow behavior of dual-phase steels using 2D representative volume element (RVE) based description of microstructure in FEM-based deformation models. Uniaxial deformation of actual microstructures is simulated under appropriate boundary conditions and the corresponding flow curve is calculated using first-order homogenization technique. While this type of analysis is reported in the literature, choices made for simulation parameters and assumptions may result in diverse outcomes. Therefore, in an effort to characterize this technique, a comparative study is conducted between plane strain and plane stress assumptions used for 2D RVE deformation modeling. Based on the studies, we have compared the efficacies of both the approaches and made our observations.

Keywords Microstructure · Uniaxial deformation · Modelling
Dual-phase steel

1 Introduction

The last few decades have seen a rapid development of advanced high strength steels for automotive applications in order to cater to the increasing requirement of enhanced fuel efficiency and passenger safety. In general, these steels are multi-phase in nature wherein the properties of each micro-constituents contribute to the

D. Khan (✉) · B. P. Gautham
TRDDC-TCS Research, Tata Consultancy Services-Pune, Pune, India
e-mail: d.khan2@tcs.com

T. K. Roy et al. (eds.), *Advanced High Strength Steel*, Lecture Notes in Mechanical Engineering, https://doi.org/10.1007/978-981-10-7892-7_11

macroscopic properties of the steel, thereby endowing the steel with right combination of diverse properties such as high strength and high ductility. However, this very multiphase nature makes it difficult to study and predict the deformation and failure of these steels using traditional analytical models, which treats them as homogeneous materials. Therefore, in order to capture the accurate stress and strain portioning between the phases and its effect on aggregate response of the steel, it becomes important to make the exact representation of the microstructure as a part of the model.

In recent times, RVE (representative volume element)-based FEM modeling of deformation of multiphase steels has been used very extensively [1–4]. The methodology involves converting a 2D micrograph or 3D microstructure to a FEM mesh which is subjected to appropriate boundary condition to simulate the uniaxial tensile loading. Since the representative microstructure (2D or 3D) of the material, in entirely, is a part of the model, the modeling technique is capable to capture the effect of exact morphology of the microstructure in predicting the properties. However, the choices made for different simulation parameters and assumptions involved lead to varied prediction and hence their predictions need to be studied in comparison to each other and experimental results. The present work focuses on the implementation of the 2D RVE-based micromechanics approach for predicting flow curve for dual-phase steels and on studying the effect of plane strain and plane stress assumption on its prediction along with comparison with experimental flow curve.

2 Numerical Modeling

The following subsections detail the important aspects of the technique in a sequential way.

2.1 RVE Selection

Numerical implementation of the microstructure-based micromechanics approach for dual-phase steels starts with a 2D or 3D RVE selection. RVE, as the name suggests, is the smallest volume element (area element in case of 2D) of the microstructure of the material that behaves similar to the macroscopic response under external stimuli. In order to be truly representative of the microstructure of the material, the RVE chosen should be statistically consistent with the microstructure of material. In the current work, 2D micrographs of DP600 steels containing 37 and 46% martensite volume fraction (V_m), published by Ramazani et al. [1], are chosen as 2D RVEs. The two RVEs are shown in Fig. 1 and the nominal chemical composition of the steel is given in Table 1.

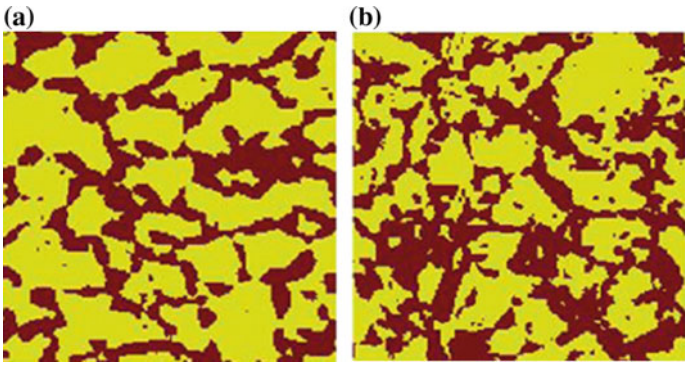

Fig. 1 2D RVEs of DP600 Steel used in this work (light region = ferrite and dark region = martensite). **a** RVE with V_m = 37% (35 μm × 35 μm) and **b** RVE with V_m = 46% (40 μm × 40 μm) [1]

Table 1 Chemical composition of the steel used in this study [1]

C	Si	Mn	P	S	Cr	Ni	Al	Cu	V
0.072	0.25	1.58	0.015	0.001	0.055	0.024	0.032	0.01	0.011

2.2 Meshing

There are number of methods reported in the literature to convert a 2D micrograph into a FEM mesh [1, 3, 5]. In the current work, the RVEs were converted to FEM meshes using open software OOF2 that converts a micrograph into a mesh using the principle that each element of the FEM mesh should have high material homogeneity [5].

2.3 Material Properties

Ferrite and martensite regions in the meshes were assigned different material properties. Dislocation-based work-hardening models for ferrite and martensite phases, based on the work of Rodriguez and Guitteraz [6], have been used. The key equation to model the work hardening of each phase is of the form as given by Eq. (1):

$$\sigma(in\,\mathrm{MPa}) = \sigma_0 + \Delta\sigma + \alpha * M * \mu * \sqrt{b} * \sqrt{\frac{1-\exp(-MK_r\varepsilon)}{K_r L}}, \tag{1}$$

where σ is the net flow stress of the phase, ε is the plastic strain, σ_0 is the Peierls stress to take into the contribution of alloying elements, $\Delta\sigma$ is the solid-solution

strengthening due to carbon, M is Taylor factor, μ is the shear modulus, b is burgers vector, K_r is the recovery rate, and L is the mean-free path for dislocation movement. The values of these model parameters for this steel are published in the work of Ramazani et al. [1] and hence are not reproduced here.

2.4 Boundary Conditions

Periodic boundary conditions (PBC) are imposed on the RVEs through multipoint constraints on the boundary nodes. Figure 2 shows the application of PBC in a typical microstructure and the following equations describe the constraints applied on the boundary nodes to achieve PBC:

$$u_{12} - u_4 = u_{11} - u_1 \tag{2}$$

$$u_{22} - u_1 = u_{21} - u_2 \tag{3}$$

$$u_3 - u_2 = u_4 - u_1, \tag{4}$$

where u_{11}, u_{12}, u_{21}, u_{22} are the displacements of the nodes of boundaries 11, 12, 21, 22, and u_1, u_2, u_3, u_4 are the displacements of the nodes 1, 2, 3, 4 as shown in Fig. 2.

2.5 FEM Analysis

The deformation of the 2D RVE with material assignment and boundary conditions are modeled in commercial FEM suite ABAQUS by applying loading at node 2 as shown in Fig. 2. In order to mimic the loading conditions of real materials through 2D RVEs, two types of assumptions are used, viz., plane strain condition and plane stress condition. In past, different researchers have used either of the two while modeling deformation of 2D RVEs. For example, Ramazani et al. [1] and Sodjit and Uthaisangsuk [2] have used plane strain condition whereas Sun et al. [3] and

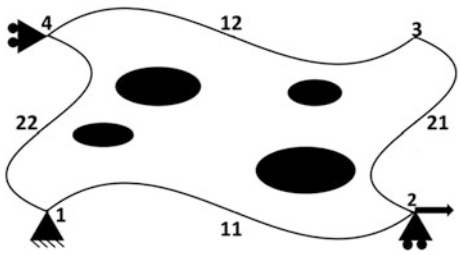

Fig. 2 A typical RVE under periodic boundary conditions

Zhuang et al. [4] have used plane stress condition. In this work, both plane strain and plane stress conditions are modeled for both the RVEs and compared with each other and experiments. The plane strain and plane stress conditions are invoked by choosing appropriate element type in ABAQUS.

2.6 *Homogenization*

The final step of this technique is the homogenization of the results obtained from FEM analysis to obtain the macroscopic response of the material. For this, stress and plastic strain values predicted by FEM analysis are volume averaged over the entire volume of RVE (first-order homogenization), for each time increment of the simulation, to obtain the final flow curve of the material. Equation 5 describes the first-order volume homogenization technique used to obtain any average property $\bar{P}_m$ of the material from its distribution over the RVE volume:

$$\bar{P}_m = \frac{1}{V}\int_V P_m dV \tag{5}$$

3 Results and Discussion

Figures 3a, b and 4a, b show the von-Mises stress and plastic strain distribution in the RVE with V_m = 37% deformed to 15% nominal strain under plane strain and plane stress conditions. First observation that can be made from these figures is that the plane strain assumption lead to homogeneous stress and strain partitioning between ferrite and martensite phases throughout the RVE without any localization for the entire loading path. On the other hand, the plane stress assumption lead to a high localization of the plastic strain in RVE that sets in at the very early stage of loading path. Since no localization is observed in real testing of DP steels at an

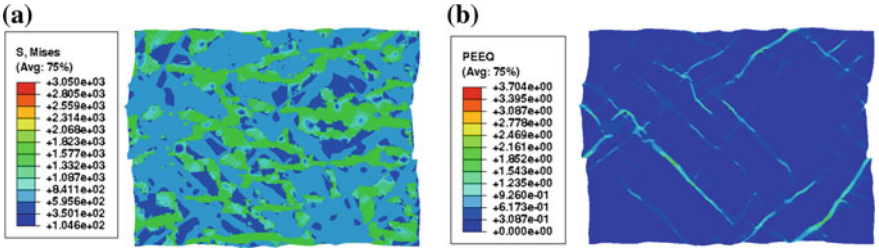

Fig. 3 Results for FEM Analysis of 2D RVE with V_m = 37% under plane strain conditions: **a** von-Mises Stress distribution **b** Equivalent Plastic Strain distribution

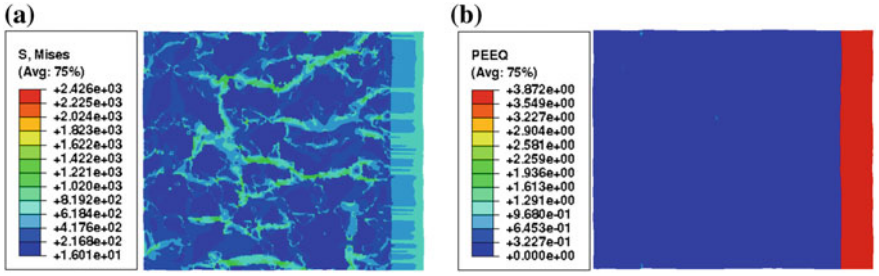

Fig. 4 Results for FEM Analysis of 2D RVE with V_m = 37% under plane stress conditions: **a** von-Mises Stress distribution **b** Equivalent Plastic Strain distribution

early stage, it can thus be concluded that plane stress condition grossly deviates from the real loading conditions. Further, it can be seen from Fig. 3a, b that martensitic regions of the RVE have higher stresses as compared to ferritic regions whereas, ferrite regions have higher plastic strain values as compared to martensite that results in formation of shear-bands. Such a kind of stress and strain partitioning was expected since ferrite being softer phase as compared to martensite shall accommodate higher plastic strain at lower stresses for the same amount of load applied. Similar results were also obtained for the RVE with V_m = 46%

Figure 5a, b shows the final homogenized flow curve obtained for both the RVEs for both plane strain and plane stress assumptions, and their comparison with experimental flow curve. The localization of the plastic strain observed in the deformed RVE for plane stress condition is also exhibited in its homogenized flow curve. The plane stress condition flow curve shows the deviation from the plane strain flow curve at an early stage of deformation and finally shows a drastic drop in the stress values due to localization of plastic strain in the ferrite dominant regions. On the other hand, plane strain assumption predicts a smooth homogenized flow curve. Further, It can be seen that the plane strain condition is able to capture effect of microstructure on the flow curve since the homogenized flow curve obtained for

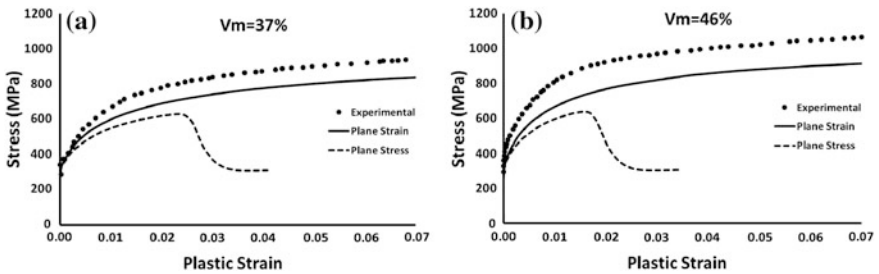

Fig. 5 Homogenized flow curves predicted from the two RVEs under plane strain and plane stress conditions and their comparison with experimental flow curves: **a** Flow curve comparison for RVE with V_m = 37% **b** Flow curve comparison for RVE with V_m = 46%

RVE with $V_m = 46\%$ is higher than the one obtained for $V_m = 37\%$. However, both these 2D assumptions underestimate the flow curve with respect to experimental flow curve. The under-prediction of flow curves from 2D RVEs has also been reported by Ramazani et al. [1] who attributed this deviation from reality to the difference between the deformation condition of a real material that deforms three-dimensionally and a 2D RVE that deforms with plane strain/plane stress condition.

4 Summary and Conclusion

Dual-phase steel contains complex microstructure that needs to be taken into account in the models in order to predict its properties accurately or to study the effect of its microstructures on macroscopic properties. A 2D microstructure-based deformation modeling technique for dual-phase steels was implemented and was used to predict the macroscopic flow behavior of the steels through first-order homogenization. Real micrographs of the steels were used as 2D RVEs and were subjected to plane strain and plane stress deformation under periodic boundary conditions using FEM. Plane stress deformation condition exhibited localization of the plastic strain in the RVE at an early stage of deformation whereas plane strain deformation condition did not show any localization. The homogenized flow curves obtained from this technique were found to underestimate the flow curves of the steel. However, the technique was found to capture the effect of the microstructure on flow curves by predicting higher flow curves for higher martensite content RVE in plane strain conditions. It can thus be concluded that such a technique based on 2D RVEs, under plane strain conditions, although under-predicts the flow curve, may still be used in studying the effect of the microstructural features on the flow curve.

References

1. A. Ramazani, K. Mukherjee, H. Quade, U. Prahl and W. Bleck, Materials Science & Engineering A, 560 (2013), 129–139
2. S. Sodjit and V. Uthaisangsuk, Materials and Design, 41 (2012), 370–379
3. X. Sun, K.S. Choi, W.N. Liu and M.A. Khaleel, International Journal of Plasticity, 25 (2009), 1888–1909
4. X.C. Zhuang, C. Xu and Z. Zhao, Science China Technological Sciences, 58 (2015), 476–484
5. A.C.E. Reid, R.C. Lua, R.E. García, V.R. Coffman and S. A. Langer, International Journal of Materials and Product Technology, 35 (2009), 361–373
6. R.M. Rodriguez, I. Gutierrez, Materials Science Forum, 426–432 (2003), 4525–4530

Effect of Flash Annealing on Ultra-Fine Grained Low-Carbon Steel Processed Through Equal-Channel Angular Pressing Followed by Cryorolling

Raj Bahadur Singh, N. K. Mukhopadhyay, G. V. S. Sastry and R. Manna

Abstract Low-carbon steel (LCS) work pieces are deformed through equal-channel angular pressing (ECAP) up to an equivalent strain of 16.8 (28 passes) at room temperature. Microstructures are characterized by optical microscopy and transmission electron microscopy. Mechanical properties are evaluated by tensile testing and hardness measurements. The material gets refined to ultra-fine level of average grain size of 0.2 μm and the ultimate tensile strength improves from 368 MPa to ultra-high strength of 1008 MPa. ECAP followed by cryorolling of low-carbon steel at −50 °C for 75% of reduction in the area produces bulk nanostructured grains of size 87 nm. The strength of the material further enhanced to 1238 MPa. The strengthening is due to reduction in grain size and high defect density. But the material loses its ductility due to high defect density and nonequilibrium nature of grain boundaries. Flash annealing at 600 °C of bulk nanostructured low-carbon steel produces the bimodal grain size distribution of UFG and micron-sized grains in the microstructure which partially recovers uniform elongation of 20% with improved strength. The material still maintains hardness which is twice as that of as-received material but it decreases with increase in flash annealing temperature.

Keywords Equal-channel angular pressing · Cryorolling · Flash annealing
Low-carbon steel · Ultra-fine grained materials · Bimodal grain size distribution
Bulk nanostructured steel

R. B. Singh · N. K. Mukhopadhyay · G. V. S. Sastry · R. Manna (✉)
Department of Metallurgical Engineering, Indian Institute of Technology,
(Banaras Hindu University), Varanasi 221005, India
e-mail: rmanna.met@iitbhu.ac.in

T. K. Roy et al. (eds.), *Advanced High Strength Steel*, Lecture Notes
in Mechanical Engineering, https://doi.org/10.1007/978-981-10-7892-7_12

1 Introduction

Low-carbon steel has low strength even though it is being used as one of the major structural materials. Strengthening of micron-sized low-carbon steel can be achieved four–five times by reducing the grain size in the ultra-fine range (200–300 nm) [1–4], as it improves through the Hall–Petch relation [5, 6] due to the hindrance of dislocation motion and discontinuity of the slip planes at the grain boundary [7, 8]. However, the ductility gets reduced due to the lack of strain hardening during plastic deformation. Ductility is low for coarse-grained as well as for ultra-fine grained (UFG) low-carbon steel [7]. There is a possibility that if a bimodal grain size distribution is developed in low-carbon steel (where majority of grains are in UFG range which can carry strength) with a mixture of micron-sized grains that can provide good ductility then both high strength with significant ductility can be achieved in low-carbon steel [9, 10].

Wang et al. experimented on electrical grade Cu where nanocrystalline Cu was given short time annealing above secondary recrystallization temperature. The bimodal grain size distribution of 1-3 μm grains was dispersed in UFG 75% matrix of <300 nm size. The ductility could be recovered almost to as-received coarse-grained level and strength still maintained five–six times to staring coarse-grained structure [11]. The bimodal grain size distribution has been reported in dual-phase steel for high strength and ductility combination [12–15]. Severe plastic deformation techniques can be adopted to produce bulk ultra-fine grained structure in low-carbon steel. Among various SPD techniques, equal-channel angular pressing has become popular to produce fully dense ultra-fine grained structure [1, 16–18]. The UFG alloys can be further refined by combining ECAP followed by cryorolling [19].

Therefore, the present work is focused to produce bulk ultra-fine grained/nanocrystalline structure in low-carbon steel to get ultra-high strength and development of bimodal grain size distribution of UFG and micron-sized grain in the steel by optimum annealing treatment to get both high strength and ductility combination.

2 Experimental Procedure

The low-carbon steel work pieces of 15 mm diameter and 80 mm length are machined from the as-received hot-rolled plate of 330 × 220 × 38 mm^3 in the rolling direction. These work pieces are deformed by ECAP using a die consisting of two equal channels intersected at an inner intersection angle (Φ) of 120° and an outer arc angle of (Ψ) 60° at room temperature adopting the route Bc (rotating the sample always in 90° anticlockwise direction between two consecutive passes) [16]. Work pieces are ECAPed using a hydraulic press of 30-ton capacity with the ram speed of 60 mm/min. The work pieces are lubricated by the molybdenum

disulphide with high-density paraffin liquid to reduce friction. A single passage of work piece through the above-mentioned die introduces an equivalent strain of ε_{vm} of 0.6, which is calculated from the following equation [18].

$$\varepsilon_{\mathbf{vm}} = \frac{N}{\sqrt{3}}\left[2\cot\left(\frac{\Phi}{2}+\frac{\Psi}{2}\right)+\Psi\mathrm{cosec}\left(\frac{\Phi}{2}+\frac{\Psi}{2}\right)\right], \quad (1)$$

where accumulated equivalent strain is denoted by $\varepsilon_{\mathbf{vm}}$ and N is the number of passes. A large equivalent strain ε_{vm} of 16.8 is applied on the material through ECAP designated as ECAP-16.8. ECAP-16.8 samples are sectioned along the Y-plane for microstructural investigation, where X-plane is the transverse plane perpendicular to the extrusion direction. The Y-plane is the flow plane vertical to the extruded billet, and the Z-plane is the horizontal but parallel to the top surface along the extrusion direction. The ECAP-16.8 samples are subsequently cryorolled at −50 °C for 75% reduction in the area without lubrication along their extrusion direction in the Y-plane designated as ECAP-16.8-CRR-75. The deformed samples are flash annealed for 5 min in $NaNO_3$ salt, maintained at required temperatures, ranging from 475 to 675 °C and the annealed samples are quenched in water designated as ECAP-16.8-CRR-75-FAT, where T indicates the temperature of annealing.

Initial microstructures are characterized by optical microscopy. The grain size is measured on micrographs by the Heyn's linear intercept method. 200 µm thick slices are cut at Y-plane from pressed work piece. The slices and the cold-rolled sheets are ground by emery papers to 50 µm thin foils. 3 mm discs are punched from these foils. The discs are electropolished in FISCHIONE twin jet polisher at 22 V using electrolyte of 95% methanol and 5% perchloric acid maintained at −40 °C. The detailed microstructure, defects, and the grain boundaries are studied by transmission electron microscopy (TEM) using Tecnai $20G^2$ operating at 200 kV. Rod-shaped samples of gauge diameter 4.5 mm and gauge length 15 mm and plate-shaped sample of gauge width 5 mm, gauge length 15 mm and thickness 1 mm are machined from the stock. Tensile testings for the rod as well as plate samples are conducted using Instron model 4201 at the crosshead speed of 1 mm per minute. Vickers microhardness is measured by Shimadzu HMV-2T Microhardness tester at 980 mN force (100 g load) in the Y—plane at ten different locations of a sample. Plots of measured hardness values versus inverse square root of measured grain size are fitted by using least square error method and Hall–Petch constants (H_o and K) are calculated.

3 Results

The microstructure of as-received hot rolled LCS consists of coarse-grained ferritic structure with an average grain size of 65 µm and 10% pearlite (Fig. 1a; Table 1). On deformation by ECAP for equivalent strain of 16.8, the material gets refined to

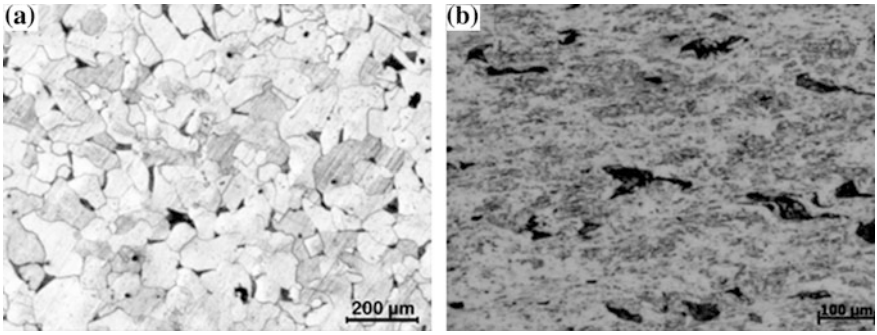

Fig. 1 Optical micrograph of low-carbon steel **a** As-received low-carbon steel **b** ECAP-16.8

Table 1 Average grain size and hardness of low-carbon steel deformed samples

Sample	Average grain size (μm)	Hardness (MPa)
As-received	65 ± 5	1548 ± 80
ECAP-16.8	0.21	4527 ± 60

the very fine level such that the ferritic boundaries are not revealed, though ferrite–pearlite boundaries are visible in the optical microstructure (Fig. 1b).

The TEM bright field image of ECAP-16.8 (Fig. 2a) reveals the ultra-fine grain structure of ferrite of grain size of 200 nm with a high density of dislocations (DDWs). On cryorolling ECAPed low-carbon steel, the microstructure contains dense dislocation walls with the cell size of 87 nm (Fig. 2b; Table 1), and scattered dislocations are present in the interior of the subgrains. These grain boundaries are indicative of highly distorted boundaries.

Annealing of ECAP-16.8-CRR-75 samples at 475 °C for 5 min shows fully recovered grains with less dislocations having unstable grain structures (Fig. 3a). When the ECAP-16.8-CRR-75 sample is flash annealed at 550 °C, the material is recrystallized and the microstructure reveals 82 vol.% of fine-equiaxed ferrite grains

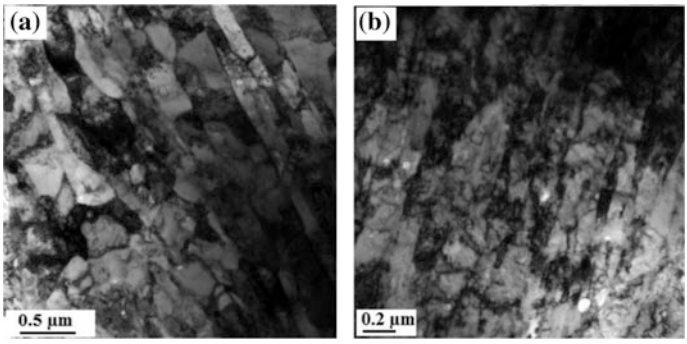

Fig. 2 Bright field TEM images of **a** ECAP-16.8 and **b** ECAP-16.8-CRR-75

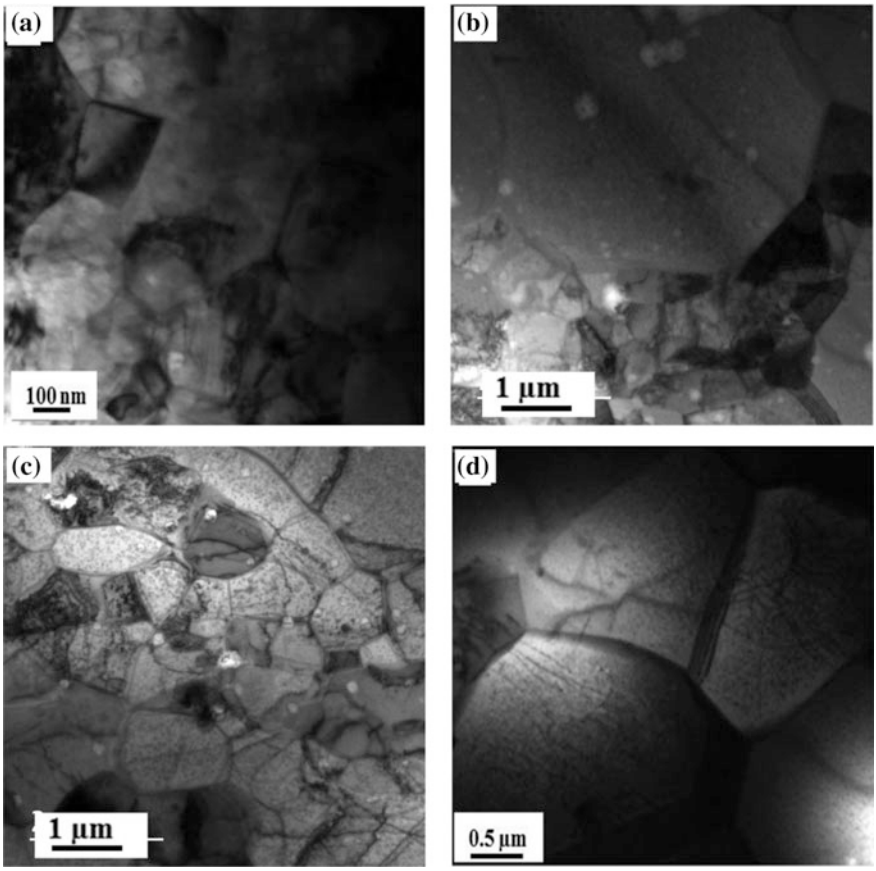

Fig. 3 Bright field TEM images of low-carbon steel **a** ECAP-16.8-CRR-75FA475, **b** & **c** ECAP-16.8-CRR-75FA600 and **d** ECAP-16.8-CRR-75FA675

of 0.77 µm and 18 vol.% of coarse grains (size 4 µm) (Fig. 4a; Table 2). Annealing at 600 °C increases the average fine grain size to 1 µm and a few grains undergo secondary recrystallization and the coarse grain size increases to 5 µm and the volume fraction of coarse grains enhances to 25%. The boundaries of coarse grains take concave shape (Figs. 3b, c and 4b).

As the temperature of annealing increases further, both the coarse grain volume fraction and size increase correspondingly by consuming recrystallized grains. At 675 °C, the microstructure consists of 93 vol.% of coarse grains of the size 10 µm whereas the size of fine grain increases to 2 µm level (Fig. 4c).

Figure 5a displays the engineering stress versus plastic engineering strain plots of deformed and annealed low-carbon steel samples. The as-received low-carbon

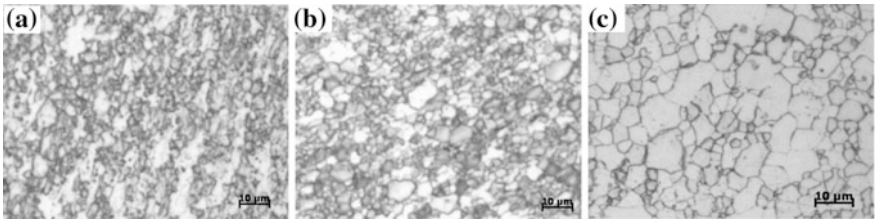

Fig. 4 Optical micrographs of ECAP-16.8-CRR-75 annealed at **a** 550 °C, **b** 600 °C, and **c** 675 °C

steel has UTS of 368 MPa with high ductility, i.e., uniform elongation 23% and total elongation of 41%. When the material is ECAPed to $\varepsilon_{vm} = 16.8$, the UTS increases to 1008 MPa (Fig. 5a) and the uniform elongation reduces drastically to1%. At the same time, the total elongation decreases to 10.6%. On cryorolling of ECAPed low-carbon steel (ECAP-16.8-CRR-75), ultimate tensile strength increases further to 1238 MPa but the total elongation reduces to 4.6% (Table 2). When ECAP-16.8-CRR-75 samples are flash annealed at 600 °C, UTS decreases to 488. However, ductility is recovered with uniform elongation of 20% and total elongation of 25% (Table 3).

Figure 5b represents variation in Vickers hardness of deformed low-carbon steel with annealing temperature. As-received hot-rolled low-carbon steel is having the Vickers hardness value of 1588 ± 80 MPa. After ECAP for $\varepsilon_{vm} = 16.8$ (ECAP-16), the hardness increases to 4527 ± 60 MPa. When deformation mode is changed from ECAP to ECAP+cryorolling, hardness of the material is increased to 4831 ± 90 MPa. As the cryorolled samples are annealed at 475 °C, the hardness begins to decrease to 4077 ± 40 MPa. At 500 °C, the hardness of the deformed samples become 3724 ± 100 MPa which further decreases to 3322 ± 70 MPa at flash annealing temperatures of 550 °C. At 600 °C, the hardness becomes 3175 ± 70 MPa. At 675 °C, hardness decreases to low value of 2744 ± 60 MPa (Fig. 4f).

A linear fit is calculated from experimental values of hardness and inverse square root of grain size in two temperature ranges—one below 600 °C and other one above 625 °C. Values for the H_o and K in low-temperature range are 2760.5 and 611.9 MPa $m^{1/2}$, respectively, and the curve is designated A. In the higher temperature range, the fitted curve is designated as B, and the values of H_o and K are 4310.6 and 18,226 MPa $m^{1/2}$, respectively, in the later case. There is a change in gradient of the fitted curve at 600 °C (Fig. 6).

Table 2 Microstructural parameters and hardness of flash annealed low-carbon steels

Sample	Average (size) coarse grain (μm)	Volume of coarse grain size (%)	Average (size) fine grain (nm)	Volume of fine grain size (%)	Average Grain Size (μm)	Hardness (MPa)
ECAP-16.8-CRR-75					0.087	4831 ± 90
ECAP-16.8-CRR-75-FA475						4077 ± 40
ECAP-16.8-CRR-75-FA500						3724 ± 100
ECAP-16.8-CRR-75-FA550	4	18	770	82	1.53	3322 ± 70
ECAP-16.8-CRR-75-FA575					1.96	3175 ± 70
ECAP-16.8-CRR-75-FA600	5	25	1000	75	2	3096 ± 70
ECAP-16.8-CRR-75-FA625					5.74	2960 ± 80
ECAP-16.8-CRR-75-FA650					6.7	2862 ± 50
ECAP-16.8-CRR-75-FA675	10	93	2000	7	9.44	2744 ± 60

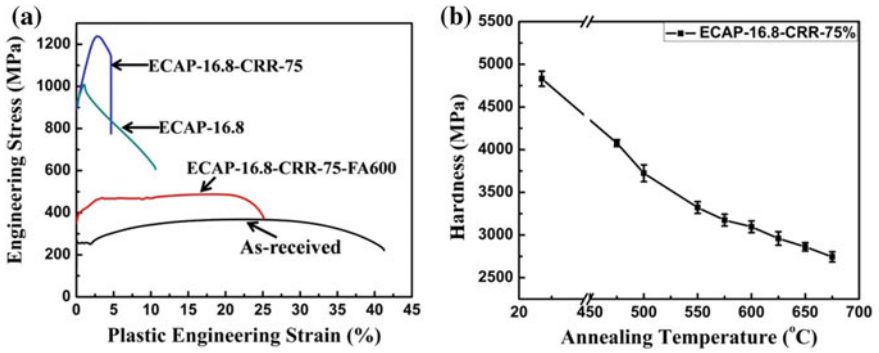

Fig. 5 **a** Engineering stress versus plastic engineering strain plot of low-carbon steel samples, **b** Variation of hardness value with flash annealing temperature of deformed sample (ECAP-16.8-CRR-75)

Table 3 Mechanical properties of low-carbon steels

Sample	YS, MPa	UTS, MPa	Uniform Elongation, %	Total Elongation, %
As-received	272	368	23	41
ECAP-16.8	902	1008	1	10.6
ECAP-16.8-CRR-75	890	1238	2.7	4.6
ECAP-16.8-CRR-75-FA600	351	488	20	25

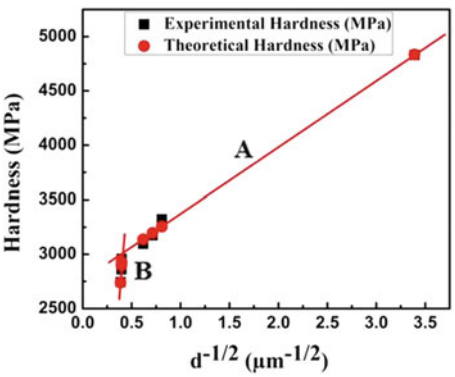

Fig. 6 Variation of hardness with inverse of square root of grain size ($d^{-1/2}$) of ECAP-16.8-CRR-75-FA

4 Discussions

At low strain, micron-sized coarse grains are subdivided into bands. With continued deformation, the bands get thin down and cellular structure is formed within the bands. At high strain ($\varepsilon_{vm} = 12$), thin bands of width one or two subgrains form ribbon grains [20–23]. On further straining, ribbon grains get broken into (Fig. 2a)

near-equiaxed grained structures by shortening ribbon grains through transverse low angle boundaries. The fragmentation of ribbon grains is enhanced by the presence of hard and soft texture components, second phase particles [24, 25] or shear banding. The interconnected boundaries of ribbon grains are diffused and straight, conforming low angle of misorientation at $\varepsilon_{vm} = 16.8$.

When ECAPed low-carbon steel is cryorolled up to 75% reduction in area, ultra-fine grains get refined to nanolevel, closely spaced extended boundaries aligned in rolling direction as DDWs. These DDWs are result of different active slip systems in neighboring regions [26]. The rolling at subzero temperature restricts recovery and increases saturation dislocation density. UFG interstitial-free steel produced by changing mode of deformation from ECAP to ECAP+cryorolling is reported to have improved fraction of refined grain boundaries of nonequilibrium state [19]. Hasegawa et al. [27] have demonstrated that grain boundaries become wavy. Since the grain boundaries contain high defect density, they become wavy and nonequilibrium in nature during deformation, due to enery imbalance between grain boundary and sub-boundaries in the grain interior.

The recrystallization temperature of ultra-fine grained interstitial-free steel is reported to be decreasing with the increase in deformation [28]. On flash annealing of ECAP-16.8-CRR-75 at 475 °C for 5 min, the material is recovered (Fig. 3a). When the annealing temperature increases to 550 °C, part of the material undergoes recrystallization and the remaining part undergoes secondary recrystallization which results in bimodal grain size distribution with a maximum fraction of fine-equiaxed ferrite grains (Fig. 4a). On flash annealing at 600 °C, amount of secondary recrystallization increases that results in increased volume fraction of coarse grains with increased average grain size. It is usually caused by inhibition of finely dispersed second phase particles or a strong single orientation of primary recrystallization texture [20]. Antonion et al. [29] demonstrated a different result that abnormal grain growth process takes place after completion of polygonization process as it completely inhibits any boundary motion. Those grains which are different in boundary energy, size and mobility relative to grain assembly get migrated relatively large. Even flash annealing at 675 °C, deformed low-carbon steel provide unstable microstructure. It contains scattered dislocations as well as significant amount of less than six-sided grains.

ECAP of low-carbon steel increases strength as well as hardness to ultra-high level due to refinement of the material to ultra-fine level with significant amount of defect density. Cryorolling of ECAPed, low-carbon steel reduces the grain size to nanometer level with higher defect density and nonequilibrium nature of boundaries due to restricted recovery at subzero temperature. This leads to further strengthening and hardening of the material. However, nanostructure low-carbon steel loses its ductility due to less work hardening ability of grains of nonequilibrium nature of boundaries.

On flash annealing of ECAPed and cryrolled low-carbon steel at low temperature (<500 °C), the material is recovered. Therefore, hardness decreases marginally. When the deformed low-carbon steel is flash annealed above 550 °C, the material is

partly recrystallized and partly by secondary recrystallized. Therefore, significant drop in hardness could be observed. Flash annealing above 600 °C leads to secondary recrystallization that results in bimodal grain size distribution. Material loses its strength but recovered ductility significantly. The fine grains carry strength but coarse grains provide ductility to the material. Below 600 °C, strengthening is due to grain refinement, high defect density, and nonequilibrium nature of grain boundaries but above 600 °C, strengthening is due to fine grain size. Because of change in mechanism of strengthening in two range of flash annealing temperature, change in gradients could be observed in the plot of hardness vs inverse square root of grain size.

5 Conclusions

Bulk nanostructured low-carbon steel of grain size 87 nm can be produced by ECAP at ε_{vm} = 16.8 followed by cryorolling at −50 °C for 75% reduction in area. Ultimate tensile strength of nanostructured steel increases to 1238 MPa due to grain refinement and high dislocation density. The ductility of the material drastically dropped due to high defect density and nonequilibrium nature of boundaries of nanograins.

ECAP followed by cryorolling and flash annealing of low-carbon steel produces novel microstructure of bimodal grain size distribution of ultra-fine grains and micron-sized grains due to combination of recrystallization and secondary recrystallization, respectively. The bimodal structure recovers ductility from micron-sized grains whereas ultra-fine grains carry the strength. Therefore, ECAP combined with cryorolling and flash annealing can be utilized to get both high strength with high ductility. However, the material is partially recrystallized because of short period of annealing.

References

1. R.Z. Valiev, R.K. Islamgaliev and I.V. Alexandrov, Progress in Materials Science, 45 (2000), 103–189
2. A.A. Karimpoor, U. Erb, K.T. Aust and G. Palumbo, Scripta Materialia, 49 (2003), 651–656
3. K.T. Park and D.H. Shin, Materials Science and Engineering: A, 334 (2002), 79–86
4. C.C. Koch, Scripta Materialia, 49 (2003), 657–662
5. E.O. Hall, Proceedings of the Physical Society. Section B, 64 (1951), 747–53
6. N.J. Petch, Journal of the Iron and Steel Institute, 174 (1953), 25
7. R. Song, D. Ponge, D. Raabe, J.G. Speer and D.K. Matlock, Materials Science and Engineering: A, 441 (2006), 1–17
8. V.M. Segal, Materials Science and Engineering: A, 386 (2004), 269
9. D.H. Shin and K.T. Park, Materials Science and Engineering: A, 410–411 (2005), 299–302
10. S.M. Hosseini, M. Alishahi, A. Najafizadeh and A. Kermanpur, Materials Letters, 74 (2012), 206–208

11. Y.M. Wang, M.W. Chen, F.H. Zhou and E. Ma, Nature, 419 (2002), 912–915
12. H.A. Alizamini, M. Militzer and W.J. Poole, A novel technique for developing bimodal grain size distributions in low carbon steels, Scripta Materialia, 57(12) (2007), 1065–1068
13. P.J. Szabo, D.P. Field, B. Joni, J. Horky and T.S. Ungar, Metallurgical And Materials Transactions A, 46a (2015), 1948–1957
14. S. Patra, S.Md. Hasan, N. Narasaiah and D. Chakrabarti, Materials Science and Engineering A, 538 (2012), 145–155
15. T.S. Wang, F.C. Zhang, M. Zhang and B. Lv, Materials Science and Engineering A, 485 (2008), 456–460
16. R.Z. Valiev and T.G. Langdon, Progress in Materials Science, 51 (2006), 881
17. M. Furukawa, Z. Horita, M. Nemoto and T.G. Langdon, Materials Science and Engineering: A, 389 (2002), 82–89
18. Y. Iwahashi, J. Wang, Z. Horita, M. Nemoto and T.G. Langdon, Scripta Materialia, 35 (1996), 143–146
19. D. Verma, N.K. Mukhopadhyay, G.V.S. Sastry and R. Manna, Transactions of the Indian Institute of Metals, (2016) https://doi.org/10.1007/s12666-016-0881-0.
20. F.J. Humphreys and M. Hatherly, Recrystallization and Related Annealing Phenomena, second Ed, Pergamon Press Oxford, (1995), pp 368–371
21. R. Manna, N.K. Mukhopadhyay and G.V.S. Sastry, Scripta Materialia, 53 (2005), 1357–1361
22. Y.T. Zhu and T.C. Lowe, Materials Science and Engineering: A, 291 (2000), 46–53
23. D. Verma, N.K. Mukhopadhyay, G.V.S. Sastry, and R. Manna, Metallurgical and Materials Transactions A, 47 (2016), 1803–1817
24. D.H. Shin, B.C. Kim, Y.S. Kim and K.T. Park, Acta Materialia, 48 (2000), 2247–2255
25. D.H. Shin, I. Kim, J. Kim and K.T. Park, Acta Materialia. 49 (2001), 1285–1292
26. N. Hansen, X. Huang and G. Winther, Materials Science and Engineering: A, 494 (2008), 61–67
27. M. Hasegawa and H. Fukutomi, Materials Transactions, 43(5) (2002), 1183–1190
28. D. Verma, S. Pandey, A. Bansal, S. Upadhyay, N.K. Mukhopadhyay, G.V.S. Sastry and R. Manna, Journal of Materials Engineering and Performance, (2016), 1–10. https://doi.org/10.1007/s11665-016-2392-x.
29. C. Antonione, G. Dellagatta, G. Riontino and G. Venturello, Journal of Materials Science, 8 (1973), 1–10

Microstructural Evolution in Boron-Added Advanced High-Strength Steel Suitable for Hot Stamping

Anjana Deva, M. Deepa, G. Sahu, A. K. Bhakat and B. K. Jha

Abstract Fuel cost, dwindling resources, and exponentially increasing traffic density have brought about a sea change in thinking of automotive designers, manufacturers, and end users. Though number of recently developed advanced high-strength steels fulfill the expectation of automobile component manufacturers in terms of weight reduction and safety norms, it suffers the inherent problem of spring back phenomena and limited formability. This problem can be addressed if the component is formed at high temperature where it has adequate formability and subsequently it is controlled cooled to get the desired combination of strength and ductility; the process is commonly known as hot stamping. As C (0.2–0.3 wt%)-Mn (1.2–1.3%)- Cr (0.1–0.2 wt%)- B (25–35 ppm) alloyed steels have been the point of focus for the choice of materials in hot stamping, study has been carried out on effect of concurrent deformation and cooling on hardening behavior and associated microstructural changes of C–Mn–Cr–B steel. Further, effect of molybdenum ($\sim$0.1 wt%) in influencing the microstructure and thereby hardening in conventional C–Mn–Cr–B steels has also been evaluated. The present study reveals that a range of tailored properties can be achieved through locally controlling strain, strain rate, cooling rate, and resultant microstructure within the stamping die.

Keywords Hot stamping · AHSS · Formability · Hardenability
Boron · Molybdenum

A. Deva (✉) · M. Deepa · G. Sahu · A. K. Bhakat · B. K. Jha
Research & Development Centre for Iron and Steel, Steel Authority of India Limited, Ranchi, Jharkhand, India
e-mail: anjana@sail-rdcis.com

T. K. Roy et al. (eds.), *Advanced High Strength Steel*, Lecture Notes in Mechanical Engineering, https://doi.org/10.1007/978-981-10-7892-7_13

1 Introduction

Abject use of natural resources has obviously led to sharp decline in their availability leading to sharp rise in their cost. Coupled with the rise in living standard, the per capita utilization of transport implements has increased tremendously, with the consequence that the traffic density has raised to the extent that probability of accidents has also escalated. These bring in the responsibility on the customized materials designers for specific use in fabrication of high-strength lightweight safe automotive components at minimum of cost, needless to state that the car bodies will require steels with ultra-high strength. On the other hand, forming of sheet becomes more and more challenging with increasing strength values along with limited elongation [1].

To encounter these problems, all the deformations need to be done at high temperature in austenitic phase. Hot stamping with die quenching appeared at the end of 1990s for producing ultra-high-strength automotive parts like door beams and bumper beams [2–4]. This novel technological process includes heating the sheet to a high temperature for austenization, soaking it completely, and then transferring it into the cooling dies for forming and quenching with optimized cooling rate to control the material phase transformations for getting the desired mechanical properties [5, 6]. In view of above, simulation study has been conducted with boron-alloyed carbon manganese steel to understand effect of thermo-mechanical processing with accelerated cooling on hardening behavior and associated microstructural changes.

Response to hardening behavior of steel with boron alone and in the presence of molybdenum (0.2–1.0 wt%) is different and researches [7–9] have been carried out to understand its influence. In this paper, with the aim of utilizing microalloyed boron effectively in hot stamping process, small amount of Mo ($\sim$0.1 wt%) has been added in boron steel, and combined addition of boron and molybdenum on microstructure and mechanical property has been examined.

2 Experimental

The material used in the simulation tests is boron (25–35 ppm) alloyed C (0.2–0.3 wt%)- Mn (1.2–1.3 wt%) steel with small amount of chromium (0.1–0.2 wt%) addition. The effectiveness of boron in increasing hardenability depends on the form of boron retained in the steel. To enhance availability of free boron for increasing hardenability, titanium ($\sim$0.02 wt%) has also been added stoichiometrically. Samples for simulation study have been prepared from 32 mm transfer bar collected after rough rolling of industrial heat made through basic oxygen furnace —ladle furnace refining—continuous casting route.

Dilatometric curves have been generated while carrying out the tests in Gleeble 3500 using 85-mm-long cylindrical samples with 10-mm diameter keeping soaking temperature of 900 °C and cooling rates ranging from 1 to 30 °C/s. Forming and

quenching processes have been simulated by hot compression and subsequent fast cooling. To conduct the tests, cylindrical samples of 15 mm length and 10 mm diameter have been soaked at 900 °C for chemical and structural homogenization and then deformed to true strain of 0.69 corresponding to reduction of 50%. In order to reveal the quenching effect, three cooling rates have been employed, viz., 5, 20, and 50 °C/s.

In addition to the above tests, simulation study has also been conducted with addition of molybdenum in above-mentioned C–Mn–Cr–B steel. Laboratory heat of 25 kg, alloyed with both boron and molybdenum, has been made using a high-frequency induction melting furnace, cast into 100 mm × 100 mm square ingots and subsequently hot rolled into 12 mm plates in experimental rolling mill. These plates have been used for preparing test samples to carry out simulation experiments.

3 Results and Discussion

Figure 1a, b depicts the dilation versus temperature plots during thermal treatments of two samples at cooling rates of 0.5 and 20 °C/s. It can be seen that along heating process there is sudden change in slope of the dilation line at ∼834 °C (Ac3 temperature). This may be perceived as beginning of transformation from phase containing ferrite–pearlite mixture to austenite. The plot remains askew till the transformation is complete. Thereafter, it assumes the linear course till the austenitization temperature of 900 °C. After soaking for about 120 s, the sample is cooled. During cooling, at Ar3 temperature, the austenite will begin to give way for the formation of proeutectoid ferrite. However, the detection of this temperature on the plot is somewhat tricky as the change of slope is gradual. To determine the temperature accurately, a different approach has been adopted. Two linear portions from upper and lower parts of the cooling side of the plot were drawn. Their joining point was interpreted as the start of separation of proeutectoid ferrite from the austenite parent phase. The detection of temperatures of start and finish of transformation to pearlite is somewhat straightforward. The plot of Fig. 1b can be interpreted on identical line.

Eight separate plots were obtained from thermal simulation experiments for each cooling rate. Each of critical transformation temperatures (Ac_3 & Ar_3) has been identified and the result has been collated in Table 1.

Figure 2a–d shows the optical micrographs from samples subjected to varying cooling rates as indicated in the figure. Ferrite–pearlite microstructures can be seen as predominant phases in samples cooled at slower rates of 0.5 °C/s (Fig. 2a) and 2 °C/s (Fig. 2a). With the help of proeutectoid ferrite formed along the prior austenite grain boundary, prior austenite grain size was measured and it was found to be in the range of 130–140 µm.

Appearance of bainite can be indicated at 10 °C/s and with further increase in cooling rate (20 °C/s), bainite and martensite become predominant resulting into

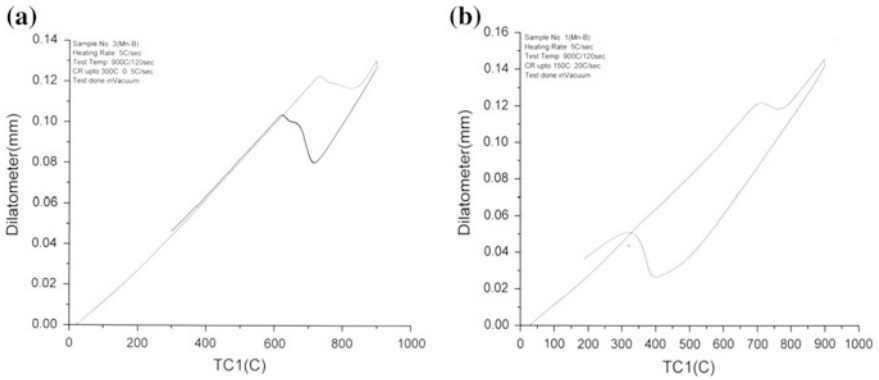

Fig. 1 Plot showing the dilatometry curves varying with temperature **a** 0.5 °C/s **b** 20 °C/s

Table 1 Temperatures of transformation as estimated from dilation plots obtained at different cooling rates

Cooling rate (C/s)	Ac_3(C)	Ar_3(C)	Ps(C)	Pf(C)
0.2	845.3	734.8	734.8	624.3
0.5	834.2	734.8	624.3	729.2
1	827.7	704.8	699.3	582.7
2	790.9	711.8	683.6	576.2
5	816.3	723.1	666.6	536.7
10	838.0	738.8	629.9	355.2
20	754.8	700.0	527.2	299.7
36	800.5	713.8	685.3	286.5

rapid increase in hardness values. These effects have been shown in Fig. 3, wherein the hardness increases almost 3.5 times; from a value 90 to ~320 on Brinell hardness scale, it corresponds to tensile strength value of ~1100 MPa.

Importance of critical cooling rate, above which hardenability effect of boron decreases, has been outlined in literature [10] where it has been reported that in low-alloyed boron containing C–Mn–Ni–Mo–Ti steel with high Mn (~2%) and Si (~0.5%), a critical cooling rate ~20 °C/s is prequisite for maximum segregation of boron at grain boundary. A cooling rate higher than this may result in decreasing hardenability of steel as a consequence of paucity of time for boron segregation to the grain boundaries [11].

4 Effect of Cooling After Deformation

Flow curves generated for the deformed specimens subjected to 50% reduction and cooled at three different cooling rates 5, 20, and 50 °C/s during hot deformation study are depicted in Fig. 4. It may be noticed that that flow curve corresponding to

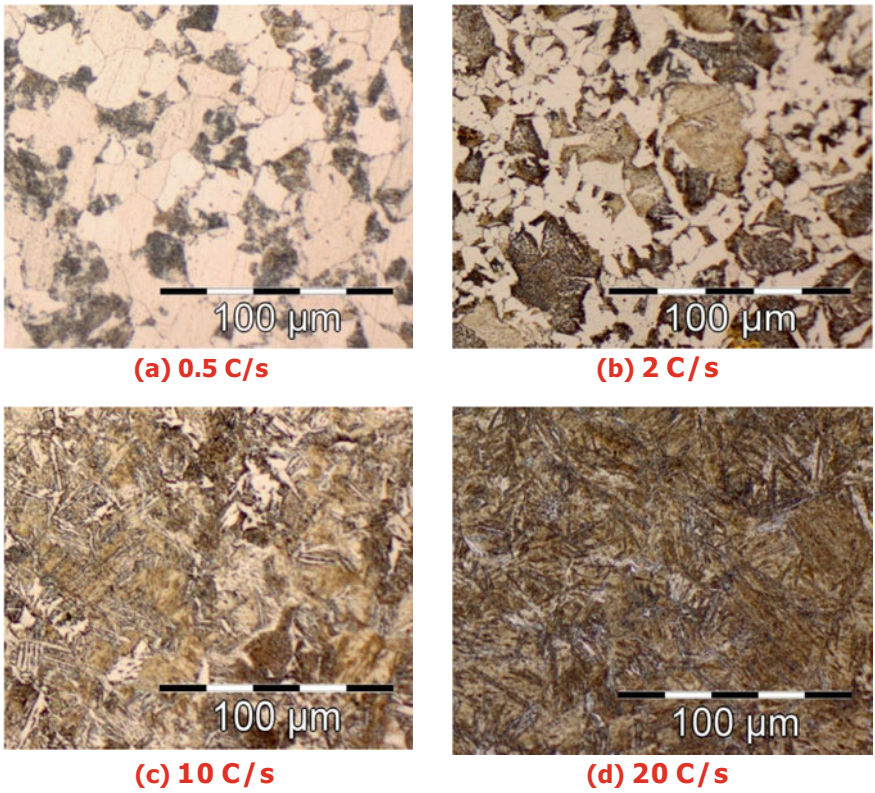

Fig. 2 Optical micrographs from samples with varying cooling rates

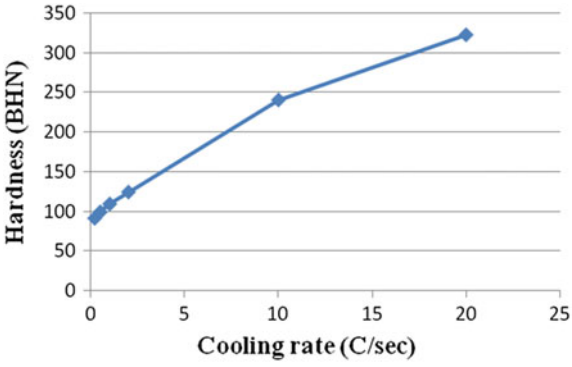

Fig. 3 Plot showing the variation of hardness with respect to cooling rate

cooling rate of 20 °C/s is higher than that achieved with samples subjected to higher cooling rate of 50 °C/s. At higher cooling rate segregation of boron seems to be restricted due to lack of diffusion time. However, cooling rate of 20 °C/s is just

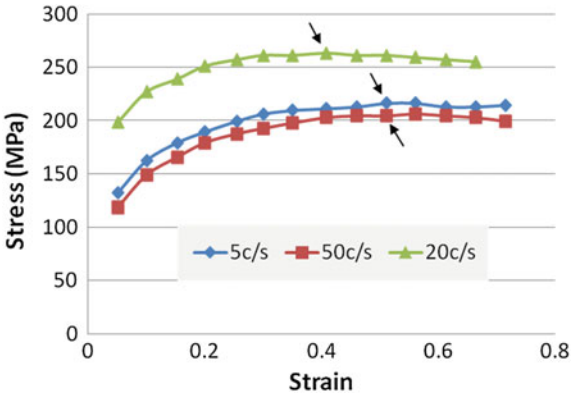

Fig. 4 Flow curves showing the variation of strain with respect to stress at 50% deformation at different cooling rates

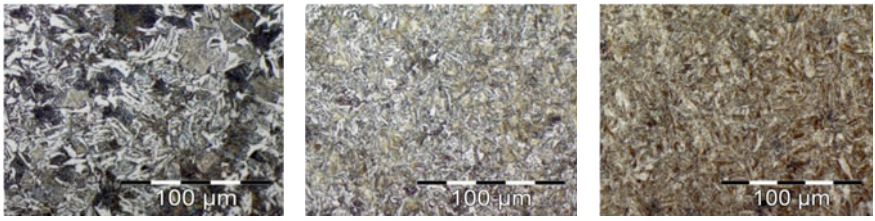

Fig. 5 Optical micrographs of samples subjected to 50% deformation at varying cooling rates

right to obtain maximum boron segregation to prior austenite grain boundary that leads to formation of martensite. Uniform strain is found to be highest with a value of ~0.58 for cooling rate of 50 °C/s with respect to those of ~0.56 and ~0.45 obtained for cooling rates of 5 and 20 °C/s, respectively. This is significant as formability is related to uniform elongation to some extent. The arrows indicate occurrence of uniform strains in various flow curves.

Isothermally deformed samples were examined in optical microscope. Micrograph of sample cooled at the rate of 5 °C/s (Fig. 5a) depicts a mixture of polygonal, acicular, and widmanstatten ferrite and pearlite structure. The presence of directional ferrite in fine ferrite–pearlite phase mixture can be seen. The structure changes to acicular phases (bainite/martensite) as the cooling rates are increased to 20 and 50 °C/s as depicted in Fig. 5b, c, respectively.

Another noteworthy point is the difference in packet size and acicularity of martensite which appear to be the deciding factors in ascertaining the strength [10].

Those with the cooling rate of 20 °C/s have much smaller size than those with greatest cooling rate of 50 °C/s. These concurrent deformation and cooling experiments validated the conjecture that cooling rates though have a threshold for the formation of martensite phase unbound accelerated cooling may not yield the desire property combinations as has been demonstrated through comparative studies on samples cooled at the rates of 20 and 50 °C/s.

5 Synergistic Effect of Boron and Molybdenum

In this section, synergistic effect of boron with molybdenum on microstructure evolution of steel has been discussed. Figure 6a, b depicts the transmission electron micrographs of C–Mn–Cr–B steel with and without molybdenum, respectively. Both the steel samples have been first soaked at 900 °C for 120 s and cooled with a rate of 30 °C/s. Hardenability of different samples treated identically may be linked to the volume fraction of martensite present and its morphology. Among the two morphological variants of martensite, the one lath type is preferred as it bestows the steel with fair amount of ductility along with increase in strength [12].

Martensite become the leading constituent phase with some amount of bainite for steel with molybdenum (Fig. 6a). The presence of harder phases can also be seen in steel without molybdenum (Fig. 6b). Fine bainite, having laths partially, has been observed in steel with molybdenum, and prerequisite for achieving good combination of high strength with ductility. Fine cementite precipitated along the prior austenite grain boundaries as well as inside the grains in Mo–B steel (Fig. 6c), while a large amount of coarse cementite precipitated in boron steel (Fig. 6d). Diffusion of carbon in austenite is reported to be slower by molybdenum [13]. Formation of coarse cementite has been suppressed by Mo addition. Reducing carbon content in Mo–B steel is also effective for suppressing formation of $Fe_{23}(C,B)_6$ and as a result, the segregated boron to the austenite grain boundary is increased and thereby retarded austenite to ferrite transformation and promoted bainite and martensite transformation. These microstructural evolution has reflected in increased hardness (495 BHN) in steel with Mo as compared to that (440 BHN) steel without boron, which are equivalent to the tensile strength values of 1700 and 1490 MPa, respectively. Both the steels are found suitable for manufacturing automotive components through hot stamping process. Depending upon the cooling rate and deformation, variation in combination of different phases can be created for desired end properties.

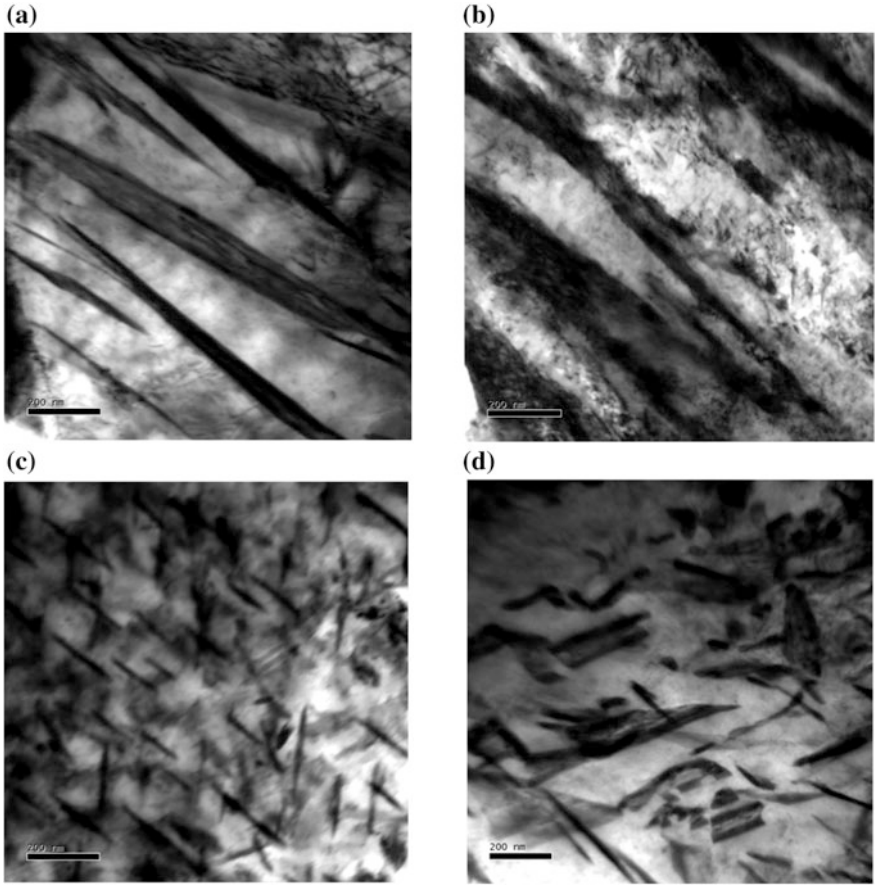

Fig. 6 Transmission electron micrographs of **a&c** C–Mn–Cr–Mo–B steel **b&d** C–Mn–Cr–B Steel subjected to cooling rate of 30 °C/s

6 Conclusion

Simulation studies on boron-added C–Mn–Cr steel have shown that a minimum cooling rate of 20 °C/s is essential for obtaining microstructure with bainite and martensite requisite for getting high strength in hot-stamped automotive components. Addition of molybdenum has helped in getting higher percentage of martensite which in turn has resulted into higher hardness (495 BHN) in steel at 30 °C/s as compared to 440 BHN in steel without molybdenum.

Acknowledgements The authors acknowledge help and support provided by RDCIS, SAIL, Ranchi.

References

1. T. Yoshida, E. Isogai, K. Sato and K. Hashimoto, Nippon Steel Technical Report, (103) May (2013), 4
2. H. Karbasian and A.E. Tekkaya, Journal of Material Processing Technology, 210 (2010), 2103
3. T. Altan, Stamping Journal, FMA publication, December (2006), 40
4. T. Altan, Stamping Journal, FMA publication, January (2007), 14
5. A. Deva, S.K. De, V. Kumar, M. Deepa and B.K. Jha, International Journal of Metallurgical Engineering, 2, (1)(201), 47
6. S. Ojha, N.S. Mishra and B.K. Jha, Bulletin of Material science, Indian Academy of Sciences, 38(2) April (2015), 531
7. T. Hara, H. Asahi, R. Uemori and H. Tamehiro, ISIJ International, 44(8) (2004), 1431
8. L. Karlsson and H. Norden, Acta Metallurgica, 36(1) (1988), 35
9. H. Asahi, ISIJ International, 42(10) (2002), 1150
10. J.M. Dong, J.S. Eun, M.K. Yang, Nuclear Engineering and Technology, 43 (2011), 1
11. A. Deva and B.K. Jha, Heat Treating of Iron and Steel, ASM Handbook, D(7) (2015), 179
12. B.L. Bramfitt and A.O. Benscoter, Metallographer's Guide: Practice and Procedures for Irons and Steels, ASM International, (2001)
13. T. Tanaka and T. Enami, Test-to Hagane, 58 (1972), 1775

A Novel Low-Carbon High-Strength Steel: Processing, Microstructure and Mechanical Properties

S. Mitra, S. K. Ghosh and S. Mukherjee

Abstract A novel alloy steel has been processed through thermo-mechanical controlled rolling with two different finish rolling temperatures (FRT: 850 and 750 °C) followed by air cooling and water quenching. Microstructural investigation using TEM showed that air-cooled steel processed at lowest FRT of 750 °C reveals nano-sized (10–20 nm) complex carbide precipitates of (TiMoV)C which are significant for precipitation hardening in ferrite matrix. Air-cooled steels exhibit 420–440 MPa yield strength and 640–680 MPa ultimate tensile strength along with 20–23% elongation. On the other hand, higher yield strength (900–1000 MPa) and tensile strength (1050–1150 MPa) along with lower 9–11% elongation are attributed to complex precipitation in primarily dislocated lath martensite structure achieved on water quenching. Evaluation of hot ductility, as measured by the reduction of area (RA), reveals that RA decreases in the temperature range of 700 to 850 °C and then rises up to 1100 °C. The maximum achievable ductility of 69% at 1100 °C is related with the stability of austenite at high temperature, whereas minimum ductility (14%) at 850 °C is related with the formation of pro-eutectoid ferrite along the austenite grain boundaries in two-phase (austenite and ferrite) region.

Keywords Alloy steel · Thermo-mechanical controlled rolling
Microstructure · Mechanical properties

S. Mitra · S. K. Ghosh (✉)
Department of Metallurgy and Materials Engineering, Indian Institute of Engineering Science and Technology, Shibpur, Howrah 711103, India
e-mail: Swarupkrghosh@gmail.com

S. Mitra
e-mail: mitra.somu@gmail.com

S. Mukherjee
R&D Division, Tata Steel Limited, Jamshedpur 831007, India

T. K. Roy et al. (eds.), *Advanced High Strength Steel*, Lecture Notes in Mechanical Engineering, https://doi.org/10.1007/978-981-10-7892-7_14

1 Introduction

Steel is always a preferred material for the automotive manufacturers for various reasons, e.g. strength, impact resistance, ease of forming, welding, etc. Since 1990, different norms were started coming into consideration due to safety purposes. To meet such norms, it became evident that either high strength steels or material of higher thickness would be required. The later will increase the deadweight of the vehicle and therefore not desired. On the other hand, increase in strength will reduce the thickness of the material and thereby weight of a vehicle. This in turn will increase the fuel efficiency of the vehicle, leading to a lower CO_2 emission and improved passenger safety [1, 2]. So far, various high strength steels are introduced. The development of high strength steel mostly involves the introduction of new phases/strengthening mechanisms but, unfortunately, many of these alloys are fully or partially restricted to the laboratory due to the complex processing and thus expensive. Funakawa et al. [3] reported the possibility to improve strength through nanoscale precipitates distributed in a ferritic matrix and processed by a conventional rolling set-up. They proposed a strength improvement of 2–3 times higher than that expected from conventional precipitation hardening (90–150 MPa) in microalloyed steels [4]. In the present study, Ti, Mo microalloyed composition was investigated. The wt% of Ti is 0.30 which is much higher than normally available microalloyed steel. The physical significance of higher amount of Ti addition is to form fine precipitates, whereas excess amount of Mo is used to inhibit the growth of MC carbides by reducing the activity of other carbide forming elements [5, 6].

Thermo-mechanical controlled rolling (TMCR) involves controlled hot working of microalloyed steel which promotes fine grain sizes and precipitation strengthening [7]. Accelerated cooling after finish rolling can result in further refinement of ferrite grain size as well as formation of low temperature phases (bainite/martensite). The loss of hot ductility of commercial low carbon or low alloy steels has received much attention nowadays because it can be used to predict the likelihood of transverse cracking produced in the continuously cast steel during straightening. It has been reported that the segregation of impurities to grain boundaries plays an important role in the loss of hot ductility in addition to the thin pro-eutectoid ferrite layer formation and the precipitation of carbides or nitrides of V, Ti, Nb or Al at austenite grain boundaries [8]. The objective of this paper is therefore to investigate the effects of finish rolling temperature (FRT) and cooling rate after controlled hot rolling as well as its hot ductility behaviour. Finally, a correlation between microstructure and mechanical property has been made.

Table 1 Chemical composition of the investigated steel (wt%)

C	Mn	Si	Al	Ti	Mo	V	Nb	Cr	S	P	N
0.12	1.60	0.29	0.10	0.30	0.44	0.028	0.04	0.15	0.003	0.002	0.006

2 Experimental Procedure

The chemical composition of the investigated steel is given in Table 1. The as-received steel was obtained in the form of hot-rolled transfer bar which was cut into suitable sizes (80 × 20 × 15 mm^3) and soaked at 1200 °C for about 60 min. Subsequently, these samples were thermo-mechanically processed (controlled hot rolled) in a laboratory scale two high rolling mill (10 HP). Two finish rolling temperatures (FRTs) were maintained at 850 and 750 °C and finally the rolled plates (≈8 mm thick) were subjected to air cooling and water quenching. Metallographic samples were etched using 2% nital solution after conventional grinding and polishing techniques. For transmission electron microscopy, typical 3 mm discs were punched from thin foil and subjected to twin-jet electro-polishing using a mixture of 5% perchloric acid, 25% glycerol and 70% ethanol at 10 °C, using a potential of 35 V. The thin electron transparent samples were examined on a Transmission Electron Microscope (TEM, Tecnai G^2), operated at 200 kV. Hardness measurement was done by using a Vickers microhardness tester (Leica, VMHT) under a 2 kg load and dwelling time of 20 s. Tensile testing was carried out using a computer-controlled Instron-5900R testing machine with an extensometer. The test specimen was prepared as per ASTM standard (ASTM: Vol. 03.01: E8M-96). The yield strength (YS), ultimate tensile strength (UTS), percent uniform elongation (%UEL) and percent total elongation (%TEL) were determined from the machine output. The hot ductility specimens of 10 mm diameter and 120 mm in length were machined from the hot-rolled plate in longitudinal direction and tests were performed in a Gleeble 3800 thermo-mechanical simulator with a strain rate of 0.001/s. The hot tensile specimens were heated to 1200 °C to dissolve all alloying additions at a rate of 20 °C/s, then held there for 600 s and finally cooled with the same rate as in heating to temperatures ranging from 750 to 1100 °C at an interval of 50 °C, at which they were maintained for 10 s before test in agreement with the test reported earlier [9]. After rupture, the specimen was quickly cooled to room temperature under a flow of argon.

3 Results and Discussion

3.1 Microstructure

Figure 1a reveals ferrite of both equiaxed and non-equiaxed morphologies of bright contrast and some other unresolved dark phases in optical micrographs, whereas the

above phases appear in dark and bright contrasts, respectively in SEM micrograph of Fig. 1b. In case of sample processed at FRT 850 °C, optical micrograph in Fig. 1c shows ferrite phase of bright contrast and some other unresolved dark phases. Unresolved dark phases appear like pearlite [10]. The SEM micrograph in Fig. 1d shows ferrite phase of dark contrast, lamellar dark phase as pearlite and some unresolved bright precipitates throughout the ferrite matrix. The cubical precipitates of 30–50 nm in diameter are also observed in the vicinity of grain boundaries and also occur at intra-granular regions. Such kind of particles are mainly titanium nitrides, however presence of other elements like Nb is also possible [11, 12].

TEM bright field image of the investigated steel (FRT 750 °C AC) specimens is shown in Fig. 2a which illustrates polygonal ferrite phase with some amount of dislocation within ferrite. Ferrite presumably contains fine precipitate (10–20 nm) particles of dark contrast in Fig. 2b which is in agreement with earlier reports [5, 12, 13]. These fine precipitates appear as spherical shape of bright phase in dark field image as shown in Fig. 2c. The EDS spectra taken from the precipitate particle (denoted by arrow) are shown in Fig. 2d which reveals that the particle is enriched with Ti, V, Mo and C. The chemical compositions of precipitate denote the presence of complex carbide precipitate (TiMoV)C. It is important to mention that these fine particles are significant for precipitation hardening [14].

Figure 3a, b shows optical and SEM micrographs of hot-rolled (850 °C FRT) specimen followed by water quenching. The micrographs essentially reveal lath martensite. It is evident that the prior-austenite grain interior is getting transformed

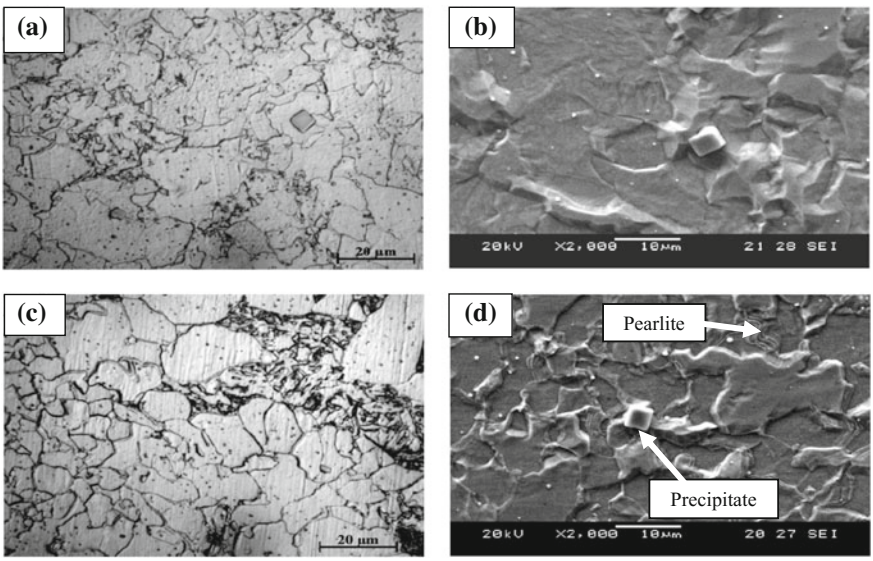

Fig. 1 **a** Optical and **b** SEM micrographs of air-cooled specimens (FRT 750 °C); **c** Optical and **d** SEM micrographs of air-cooled specimens (FRT 850 °C)

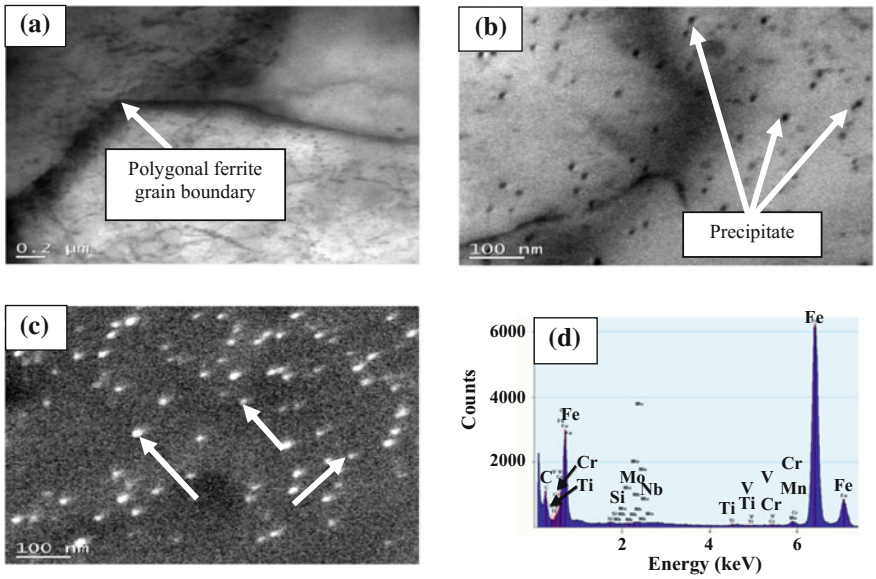

Fig. 2 TEM bright field image (BF) of air-cooled sample (FRT 750 °C) showing **a** polygonal ferrite; **b** fine dark precipitate particles dispersed in ferrite matrix; **c** dark field image of precipitates; **d** EDS spectra obtained from fine precipitate (denoted by arrow in (**c**))

into martensite laths [15]. It is important to note that while morphology of martensite is unclear in optical micrograph, the same appears to be the lath type in SEM micrograph (Fig. 3b).

Figure 4a shows the TEM bright field image (BF) of FRT 850 °C WQ sample which reveals martensite lath with high dislocation density. The dislocation density is very high and almost evenly distributed. Such dislocation density is attributed to the accommodation strain during formation of lath martensite. However, the possibility of formation of some bainite cannot be ignored [15]. Figure 4b shows TEM

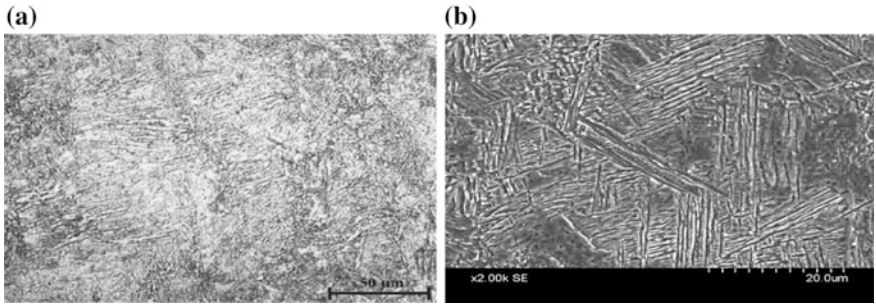

Fig. 3 **a** Optical micrograph; **b** SEM micrograph of the hot rolled (850 °C FRT) followed by water quenching

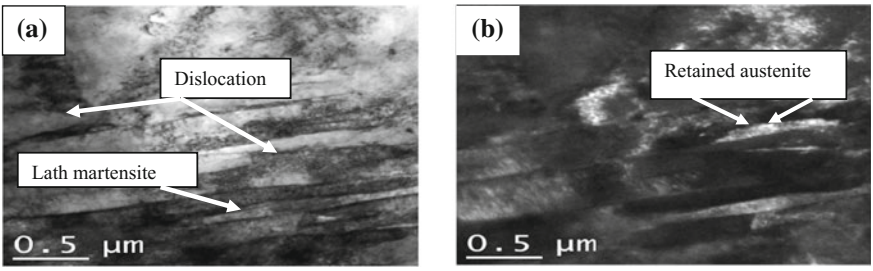

Fig. 4 TEM bright field image (BF) of FRT 850 °C WQ sample showing **a** martensite lath with high dislocation density; **b** corresponding dark field image

dark field image (DF) of FRT 850 °C WQ sample which reveals martensite of dark contrast and thin film like retained austenite of bright contrast in the interlath position.

3.2 Hardness and Tensile Properties

Hardness of the specimen in as-received condition (hot rolled transfer bar) is 290 HV. Presence of precipitates and small amount of pearlite (~0.05) in the ferrite matrix results in high hardness value. Hardness value of air-cooled samples decrease (from 191 ± 3 HV to 181 ± 2 HV) with the increase of finish rolling temperature (from 750 to 850 °C). The lower value of hardness in air-cooled condition may be correlated primarily with the coarse ferritic microstructure (~20 μm) with little amount of pearlite present in the microstructure obtained at 850 °C FRT. The highest hardness value of 361 HV could be related to lath martensitic microstructure obtained after 850 °C FRT followed by water quenching whereas in 750 °C FRT, hardness value reaches a lower value of 308 HV. This is attributed to the fact that in case of 850 °C FRT, volume fraction of martensite (~0.98) is higher than that (~0.87) of 750 °C FRT on water quenching which is consistent with the earlier results [16].

The tensile properties of the investigated steels are summarised in Table 2 and Fig. 5. It is evident that yield strength (YS) and ultimate tensile strength (UTS) values of air-cooled steels that remain within the selected range of FRT (750–850 °C) are lower than those of water-quenched steels. On the other hand, uniform and total elongation (TEL) values of air-cooled steels are higher than those of water-quenched steels. The tensile toughness lies in the range of 60–65 J/cm^3 for air-cooled steels, whereas for water-quenched samples, it lies in the range of 40–52 J/cm^3. It is supportive from Fig. 5 that air-cooled specimens indicate higher area under the stress–strain curve as a measure of tensile toughness as compared to water-quenched steels. It is further noticed that ultimate tensile strength (UTS) increases with the reduction of FRT in case of air-cooled specimens and the

Table 2 Tensile properties of the investigated steels subjected to different FRTs and cooling conditions

FRT (°C)	YS (MPa)	UTS (MPa)	YR = YS/UTS	Uniform elongation (%)	Total elongation (%)	Strain hardening exponent (n)	Tensile toughness (J/cm^3)
850 AC	441	643	0.68	11.41	22.60	0.16	64.95
750 AC	428	683	0.62	11.52	21.14	0.20	60.00
850 WQ	1026	1154	0.88	2.79	10.88	0.09	51.95
750 WQ	931	1057	0.80	2.55	9.25	0.08	39.86

reverse trend is observed for water-quenched specimens. However, the total elongation values increase with the increasing FRT irrespective of cooling rate of all the investigated samples which are in line with the earlier research [15]. The yield ratio values of air-cooled specimens are 0.62–0.68, whereas this is higher (0.80–0.88) for water-quenched specimens. The lower yield ratio and higher uniform elongation of air-cooled specimens indicate higher strain hardening capacity as compared to water-quenched specimens which is consistent with the results of strain hardening exponent (n) in Table 2.

3.3 Hot Ductility Behaviour

Hot ductility curve generated by plotting %RA (reduction of area) against different test temperatures is shown in Fig. 6. It is important to note that ductility is varying significantly with the test temperature. The maximum ductility of 69% is achieved at 1100 °C, whereas lowest hot ductility (14%) is obtained at 850 °C. The high

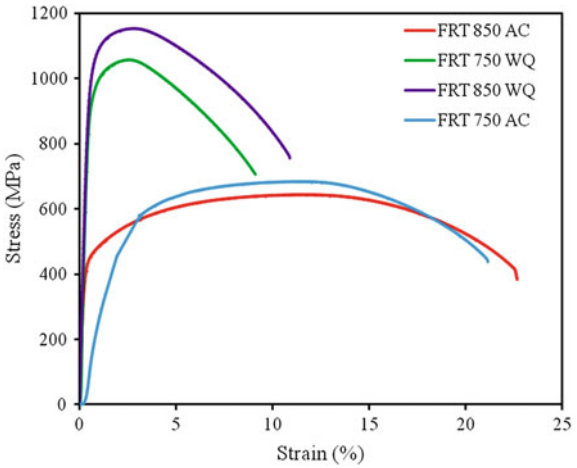

Fig. 5 Tensile stress–strain curves obtained in different processing conditions

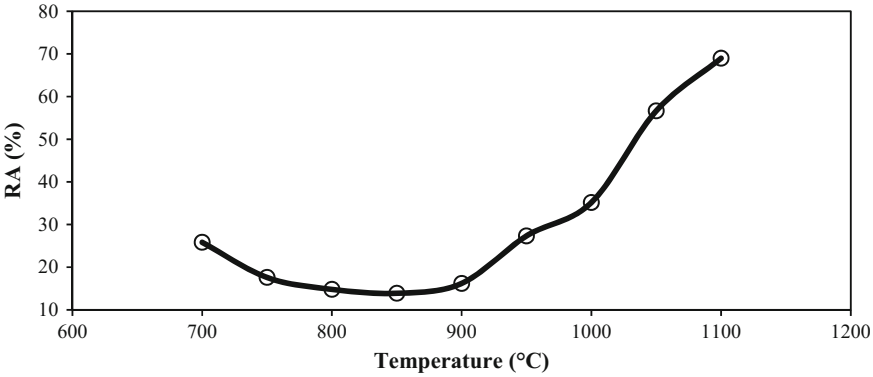

Fig. 6 Hot ductility curve in terms of variation of reduction of area at different temperatures

ductility at the high temperature range is attributed to stabilisation of single phase austenite. On the other hand, lower ductility at the low temperature range of the austenite (900–950 °C) as well as at the two-phase region of austenite-ferrite (800–900 °C) could be related to the formation of the very thin pro-eutectoid ferrite along the austenite grain boundaries.

4 Conclusions

The main conclusions are presented as follows:

1. Finish rolling temperature (FRT) plays an important role in the development of microstructure of the investigated steel. As the FRT decreases to 750 °C, ferrite and pearlite structures are formed in air-cooled steels, whereas water-quenched steels show predominantly martensitic microstructure.
2. Air-cooled sample with 750 °C FRT comprises ferrite matrix with some liner dislocation along with some fine dispersed precipitate particles. The fine complex precipitates of Ti, V, Mo and C (10–20 nm) are significant for precipitation hardening, whereas water quenching from 850 °C FRT, lath martensite with high dislocation density is achieved which contribute high strength to steel.
3. The strength level of 428–441 MPa yield strength and 643–683 MPa ultimate tensile strength along with moderate percentage of elongation has been obtained in air-cooled steel, whereas, higher strength in the range of 931–1026 MPa yield strength, and 1057–1154 MPa ultimate tensile strength along with lower elongation has been obtained on water quenching.
4. It is evident that the maximum amount of achievable hot ductility is 69% at 1100 °C and has low ductility (17%) in the low temperature range of 700–850 °C.

Acknowledgements The authors gratefully acknowledge the financial support provided by TEQIP-II, IIEST, Shibpur, Howrah-711 103, India, in the present investigation.

References

1. URL: http://www.aa.co.nz/cars/licensing-safety-fees/warrant-of-fitness-wof/vehicle-modification-rules-and-regulations/
2. D. Park, M. Huh, J. Shim, J. Suh, K. Lee and W. Jung, Strengthening mechanism of hot rolled Ti and Nb microalloyed HSLA steels containing Mo and W with various coiling temperature, Materials Science and Engineering: A, 560 (2013), 528–534.
3. Y. Funakawa, T. Shiozaki, K. Tomita, T. Yamamoto and E. Maeda, Development of high strength hot-rolled sheet steel consisting of ferrite and nanometer-sized carbides, ISIJ International, 44(11) (2004), 1945–1951
4. T. Gladman, Precipitation hardening in metals, Materials Science and Technology, 15(1) (1999), 30–36
5. S. Mukherjee, I.B. Timokhina, C. Zhu, S.P. Ringer and P.D. Hodgson, Three-dimensional atom probe microscopy study of interphase precipitation and nanoclusters in thermomechanically treated titanium–molybdenum steels, Acta Materialia, 61 (2013), 2521–2530
6. S. Mukherjee, I. Timokhina, C. Zhu, S.P. Ringer and P.D. Hodgson, Clustering and precipitation processes in a ferritic titanium-molybdenum microalloyed steel, Journal of Alloys and Compounds, 690 (2017), 621–632
7. F.J. Humphreys, P.B. Prangnell and R.Priestner, Fine-grained alloys by thermomechanical processing, Current Opinion in Solid State & Materials Science, 5 (2001), 15–21
8. M. Merklein and J. Lechler, Investigation of the thermo-mechanical properties of hot stamping steels, Journal of Materials Processing Technology, 177 (2006), 452–455
9. Z.H. Zhang, Y.N. Liu, X.K. Liang and Y. She, The effect of Nb on recrystallization behavior of a Nb micro-alloyed steel, Materials Science and Engineering: A, 474 (2008), 254–260
10. J. Chen, M. Lv, S. Tang, Z. Liu and G. Wang, Influence of cooling paths on microstructural characteristics and precipitation behaviors in a low carbon V–Ti microalloyed steel, Materials Science and Engineering: A, 594 (2014), 389–393
11. Y.F. Shen, C.M. Wang, X. Sun, A micro-alloyed ferritic steel strengthened by nanoscale precipitates, Materials Science and Engineering: A, 528 (2011), 8150–8156
12. G. Xu, X. Gan, G. Ma, F. Luo and H. Zou, The development of Ti-alloyed high strength microalloy steel, Materials & Design, 31 (2010), 2891–2896
13. T. Wang, F. Kao, S. Wang, J. Yang, C. Huang and H. Chen, Isothermal treatment influence on nanometer-size carbide precipitation of titanium-bearing low carbon steel, Materials Letters, 65 (2011), 396–399
14. H.-l. Yi, L.-x. Du, G.-d. Wang and X.-h. Liu, Strengthening mechanism of a new 700 MPa hot rolled high strength steel, Journal of Iron and Steel Research, International, 15(2) (2008), 76–80
15. P.S. Bandyopadhyay, S.K. Ghosh, S. Kundu and S. Chatterjee, Evolution of microstructure and mechanical properties of thermomechanically processed ultrahigh-strength steel, Metallurgical and Materials Transactions A, 42 (2011), 2742–2752
16. H.-l. Yi, Z.-y. Liu, G.-d. Wang and D. Wu, Development of Ti-microalloyed 600 MPa hot rolled high strength steel, Journal of Iron and Steel Research, International, 17(12) (2010), 54–58

Recrystallization Texture Evolution in HSLA Steel

S. Janakiram and Jai Prakash Gautam

Abstract The role of ferrite and pearlite constituent phases on the recrystallization texture of an HSLA steel is addressed. For the purpose of monitoring the microstructure and texture evolution, two different starting hot bands obtained after hot rolling above and below the Tnr are considered. 80% cold-deformed and subsequently recrystallized samples from each of these hot bands are examined with high-resolution electro-scanning microscopy. Recrystallization kinetics are evaluated with a Vickers microhardness tester. Results support a faster recrystallization kinetics in below Tnr (BT) sample. Preliminary results suggest the reappearance of hot band texture components at the onset of recrystallization.

Keywords HSLA · Ferrite · Pearlite · Deformation · Tnr · EBSD
Recrystallization texture

1 Introduction

High-strength low-alloy steels (HSLA) are low-carbon low-alloy steels consisting of a ferrite matrix containing finely dispersed alloy carbides and ferrite–pearlite aggregates with refined grain size for increased strength. Being manufactured through a thermomechanical-controlled processing route (TMCP) [1], HSLA are among the first type of high-strength steels (HSS) to be widely used for automotive applications in the form of thin gauges [1–3]. The use of HSS along with the later developed advance high-strength steels (AHSS) in the automotive sector has led to a significant reduction in weight while improving materials performance properties, particularly strength and ductility, to comply with current environmental and safety regulations and keep production cost low [2, 3]. In terms of material performance, properties of HSLA steels show a combination of high strength and moderate

S. Janakiram (✉) · J. P. Gautam
School of Engineering Sciences and Technology, University of Hyderabad, Gachibowli, Hyderabad, Telangana 500046, India
e-mail: sabavath.janakiram@gmail.com

T. K. Roy et al. (eds.), *Advanced High Strength Steel*, Lecture Notes in Mechanical Engineering, https://doi.org/10.1007/978-981-10-7892-7_15

formability. The final microstructure (grain size, presence of second phase, etc.) contributes to increase the strength, whereas formability properties are attributed to the crystallographic texture of the final product. Crystallographic texture develops throughout the sequence of events occurring during the thermomechanical processing of the steel. A good level of understanding of recrystallization texture development in single-phase ferritic steels like IF steels has been accumulated through the extensive body of research carried out during the last decades [4]. Hence, a recrystallization texture consisting of a strong γ-fibre (ND//⟨111⟩) with a large amount of grains oriented with {111} planes parallel to the plane of a sheet is well established to be the preferred texture for improved formability in IF steels [4].

With current increasing demand for HSS, it is of both academic and industrial interests to evaluate the effect of hot deformation temperature on the final product texture in HSLA aiming to gain a better understanding of texture development in these materials. In line with this, the primary role of hot band texture on the resulting recrystallization texture over the chemistry and the presence of precipitates for low and extra low-carbon steels has been reported by Ray et al. [4]. However, no significant literature is available, on effect of hot deformation temperature for texture development in high-strength steels.

On the other hand, although the influence of second phase on recrystallization kinetics is being reported in literature [5–7], no data on the effect of second phase like pearlite (5–6% volume fraction) on recrystallization in HSS is reported in literature.

In this paper, effect of hot deformation temperature (Tnr) on the recrystallization texture after cold rolling is of interest. Special attention is paid to the contribution of ferrite and pearlite constituent phases to the final recrystallization texture.

2 Experimental Procedure

HSLA steel with composition 0.06% C, 1.32% Mn, <0.008% Si, 0.0034% Nb, <0.006% Cr (wt%) is presently investigated. Two hot bands are produced by hot deforming material above and below the non-recrystallization temperature (Tnr) as described by Gautam et al. [8]. The starting hot band microstructures consist of a coarse grain ferrite–pearlite matrix in material hot-deformed above the Tnr (hereafter referred to as AT), whereas a banded ferrite–pearlite microstructure is obtained in material hot-deformed below Tnr (hereafter referred to as BT). Bulk texture of the hot-deformed materials is examined by X-ray diffraction in a conventional texture goniometer. The MTM-FHM software [9] is used to calculate the ODF from pole figure data obtained from X-ray texture goniometer. Both hot bands are then cold-rolled to 80% deformation and subsequently annealed at 700 °C for various time length (0–300 s) in a salt bath furnace. Microstructural and textural data of both cold-deformed and recrystallized samples is acquired with an FEI NOVA NANO FESEM 450 coupled with an EDAX-TSL® electron backscatter facility. Samples are mechanically polished and then electro-polished using standard electrolyte.

3 Results

3.1 Hot Rolling Microstructure and Texture

The microstructures of AT and BT materials gathered on the RD-ND section is depicted in Fig. 1. From Fig. 1a, it can be seen that microstructure of AT sample consists of coarse-grained ferrite matrix and a dispersed distribution of pearlite, whereas a fine-grained severely pancaked ferrite matrix with pearlite elongated along prior grain boundary is noticed in the case of BT sample (see Fig. 1b). The total volume fraction of pearlite is 5% in both cases. Hot band textures depicted in Fig. 1c, d, on the other hand, exhibit transformation texture components that can be traced back to the austenite condition during hot rolling as described elsewhere [10]. Therefore, a hot band texture with a maximum of intensity at the rotated cube component $(001)\langle 110\rangle$ in sample AT (Fig. 1c) indicates the previous recrystallization of austenite during hot deformation. On the contrary, a hot band texture shows maximum of intensity around $(112)\langle 110\rangle$ and $(554)\langle 225\rangle$ components correlating with previous deformed austenite in the case of BT sample (Fig. 1d). Intensity of hot band textures is weak in both cases.

3.2 Cold-Rolled Microstructure and Texture

After 80% cold reduction, both materials show a typical deformed microstructure with elongated grains along the rolling direction. The detailed analysis of the deformed microstructures given in Fig. 2, however, shows differences regarding the strain accumulation and fragmentation of both ferrite and pearlite grains based on the starting hot band condition. Therefore, a more pronounced pearlite fragmentation is obtained in the case of BT sample. The evaluation of the cold-deformed textures in Fig. 3b, d reveals the minimization of the textural differences observed in the hot band textures at a large scale. The strengthening of both RD//$\langle 110\rangle$ and ND//$\langle 111\rangle$ fibres is observed in both AT and BT samples.

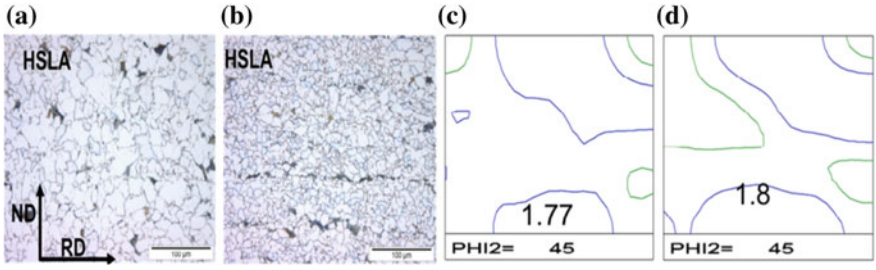

Fig. 1 Microstructure and texture corresponding to **a**, **c** AT and **b**, **d** BT hot bands, respectively

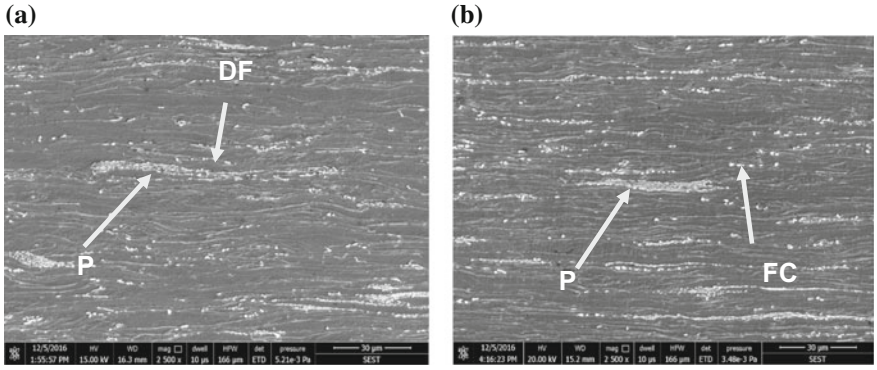

Fig. 2 FESEM micrographs of 80% cold-rolled material **a** AT hot band, **b** BT hot band. Abbreviations: *P* pearlite, *FC* fragmented cementite, and *DF* deformed ferrite

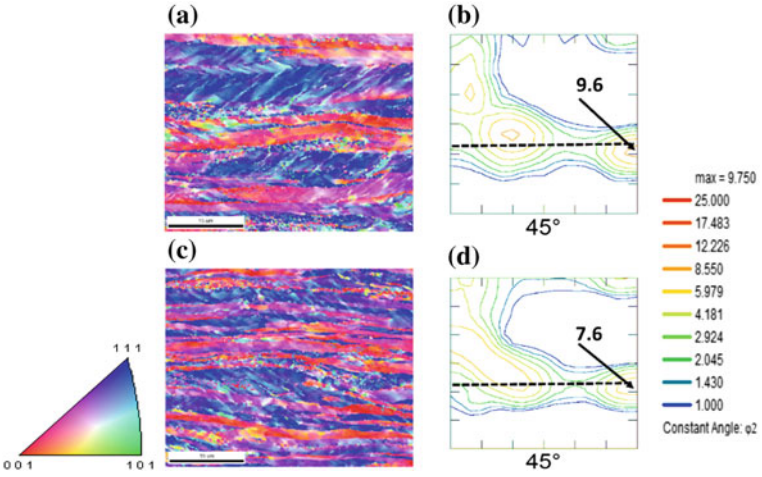

Fig. 3 **a** IPF map and **b** ODF of sample 80% cold-rolled AT hot band, and **c** IPF map and **d** ODF of sample 80% cold-rolled BT hot band

3.3 Recrystallization Kinetics

Recrystallization kinetics are followed through Vickers microhardness measurement of cold-rolled material annealed at 700 °C for different annealing times (HV 500 g load). Figure 4 displays the hardness values for both materials, AT and BT. The latter trend is characterized by an initial slow kinetics region, which could be attributed to the initial recovery (up to 30 s in the case of BT and up to 60 s in the case of AT), followed by a faster kinetics region indicating for the occurrence of recrystallization. It is worth highlighting here the difference in the recrystallization kinetics of both materials, being significantly faster in the case of BT sample.

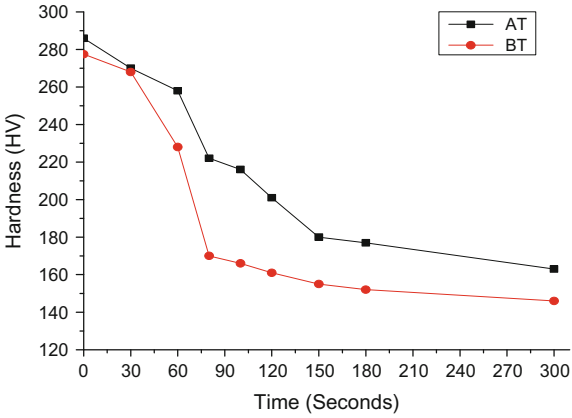

Fig. 4 Vickers hardness at 700 °C annealing temperature and different soaking times

3.4 Recrystallization Texture

With the purpose of monitoring the evolution of texture during recrystallization, an interrupted annealing test is presently conducted at 700 °C and soaking times varying from 0 to 300 s. Recrystallization is found to occur primarily within ferrite grains, whereas a change of morphology within the pearlite (namely the spheroidization of cementite) is observed as illustrated in Fig. 5. In this study, recrystallized grains are identified from the inverse pole figure maps (IPF) applying a fifth nearest-neighbour kernel average misorientation (KAM) method together with a 10-degree misorientation criteria. The ODFs of cold-deformed and partially recrystallized samples for both AT and BT materials are given in Fig. 6.

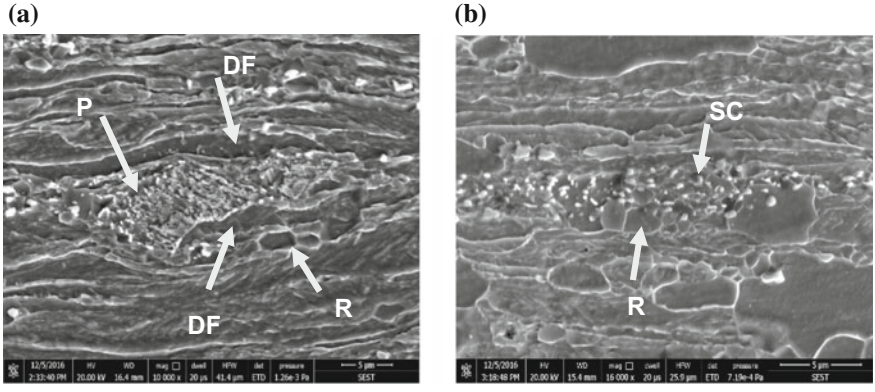

Fig. 5 FESEM micrographs of **a** AT annealed for 100 s and **b** BT annealed for 80 s. Abbreviations: *P* pearlite, *SC* spheroidized cementite, and *R* recrystallized

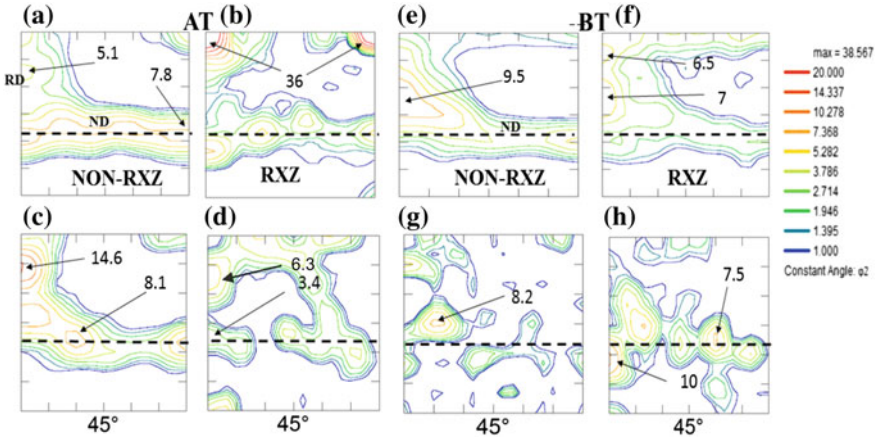

Fig. 6 ODF of **a**, **c** deformed and **b**, **d** recrystallized ferrite for AT, **e**, **g** deformed, and **f**, **h** recrystallized ferrite of BT after annealing at 30 and 150 s

3.5 AT Sample

Earlier, ferrite recrystallized grains appear after 30 s in the case of AT sample, the area fraction being 9%. The texture of these grains is composed of a dominant rotated cube component and a weak ND//⟨111⟩ fibre (Fig. 6b). After an annealing time of 150 s, the recrystallized area fraction increases to 14%. An overall weakening of the texture carried by the recrystallized ferrite grains is observed with a maximum of intensity shifting towards (112)⟨110⟩ component (Fig. 6d).

3.6 BT Sample

The area fraction of recrystallized grains in BT sample after 30 s is 38%. The texture carried by these recrystallized grains is composed of a well-defined RD//⟨110⟩ fibre with maximum of intensity around (112)⟨110⟩ and (113)⟨110⟩ components (Fig. 6f). After 150 s of annealing time and with an area fraction of 96% recrystallized ferrite grains, the strengthening of ND//⟨111⟩ fibre is noticed with a maximum of intensity around the (111) [0–11] component (Fig. 6h).

3.7 Discussion

The effect of deformation temperature on the texture of the two starting hot band samples, AT and BT, is in agreement with that reported in Reference Ray et al. [10].

The resulted textures show typical transformation texture components that can be traced back to the condition of the austenite during hot deformation, namely recrystallized austenite in the case of AT sample and deformed austenite in the case of BT one. The austenite condition reflects in the hot band microstructure both in terms of the ferrite grains size and in terms of the pearlite second phase distribution. A dispersed distribution of pearlite is found in the case of AT materials, whereas a pearlite banding is characteristic of the microstructure in the BT material.

Regarding cold deformation texture, the strengthening of RD//⟨110⟩ and ND//⟨111⟩ fibres with cold rolling of ferritic steels has been reported by [4]. The same trend is observed in the present case for an HSLA with 5% volume fraction of pearlite. Moreover, the detailed evaluation of the cold-rolled microstructures revealed the strain accumulation within ferrite as well as a fragmentation of pearlite, with the fragmentation of pearlite being more pronounced in the case of BT material. The relevance of the amount of deformation to the recrystallization process has been extensively addressed in literature [4, 11, 12]. According to that, highly strained regions are proned for faster recrystallization on the basis of faster driving force and therefore, faster kinetics. Present results showing faster recrystallization kinetics in BT sample, with increased strain as compared to AT one, confirm that reported in literature.

Preliminary results of the recrystallization texture after interrupted annealing test indicate that early nuclei form in highly deformed microstructural features such as ferrite grain boundaries, shear bands within deformed grains, ferrite/pearlite interphase, etc. On the other hand, initial results indicate that recrystallization texture of early nucleated grains is influenced by the initial texture in the hot band, having said that further investigation of the recrystallization is required to statistically confirm these findings.

3.8 Summary

In this study, the effect of deformation temperature on the recrystallization texture of an HSLA with a 5% volume fraction of pearlite is investigated through the monitoring of the microstructure and texture evolution during cold deformation and subsequent interrupted annealing.

After cold rolling, the strain accumulation in the ferrite grains along with the fragmentation of pearlite is observed. The degree of pearlite fragmentation is found to be dependent on the initial hot band condition being more pronounced in the case of BT sample. The resulting cold-deformed textures displaying the strengthening of the RD//⟨110⟩ and ND//⟨111⟩ fibres are in agreement with that reported for ferritic steels. Preliminary results on the recrystallization texture during interrupted annealing test indicate that the texture components of the initial hot bands prevail at the onset of recrystallization.

References

1. J. Patel, C. Klinkenberg and K. Hulka, Hot rolled hsla strip steels for automotive and construction applications, niobium Products Company GmbH SteinStr. 28 Dusseldorf 40210 Germany.
2. Advanced High-Strength Steels Application Guidelines Version 5.0, May (2014), 1–16.
3. A. Ilic, L. Ivanovic, D. Josifovic and V. Lazic, Application of high-strength steels in vehicle design Innovative Automotive Technology—IAT 2012, Novo mesto/Dolenjske Toplice 12th–13th April (2012)
4. R.K. Ray, J.J. Jonas and R.E. Hook, Cold Rolling and Annealing Texture in Low Carbon Extra Low Carbon Steels, International Materials Reviews, 39(4) (1994), 129–172.
5. M. Blicharski and S. Gorczyca, Recrystallization with the second phase. Wyd. Slask, Katowice, (1980)
6. F.J. Humphreys and M. Hatherly, Recrystallization and related annealing phenomena. Elsevier Ltd., Oxford, U.K., 1st Edition, (1995)
7. P. Matusiewicz, W. Ratuszek and A. Zielinska-Lipiec, Recrystallization of Ferrite in Spheroidite of Fe-0.67%C Steel, Archives of Metallurgy and Materials, 10172-011-0007, 56 (2011)
8. J. Gautam, A. Miroix, J. Moerman, C. Barbatti, P. Van Liempt and L.A.I. Kestens, Determination of non-recrystallization temperature (Tnr) of austenite in HSS C-Mn steels materials science forum. Vol. 706–709 (2012), 2722–2727.
9. P. van Houtte, The MTM-FHM Software System Version 2, User's Manual, (1995)
10. R.K. Ray, J.J. Jonas, M.P. Butron-Guillen and J. Savoie, Transformation Textures in Steels ISIJ International, 34(12) (1994), 927
11. R. Saha and R.K Ray, Effect of Severe Cold Rolling and Annealing on the Development of Texture, Microstructure and Grain Boundary Character Distribution in an Interstitial Free (IF), Transformation Textures in Steels, ISIJ International, 48 (2008), 973
12. R. Saha and R.K. Ray, Texture and grain growth characteristics in a boron added interstitial free steel after severe cold rolling and annealing, Materials Science and Engineering: A, 527 (2010), 1882–1890

Technological Challenges and Solutions for the Production of State-of-the-Art Second- and Third-Generation AHSS Grades

Jens Kempken

Abstract The challenge to develop new steel grades with superior mechanical properties in terms of yield strength and deformation behavior has to take into consideration technical, processing, marketing, and economic aspects. The environmental impact in regard to a life cycle assessment is already for AHSS grades very favorable as less material has to be produced and processed on one hand coupled with substantial lower weight to logistically be handled. The technical challenges during production and processing cover the complete process chain from steelmaking, casting, rolling, coating, and annealing.

AHSS steel grades are characterized by complex alloying concepts with increased Al and Mn contents; the grades show the tendency for crack formation during solidification. High-strength and strong deformation force leads to high loads and torques in the rolling mills. The superior mechanical properties in regard to elongation and yield strength are derived by complex microstructure engineering with dedicated or accelerated cooling patterns. Therefore, a comprehensive review of the complete process chain is required to identify obstacles and bottlenecks.

The paper gives insights how to overcome the challenges and shortcomings during the production and processing of these grades. The already developed solutions as

- adopted caster design and adjusted cooling,
- belt casting technology for the production of HSD-TWIP grades,
- accelerated cooling technologies in hot rolling, and
- I-Furnace solution for Q + P grades

are described in this paper.

Finally, an indispensable prerequisite for production of AHSS grades is strict conformance to process and quality management through the entire process chain, which demands a powerful tool to monitor, document, analyze, and secure the operation. A PQA quality management solution including an expert-based

J. Kempken (✉)
SMS Group AG—MET/Con GmbH, EVP Project Development,
Düsseldorf, Germany
e-mail: jens.kempken@sms-group.com; jens.kempken@metcon-gmbh.de

T. K. Roy et al. (eds.), *Advanced High Strength Steel*, Lecture Notes
in Mechanical Engineering, https://doi.org/10.1007/978-981-10-7892-7_16

know-how software kernel can respond in time to ensure highest yield at optimum quality for utmost customer satisfaction.

Keaywords AHSS grades · Belt casting technology · Slab caster design Quality management

1 Market Drivers and Solutions

To ensure long-term success of demanding steel processors and consumers like automakers, tube and pipe manufacturers, shipbuilders, etc., business strategies and operational models have always been based on three major drivers [1]:

- Consumer demands for optimized TCO (total cost of ownership): optimized purchasing, high quality, better performance, good reliability, higher safety, advanced features, and lightweight engineering linked with improved fuel and resource economy;
- Environmental government regulations on fuel consumption, crash safety, and gas emissions; and
- Competitive market pressures on cost, quality, performance, and manufacturability.

Four basic solutions are taken into consideration to serve customers and to meet their business goals:

- Optimized product design,
- Reduced product (vehicle) weight,
- Utilization of low-cost materials, and
- Adaptation of innovative manufacturing processes.

All four levers will lead to the selection of lightweight materials that meet performance and cost requirements. In this regard, the competition toward alternative materials (aluminum and its alloys, magnesium, and carbon-reinforced composites) is open. Many studies have demonstrated the cost advantage of steel over aluminum alloys.

2 Process Challenges and Solutions

Next to superior mechanical properties and additional benefits, the market demand for AHSS grades is growing into double-digit. Nevertheless, technical challenges cover the complete process chain from steelmaking, casting, rolling, coating, and processing.

AHSS steel grades are characterized by complex alloying concepts with increased Al and Mn contents. These grades show the tendency for crack formation during solidification.

High-strength and deformation forces during rolling lead to high loads and torques and influences geometry and flatness.

Superior mechanical properties in regard to elongation and yield strength are derived by complex microstructure engineering with dedicated annealing or accelerated cooling patterns during galvanizing and annealing.

Therefore, a comprehensive review of the complete process chain is required to identify obstacles and bottlenecks during production.

This paper describes specific solutions to deal with the challenges and the shortcomings during production and processing of advanced state-of-the-art AHSS grades.

3 Slab Caster Design and Adjusted Cooling

AHSS grades show the tendency toward crack formation during solidification in the mold and the first segments of the strand.

Next to the metallurgical issues of the utilization of the right mold powder, high Al and Si contents in the melt will lead to a chemical REDOX reaction with the mold powder. Stress formation within the shell can become critical. Deformation of the strand shell and the slab during bending and unbending takes place in critical temperature regions.

The bow-type caster design (elimination of the bending in segment no. 1) is back to the picture, as the trend over the two last decades had been the integration of a vertical mold and segment 0. A recent revamp of a caster dedicated to the production of state-of-the-art AHSS grades is following this principle of stress minimization in the strand.

It should be mentioned that IF-ULC Ti–Nb alloyed grades show a complete different behavior during production; in this case, the vertical mold designed caster shows advantages due to higher casting speeds and better cleanliness with the capability for absorption by floatation of nonmetallic inclusions and argon bubbles. Another prerequisite in caster design is a state-of-the-art secondary cooling technology in air mist design and dry casting (no water) in the runout area. These solutions guarantee a controlled temperature evolution and maximum temperature in the unbending section with the result of a crack-free surface.

4 Belt Casting Technology (BCT) for Advanced HSD-TWIP Grades

High strength ductility steel grades (HSD) utilize the twinning introduced plasticity effect to gain superior mechanical properties of a new class of AHSS grades (1000 MPa with 35% elongation). A lot of interesting applications can be foreseen

in automotive, construction, and oil and gas sector. HSD steel grades have a unique alloying concept, 15–20% manganese and 1–3% aluminum and silicon. The conventional casting technique cannot be applied in an economic way, and special mold powder has to be developed; HSD grades are highly crack sensitive.

A newly developed solution is the horizontal, tension-free casting on a rotating belt in an inert atmosphere without any mold powder. The isokinetic feeding device of the melt from the tundish on the moving strip including the electromagnetic width distributor is the key principle and key element. The strip thickness as cast lies in the range of 8–20 mm, with a casting speed of 15–30 m/min [2].

A pilot plant on industrial scale size is now in operation at Salzgitter/Germany for 3 years. In this case, for further processing, the strip is rolled in a Steckel mill.

5 Accelerated Cooling Technologies in Hot Rolling

High-strength, low-alloy steel grades are often produced by means of thermomechanical rolling (TM rolling) and accelerated and adjusted cooling. Combined with micro-alloying elements such as Nb, V, or Ti, the grain size is reduced by means of targeted carbon nitride segregations, which leads to an improvement of the mechanical properties. The addition of alloying elements has a positive effect on the mechanical properties, but is often expensive. The average surcharge for a strength increase of 100 MPa is around 30 USD/t [3].

By means of intensified cooling, the mechanical properties can be modified significantly. In this way, it is possible to save alloying elements, which leads to a more cost-efficient production of high-strength steel grades. The modification of a cooling section with the goal of obtaining significantly higher cooling rates is beneficial. The higher cooling rates have an effect on the microstructure, reduced grain size, and therefore on the mechanical properties.

Experiments have confirmed this; in trials on HSLA grades, the yield strength was increased by 20 MPa and the tensile strength by 15 MPa. The gained increase in strength provides the possibility of implementing a simpler chemical composition, which leads to partial savings in regard to alloying elements and alloying costs.

6 I-Furnace Technology for Quench and Partitioning Grades

Crucial for the production of second- and third-generation automotive grades in galvanizing and annealing is an appropriate furnace technology. Several developments, as a reaction to the new requirements, had been developed and introduced to the market [4].

The modern and highly efficient radiant tube furnaces are equipped with pre-oxidation chambers. The introduction of a pre-oxidation chamber allows the processing of high silicon/manganese steels. With a controlled infusion of humid air into the chamber, the dew point increases resulting in a closed iron oxide layer on the surface due to the suppression of migration of silicon and manganese to the surface. At the end of the furnace, a reduction of the iron oxide layer takes place and the resulting surface has the required wettability. Various cooling options (gas or water) or facilities for quench and tempering are implemented. With ultra-fast cooling solutions, cooling rates of up to 150 K per second per millimeter can be achieved due to the injection of pure hydrogen into the cooling chamber (up to 50% hydrogen content). The diffusion of hydrogen into the adjacent chambers is limited by a patented line design.

The newly developed I-Furnace optimizes the heat treatment and production process. It smartly combines a mathematical and physical model to control the furnace and to optimize production with an online strength measurement system and a newly developed annealing microstructure model to predict material properties after the heat treatment. The I-Furnace allows closer process limits and a stronger consideration of the upstream processes. Special sophisticated grades can be produced more easily and homogeneous material characteristics can be achieved. A capacity increase up to 15% is possible due to a better utilization of the furnace.

7 Quality Management by PQA Software Solution

The process and quality management of the entire process chain for state-of-the-art advanced AHSS grades require a powerful tool to monitor, document, analyze, and secure the operation of the complete process chain. The PQA, a product quality analyzer and assurances system, has been developed and is implemented in different plants as a quality decision support solution next to existing level 2 and level 3 systems [5, 6, 7].

Based on online process event assessment, taking an expert know-how rule-based software suite into consideration, an early identification of “unsuitable” material can be achieved.

The software package provides a real-time comprehensive product preview. The system tracks the material over the complete process chain and provides all sensitive coil data at a glance.

PQA will be utilized for statistical process and quality evaluations and provides a long-term data storage. User benefits are reliable quality, yield increase, cost reduction, and satisfied customers. The integration of continuous improvement by flexible rule adaption and self-learning options will accompany steel producers to the next performance level.

8 Conclusion

The development and the introduction of advanced AHSS steel grades had been driven by market requirements and customer demands.

With complex alloying concepts to engineer-specific microstructures in the steel in accordance with defined quality-specific process windows, superior mechanical properties can be achieved.

Experience and know-how had been the drivers for new technical solutions along the complete process chain via steelmaking, casting, rolling, and processing in regard of the capability to produce AHSS grades.

Specific technical solution along the production and process chain had been customized for each application.

References

1. M.Y. Demiri, Advanced High-Strength Steels—Science, Technology, and Applications, ASM International, (2013)
2. SMS—Group corporate information: www.sms-group.com/plants/all-plants/belt-casting-technology/concepts/
3. Ch. Hassel, A. Sprock and S. Krämer, The influence of an enhanced runout table cooling on the microstructure, mechanical properties andalloy savings: AISTech 2016, Pittsburgh, PA, USA.
4. H. Behrens, F. Brühl, L. Kümmel, C. Sasse and J.P. Crutzen, Conditions for galvanizing modern automotive steel grades, 108th Galvanizers Association Conference, Farmington PA, USA, (2016)
5. J. Kempken, M. Reifferscheid, et al., Integrated Product Improvement by Quality Analysis and Modeling, European Continuous Casting Conference – ECCC, Nizza 2005.
6. J. Kempken and T. Hüper, State of the Art Product Quality Management—Operational Success with State of the Art Product Quality Analysis (PQA) Solutions, ABM Conference Proceedings, Rio de Janeiro, (2016)
7. J. Kempken and T. Hüper, PQA—The Success Factor to reach next Performance Level in Hot and Cold Rolling, AISTec Conf., Nashville, (2017)

Gas–Liquid Flows in Ladle Shroud and Their Impact on Tundish Process Performance and Steel Quality

Prince K. Singh, Subham Ranjan and Dipak Mazumdar

Abstract A physical and mathematical modelling investigation has been carried out to study gas–liquid, two-phase, flow phenomena in a ladle shroud and underscore their associated impact on tundish process performance. To this end, Perspex™ model of a full-scale ladle shroud, operating with a bloom caster, has been fabricated and flow dynamics was studied as a function of argon injection rate, throughput and discharge environment (i.e. open vs. submerged). It is observed that liquid flow regimes in a shroud are critical to the choice of argon injection rate and this has significant bearing on the extent of slag–metal–air (ambient) mixing in tundish. In such context, the role of a tundish physical cover and continuous argon flushing of tundish has also been investigated computationally. Based on this, a novel design is proposed so that both air ingression and slag–metal interactions in tundish can be contained helping produce clean steel.

Keywords Physical and mathematical modelling · Ladle shroud
Reoxidation · Tundish flushing · Continuous casting

1 Introduction

In early 70s, open-air casting was common. However, with more and more stringent requirement on final steel quality, open-air teeming has been discontinued. Instead, ladle shroud employed and this prevents any unwarranted chemical reaction between molten steel and ambient minimising possible contamination of steel. In continuous casting, a ladle shroud is typically mounted on the collector plate nozzle and during casting, every effort is made to ensure near perfect sealing at collector nozzle and ladle shroud joint. However, perfect sealing is rarely accomplished at high operating temperature and this often leads to ingression of air from the surrounding into shroud

P. K. Singh · S. Ranjan · D. Mazumdar (✉)
Department of Materials Science and Engineering, Indian Institute of Technology, Kanpur, India
e-mail: dipak@iitk.ac.in

T. K. Roy et al. (eds.), *Advanced High Strength Steel*, Lecture Notes in Mechanical Engineering, https://doi.org/10.1007/978-981-10-7892-7_17

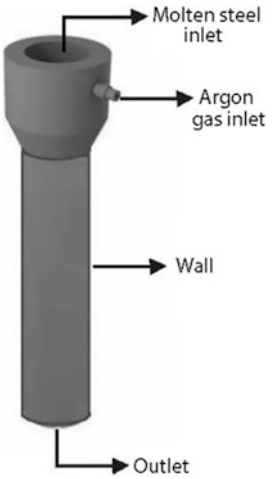

Fig. 1 Photograph of a ladle shroud

impairing steel cleanliness and castability. To control air ingression, argon is therefore injected through the upper part of the shroud as shown in Fig. 1. Some steel plants operate ladle shroud without argon injection as well.

Gases (typically argon and/or air), present in a shroud, are advected downward by the flowing molten metal stream to be ultimately released in the tundish, wherein extensive gas–liquid mixing can occur. Furthermore, at significantly high volume of gas, severe gas–liquid mixing in the tundish is expected disturbing the protective slag cover present in the vicinity of the shroud. This, particularly in the absence of a physical cover as well as a protective tundish atmosphere, can initiate many unwarranted chemical reactions destroying steel quality completely. Given such interplay of gas–liquid, both in a shroud and tundish must be looked carefully and controlled effectively, if highest metallurgical performance of steelmaking tundish system is to be ensured. Despite many studies on ladle shroud [1–8], practically very little or no information is available on the characteristics of two-phase flows in shrouds and their possible impact on tundish process performance.

Consequently, the purpose of the present study has been to investigate in-depth, simultaneous, two-phase flows of gas and liquid in a ladle shroud and to make an assessment of the associated impact on tundish process performance, particularly with reference to reoxidation and steel cleanliness. To this end, results of a physical and mathematical model investigation are presented in the following.

2 Present Work

2.1 Physical Modelling

A full-scale, Perspex™ model of a bloom casting shroud has been fabricated to underscore fluid flow phenomena within a ladle shroud. Corresponding full-scale tundish was not fabricated and instead, a sufficiently big reservoir was considered

to mimic the tundish wherein, only dimensions along the vertical direction (viz. depth of shroud submergence, distance of shroud tip from the base of tundish, etc.) were adequate considerations. A photograph of the experimental setup is shown in Fig. 2. Physical dimensions and operating parameters in the model *vis a vis* those in the prototype are summarised in Table 1.

Fig. 2 Water model setup of a ladle shroud

Table 1 Operating parameters and physical dimensions of a ladle shroud employed in continuous casting of steel blooms

Parameters	Industrial ladle shroud	Full-scale model shroud
Length (mm)	1215	1215
Inside diameter at throat (mm)	65	63
Inside diameter at tip (mm)	60	63
Outer diameter (mm)	98	74
Collector nozzle diameter (mm)	45	45
Argon injector diameter (mm)	6.35	6.35
Liquid	Steel	Water
Mass flow rate (kg/s)[a]	12.5–17.0	1.74–2.36
Volumetric flow rate (m^3/s)	17.36×10^{-4}–23.61×10^{-4}	17.36×10^{-4}–23.61×10^{-4}
Separation distance from tundish base (mm)	460–500	480

[a]Based on density of liquid steel = 7200 kg/m^3

2.2 Mathematical Modelling

A multiphase, turbulent flow calculation procedure, based on the concept of volume of fluid (VOF) [9], has been applied to predict fluid flow phenomena inside the model ladle shroud. The VOF approach relies on the concept of a mixture velocity and therefore, as one might anticipate, solves only one set of continuity and momentum equations. For two-phase, gas + liquid flow system, such as the present one, in addition to the mixture continuity and momentum conservation equations, an additional volume advection equation was solved to compute simultaneously phase volume fractions. In addition to the governing PDEs, VOF procedure employs suitable, grid-based, geometrical schemes for maintaining sharp interfaces between mutually interacting phases. Numerical calculations were carried out for both isolated (shroud only) and integrated (shroud + tundish) flow domains. In the present study, an unsteady-state, 3-D, VOF formulation has been applied. Thus, even when the steady-state behaviour is of interest, VOF method was made to approach the final steady state through a series of transient or unsteady-state solutions. To solve the governing flow and turbulence model equations, appropriate initial and boundary conditions on pressure, velocity, volume fractional and turbulence parameters were applied. Relevant details on the VOF calculation procedure, governing equations, etc. are found elsewhere [9] and consequently, not reproduced here. All simulations reported in the study were carried out under isothermal conditions via the ANSYS Fluent 14.5™.

2.3 Results and Discussion

To investigate all possible conditions under which molten steel is generally teemed via a shroud into a tundish, two-phase, gas–liquid flow inside the model shroud was studied under different operating conditions. These, for example, included

(i) Teeming into an empty tundish in the absence of any gas injection in the shroud,
(ii) Teeming through a shroud submerged in a tundish in presence of argon injection and
(iii) Teeming through a submerged shroud in a filled tundish without any argon injection.

Case (i), as one would note here, corresponds to the initial stage of tundish filling wherein typically, a shroud delivers molten steel under normal atmospheric condition. This leads to large-scale melt–ambient mixing inside a tundish. The latter two cases (ii) and (iii), on the other hand, correspond to the situation when tundish is operated under near steady-state condition and shroud remains partly submerged in steel melt inside tundish. Visual observation of flows inside the model shroud suggests that the characteristics of the two-phase flow phenomena, under the three

above-mentioned operating conditions, are substantially different. It is also observed that flow conditions prevalent inside a shroud influence tundish hydrodynamics and the associated process performance significantly. For example, while gas–liquid mixing in tundish for condition (iii) is minimal, severe gas–liquid interaction was found to occur for condition (i). Physically observed gas–liquid flows as well as corresponding idealised schematics for the three above conditions are shown in Fig. 3a–c.

These figures suggest that during the initial period of tundish filling, as the shroud is exposed to the atmosphere, molten steel, without much interaction with the surrounding, flows practically smoothly, vertically downward to enter an empty tundish where extensive gas–liquid mixing results. In contrast, when the shroud is partly submerged (Fig. 3b) in a partly/completely filled tundish and argon gas is injected in the shroud, some gas–liquid mixing can occur inside the shroud establishing a bubbly, two-phase flow regime. This implies that should there be any leakage at the shroud–collector plate joint, considerable air ingression and large-scale reoxidation of steel inside the shroud can result. Furthermore, while at small argon flow rate, gas and liquid phases tend to remain in an intricately mixed state, at relatively higher flow rate; however, intensity of two-phase mixing is reduced and simultaneous downward flows of air (along periphery) and water (in the core) are observed. Interestingly, as shown in Fig. 3c, when the shroud is

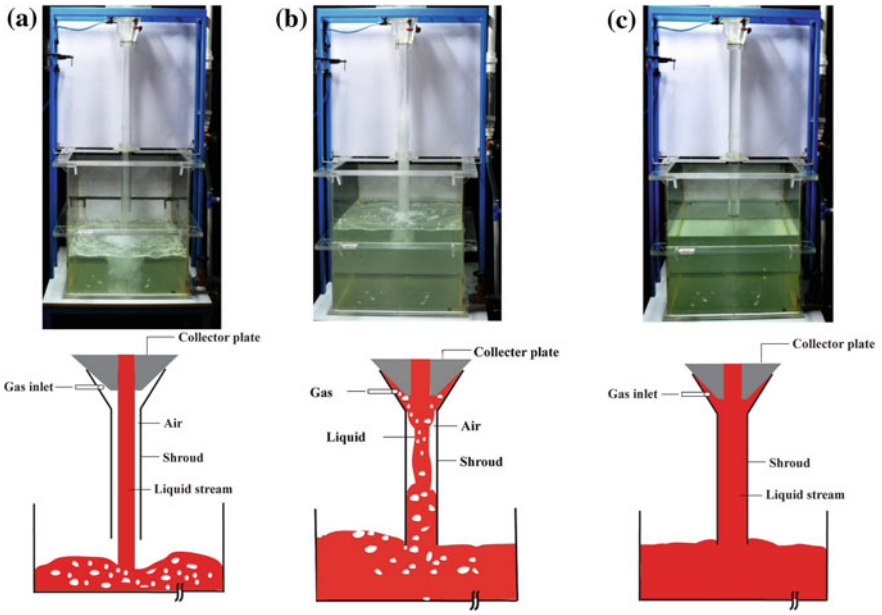

Fig. 3 Physical model photographs and corresponding schematics of different operating conditions of a shroud. **a** shroud open to atmosphere, **b** submerged shroud with gas injection, **c** submerged shroud with no gas injection

submerged and no gas is injected in the shroud, the shroud becomes completely filled with liquid and operates in a manner analogous to a submerged entry nozzle (SEN) used in feeding of liquid steel into continuous casting mould. These results evidently indicate that service life of a shroud, extent of heat loss or temperature drop across shroud's vertical length as well as cleanliness of steel is expected to be dependant on the mode of liquid steel–argon flow inside a ladle shroud.

Molten metal, discharged into tundish with high downward velocity (typically 1–3 m/s), generates intense stirring conditions particularly in the vicinity of the shroud. This, as one might anticipate, can significantly change depending on the mode a shroud is operated and could in practice promote extensive argon–steel (and also slag/air, when present) mixing inside the tundish. Thus, during transfer of molten steel and its subsequent discharge from a shroud into an empty tundish (viz., Fig. 3a), considerable entrainment of the tundish atmosphere is likely to occur leading to vigorous gas–liquid–slag mixing in tundish. On the other hand, corresponding to Fig. 3c, with no gases present within the shroud, practically little or no gas–liquid–slag mixing in tundish is expected. The corresponding situation, for the configuration shown in Fig. 3b, is likely to be intermediate and lead to only moderate gas–liquid–slag mixing in the tundish, provided gas injection rate is not appreciable. Given such, overwhelming impact of how a shroud is operated in practice on steel quality can be readily anticipated.

VOF-based predictions on phase volume distributions under the three above-mentioned operating regimes are shown, respectively, in Fig. 4a–c. There, it is readily apparent that physically observed flow patterns illustrated in Fig. 3 have been captured reasonably realistically by the numerical model developed in this work.

To demonstrate the predictive capabilities of the present model, progressive establishment of a two-phase flow regime in a shroud, initially completely filled with liquid, is illustrated in Fig. 5 for different instants of time at an argon injection rate of 10 lit/min. Although elaborate comparisons are yet to be made, such predictions, as one would note here, are qualitatively very similar to those observed in the physical model. These computational results supported by physical model

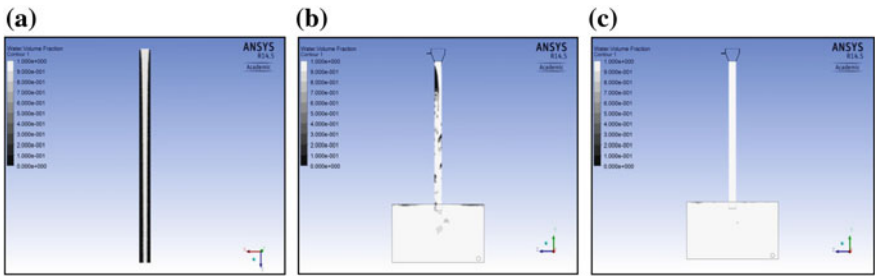

Fig. 4 Contours of volume fraction distribution (white: liquid and black: gas) for different operating conditions of a shroud. **a** open to atmosphere, **b** submerged with gas injection, **c** submerged without gas injection

observations indicate that escape of shrouding (as well as entrained) gases from the tundish into the ambient is likely to create a slag eye in an actual steelmaking tundish system making avenues for unwarranted chemical and thermal interactions between liquid metal and the tundish ambient. It is therefore important to contain slag eye, by engineering shroud operating regimes such that interaction between steel and ambient (i.e. the tundish atmosphere) as well as intermixing between slag and metal could be largely avoided.

The preceding discussion suggests that during transfer of molten steel from ladle to tundish via a shroud, the environment present in the tundish is likely to be an issue of concern. In case of high-argon injection rate into a shroud leading to the formation of a large slag eye in tundish, reoxidation, nitrogen pickup, aluminium fading, etc. can occur particularly if the tundish is not physically covered and continuous argon flushing, from before the starting of teeming, not practised. To investigate this further, the effect of flushing of an empty, physically covered tundish by argon (viz. to essentially drive out the initially present air) was numerically modelled via a homogeneous turbulent, mixing flow model embodied in ANSYS Fluent. The effect of argon flushing was investigated as a function of argon inlet numbers, argon flow rate and injector design. While progressive removal of air from an empty, initially air filled tundish is readily apparent from Fig. 6, it is evident from Fig. 7 that even after 7 min of argon injection, as much as 30% of the initial air could be present inside the covered tundish. This can pose a serious, albeit somewhat reduced, threat to atmospheric reoxidation of steel as the latter starts filling the tundish. The present study has indicated that for the same net effective volume flow, the number of injectors is not important. In contrast, the total volume of argon injected and nozzle design/orientation are decisive variables and determine the efficiency of argon flushing to a large extent.

Slag–metal mixing and the associate interphase chemical reactions such as $[Al] + (SiO_2) = [Si] + (Al_2O_3)$ are common in tundish, particularly when rice husk or other silica-based top covering compounds are employed as tundish slag. It is also well known that slag–metal reactions in tundish systems are more rampant in the shroud inlet region due to intense stirring conditions prevalent locally. The present study has appeared to indicate that the veracity of slag–metal reactions in

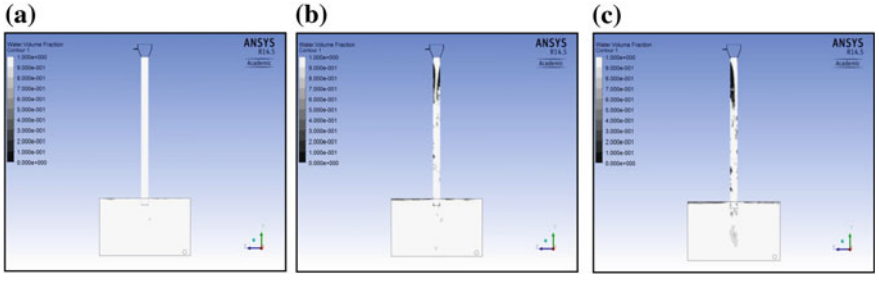

Fig. 5 Contours of volume fraction distribution in shroud and reservoir at different instants of time **a** $t = 0$ (no gas injection), **b** $t = 5$ s and **c** $t = 30$ s (with gas injection at 10 lpm)

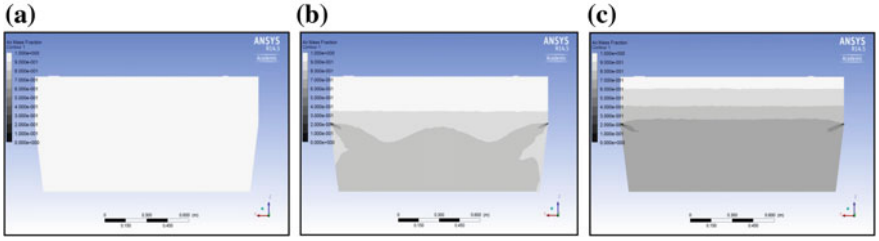

Fig. 6 Contours of residual air volume fraction (white: air and black = argon) in tundish at **a** t = 0, **b** t = 5 min, **c** t = 10 min

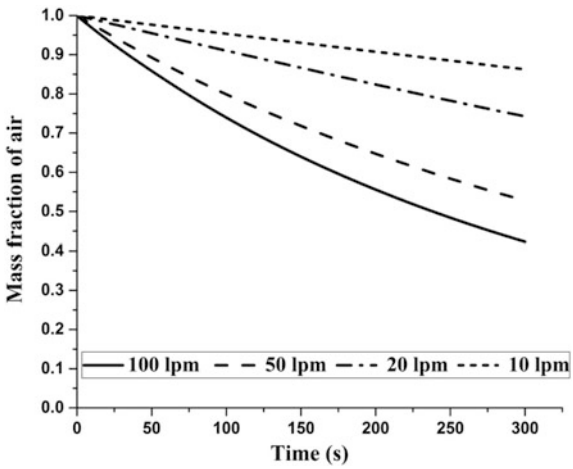

Fig. 7 Residual air mass fraction in tundish at different argon flushing rates

the vicinity of the shroud can be further aggravated depending on the way a ladle shroud is operated (small vs. large argon injection, large-scale leakage, etc.). Such unwarranted interactions can be prevented, to a large extent, if a central slag-free region is created using a snorkel around the shroud, similar to the one employed in the CAS alloy addition procedure [10]. A proposition of the same, aimed to produce steel of adequate cleanliness, is shown schematically in Fig. 8. There, it is readily apparent that air–melt as well as slag–metal contacts can both be simultaneously contained by (i) injecting argon inside shroud at relatively high pressure (to minimise air ingression), (ii) deploying a snorkel around the submerged shroud and (iii) adopting continuous argon flushing of an otherwise physically covered tundish system. This approach to completely eliminate reoxidation of steel during the final stages of continuous casting, to produce steel of high cleanliness, is being evaluated rigorously through extensive physical and mathematical modelling as well as plant-scale trials.

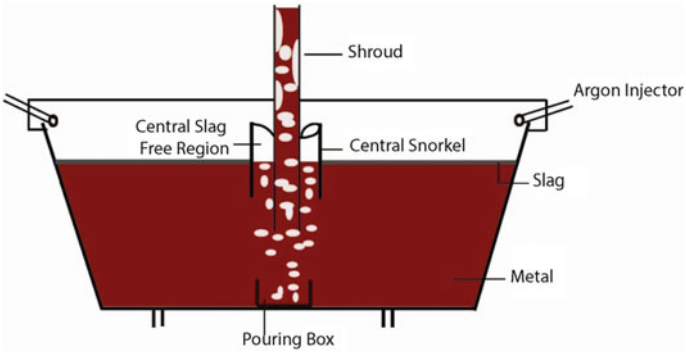

Fig. 8 Tundish practice for eliminating reoxidation during final stages of continuous casting

3 Conclusions

Gas–liquid flows inside a vertical shroud have been investigated through physical and mathematical modelling. To this end, while a Perspex model of as full-scale, bloom casting shroud was fabricated for physical observation, a two-phase, turbulent flow model was developed via ANSYS Fluent. It is shown that argon flow rate, extent of external leakage as well as submergence of shroud are important process variables that dictate the characteristics of gas–liquid flow within a ladle shroud and in turn tend to exert considerable influence on the resultant induced flow in tundish. Teeming practice (via shroud) can therefore influence the metallurgical performance of steelmaking tundish system as well. It is demonstrated that VOF-based flow calculation procedure is able to capture the observed flow phenomena within a shroud under different operating conditions reasonably realistically. Parallel to such, the efficacy of tundish flushing with argon was also analysed computationally. On the basis of such, operating practice of shroud–tundish assembly was rationalised and a novel casting condition, having potential to eliminate reoxidation (either from atmosphere or from the overlying slag) completely, was advocated to help produce clean steel.

References

1. L. Zhang and B.G. Thomas, ISIJ International, 43 (2003), 271–291
2. C. Perkin and K. Flynn, 78th Steelmaking Conf. Proc. ISS, Warrendale, PA, (1995), 431–437
3. L. Wang, H.G. Lee and P. Hayes, Steel Research, 66 (1995), 279–286
4. A. Laihua Wang, H.G. Lee and P. Hayes, ISIJ international, 36 (1996), 17–24
5. L.T. Wang, Q.Y. Zhang, C.H. Deng and Z. Bang Li, ISIJ International, 45 (2005), 1138–1144
6. K. Chattopadhyay, M. Isac and R.I.L. Guthrie, ISIJ International, 51 (2013), 759–768
7. G. Solorio-Diaz, R.D. Morales, J. DeJesus and B. Sandoval, Steel Research International. 85 (2013), 863–874

8. M. Alam, T.Q. Hashmi and I.H. Siddiqui, Journal of Basic and Applied Engineering Research, 22 (2015), 1941–1945
9. D. Mazumdar and J.W. Evans, Modelling of Steelmaking Processes, CRC Press, Boca Raton, USA, (2009), 217–219
10. D. Mazumdar and R.I.L. Guthrie, Ironmaking Steelmaking, 12 (1985), 256–264

Novel Casting Technology Preventing Slab Transverse Corner Cracks of Typical Micro-alloyed Steels

Zhang Hui, Wang Minglin, Wu Yeming, Wang Mei and Lyu Xilin

Abstract A novel casting technology based on chamfered mould was successfully developed in order to control slab transverse corner cracks of typical micro-alloyed steels. By using the established models for the typical niobium, vanadium, titanium micro-alloyed steels, the slab casting process during solidification and straightening can be simulated for both conventional and chamfered moulds. The simulation results provide guidelines for designing chamfered mould with optimum geometry in terms of heat transfer, slab strain and controlling of slab cracks. Results from the industrial applications over last few years confirm that the slab corner temperature at straightening segment is about 100 °C higher by using a chamfered mould than the conventional mould. Consequently, the slab transverse corner cracks can be reduced by more than 99.5% during casting of micro-alloyed steel, such as X65 (yield strength is 450 MPa), Q550D (yield strength is 550 MPa) and Q690 (yield strength is 690 MPa). This novel casting technology with chamfered mould has been successfully applied by more than 20 major steel plants in China such as Shougang Jingtang Iron and Steel Company, Handan Iron and Steel Company, Anshan Iron and Steel Company, etc. and brought enormous economic benefits to the users.

Keywords Slab casting · Transverse corner cracks · Micro-alloyed steels Chamfered mould

Z. Hui (✉) · W. Minglin · W. Yeming · W. Mei
Central Iron and Steel Research Institute, Beijing 100081, China
e-mail: zhangh@cisri.com.cn

L. Xilin (✉)
Demate Technology (Beijing) Co. Ltd., Beijing, China
e-mail: xilinlu@vip.sina.com

T. K. Roy et al. (eds.), *Advanced High Strength Steel*, Lecture Notes in Mechanical Engineering, https://doi.org/10.1007/978-981-10-7892-7_18

1 Introduction

The transverse corner crack is one of the main quality problems in the slab surface during the continuous casting process of micro-alloyed steel. The locations of the cracks are uncertain and could occur at the outer arc and the inner arc of the strand, which have not been controlled effectively. Usually, the slab corners are cut off by flame offline in some domestic steel companies. However, flame cutting causes not only waste of energy, materials, human resources and the increasing of storage area, but also makes hot charge and hot delivery impossible. Many researchers have studied the formation mechanism and control method for transverse corner crack of micro-alloyed steel systematically [1–5], through which the occurrence of transverse corner cracks was to some extent reduced, but not solved fundamentally. A numerical simulation of the fluid flow, heat transfer, and macro-solidification in the conventional mould and chamfered mould was performed, with the help of a finite element stress–strain model for the straightening process. This provides a theoretical basis for the optimization of the chamfered mould. In industrial production, the transverse corner cracks have been significantly reduced (more than 99.5%) by using chamfered mould than conventional mould.

2 Influence of the Corner Shape on Fluid Flow, Temperature Distribution and Solidification at Slab Corner

2.1 Influence of the Chamfer Angle on the Fluid Flow, Heat Transfer and Solidification of the Molten Steel in Mould

Figure 1 shows the effect of the chamfer angle on the fluid flow and temperature distribution on slab corner at the mould outlet ($Z = 0.8$ m). As can be shown in Fig. 1, the surface temperature on the slab corner is increased and the fluid flow is enhanced near the intersection of the wide side and the narrow side of the slab with increasing chamfer angle. Compared with other chamfer angle, there is a stronger vortex and impingement of the fluid flow on slab corner with a chamfer angle of 45°, which will adversely affect the uniform growth of solidified shell.

The effect of the different chamfer angles on the temperature of slab corner is shown in Fig. 2. It can be seen that the increasing chamfer angle leads to an approximately linear increase of the slab corner temperature. Compared to the conventional mould, when the chamfer angle is 22°, 30° and 45°, the temperature of slab corner at mould outlet increases by 160, 220 and 288 °C, respectively. The temperature of slab corner at a distance of 3 m from the meniscus of the mould will be increased by 120, 198 and 260 °C. Although the chamfer angle of 45° is the best shape for raising the temperature of the slab corner, however, it is not the optimal

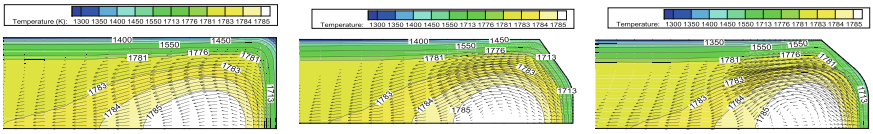

(a) conventional mould (b) chamfered mould (α=30°) (c) chamfered mould (α=45 °)

Fig. 1 Effect of the chamfer angle on fluid flow and temperature distribution of slab corner at mould outlet

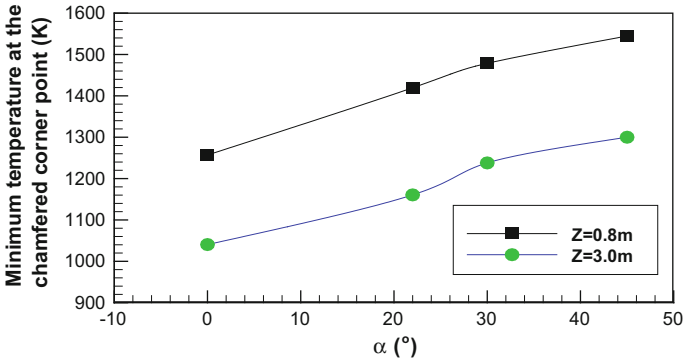

Fig. 2 Effect of the chamfer angle on the temperature of the slab corner

solution because of the negative effect of the enhanced fluid flow at the slab corner, as shown in Fig. 1c. It is necessary to take account of both the influences of the temperature distribution and the fluid flow to design the chamfer shape.

The effect of the chamfered angle on the thickness of the solidified shell and the fluid flow at the mould outlet is illustrated in Fig. 3. As can be seen, the thickness of the solidified shell at the wide side of slab is relatively uniform, and the solidified shell close to narrow side is a little thinner because of the impingement of the jet from the nozzle on the solidified shell of the narrow side. When the chamfer angle

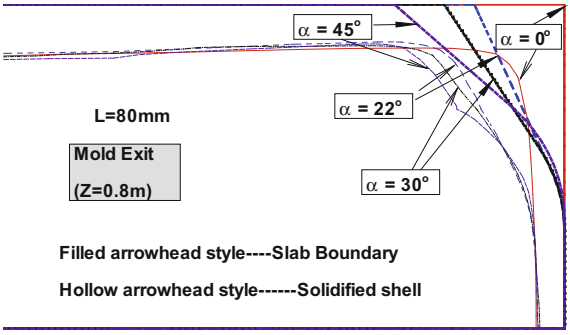

Fig. 3 The effect of the chamfer angle on the solidification of the slab corner (Z = 0.8 m)

is 22°, the fluid flow pattern of the chamfered mould is similar to the conventional mould. But the growth of the solidified shell at the slab corner is inhibited because of the strong fluid flow at the slab corner when the chamfer angle increases to 45°. Therefore, increasing chamfer angle contributes to higher temperature of the slab corner at the same cooling condition, but the stronger fluid flow at the slab corner reduces the thickness of the solidified shell simultaneously. Thus, it is necessary to modify the cooling structure of the narrow side copper for designing the chamfered mould.

2.2 *The Influence of the Chamfered Length on Fluid Flow, Heat Transfer and Solidification of the Molten Steel in Mould*

Figure 4 shows the effect of the chamfer length on the fluid flow and temperature distribution on the slab corner at the mould outlet. The surface temperature of the slab corner increases and the fluid flow gets stronger near the intersection of the wide side and the narrow side with increasing chamfer length. With a chamfer length of 80 mm, exists a vortex at slab corner, which indicates that the long chamfer length will change the flow pattern of the slab corner at the mould outlet.

Figure 5 shows the effect of chamfer length on the temperature of slab corner. Comparing with the conventional mould, very small chamfered length (e.g. L = 10 mm) can lead to the significant increase in the temperature (about 102.2 °C). With increasing chamfer length, the temperature increase reduces. While the chamfer length increases to 40 mm, the temperature of the slab corner increases by 169.1 °C compared to that of the conventional mould. When the chamfer length increases from 40 to 80 mm, the temperature of the slab corner increases by 52.5 °C. As the chamfer length is increased from 60 to 80 mm, the temperature of the slab corner increases slightly while the fluid flow near the chamfered corner of the slab is enhanced remarkably.

Figure 6 shows the effect of chamfered length on the thickness of the solidified shell in detail. The thickness of the solidified shell at the slab corner becomes thinner when the chamfered length is 80 mm. Therefore, the appropriate chamfered length should be between 40 and 60 mm.

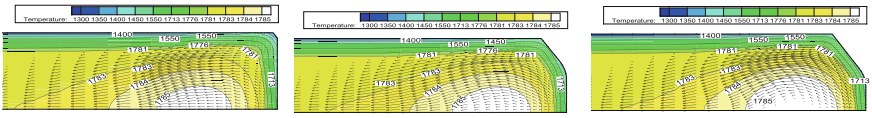

Fig. 4 The effect of the chamfer length on the fluid flow and temperature distribution of the slab corner

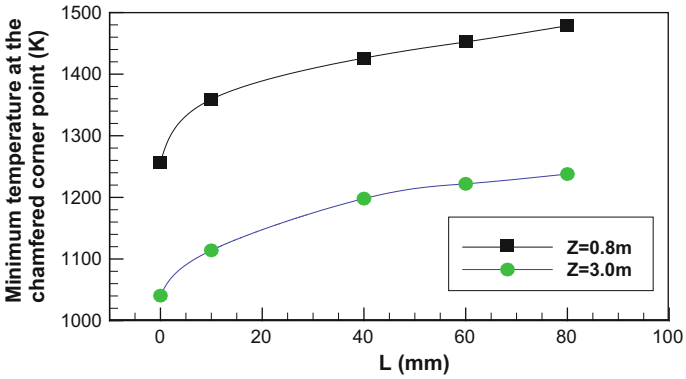

Fig. 5 The effect of the chamfered length on the temperature of the slab corner

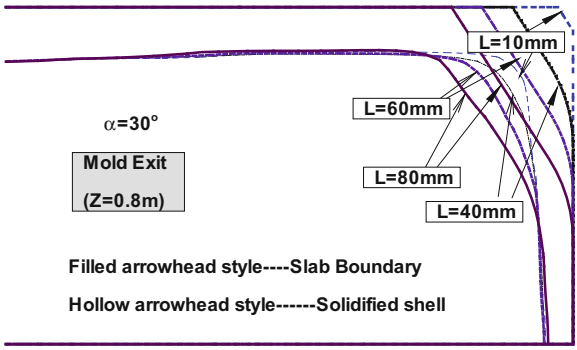

Fig. 6 The effect of the chamfered length on the solidification of the slab corner

3 The Influence of the Chamfered Shape on the Stress and Strain of the Slab During Straightening Process

3.1 The Influence of the Chamfered Angle on the Stress and Strain of Slab During Straightening Process

The effect of the chamfer angle on the slab during the straightening process is simulated at the following conditions. The section size of the slab is 230 × 1500 mm^2, the temperature is 900 °C, the chamfer length is 75 mm, and chamfer angle is 0°, 22°, 30° and 45°, respectively.

Figure 7 shows the equivalent tangential strain distribution on the cross section of the slab at the straightening segment along the casting direction. As can be seen, with increasing chamfer angle, not only the equivalent strain on the cross-sectional corner of the slab is reduced during the straightening process but also the location of the maximum equivalent strain is changed obviously, which moves from the corner to the chamfer side. The moving distance varies with the chamfer angle. The

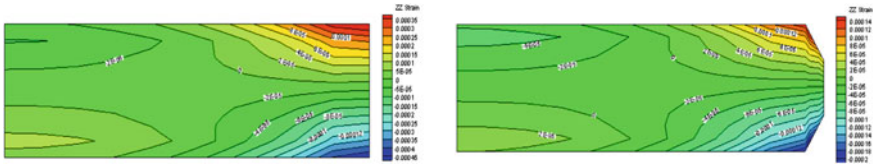

(a) α=0° (b) α=45°

Fig. 7 The equivalent strain distribution of the slab through straightening segment along the casting direction

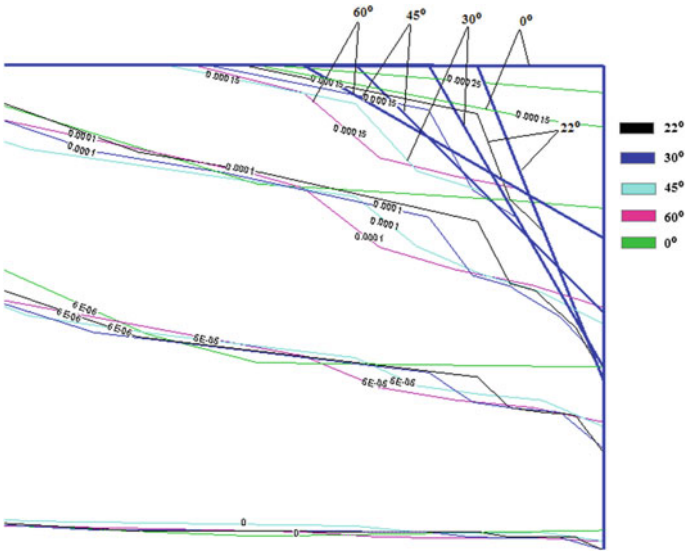

Fig. 8 The effect of the chamfered angle on the equivalent strain distribution

chamfer angle has a great influence on the equivalent tangential strain distribution on the slab cross section at a constant casting speed and slab temperature. The strain on the slab corner is relatively small when the chamfer angle is 30°.

At the same chamfer length, if the chamfer angles are chosen as 30° and 45°, the equivalent tangential strain on the slab corner is relatively small, which is only 40–46% of those of the rectangular slabs with the same cross-sectional area. The position of the maximum equivalent strain changes from the corner near the wide side to near the narrow side if the chamfer angle is larger than 45° (Fig. 8). The maximum equivalent strain on the slab corner with different chamfer angles is illustrated in Fig. 9. The optimal chamfer angle should be between 30° and 45°. However, 30° is found to be better than 45°.

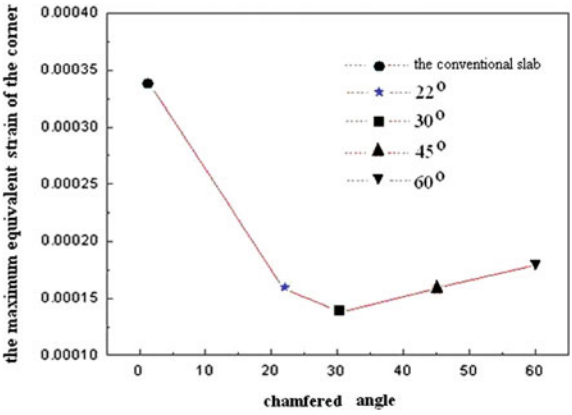

Fig. 9 The maximum equivalent strain distribution of slab corner

3.2 *The Influence of the Chamfered Length on the Stress and Strain of Slab During Straightening Process*

For a cross-sectional size 230 × 1500 mm^2 of the slab and a temperature of 900 °C, the effect of the chamfer length on the equivalent tangential strain on the cross section of the slab is calculated for different chamfer lengths of 55, 65, 75 and 85 mm.

Figure 10 shows the relationship between the chamfer length and the equivalent tangential strain on the slab cross section while casting speed and temperature are constant. Figure 11 presents the effect of the chamfer length on the equivalent strain distribution on the slab cross section along the casting direction at the straightening segment. With a chamfer angle of 30° and controlled chamfer length from 65 to 85 mm, the equivalent tangential strain on the slab corner is relatively minimal, and does not exceed 70% of that of the conventional slab with the same cross-sectional area. While the chamfer length is 75 mm, the equivalent tangential strain on the slab corner is only 40% of that of the conventional slab with the same cross-sectional area (Fig. 12).

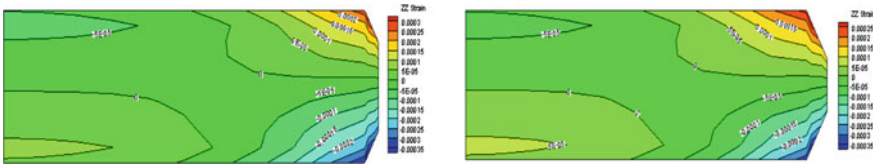

(a) chamfered length L=55mm (b) chamfer length L=85mm

Fig. 10 The equivalent strain distribution on the slab along the casting direction

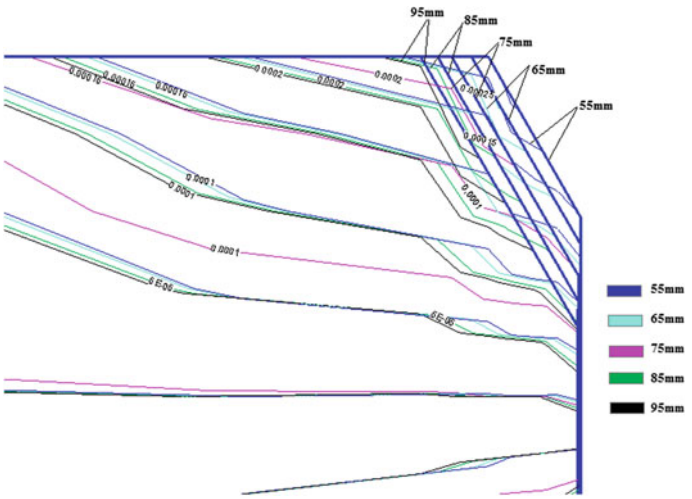

Fig. 11 The effect of the chamfer length on the equivalent strain distribution

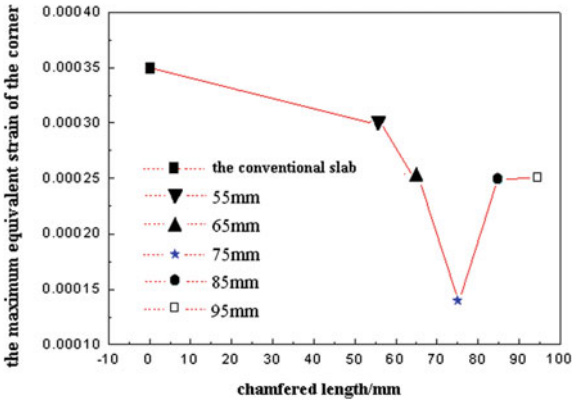

Fig. 12 The maximum equivalent strain distribution on the slab corner

4 The Application of Chamfered Mould

This novel casting technology with chamfered mould has been successfully applied by more than 20 major steel plants in China such as Shougang Jingtang Iron and Steel Company, Handan Iron and Steel Company, Anshan Iron and Steel Company, etc. and brought enormous economic benefits to them. Figure 13 shows the photo of the chamfered mould applied in industrial production.

Fig. 13 The photo of the chamfered mould applied in industrial production

The applied steel grades include X65, Q550D, Q690, Q345B, SS400, L290, SPHC, SPHD, Q235A, Q235B, A36, 45, etc. Most of these are typical niobium, vanadium and titanium micro-alloyed peritectic and sub-peritectic steels. The typical micro-alloyed steel composition is shown in Table 1. The thickness of the slab varies from 170 to 300 mm, and the width from 1000 to 2150 mm. The average casting speed changes from 1.15 to 1.40 m/min for most steel plants. The corner temperatures of the chamfered slabs and the conventional slabs are measured by infrared thermometer. The measurement results show that the temperature of the chamfered slab corner at the straightening segment is approximately 100 °C higher than that of the conventional slab. Figure 14 indicates the narrow side of the slabs observed in different locations of the caster. As can be seen, the temperature at the corner of chamfered slabs is significantly higher than conventional slabs.

The industrial application results show that the transverse corner cracks in niobium, vanadium, titanium micro-alloyed steels produced using chamfered mould have been reduced more than 99.5% than that of the traditional mould. The corners of the casting slab which are produced using the chamfered mould technology do not need to be scarfed. There is no longitudinal edge crack and other surface defects in the chamfered casting slab after rolling. The casting speed can reach up to 1.5 m/min for low carbon steel and 1.3 m/min for micro-alloyed steel. The chamfer copper life is more than 60,000t at normal operating condition. The successful application of the chamfered casting slab technology shows that the transverse corner cracks of micro-alloyed steel can be expected to be solved fundamentally.

Table 1 Typical micro-alloyed steel composition

	C	Si	Mn	P ≤	S ≤	Alt	Cr	Nb	Ti
J55	0.16–0.20	0.07–0.16	1.00–1.20	0.020	0.010	0.02–0.05	0.30–0.35	0.018–0.030	0.008–0.025
510L	0.08–0.12	0.07–0.15	1.10–1.30	0.020	0.010	0.025–0.055		0.02–0.04	
X60	0.070–0.100	0.07–0.16	1.20–1.40	0.015	0.005	0.020–0.050	0.10–0.20	0.024–0.040	0.010–0.020
X70	0.05	0.19	1.54	0.009	0.001	0.03	0.2	0.07	0.02

(a) the chamfered slab at the exit of the 7^{th} segment

(b) the conventional slab at the exit of the 7^{th} segment

Fig. 14 The photo of the slab narrow side

5 Conclusions

The simulation results show that the temperature of the slab corner increases approximately linear with the chamfer angle, and at the same time, the fluid flow is enhanced near the corner between the wide side and the narrow side of the slab. Very small chamfer length can lead to the significant increase in temperature near slab corner. With the increasing chamfer length, it is found that the temperature on the slab corner increases slightly while the fluid flow near the chamfered corner of the slab gets obviously stronger and the thickness of solidified shell becomes thinner. Under the condition of the same chamfer length and straightening speed, the equivalent tangential strain on the slab corner is relatively minimal for the chamfer angles 30° and 45°, which is only 40–46% of that of the rectangular slabs with the same cross-sectional area. At the condition of the same chamfer angle (30°) and controlled chamfer length of 75 mm, the equivalent tangential strain is only 40% of that of the conventional slab with the same cross-sectional area.

The industrial applications show that the cooling conditions and the stress state have been improved by application of the chamfered mould. The temperature on the corner of a chamfered slab at the straightening segment is approximately 100 °C higher than the conventional slab. The transverse corner cracks of the chamfered slab have been reduced more than 99.5% compared to those of the conventional mould.

References

1. P. Zhao, X.H. Wang, S.P. Wu, et al., Iron and Steel, 31(2) (1996), 21–24
2. X.H. Wang, W.J. Wang, X.Y. Liu, et al., Iron and Steel, 33(1) (1998), 22–25
3. J.J. Zhi, Iron and Steel, 36(1) (2001), 22–24
4. Y. Chen, S.B. Yang, M.Y. Zhu, Iron Steel Vanadium Titanium, 29(3) (2009), 55–62

5. J.N. Lin, F.C. Ma, X.Z. Zhao, J UnivSciTechnol Beijing, 29(1) (2007), 118–121
6. H.P. Liu, Numerical simulation of transport characteristics during the solidification process in a continuous slab caster based on the continuum model. Doctoral Dissertation. Beijing:Central Iron & Steel Research Institute, (2002)

Non-metallic Particles Benefit or Burden for AHSS?

Gert Abbel and Begoña Santillana

Abstract This paper describes a Tata Steel approach to investigate the production of new AHSS grades in relation to non-metallic inclusions. The work includes thermodynamic and phase modelling, as well as fractography and postmortem analyses on a sample from a newly developed cracking simulator. Examples will be shown on how the MnS and TiN formations do influence the cracking susceptibility during solidification.

Keywords Non-metallic inclusion · AHSS · Mould cracking simulator
Precipitates · Hot tearing · Solidification structure

1 Introduction

Non-metallic particles in steel alloys are amongst others the result of chemical reactions such as de-oxidation and alloying, entrained process slags or segregation during solidification. Inclusions that are the results of alloy composition can have an effect on steel quality and cracking susceptibility during solidification. The most common example is manganese sulphide (MnS); however, (Ti,V,Nb) (C,N) precipitates are included in this category as they are another phase formed during cooling and as such are also a non-metallic particle.

Due to the high concentration of Mn in the new generation AHSS grades, the formation of MnS during solidification is inevitable, even at the low sulphur concentrations that can be achieved in steel processing nowadays. The solidification temperature of the MnS enriched phase is much lower than the solidus calculated from the initial composition of the steel [1]. In this way, the segregating elements in the steel can increase the cracking susceptibility as they widen the brittle temperature range, i.e. the difference between zero strength and zero ductility temperature ($\Delta TB = ZST - ZDT$) displacing its lower limit to lower temperatures [2–5], Fig. 1.

G. Abbel (✉) · B. Santillana
Tata Steel, P.O. Box 10000, 1970 Ijmuiden, CA, The Netherlands
e-mail: gert.abbel@tatasteel.com

T. K. Roy et al. (eds.), *Advanced High Strength Steel*, Lecture Notes
in Mechanical Engineering, https://doi.org/10.1007/978-981-10-7892-7_19

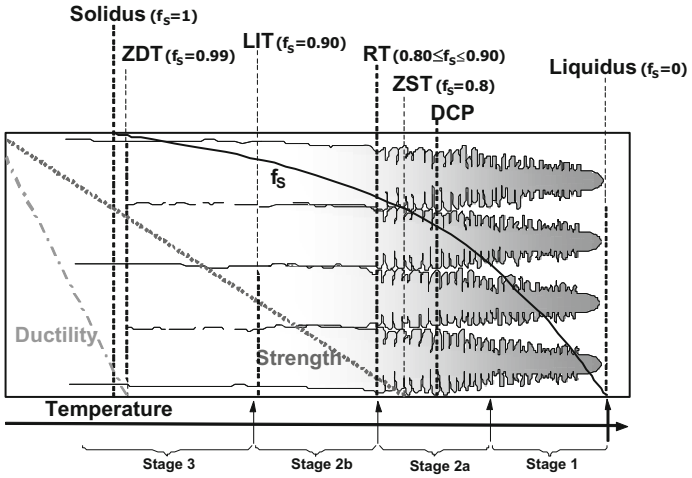

Fig. 1 Solidification structure with characteristic temperatures (explanations on abbreviations in text)

Cracking during solidification appears in many forms, one of them is referred as hot tearing. Hot tears are separations of the dendrites during solidification, more specifically, at the semi-solid region where a considerable amount of liquid phase is still present, between solidus (T_S) and liquidus (T_L) temperatures [1]. The dendrites will separate because they are subjected to simultaneously acting tensile stresses [6–8]. Moreover, the separation will typically initiate above the (non-equilibrium) solidus temperature at volume fractions of the solid phase above 0.85–0.9 and propagate mainly through the interdendritic liquid film, where one of the conditions for hot tearing is the lack of liquid feeding between dendrites, particularly when the grains start to touch one but are still separated by a liquid film [1, 7].

Traditionally, sulphides are classified as type I, II and III [9–11]. Type I sulphides are spheroids that appear scattered randomly in the interdendritic spaces. Type II have the morphology of a degenerate eutectic phase delineating the dendrite arm boundaries. Type III are either idiomorphic crystals or angular particles often with projected arms which join type II particles; they are frequently situated in interdendritic spaces [10].

Precipitates can form at different rates, stages and locations during steel processing, in the mushy-zone between dendrites due to rapid diffusion in segregated liquid, at solid state inside the grains due to slow diffusion, or at the grain boundaries faster diffusion [12, 13]. Different mechanisms cause the precipitate particles to show a variety of compositions, morphologies and size distributions [14]. Micro-alloyed or HSLA steels are available in a variety of compositions [15]. These steels have the addition of B, Nb, V, Ti or Al to form carbonitrides to enable the grain refinement during further processing and thus improve toughness, plasticity, wear- and corrosion-resistant properties [16]. The carbonitrides are formed at the final stages of solidification and their precipitation at grain boundaries can be detrimental for

cracking at the second ductility trough [15]. However, the microsegregation of Ti and N during solidification at the solute-enriched interdendritic zones leads to the precipitation of TiN in this interdendritic liquid. According to Turkdogan [17], the solubility product of TiN in low-alloyed liquid steels is [wt%Ti] × [%N] = 6.15 × 10^{-4} at 1500 °C, i.e. the average solidus temperature of low-alloyed steels. For a steel containing 0.02%Ti and 60 ppm N, about 55% of the nitrogen is converted to TiN at 99% local solidification. Upon complete solidification, most of the remaining N in solution will precipitate as TiN, provided that %Ti/%N $\geq$ 3.42. The TiN precipitated in the interdendritic liquid, which subsequently becomes the austenite grain boundaries, will be the sites upon which other carbides will precipitate during further cooling [17]. Moreover, the carbides and nitrides of vanadium, titanium and niobium show extensive mutual solubility which arises from the fact that they have the same cubic crystal structure and have very similar lattice parameters.

The next sections will discuss MnS, TiN and Nb(C,N) precipitation and investigate the effect on product Quality.

2 Approach and Results

2.1 Fe–Mn–S System

One of the most powerful tools to study the development of microstructure is the phase diagram. It shows the phases present in equilibrium and their relative quantities, as well as the composition of the phases over a range of temperatures. It should be noted that thermodynamics tells us what should happen in equilibrium but what will happen in the real system is constrained by kinetic processes [3].

The ability of manganese to react with sulphur during solidification of steel and its effect on hot tearing has induced great interest in the Fe–Mn–S system. The phase diagram, Fig. 2, has been calculated with the FactSage 6.2 software package using the FSstel database [18].

A liquid miscibility gap that originates on the Mn–S side of the ternary diagram dominates this region. During solidification the Mn and S concentration increases in the residual liquid. When the concentration of these two elements in the residual liquid is higher than the solubility product constant, MnS will begin to precipitate [19]. Hence, the composition starts to deviate from the equilibrium phase diagram. If there is some segregation of S and Mn and the fraction of MnS reach above 0.75 in the interdendritic liquid, then the solidus will lower to 1400 °C according to the pseudo-binary Fe–MnS phase diagram (see point 1 in Fig. 2). Moreover, many investigators have studied the influence of S and Mn/S ratio on the cracking susceptibility of continuously cast steel [2–4, 10, 18–21], concluding that a low Mn/S ratio gives place to the formation of low-melting interdendritic liquid FeS phases (point 2 in Fig. 2) during solidification. These low-melting phases enhance internal cracking during continuous casting or intergranular cracking during hot rolling [18], because sulphur is expected to segregate strongly to grain boundaries. Moreover,

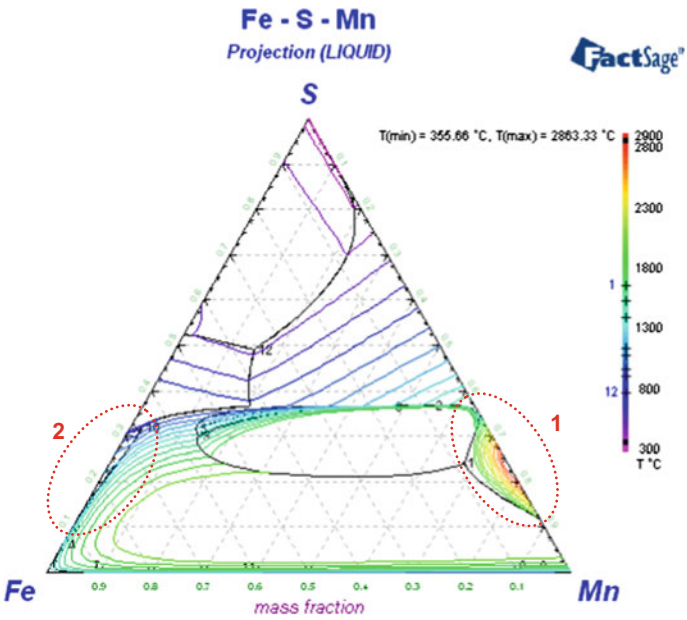

Fig. 2 Fe–Mn–S ternary diagram (liquidus projection) [18]

the mobility of sulphur is about a thousand times greater than that of Mn at high temperature [22], and thus it will segregate stronger and because it has a lower surface energy it will always try to form a precipitate on a grain boundary. When Mn and S are present in the steel composition and MnS type II particles form during solidification, it is sufficient to examine the Fe–MnS pseudo-binary system to understand their formation. In the solidification of a steel grade with a fraction of MnS below 0.02, precipitation of iron continues until, just before the eutectic temperature is reached and at the eutectic temperature this liquid solidifies to give type II MnS with its characteristic morphology [9].

2.2 *Precipitates Formation During Solidification—TiN During Solidification*

While most micro-alloying elements will form carbonitrides at the last stages of solidification, titanium is the only micro-alloying element which is known to form nitrides at rather high temperatures [1]. When Ti in combination with other micro-alloying elements precipitates as (Ti,V,Nb)(C,N) at the end of solidification [23], a positive effect on cracking susceptibility is possible. In some steel grades, Ti is not specified as an alloying element but is still present with a typical content of 0.002–0.004%.

In order to find out whether carbonitride particles could affect the hot-cracking behaviour of the selected steel grades, the first question to be addressed is at which temperature and at which sites precipitation of this phase can occur. Therefore, Scheil calculations and DICTRA simulations [24] were performed for the two steel compositions listed in Table 1, including 0.003 wt% Ti. Figure 3 shows the amount of carbonitrides for HSLA and LR-HSLA in a temperature range between 1250 and 1520 °C, where particles precipitated at different stages, from the melt, δ-ferrite or γ-austenite were evaluated separately [1].

According to these simulation results, most of the carbonitrides formed in this range are TiN, but they either precipitated in the melt at temperatures above about 1450 °C or from the γ-austenite at much lower temperature. Meaning that, in accordance with empirical knowledge [23], the formation of these particles could be linked with the strength of the steel at high temperatures strongly depends on the Ti and N contents of the alloy [29].

Although TiN precipitation from the γ-austenite is shifted to a slightly higher temperature in HSLA compared to LR-HSLA, it could also increase cracking susceptibility at temperatures below 1350 °C because the largest amount of precipitates are formed at the γ-austenite phase and at this temperature carbonitrides are promoting intergranular cracking.

To further study the precipitates formation at the interdendritic liquid, a phase field simulation with the package MICRESS [1] was performed, taking into account a Ti content of 0.003 wt% and nucleation of TiN from the liquid phase. Figure 4 shows a small section of the simulation domain at $t = 0.7$ s and a magnified subsection revealing that the precipitation of TiN takes place at the interdendritic region, just before solidification is completed.

If the precipitation takes place at the interdendritic liquid pockets, the neighbouring dendrites could be joint together and trigger their coalescence. In this case, TiN precipitation from the liquid can increase the coalescence temperature point and reduce the hot tearing risk.

Obviously, TiN precipitation will depend on the N content of the alloy and co-precipitation of other micro-alloying elements such as (Ti,V,Nb)(C,N) [23]. The higher V and N contents in the HSLA could positively reduce the cracking susceptibility of this alloy.

Table 1 Chemical composition of the HSLA and LR-HSLA steel grades

Grade	LR-HSLA	HSLA
C (wt%)	0.045	0.045
Mn (wt%)	0.8	0.8
S (wt%)	0.005	0.005
V (wt%)	0.04	0.13
Nb (wt%)	0.013	0.013
N (ppm) max.	100	150
Liquidus temp. (°C)	1528	1528
Solidus temp. (°C)	1507	1505
Hot tearing susceptibility	High	Low

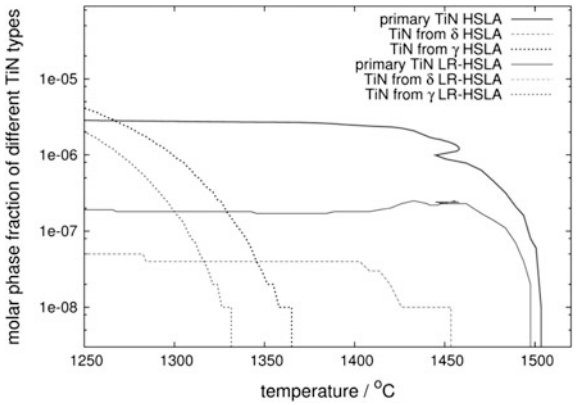

Fig. 3 Logarithmic plot of the carbonitride phase fraction versus temperature down to 1250 °C for a Ti composition of 0.003 wt%. Independent values are given for those particles which nucleated in the melt, in the δ-ferrite and the γ-austenite phases [29]

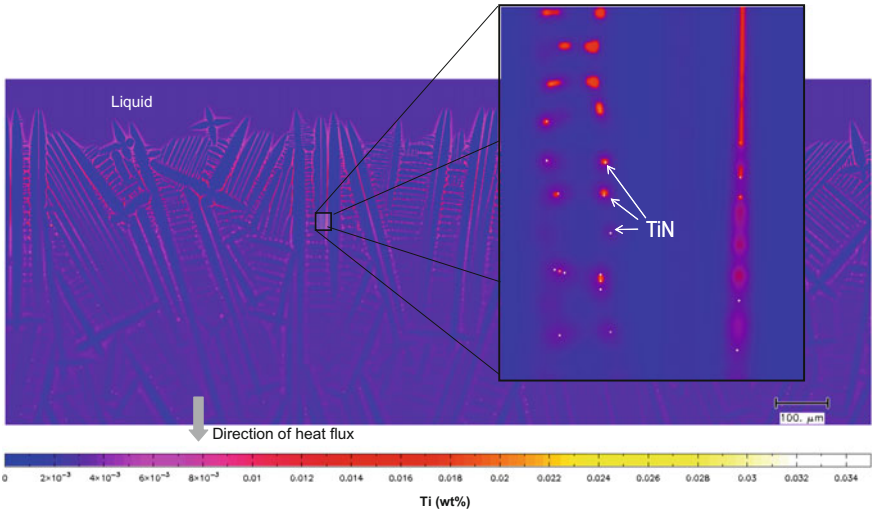

Fig. 4 Concentration distribution of Ti in HSLA + 0.003 wt% Ti at 0.7 and a section revealing that the precipitation of TiN at the interdendritic region

2.3 Precipitation of Nb(C,N) During Solidification

The first physical model to simulate at lab scale of the main casting parameters such as casting speed, oscillation characteristics and mould slag viscosity on shell growth and slag infiltration in a continuous casting mould was done in the early 1980s [26]. This device has been called since then ‘mould simulator’.

Such mould simulator has been available at Tata Steel R&D, The Netherlands [27, 28] since 1998. The capabilities of the mould simulator have been expanded to investigate and accurately cause hot tearing (cracking) during solidification under continuous casting conditions, fulfilling the following demands:

1. The existence of a deformable solid–liquid two-phase region together with a columnar grain structure,
2. The conformity of the solidification structure with that of a continuous cast shell and
3. Main load directions are perpendicular to the main dendrite growth axis [28].

The proposed modification is called Mould Cracking Simulator (MCS) and its design is shown in Fig. 5, where the blue half-ring will create an extra tensile stress in the solidifying steel shell, producing cracking in the longitudinal and transverse directions. The MCS allows measurement of the strength of the steel shell while reproducing the complex casting conditions, including the influence of major casting parameters such as casting speed, heat transfer, oscillation characteristics and mould slag on shell growth, while including the features of a tensile test to generate cracking under these controlled conditions. A case-hardening steel grade (Nb = 0.0043 wt%) has been tested in the MCS to investigate the steel strength in relation to non-metallic inclusions. Precipitates of Nb(C,N) along with nonmetallic inclusions of MnS were observed in the postmortem samples taken for metallography and fractographic analyses.

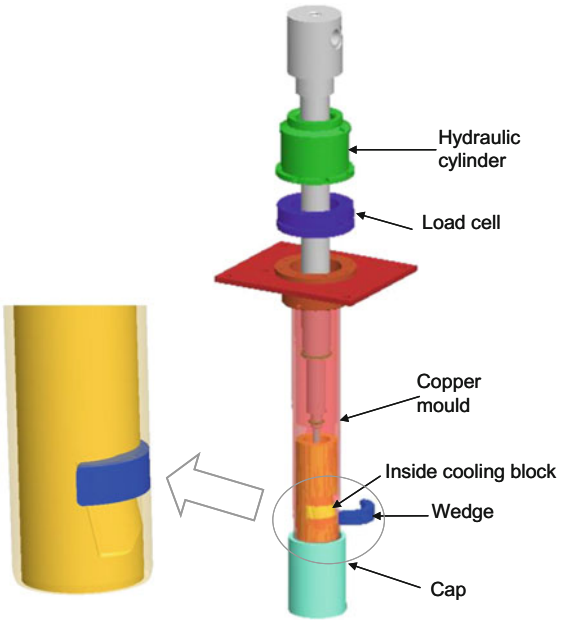

Fig. 5 Schematic representation of the mould cracking simulator [28]

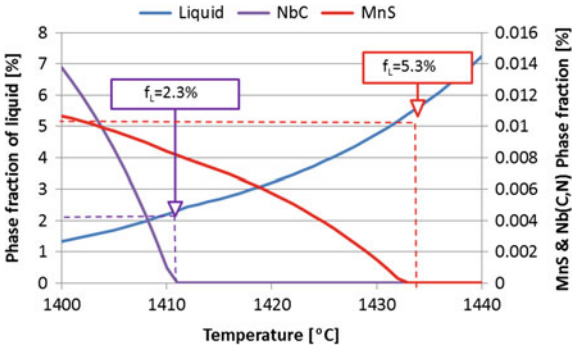

Fig. 6 Scheil simulations showing the phase fraction precipitates [30]

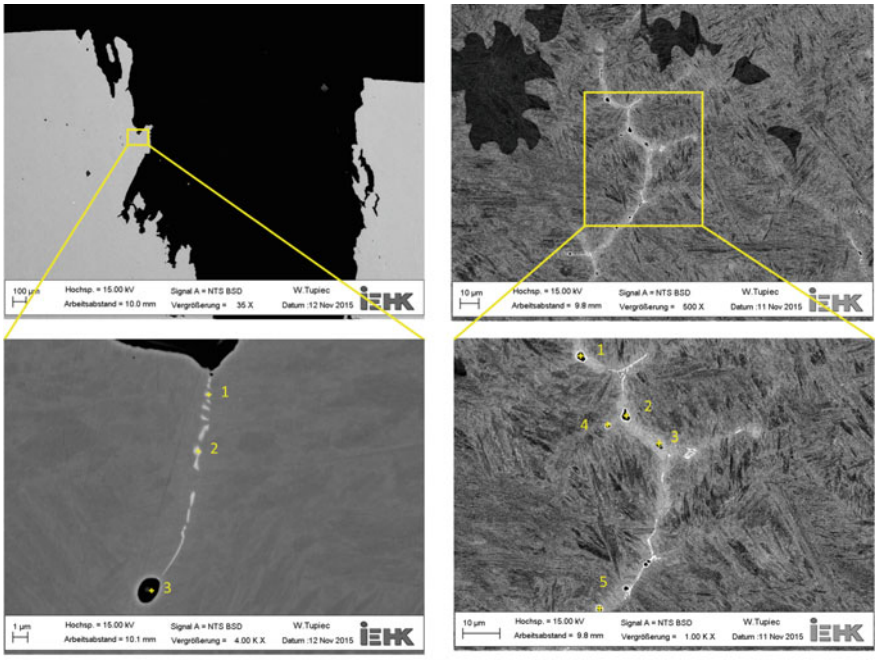

	C [wt%]	N[wt%]	O[wt%]	Al[wt%]	Si[wt%]	P[wt%]	S[wt%]	Cr[wt%]	Mn[wt%]	Fe[wt%]	Nb[wt%]	Mo[wt%]
Point-1	21.42	0.62	0	0	0.17	0.23	0	2.45	1.14	46.28	21.82	5.87
Point-2	24.55	0.57	1.36	0	0.23	0	0	2.17	0.66	27.7	34.77	7.99
Point-3	14.46	0	1.47	0.3	0.38	0.41	19.49	1.92	36.4	24.21	0.22	0
Point-4	6.52	0.04	3.15	0.45	0.2	0.19	15.05	1.94	29.59	42.87	0	0
Point-5	4.94	0	4.12	2.49	0	0	28.09	0.5	53.78	3.94	0	0
Point-6	3.21	0.15	0	0	0.25	0.13	2.43	3.12	7.51	80.69	0	1.92

Fig. 7 Precipitation of Nb(C,N) in mould cracking simulator postmortem samples [30]

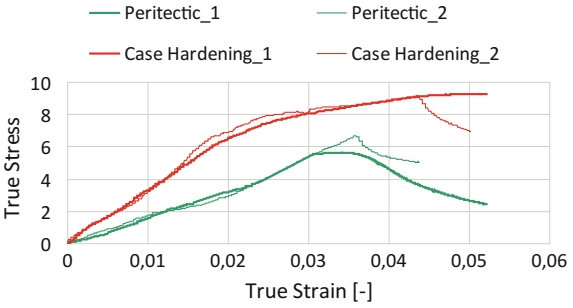

Fig. 8 Mould cracking simulator results

The precipitates are formed in interdendritic segregated liquid from which it is concluded that they are formed during the last stages of solidification. The non-equilibrium Scheil calculations (see Fig. 6) show that the precipitates began to form when there is still 2–3% liquid available between the dendrites [30]. Therefore, primary precipitation of Nb(C,N) has also an influence on the hot tearing behaviour during last stages of solidification. The location and morphology of the precipitates are shown in Fig. 7.

Precipitates of Nb(C,N) have been adequately observed at the crack initiation points and in the segregated regions between the secondary dendrite arms as shown in Fig. 7. To increase the conductivity of the electrons during SEM, the samples were carbon coated. So, the composition of these particles could only be quantitatively analysed. Likewise, it is observed that the Nb(C,N) have small amount of Molybdenum due to the presence of minute solubility in that phase.

Out of four tests shown in Fig. 8, a good reproducibility is seen between similar steel grades. It is observed that the results for the case-hardening steel with high amount of alloying elements show better mechanical properties, in terms of strength and ductility, when compared with a peritectic grade. This is possibly due to a finer dendritic structure for the higher alloyed steel [30].

Moreover, the carbides and nitrides precipitates in a chain-like formed at the dendrites boundaries can have a positive effect on the hot tearing and mechanical properties of the partially solidified shell.

As stated in many theories of hot tearing [13, 28], when this precipitates nucleate in the segregated liquid between the dendrites and grow by substituting the liquid phase, a drastic decrease in the liquid fraction and increasing in solid fraction can result in improving the coalescence between the dendrite arms and also strength of the material, just like in the case of TiN precipitation.

3 Conclusions

Thermodynamic modelling was used to investigate MnS formation. Thermodynamic, kinetic and phase field modellings were used to determine TiN precipitation. Fractography and postmortem analyses on a sample from the Mould Cracking

Simulator were done to understand the effect of NbC on steel strength during solidification. The results show that nonmetallic inclusions can be a foe as well as a friend for the modern steelmaker.

References

1. B. Santillana, PhD Thesis, TU Delft, (2013)
2. A. Chojecki, I. Telejko, Theoretical and Applied Fracture Mechanics, 27 (1997), 99–105
3. K. Hansson, PhD Thesis, Royal Institute of Technology, Stockholm, Sweden, (2001)
4. T. Nakagawa, T. Umeda, J. Murata, Y. Kamimura and N. Niwa, ISIJ International, 35 (1995), 723–729
5. R. Pierer, C. Bernhard and C. Chimani, La Revue de Metallurgie, 2 (2007), 72–83
6. J.M. Drezet, M. Gremaud, R. Graf and M. Gäumann, Metallurgical and Materials Transactions A, 30(2) (1999), 449–455
7. P.D. Grasso, J.M. Drezet and M. Rappaz, JOM, web-only supplement No. January, 2002, http://www.tms.org/pubs/journals/JOM/0201/Grasso/Grasso-0201.html (2002)
8. M. Rappaz, J.M. Drezet and M. Gremaud, Metallurgical and Materials Transactions A, 30 (1999), 449–455
9. T.J. Baker and J.A. Charles, Journal of The Iron and Steel Institute, 210 (1972), 702–706
10. M.C. Flemings and T.Z. Kattamis, Investigation of Solidification of High-Strength Steel Castings, Massachusetts Institute of Technology, Massachusetts, USA, (1968)
11. M.C. Flemings and L. Bigelow,Metallurgical and Materials Transactions B, 6 (1975), 275–283
12. M.C. Flemings, Solidification processing, McGraw-Hill, USA, 1974. ISBN 0-07-021283-x
13. B.G. Thomas, Q. Yuan, B. Zhao and S.P. Vanka, JOM-e, (2006)
14. P. Nieto, V. Suarez, J.C. Alvarez Anton, J. Blanco and A. Fernandez, Materials, 8 (2015), 3562–3583
15. The Making, Shaping and Treating of Steel, 11th, The AISE steel foundation, Pittsburg, Pa, USA, (2003)
16. H. Fu, Y. Qu and J. Xing, Journal of Materials Engineering and Performance, 18 (2009), 333–338
17. E.T. Turkdogan, Iron Steelmaker, 16 (1989), 61
18. FactSage, 6.2, Thermafact & GTT Technologies, Ecole Polytechnique CRCT, Montreal
19. G. Alvarez de Toledo, O. Campo and E. Lainez, Steel Research, 64 (1993), 292–299
20. ASM Handbook, 8th, ASM International, Materials Park, OH, USA, ISBN ISBN 978-0-87170-018-6, (1987)
21. ASM Handbook, 8th, ASM International, Materials Park, OH, USA, ISBN ISBN 978-0-87170-706-2, (2004)
22. W.T. Lankford, Metallurgical and Materials Transactions B, 3 (1972), 1331–1357
23. R. Lagneborg, T. Siwecki, S. Zajac and B. Hutchinson, The Scandinavian Journal of Metallurgy, (1999) 186–241
24. Thermo-Calc software, Solna, Sweden, (2012)
25. MICRESS, ACCESSe.V., Aachen Germany, (2012)
26. Simulator for solidification in continuous casting mold, ISIJ International, 25 (1985), 352
27. B. Santillana and M. Cruijff, Mould Simulator, WO 2012/136308 A1, International Application Published under the Patent Cooperation Treaty (PCT), (2011)
28. C. Bernhard, R. Pierer and S. Michelic, The Working Group "Continuous Casting: Metallurgy and Materials (M^2CC)" at Leoben University, Austria
29. B. Böttger, M. Apel, B. Santillana and D.G. Eskin, Metallurgical and Materials Transactions A, 44(8) (2013), 3765–3777
30. V. Paruchuri, MSc thesis, Institut für Eisenhüttenkunde IEHK, Rheinisch-Westfälische Technische Hochschule RWTH, Aachen, Germany, (2016)

Advanced High-Strength Steel—Challenges to a Steelmaker

Akshay Khullar, Shainu Suresh, Akasmita Biswal, V. V. Mahashabde and Sudhansu Pathak

Abstract The need for reducing auto body weight has led to widespread studies and development of high-strength steels over the past decade or so. There are numerous studies on the microstructure–property relationship but little attention has been paid to the challenges in producing these grades without harmful inclusions which affect the performance of final product. Also many of these steels pose difficulties in castability due to clogging as well as harmful inclusions which in themselves are surrogate indicators of cleanliness of steel. This paper seeks to shed some light on the approaches taken by Tata Steel to mitigate such problems in the development of these grades some of which are being commercially supplied and some of which are under development.

Keywords AHSS · Inclusion · Re-oxidation · Continuous slab casting
Slag entrapment

1 Introduction

The seemingly conflicting demand of down-gauging steel sheet to reduce emissions by improving fuel efficiency while improving safety has necessitated a revolution in automotive steel grades. To meet these challenging demands, steelmakers are developing and producing a wide variety of advanced high-strength steels (AHSS). High-strength steels, by virtue of their high alloy content, suffer from greater propensity towards cracking on account of micro/macro-segregation and non-metallic inclusions. Non-metallic inclusions in steel can serve as crack nuclei. Therefore, there is a need to continuously monitor cleanliness of steel with respect to oxygen, hydrogen and sulphur. Figure 1 and Table 1 summarize the span of products developed and grades under development in Tata Steel India.

A. Khullar (✉) · S. Suresh · A. Biswal · V. V. Mahashabde · S. Pathak
Tata Steel Limited, Jamshedpur 831001, India
e-mail: akhullar@tatasteel.com

T. K. Roy et al. (eds.), *Advanced High Strength Steel*, Lecture Notes in Mechanical Engineering, https://doi.org/10.1007/978-981-10-7892-7_20

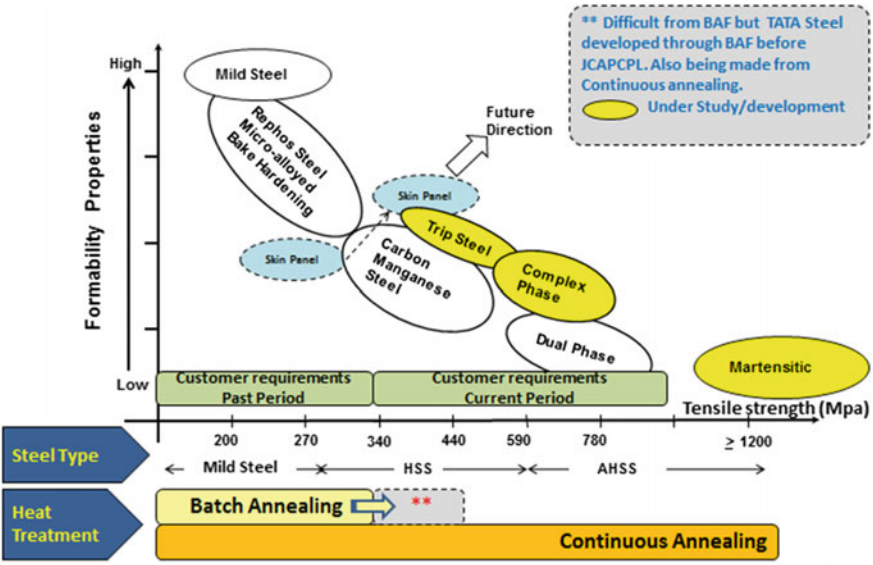

Fig. 1 Type of steel products made in Tata Steel Jamshedpur

Tata Steel India started manufacturing high-strength steel in early 2000s. In the initial supply of these steel problems such as cracking during forming, splitting during rolling and cracking on account of the surface cracks were experienced. Investigations suggested that inclusions, slab surface crack and steel cleanliness were the major reason for the failures. The major sources of inclusions were

(I) Oxides
(II) Sulphides and Nitrides.

2 Part I—Approach Towards Oxide Inclusions

2.1 Deoxidation Products—Reduction in Oxygen Levels

It is desired to reduce the generation of oxide inclusions, i.e. minimize the dissolved oxygen in the primary steelmaking before deoxidation. To this end, bottom blowing elements were installed at the LD converters in 1998 which were subsequently optimized by water modelling for both position and numbers. The numbers were increased from 6 to 8, asymmetric configurations were tried and a differential flow bottom stirring scheme was developed. These modifications showed 30–35% reduction in mixing time and 30% enhancement in mass transfer rate between slag and metal [2] which is depicted in Fig. 3a, b (Fig. 2).

Table 1 Steel grades, its strengthening mechanism and typical inclusions found

Steel category	Typical steel grade	Strengthening mechanisms	Alloying elements	Types of inclusions [1]
Low strength	IF through BAF IF through CAL	Low strength material	Ti and/or Nb	G: TiN
	IF high strength	Solid solution strengthening	P, Mn, Nb, Ti	NG: Al_2O_3, Al–Ti–O, mould slag, CA6, CA12
	BH-180, BH-220	Solid solution strengthening and bake hardening	Mn, P	
High-strength steel	SPC440, SP152-440 CR, TATA SP 440, CMn 440 GA	Solid solution strengthening, grain refinement and second phase strengthening	C, Mn, Nb, P	NG: Al_2O_3, MnS, Alumina Silicates, mould slags
	HSLA 240, HSLA 300, HSLA 340, HSLA-380	Finely dispersed alloy carbides and ferrite–pearlite aggregates in a ferrite matrix with alloying content	Nb/Ti/V or combination	
Advanced high-strength steel (AHSS)	Dual phase 590, 600	Soft ferrite matrix with martensite	Mn, Si, Cr	G: Liquid CA, CaMnS
	CQ-HSS590, HS620	Grain refinement and precipitation hardening	C, Mn, Si, Nb	
	HS 800	Micro-alloyed with nanoprecipitates	Mn, Ti, Mo	NG: Al_2O_3, CA6, CA12, CaS, MnS, alumina silicates, coarse TiN, mould slags
	FB590	Soft ferrite matrix with hard bainite	Mn, Si, Nb	
	Martensitic steel (under development)	Martensitic matrix with very fine ferrite and bainite		
	Complex phase steel: under development	Ferrite–bainite matrix with martensite, retained austenite and pearlite		

Note G—good and NG—not good

Currently, the LD converters are installed with eight bottom elements of the multihole plug design. It is noteworthy that Tata Steel is able to run at least two–three elements till the end of the vessel campaign of approximately 5500–7000 heats life for LD2 shop which does not have any slag splashing feature.

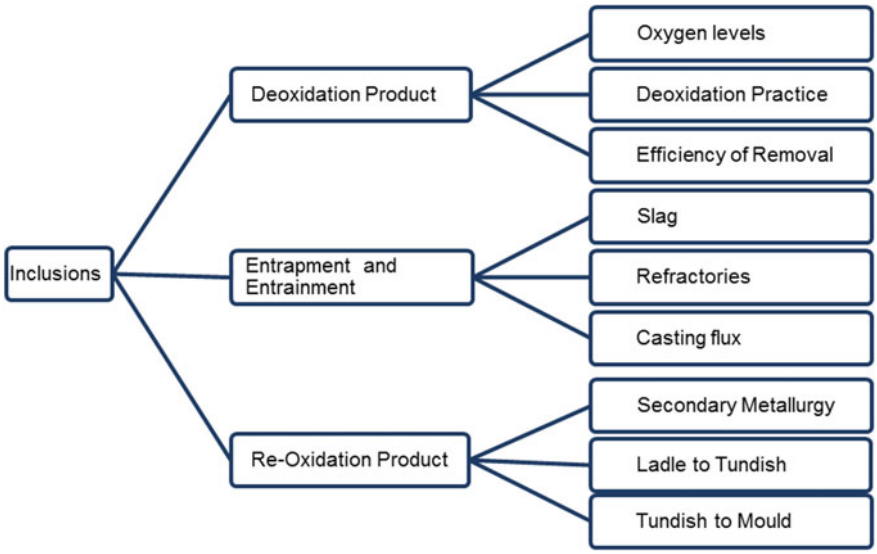

Fig. 2 Sources of oxide inclusions

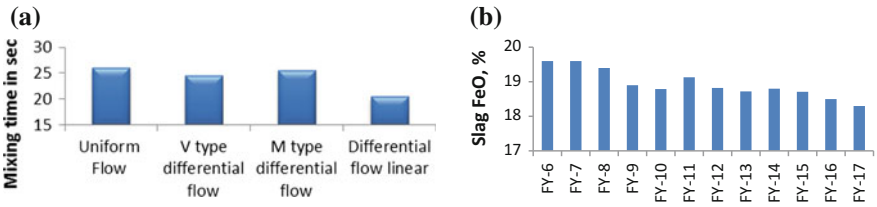

Fig. 3 **a** Comparison of mixing time at LD—bottom blowing tuyere configuration **b** trend of LD slag FeO over the years

In addition to keeping the elements active till the end of the campaign, a post blow stir of less than one minute is ensured to push the slag and metal closer to equilibrium resulting in lower dissolved oxygen of less than 800 ppm. All high-strength grades are preferentially made in converters with lower life and more number of active bottom elements.

2.2 Deoxidation Product—Deoxidation Practice

There are two opposing practices employed by steelmakers in reducing the alumina inclusions during deoxidation.

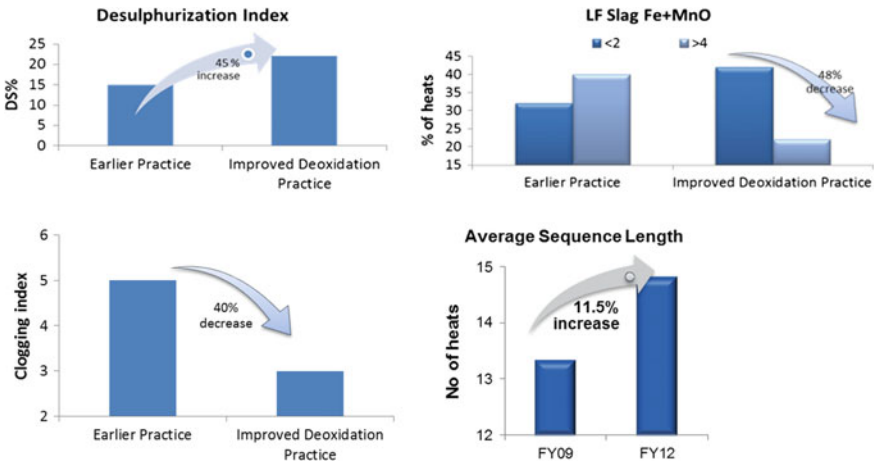

Fig. 4 Impact of improved deoxidation practice on clogging index and desulphurization Index

- Reduce aluminium (Al) addition at tap so that other elements and natural agitation reduce the dissolved oxygen and trim the required amount of Al at the secondary metallurgy stations later. The logic is that if Al is added later, fewer inclusions will form resulting in fewer inclusions to be floated out.
- Maximize Al addition at tap so that large alumina inclusions are formed which are easier to float out. Also, the violent agitation at tap will ensure that the alumina-rich slag is formed quickly which improves desulphurization. This practice affords longer time for alumina inclusions to float out in subsequent ladle furnace (LF) treatment if further Al-wire addition is not done towards the end of LF [3, 4].

Both approaches were tried with the de-sulphurizing index (Sulphur drop at ladle furnace), frequency of clogging and tundish life (Fig. 4) as a surrogate indicator for cleanliness of steel at casting. It was found that option 2 was better for steel cleanliness.

2.3 *Deoxidation Products—Efficiency of Removal*

Floatation of deoxidation products depends primarily on the following:

(i) Size and morphology of inclusions
(ii) Rinsing/stirring practices employed
(iii) Time provided to the deoxidation product to float out.

2.3.1 Size and Morphology of Inclusions

The studies by various researchers indicate that larger clusters of inclusions are formed when deoxidation is done at higher oxygen content of steel (during tapping) and dendritic alumina inclusions [5]. Studies at Tata Steel Ltd metallography labs suggest similar phenomenon for all categories of steel.

2.3.2 Rinsing and Stirring Practices

Literature also suggests that stirring practices have an effect on the size and floatation of the inclusions

- Violent agitation of the melt results in the Al_2O_3 inclusions combining together into larger inclusions [6]
- Gentle rinsing (ripple) of the melt towards the end of treatment results in optimal inclusion floatation
- Desulphurization requires a good interaction between the slag and metal and hence violent agitation is desired.

High-strength steels require a low sulphur as well as low inclusion rating and hence the requirements are contradictory. Hence, a combination of the two strategies is desirable.

Extensive CFD (Computational Fluid Dynamics) studies with double porous plug have been done to improve floatation of inclusion and one of steel melt shops has ladles designed with a double porous plug to enhance the mixing and floatation. This has further enhanced desulphurization and inclusion floatation [7] (Fig. 5).

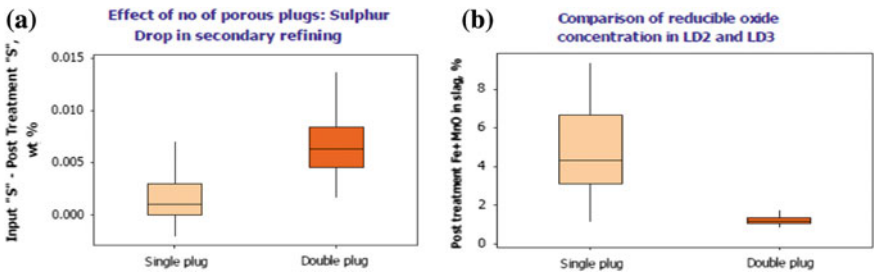

Fig. 5 Impact of single and double porous plug on **a** sulphur drop **b** reducible oxides

2.3.3 Time for Floatation

There is a direct correlation in the incidences of clogging and the time provided after last addition of aluminium. This implies that the period of ripple purging after the last addition of Al is a critical process variable for cleanliness for all types of steels and more so for steel requiring higher strength.

3 Entrainment and Entrapment of Inclusions

Large macro-inclusions in steel are typically introduced due to entrainment and/or entrapment of refractory materials, slag or casting powder. These are specially deleterious as they open up during subsequent metal working and if undetected can lead to catastrophic failure.

3.1 Inclusions from Refractory

Tata Steel, over the years, has tried a number of ladle refractories, such as dolomite, tar dolomite, mag carbon and spinel, both with a view to increase ladle life as well as to prevent entrainment of inclusions from refractories.

Tata Steel started with MgO spray tundishes but this was suspected to contribute to hydrogen pickup as well as inclusions. The lining has since then been changed to MgO-based dry vibratable mass which was without water, and due to the uniformity of application resulted in less entrainment.

3.2 Slag Entrainment

Extensive CFD models were run both by Tata Steel R&D as well as Refractory suppliers to arrive at the ideal tundish configuration with a view to reduce the possibility of entrainment of inclusions and to improve inclusion floatation.

3.3 Inclusions from Casting Flux

(i) Immersion Depth

Tata Steel slab casters had a very low immersion depth of 150 mm which implied large-scale entrainment of casting flux inclusions. To mitigate this initially, the port angle of the SEN was modified. Compared to normal SEN, casting with 15°down port SEN revealed relatively stable mold level and stopper position showed encouraging results with respect to severity and occurrence of sliver in auto exposed grade Fig. 6a.

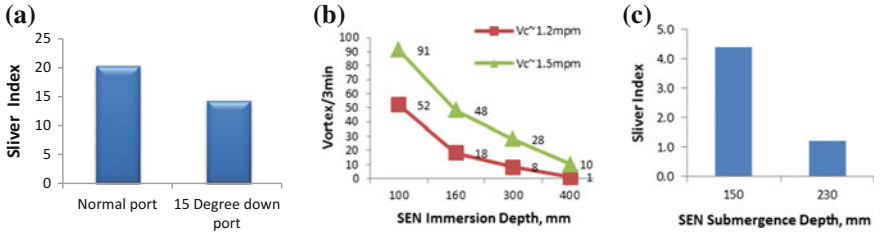

Fig. 6 **a** Impact of port angle on sliver index **b** result of water modelling. **c** Impact of increase in submergence depth on sliver index

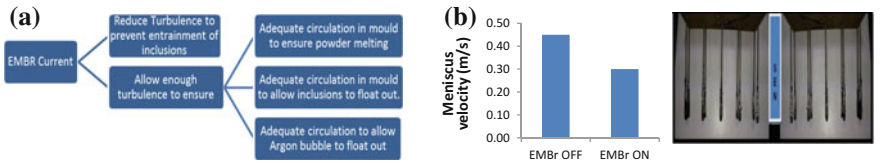

Fig. 7 **a** Optimizing EMBR Parameters **b** evaluation of meniscus velocity through nail board for EMBR optimization

However, the results obtained by these modification showed improvements but were inadequate for critical steels grades such as HSS. Subsequently, an in-house modification of tundish car was carried out to increase the immersion depth from 150 to 230 mm Fig. 6b, c.

(ii) EMBR

Tata Steel slab caster 1 has been installed with a Flow Control mould (FC mould) to prevent macro-inclusion entrapment due to turbulence in mould. The FC mould generates two independent static magnetic fields, one field at meniscus level to control the meniscus metal flow speed and turbulence while the second field at the bottom of the mould controls the penetration depth of the steel jets from the casting nozzle. The higher the metal flow speed and turbulence, the greater will be the braking force, i.e. the FC mould is to a large extent self-controlled.

A dramatic decrease in the incidences of sliver was observed post the installation of EMBR. However, EMBR currents have to be fine-tuned to achieve two opposing requirements. To this end, nail board studies to optimize the parameters are continuing [8] (Fig. 7).

4 Reoxidation of Steel

The major sources of reoxidation occur during secondary metallurgy, transferring steel from ladle to tundish and from tundish to mould. Clog material collected from SEN was analysed and observed with 2–5 μm pure alumina grains, linked by spinel and alumina bridges (Fig. 8).

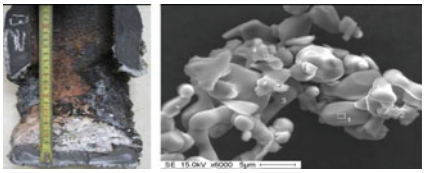

Element	1	2	3	4	Oxides	1	2	3	4	XRD
OK	36.6	33.8	35.6	35.9		Alumina	Spinel	Spinel	Alumina	
AlK	63.4	48.5	53.3	57.7	Al2O3	100	76.2	84.6	91.8	Corundum
FeK				2.7	FeO					
MgK		15.8	11.1	3.8	MgO		21.8	15.4	5.3	Spinel
MnK		1.9			MnO					

Fig. 8 EDS analysis of clog material

4.1 Secondary Metallurgy

In earlier section of this paper, slag doctrine and ladle refractory have been talked about which also take care of reoxidation in secondary metallurgy operations.

4.2 Ladle to Tundish

Reoxidation products are transported to casting channel by steel stream and contribute to clogging. The steps having a strong influence are:

- Ladle draining and slag control
- Sealing and cleaning of shroud
- Opening of the new ladle
- Tundish sealing.

The tundish skull after casting was collected and analysed. It was around 75-mm thick having traces of MgO, Al_2O_3 and CaO which confirms slag entrainment. Based on this revelation, ladle bottom design was modified from flat to step type. AMEPA setting was also optimized to minimize the slag depth in tundish.

Oxygen lancing of shroud between heats as cleaning practice is adopted as a normal procedure. However, the FeO, as a result of cleaning, discharged into tundish and reacts with Al in steel to form alumina. Practice of shroud cleaning was changed, the debris is now released outside tundish or oxygen cleaning is done in stand.

Opening of ladle shroud is not submerged; resulting in intermixing of slag with incoming stream causing in huge reoxidation product generation. Tata Steel along with supplier developed bell-type submerged shroud and trials are being carried out with submerged opening in one of the caster.

4.3 Tundish to Mould

Another major source for reoxidation is the air ingress during steel flow from tundish to mould. A new ultimate SEN quick changer 'JUQC' for stopper control system was developed along with supplier to address this concern. This new system has multiple micro-holes provided on top to purge inert gas to prevent alumina built

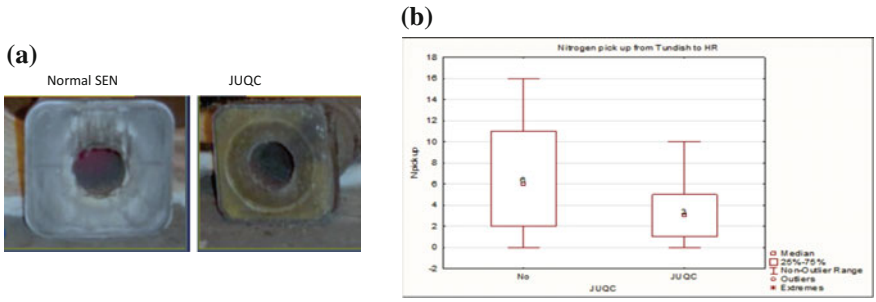

Fig. 9 Shows **a** the earlier and JUQC after service and **b** comparison of nitrogen pickup from tundish to product

up between upper nozzle and stopper. The slide gate plate material applied on bottom and inert gas purge channel is provided to eliminate air ingress. In addition to this, an anti-oxidation material on the top face provides resistance against oxidization and abrasion. Introduction of new system also showed reduction in nitrogen pickup from tundish to product (Fig. 9).

5 Part II—Approach Towards Sulphides and Nitrides

Most AHSS steels use alloys like Mn, Ti, V, Nb and Cr to achieve higher strengths. These alloys have a tendency to form harmful inclusions or precipitates which enhance hot/cold cracking during forming which defeats the purpose of producing AHSS steels. Tata Steel has experienced problems with sulphides and nitrides of these elements.

5.1 Sulphides

A common problem with high-strength and advanced high-strength steel is the segregation of alloying elements along the centerline of slabs which lead to cracking during forming (Fig. 10). While technological interventions such as electromagnetic stirring and Dynamic Soft Reduction are available, the approach of Tata Steel to mitigate segregation is by maintaining the basic conditions during continuous casting, viz.

- Lowering sulphur in steel
- Superheat and casting speed control
- Segment health, roll gap and misalignment control
- Tapering of segment gap
- Adjusting secondary cooling intensity
- Introduction of cooling in horizontal segments.

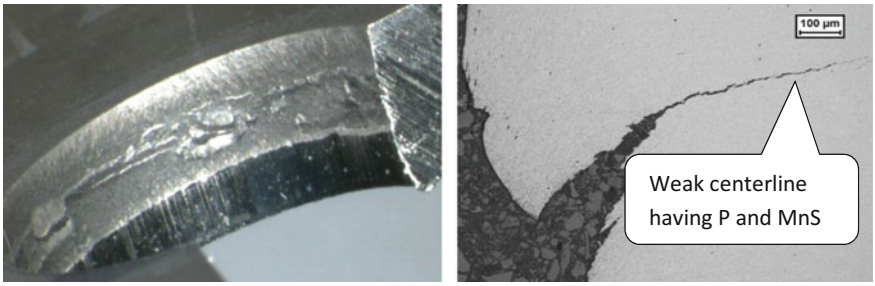

Fig. 10 Centerline segregation in HS 800

The best way of avoiding formation of MnS is to reduce the sulphur in steel. Precaution like hot metal desulphurization, clean scrap and good slag making at ladle furnace is done for ensuring sulphur level below 50 ppm in all AHSS grades. Superheat and segment gap is maintained through SARCLAD for achieving low segregation index.

It was experienced that secondary cooling can influence segregation to a great extent. In case the cooling is too intense, localized bridging can result which can be associated with segregation as the solute does not get any opportunity to circulate in the liquid core. Also in case of no cooling in the horizontal segments, the solidification rate slows down and more segregation is seen. Trials at the slab casters with these opposing strategies are going on and results are encouraging. Figure 11 shows sulphur print before and after the improved cooling strategy.

5.2 Nitrides

The splitting was experienced during rolling and subsequent processing of high tensile grades. Fractograph revealed bimodal distribution of shear dimples. Ridges and facets found on the inner-wall of large dimples. Large dimples were associated with TiN particles at the core (Fig. 12). Therefore, nitrogen levels in these steel grades should be kept minimum to prevent any deleterious coarse TiN formation and therefore ineffective austenite pinning during reheating. Additionally, higher nitrogen also makes steel susceptible to transverse cracks which result in surface defects on product.

Fig. 11 Centre line segregation before and after improved cooling strategy

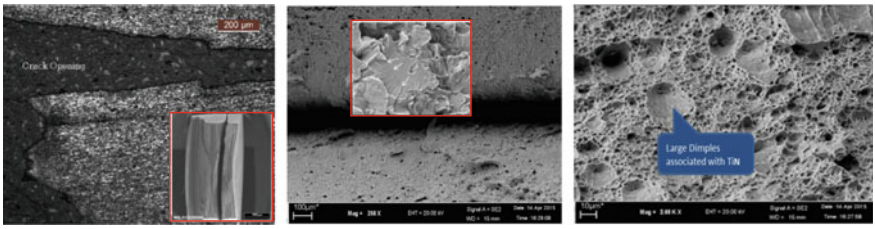

Fig. 12 Spillting in HS 800: large TiN shown in fractograph of as-rolled sample

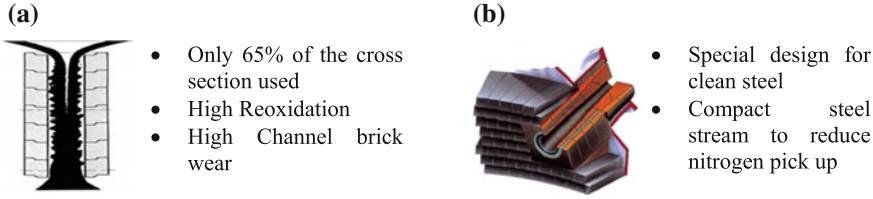

Fig. 13 **a** Cylindrical tap hole design **b** ISOJET C tap hole design

Better control of blow by hood pressure control, argon through bottom tuyeres and good end point control is done to reduce nitrogen level.

It is well known that level of nitrogen pickup is dependent on the coherence of tapping stream—a spraying stream increases the incidence of nitrogen pickup. To this end, Tata Steel is going in for the ISOJET C. System supplied by RHI which has a more coherent tapping stream as compared to purely cylindrical systems (Fig. 13a, b).

Nitrogen pickup from ferro alloys is also restricted by limiting alloy sources which have low nitrogen. Many of the alloys added for steelmaking typically do not have nitrogen specified for conventional alloys. However, it has been observed that this is very important for attaining low nitrogen specially for AHSS. Furthermore, care is taken in secondary metallurgy stations and at caster to keep nitrogen pickup less than 2 ppm.

6 Conclusion

While a lot of work has been published on the basic alloy design for high-strength steels, adequate attention to the inherent cleanliness of the steel also has to be ensured if components are not to fail during forming and subsequent service. Therefore, it is equally important to consider strategies for ensuring steel cleanliness as well as desired precipitates. The strategies for cleanliness have an added advantage of reducing the challenges of steelmaking and casting so that large volumes of these steels can be made commercially available.

References

1. G. Abbel, Internal Report on In or On? – About inclusion entrapment in slabs, Research & Development/IJmuiden Technology Centre, (2014)
2. V. Singh, S.N. Lenka and S.K. Ajmani, Chaitanya Bhanu and Sudhansu Pathak, ISIJ International, 49(12) (2009), 1889–1894
3. C.-H. Keum, W.-W. Huh, S.-C. Shim and J.-H. Park, Electric Furnace Conference Proceedings, (2001), 547–555
4. S.F. Mayowa, Luleå University of Technology, Master Thesis in Minerals and Metallurgical Engineering, Improvement of desulphurization process by slag composition control in ladle furnace, Professor Bo Björkman (LTU), Sven-Ol of Ericsson(OVAKO), (2009)
5. L. Zhang and B.G. Thomas, 7th European Electric Steelmaking Conference, Venice, Italy, May 26–29, (2002), 2.77–2.86
6. R. Dekkers, B. Blanpain, P. Wollants, F. Haers, C. Vercruyssen and B. Gommers, Iron making and Steelmaking, 29(6) (2002), 437–444
7. M.K. Sardar, S. Mukhopadhyay, S. Majumder, S. Mallick and R.K. Singh, Canadian Metallurgical quarterly, 45(2) (2006), 175–180
8. P. Palai, Internal report on Optimization of EMBR current through Nail board Experiment, Tata Steel Jamshedpur, (2014)

Macrosegregation of Multicomponent Steel in Round Billet Continuous Caster

Saurabh Mangal, Himanshu Nirgudkar and Gerald Tennyson

Abstract During solidification, macrosegregation of alloying elements results in inhomogeneous properties of cast product. Segregation level of alloying elements is different because of the difference in solubilities. It is required to study the distribution of all alloying elements as it affects microstructure evolution during subsequent processes. In the present study, a numerical model is developed to predict the segregation of multicomponent (Fe–C–Mn–Si) alloy steel during solidification in a round billet continuous caster. The distribution of individual alloying elements is calculated by solving coupled turbulent flow, energy and species conservation equations. Solidification is considered to be governed by Lever rule and the liquidus temperature varies with local composition. Segregation index is then determined by calculating ratio of final to initial carbon equivalent at the center of cast billet. Casting speed and pouring temperature are parameterized to study their effect on solidification profile and segregation.

Keywords Continuous casting · Numerical modeling · Computational fluid dynamics (CFD) · Solidification · Macrosegregation

1 Introduction

Advanced high-strength steels (AHSS) contain high-strength phases such as martensite or bainite along with retained austenite to improve strain hardening characteristics. Manganese being an austenite stabilizer is added to AHSS to retain more amount of austenite. Silicon is added as it retards carbide formation and also promotes ferrite transformation. The phase transformation characteristics are dependent on the local composition. As a result, it is important to predict the segregation profile of all alloying elements so that the final microstructure can be predicted correctly.

S. Mangal (✉) · H. Nirgudkar · G. Tennyson
TCS Research, Tata Research Development and Design Centre, Pune, India
e-mail: mangal.saurabh@tcs.com

T. K. Roy et al. (eds.), *Advanced High Strength Steel*, Lecture Notes in Mechanical Engineering, https://doi.org/10.1007/978-981-10-7892-7_21

Segregation is caused because of the difference in solubility of the alloying element in the solid and liquid phases. The segregation of different alloying elements in a multicomponent system depends on the partition coefficient of each element and the diffusivity of the element in the solid and liquid phases. Macrosegregation occurs at a scale comparable to the dimensions of the product due to continuous rejection—of solute by the solidifying front into the bulk liquid. This solute is redistributed by diffusion as well as by convective flow pattern in the liquid. The fluid flow is affected by the inertia force of the liquid, thermal, and solutal buoyancy induced flow, flow induced by thermal contraction, and any external flow modifier such as electromagnetic stirring. It is difficult for a plant operation to do design changes in the equipment for reduced segregation. Thus, the final macrosegregation profile across the billet can be modified by controlling the operating conditions such as casting speed, superheat, and heat extraction rates.

There are numerous studies on segregation and in Fe–C systems [1–4]. Studies related to multicomponent alloy segregation are limited and largely restricted to bounded domains [5]. Extended studies for predicting multicomponent segregation in steels pertaining to continuous casting are not present to the best of the authors' knowledge. This study attempts to propose a comprehensive model to predict segregation during continuous casting of Fe–C–Mn–Si in a round billet continuous caster by varying the casting speed and the superheat. The distribution of alloying elements along with evolution of solidification is analyzed by taking into account the effect of turbulence and density differences caused by temperature and concentration gradients on fluid flow. Segregation index of the cast billet is calculated based on the chemical composition at the center.

2 Mathematical Model

Coupled fluid flow, heat and solute transport equations are solved to predict solidification and macrosegregation in a round billet caster. The major assumptions of the model [6] are:

1. The casting process is assumed to be in steady state.
2. Solidification is assumed to occur in equilibrium condition.
3. Constant physical properties are assumed.
4. Effects of fluctuation and argon flow in mold are not considered.
5. Heat absorption/release during phase transformation reaction is neglected.
6. Darcy's law is applied as flow resistance through mushy zone.

The model solves conservation equations of mass, momentum, energy, and solute concentration. Solidification is modeled by an enthalpy-porosity technique [7]. Enthalpy balance based analysis of liquid fraction is used to track the movement of the melt interface. The mushy zone is modeled as a pseudo-porous medium. The porous source term in the momentum equation [1] is:

$$S_P = \frac{(1-f_l)^2}{f_l^3+\epsilon}\cdot A_{\text{mush}}\left(\overrightarrow{v}-\overrightarrow{v_s}\right), \quad A_{\text{mush}} = \frac{\mu}{K_P}, \quad K_P = \frac{180}{d^2} \tag{1}$$

where f_l is liquid fraction, $\vec{v}$ is velocity, $\overrightarrow{v_s}$ is pull velocity, μ is viscosity, K_P is permeability coefficient, and d is secondary dendritic arm spacing.

The change in density of liquid because of temperature and concentration differences is taken into account using Boussinesq approximation. The species conservation equation is solved for C, Mn, and Si separately considering respective diffusivities of each element in solid and liquid phase. The conservation equation for the ith species is:

$$\nabla\cdot\left[\rho\left(f_l\overrightarrow{v_l}c_{l,i}+f_s\overrightarrow{v_s}c_{s,i}\right)\right] = \nabla\cdot\left[\rho\left(f_l D_{l,i}\nabla c_{l,i}+f_s D_{s,i}\nabla c_{s,i}\right)\right] \tag{2}$$

where $D_{l,i}$ and $D_{s,i}$ are the diffusivity of ith element in liquid and solid, respectively.

The liquid fraction is calculated by Lever Rule as follows:

$$\begin{bmatrix} f_l = 0 & \text{if } T < T_{\text{solidus}} \\ f_l = 1-\frac{1}{1-P}\cdot\frac{T-T_{\text{liquidus}}}{T-T_m} & \text{if } T_{\text{solidus}} < T < T_{\text{liquidus}} \\ f_l = 1 & \text{if } T > T_{\text{liquidus}} \end{bmatrix} \tag{3}$$

$$T_{\text{liquidus}} = T_m + \sum_i\left(\frac{T_{e,i}-T_m}{C_{e,i}}\right)\cdot C_i,$$

$$T_{\text{solidus}} = T_m + \sum_i\left(\frac{T_{e,i}-T_m}{C_{e,i}}\right)\cdot\frac{C_i}{k_{p,i}},$$

$$P = \frac{T-T_{\text{liquidus}}}{T-T_{\text{solidus}}}$$

where T_m is the melting temperature of pure iron and k_p is the equilibrium partition coefficient.

Turbulence is modeled using realizable k–e model and the wall effects are captured using enhanced wall treatment [8]. The conservation equations are solved numerically by control-volume-based finite volume method using ANSYS Fluent®.

2.1 Geometry Details

The geometry of round billet caster considered in the present study is shown in Fig. 1. To reduce the computational cost, the round billet is modeled as 2D axisymmetric domain. The details of the various zones considered are tabulated in Table 1.

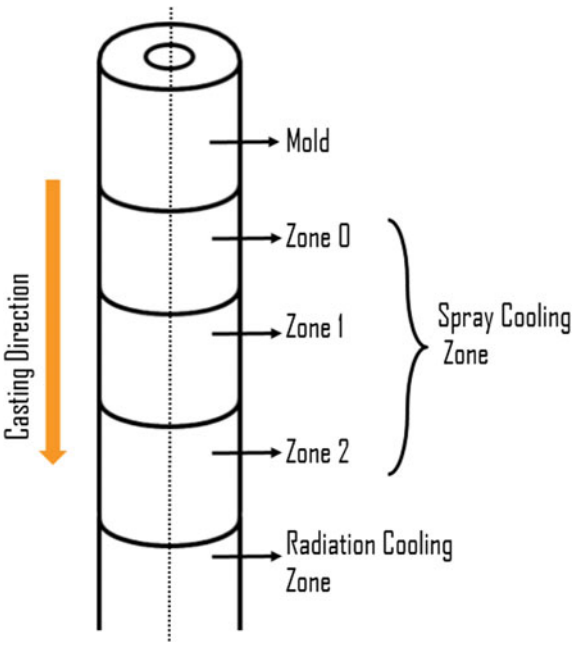

Fig. 1 Schematic diagram of round billet

Table 1 Geometry details

Billet diameter	0.146 m
Length of mold	0.741 m
Length of spray zones	
Zone 0	0.431 m
Zone 1	1.121 m
Zone 2	3.874 m
Total simulated length	20 m

2.2 Boundary Conditions

A constant inlet velocity calculated based on casting speed by applying mass flow rate conservation was specified as inlet condition. The values of turbulent kinetic energy (k) and the rate of turbulent energy dissipation (ϵ) at the inlet were approximated using semiempirical relations based on inlet velocity [9]. The inlet temperature was taken to be constant and equal to the pouring temperature. The concentration of elemental species was also taken to be constant according to the composition of molten steel. At outlet of the caster, zero normal gradient of the variables was specified as the boundary condition. The walls were considered to be

moving with speed equal to the casting speed. The heat transfer from mold and spray zone walls was through convection and thereafter the billet was cooled by radiation heat transfer.

$$\begin{aligned} q_{\text{convection}} &= h_s(T_S - T_w), \\ q_{\text{radiation}} &= \sigma \epsilon_s \left(T_S^4 - T_a^4\right) \end{aligned} \tag{4}$$

3 Validation

The solidification model was validated with the work of Aboutalebi et al. [1] by comparing the evolution of solidification profile along the axial direction. For this purpose, solidification of low carbon steel (0.1 %C) in a round billet caster of 115 mm diameter was modeled by considering an axisymmetric domain of 3.25 m length. The casting of billet was done at a speed of 1.8 m/min. The results of the solidification profile obtained from the present simulation compare well with those predicted by Aboutalebi et al. [1] and experimental results of Ushijima [10] and are shown in Fig. 2.

The macrosegregation model was validated for different binary alloys systems such as Fe–C system by Singh and Basu [11], aqueous NH_4Cl solution by Voller et al. [7], and Pb–Sn system by Ahmad et al. [12]. Currently, Fig. 3 shows validation of results for segregation of Pb–48Sn alloy. In this work, a rectangular cavity of 0.1 m × 0.06 m is taken into consideration and heat is extracted through convection boundary condition at left wall. In Fig. 3, the numbers indicate % change of composition of Sn after 400 s. It can be seen from figure that segregation predicted by the current model matches with the result predicted by Ahmad et al. [12].

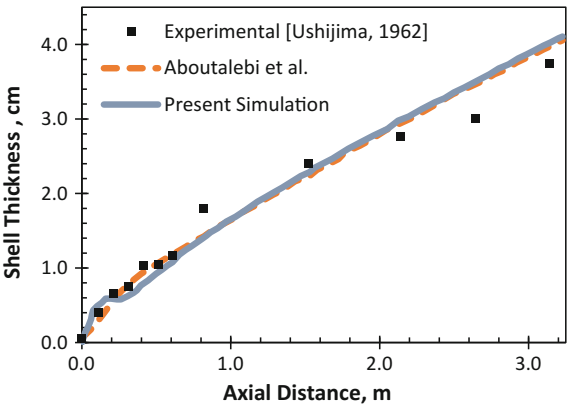

Fig. 2 Comparison of predicted solidified shell thickness for a round billet caster

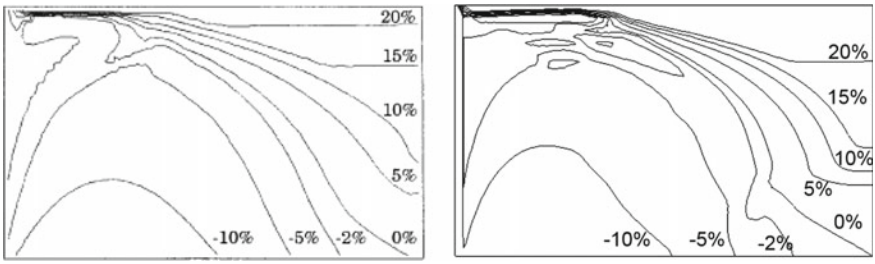

(a) Ahmad *et al.* predictions (b) Present simulation predictions

Fig. 3 Relative mass fraction of Sn variation after 400 s. **a** Ahmad et al. predictions, **b** present simulation predictions

4 Results

In the present study, steel of composition 0.15 %C, 1.38 %Mn, and 0.29 %Si was cast into a round billet of 146 mm diameter. The carbon equivalent based on the nominal composition at the inlet was 0.428% using the empirical relation $C_{eq} = \%C + \frac{\%Mn + \%Si}{6.0}$ [13]. The material properties of steel [1] are given in Table 2. The properties of solute elements such as partition coefficient and diffusivity were taken from Schneider and Beckermann [5]. The heat transfer coefficients corresponding to the casting speed of 3.0 m/min and superheat of 32 °C are shown in Table 3 [6].

The results obtained for a casting speed of 3.0 m/min and pouring temperature 1547 °C are given in Figs. 4 and 5. The liquidus temperature of steel is 1515 °C, resulting in a superheat of 32 °C. Figure 4a, shows the growth of shell along casting direction corresponding to a liquid fraction of 0.3. Figure 4b shows contour of liquid fraction of half-axial plane of caster up to a distance of 1.0 m from meniscus. The shell thickness at mold exit is found out to be 11.5 mm and the metallurgical length is 15.7 m.

The segregation profile of C, Mn, and Si along the radial direction of cast billet is shown in Fig. 5a. A rise in composition is observed at the center of billet because of solute redistribution. As the partition coefficient of carbon is highest, the maximum segregation is observed for carbon. In addition, normalized carbon equivalent is also plotted in Fig. 5a. The value of carbon equivalent of cast billet is normalized

Table 2 Material properties

Density (kg/m^3)	7200.0
Specific heat (J/kgK)	735.0
Thermal conductivity (W/mK)	34.6
Viscosity	6.2E − 3
Latent heat (J/kg)	271,954

Table 3 Heat transfer coefficients

Region	Heat transfer coefficient ($Wm^{-2}K^{-1}$)
Mold	1700
Zone 0	1500
Zone 1	1000
Zone 2	600

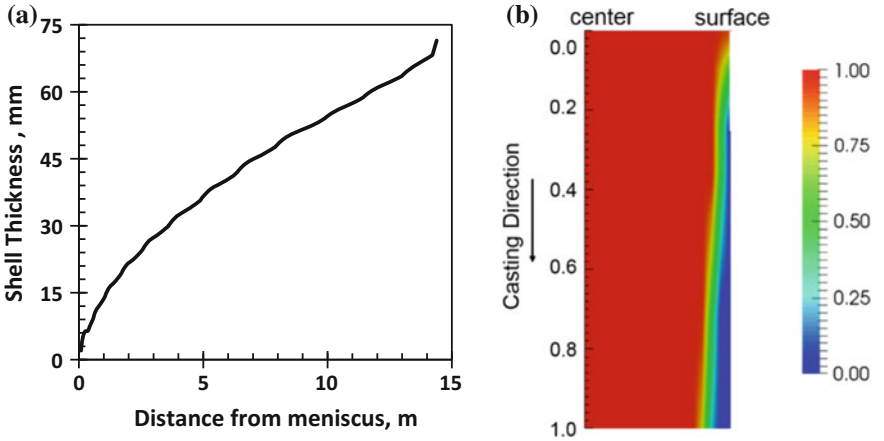

Fig. 4 **a** Shell thickness along length of caster for casting speed 3.0 m/min, **b** liquid fraction contour of caster half-axial plane

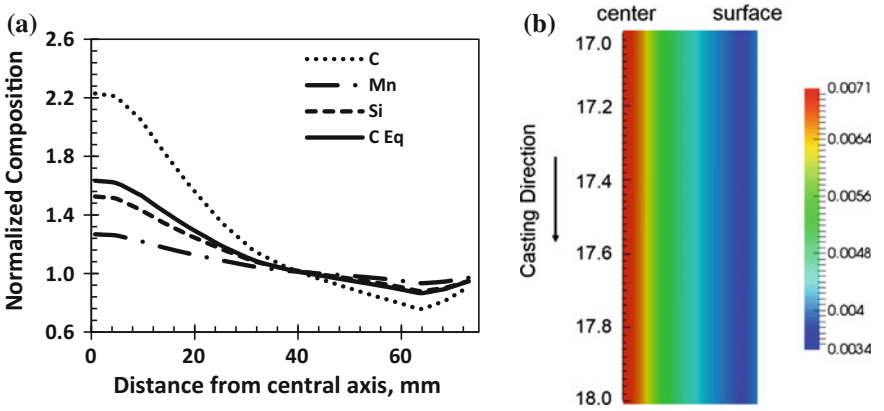

Fig. 5 **a** Macrosegregation of alloying elements along radial direction, **b** carbon equivalent contour of caster half-axial plane

with respect to initial carbon equivalent. The normalized carbon equivalent at the center of the billet is referred to as segregation index. Thus, the segregation index for casting speed 3.0 m/min and 32 °C superheat is 1.63. Figure 5b shows contour

of carbon equivalent of half-axial plane of caster from a distance of 17.0 to 18.0 m. The maximum value 0.0071 carbon equivalent is achieved in center of caster and minimum carbon equivalent obtained at surface is 0.0034.

In order to study the effect of process parameters on the segregation index of the billet, a parametric study was carried out by varying the casting speed and superheat. The heat transfer coefficients in different zones are considered to be linear function of casting speed and superheat. The weightage to casting speed and superheat was decided on the basis of experimental data provided by Chaudhuri et al. [14]. In their work, it was observed that with change in casting speed of 0.2 m/min, heat transfer coefficient changed by 50 W/m^{2}K. However, up to 40 °C of superheat, there was less variation in heat transfer coefficient.

Figure 6a shows the effect of casting speed on metallurgical length and segregation index for a constant superheat of 32 °C. It can be seen that both metallurgical length and segregation index increase with an increase in casting speed. As the casting speed increases, more energy is convected in the casting direction which results in increase in the metallurgical length. The thermal gradients also increase because of high cooling rates which facilitates faster movement of solidification front leading to more solute rejection. The rejected solute will be carried with flow toward center of billet increasing the overall segregation. However, this was not the case with superheat. The effect of superheat on metallurgical length and segregation index is shown in Fig. 6b. Superheat was varied between 20 and 40 °C at a constant casting speed of 3 m/min. It was observed that there is no significant change in metallurgical length as well as segregation index with change in superheat. The reason is that in the given range of superheat, thermal gradients formed are almost same because of less variation of heat transfer coefficients. Hence, solute rejection occurs in similar manner resulting in less variation in segregation index with superheat. Though macrosegregation reduces with decrease in casting speed, it hampers the productivity. An optimization study is called for to take informed decisions on casting speed for maximizing productivity and minimal macrosegregation.

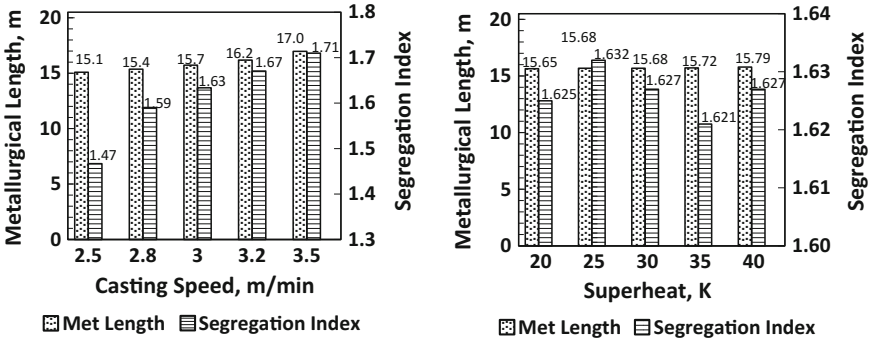

(a) Variation with casting speed

(b) Variation with superheat

Fig. 6 Effect of process parameters on segregation index and metallurgical length **a** variation with casting speed, **b** variation with superheat

5 Conclusion

A numerical model to predict solidification and macrosegregation during continuous casting of a multicomponent Fe–C–Mn–Si steel is presented. The model solves coupled fluid flow, heat, and solute transport equations including thermal and solutal buoyancies. The multicomponent model was able to capture the segregation of the individual solutes and their effect on the overall segregation level. Higher segregation levels and metallurgical lengths were observed for higher casting speeds due to enhanced cooling and solidification rates. Whereas with change in superheat up to 40 °C, there is no significant variation in segregation index and metallurgical length because of similar cooling conditions.

References

1. M.R. Aboutalebi, M. Hasan, R. Guthrie, Metallurgical and Materials Transactions B 26(4), (1995), 731–744
2. Y. Zheng, M. Wu, A. Kharicha and A. Ludwig, in IOP Conference Series: Materials Science and Engineering, (IOP Publishing, 2016), 143, 012032
3. H. Yang, X. Zhang, K. Deng, W. Li, Y. Gan and L. Zhao, Metallurgical and materials transactions B, 29(6) (1998), 1345–1356
4. C. Beckermann, International Materials Reviews, 47(5) (2002), 243–261
5. M. Schneider and C. Beckermann, Metallurgical and Materials Transactions A, 26(9) (1995), 2373–2388
6. M. Shamsi and S. Ajmani, Steel Research International, 81(2) (2010), 132–141
7. V.R. Voller, A. Brent and C. Prakash, International Journal of Heat and Mass Transfer, 32(9) (1989), 1719–1731
8. T.H. Shih, W.W. Liou, A. Shabbir, Z. Yang and J. Zhu, Computers & Fluids, 24(3) (1995), 227–238
9. K. Lai, M. Salcudean, S. Tanaka and R. Guthrie, Metallurgical Transactions B, 17(3) (1986), 449–459
10. K. Ushijima and Tetsu-to-Hagane, 48(6) (1962), 747–752
11. A. Singh and B. Basu, Metallurgical and Materials Transactions B, 26(5) (1995), 1069–1081
12. N. Ahmad, J. Rappaz, J.L. Desbiolles, T. Jalanti, M. Rappaz, H. Combeau, G. Lesoult and C. Stomp, Metallurgical and Materials Transactions A, 29(2) (1998), 617–630
13. M. Bruneau, C. Uang and A. Whittaker, Ductile design of steel structures, McGraw-Hill Professional, ISBN 978-0-07-008580-0, (1998), 31
14. S. Chaudhuri, R.K. Singh, K. Patwari, S. Majumdar, A. Kumar Ray, A.K.P. Singh and N. Neogi, ISA transactions, 49(1) (2010), 121–129

Production of High-Strength Plates Through New Plate Mill at RSP

Sanjay Kumar Gupta, Suman Kant Thakur, Kuntal Patwari, Manish Kumar Singh, Abdhesh Prasad, Amit Pradhan, Somnath Ghosh and Basudev Mishra

Abstract The production of value-added plates with stringent international standards has been established at RSP, Rourkela through new plate mill. The mill is equipped with state-of-the-art technology to produce up to 4.2 m wide plates with close tolerances. For enhancing the mill capacity, wide range of special steel grades is identified to produce in the dimensions of 6–100 mm (thickness), 1500–4100 mm (width) and 6300–15,000 mm (length) with superior surface finish. The necessary high-quality thick and wide defect free slabs (both internal & external) are cast at newly installed Slab Caster-3. The productivity and quality of the liquid steel has been ensured by the successful implementation and production from new Blast Furnace-5, BOF-3 and RHOB. This paper elaborates the efforts made for improvement and optimization of steelmaking and rolling practices for the production of special quality high-strength plates such as IS 2062, E350/E410/E450 and API X70, etc. The major modifications were carried out in each stage of its production, i.e., BOF steelmaking and secondary refining to optimize the quality of steel with respect to lower residue of sulfur and phosphorus and rolling of slabs in the plate mill. Reduction in UST failure of the plates has been observed for the liquid steel processed through newly commissioned RHOB at the shop. The rolling parameters were optimized to achieve the desired mechanical properties, however ultrasonic soundness of the plates were found to be more dependent on clean steel than the higher reduction schedule given during initial passes at plate mill.

Keywords High strength steel · Thick and wide plate · Sulphur and phosphorus control · Dynamic soft reduction · RHOB

S. K. Gupta (✉) · S. K. Thakur · A. Prasad · S. Ghosh · B. Mishra
RDCIS, SAIL, Ranchi 834001, India
e-mail: skgupta@sail-rdcis.com

K. Patwari · A. Pradhan
RSP, SAIL, Rourkela 769001, India

M. K. Singh
RDCIS, SAIL, Rourkela 769001, India

T. K. Roy et al. (eds.), *Advanced High Strength Steel*, Lecture Notes in Mechanical Engineering, https://doi.org/10.1007/978-981-10-7892-7_22

1 Introduction

Rourkela Steel Plant (RSP) is one of the pioneering integrated steel plants owned by Steel Authority of India Limited (SAIL), India. It is an exclusive value-added flat steel producer engaged in production of HR coils, electrical steels, cold rolled (CR) sheets and coils and plates, and commands premium in the market. The process route for production of hot metal is blast furnace with about 80% sinter usage in the burden. Hot metal is pretreated in desulfurization stations before being used for steelmaking. Steelmaking process includes Basic Oxygen Furnace (BOF) route and steel is subsequently treated in off-line Ladle Furnaces (LFs) and RH degasser. Continuous casting of liquid steel is undertaken through existing as well as new slab casters. The slabs produced in steel melting shop (SMS) are rolled in hot strip mills and existing and new plate mills. Products from hot strip mill are utilized for rolling in cold mill for production of various grades of electrical steels, galvanized sheets, CR sheets and coils, etc. Plates are used for manufacturing SWPP pipes, ERW pipes, tin plates, etc.

1.1 Modernization Cum Expansion of RSP

With the growing demand of steel in domestic market, Indian steel industry is setting up new benchmarks in the utilization of new technologies. RSP has also expanded its production capacity to 4.2 mt per annum of crude steel to meet the market requirements. In the course of expansion, many new units with modern technologies have been augmented along with revamping of old units. The major new units with latest technologies added are: 7 m tall coke oven, a new sinter plant, Blast Furnace#5 with useful volume of 4060 m^3, 150 t BOF and 1 mt plate mill. The new units added at RSP have given it an edge in the competitive market with increased value-added product and lower cost of production with utilization of energy efficient process.

1.2 Steel Melting Shop

The present liquid steel production at RSP is achieved from both Steel Melting Shop-I and Steel Melting Shop-II. The major technological facilities in the above shops are given in Table 1. The shops have matching secondary refining units and casting facilities to take care of refining and casting of liquid steel.

Table 1 Major technological facilities in steelmaking and casting area

Sl no	Facilities	Plant configuration	
		SMS-I	SMS-II
1	Steelmaking facilities, no. x nominal heat size	2 × 66 t BOFs	3 × 150 t BOFs
2	Secondary refining units	1 × 66 t VOR 1 × 66 t VAR 1 × 66 t LF	1 × 150 t ARS 3 × 150 t LF 1 × 150 t RHOB
3	Continuous casting facilities	1 × 1 strand slab caster	3 × 1 strand slab caster

The new Basic Oxygen Furnace (3rd converter of SMS-II) with production capacity of 1.584 mt liquid steel per annum has been commissioned with facility of combined oxygen blowing from top and inert gas stirring (with Argon and Nitrogen) from bottom. To improve the quality of input hot metal, external desulfurization facility has been installed. Further, steel ladle refining facilities have also been upgraded with the addition of new RHOB along with existing 2 nos of ladle furnaces to produce high-quality steel.

1.3 New Plate Mill

The regular production at new plate mill at RSP started in April, 2015 with a production capacity of 1.0 mt per annum. The 4 Hi reversing mill is equipped with Level 2 roll gap setting, hydraulic automatic gauge control system, work roll bending, and shifting facilities. Schematic layout of the mill is shown in Fig. 1. One 3 point profile gauge and width meter are installed after the mill. Thereafter, accelerated cooling and hot leveler are provided. The hot leveler can operate in the plate temperature range of 550–900 °C. Further, online ultrasonic testing facility is provided to testing the internal soundness of the plates produced as per customer requirement. With the modern technology, value-added plates such as API, boiler quality, high-strength plates are being processed at RSP to cater the need of the special steel customers.

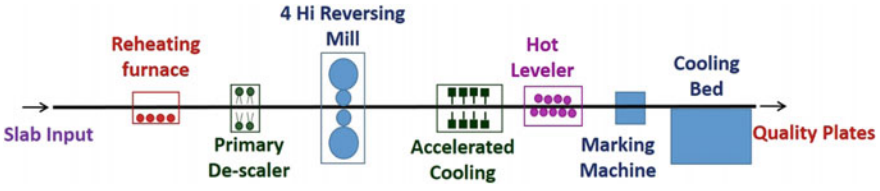

Fig. 1 Schematic layout of new plate mill

2 Production of High-Strength Plates

With the enhancement of mill capacity, a wide variety of special quality high-strength plates is identified to produce in the dimensions of 6–100 mm (thickness), 1500–4100 mm (width), and 6300–15000 mm (length) with superior surface finish. The ASTM specifications of these grades are given in Table 2. Microalloying elements like Nb, V, and Ti may be added singly or in combination to achieve the mechanical strength as given in Table 3. The total microalloying elements are restricted below 0.25%. The alloying elements like Cr, Ni, Mo, and B can be added as per the demand of the customer. The restriction of alloying elements Cr + Ni < 0.5% for E 600 and Cr + Ni < 0.6 for E650 is applied. Copper addition is generally done in the range of 0.2–0.35%. For such heavy steel plates, the demand for their higher strength, larger plate thickness, weld-joint characteristics, and so on has increased, and thus, enhancing steelmaking technologies has been the focus.

Even though, the higher permissible range for sulfur and phosphorus in steel specification, lower level of residues with respect to 'S' and 'P' is important to meet the stringent quality requirements for achieving defect free (both surface as well as internal) slabs. In the production of high-quality steels plates, the following technologies are needed in the steelmaking process: (1) Desulfurizing technology to lower sulfur to an ultra-low level, (2) Shape control of nonmetallic inclusions (3) Harmful inclusion eliminating technology, and (4) Center segregation and center porosity eliminating technology.

The micro-cracks propagate and expand along the finally solidified area in continuous casting, enriched with S, Mn, P, C, etc. in the center segregation zone [1, 2]. Therefore, to suppress the initiation and propagation of the cracks, high purification to the maximum extent possible, lowering of sulfur content to an ultra-low level in particular, and reduction of center segregation in continuous casting are necessary. Furthermore, coarse inclusions must be removed in the casting process as they can be the initiating points of hydrogen-induced crack.

Table 2 Specified chemical composition of ASTM grades of special quality plates

Grade designation	C	Mn	S	P	Si	CE	Mode of deoxidation
	Ladle Analysis, wt% max						
E 250	0.23	1.5	0.045	0.045	0.40	0.42	Semi-killed/killed
E 275	0.23	1.5	0.045	0.045	0.40	0.43	Semi-killed/killed
E 300	0.2	1.5	0.045	0.045	0.45	0.44	Semi-killed/killed
E 350	0.2	1.55	0.045	0.045	0.45	0.47	Semi-killed/killed
E 410	0.2	1.6	0.045	0.045	0.45	0.50	Semi-killed/killed
E 450	0.22	1.65	0.045	0.045	0.45	0.52	Semi-killed/killed
E 550	0.22	1.65	0.02	0.025	0.50	0.54	Semi-killed/killed
E 600	0.22	1.7	0.02	0.025	0.50	0.54	Semi-killed/killed
E 650	0.22	1.7	0.015	0.025	0.50	0.55	Semi-killed/killed

Table 3 Specified mechanical properties for ASTM grades of special quality plates

Grade	Tensile strength MPa min.	Yield strength MPa, min.			Percentage elongation GL = $5.65\sqrt{A_o}$ min.	Internal bend diameter, max.	
		<20 mm	20–40 mm	>40 mm		<25 mm (t)	>25 mm (t)
E 250	410	250	240	230	23	2	3
E 275	430	275	265	255	22	2	3
E 300	440	300	290	280	22	2	–
E 350	490	350	330	320	22	2	–
E 410	540	410	390	380	20	2	–
E 450	570	450	430	420	20	2.5	–
E 550	650	550	530	520	12	3	–
E 600	730	600	580	570	12	3.5	–
E 650	780	650	630	620	12	4	–

In recent years, the demand of heavy steel plates with higher strength, larger plate thickness, ultra-low temperature toughness, and so on has increased. In continuous casting, porosity defects are caused at the center of a cast slab owing to the solidification and shrinkage of molten steel. For the production of such thick plates, crimping of center porosity by rolling is becoming difficult. Therefore, countermeasures for the reduction of cast slab center porosity by soft reduction during casting became very important. In steelmaking, it is also required that the processing and casting of steel is performed in such a manner as to control the nonmetallic inclusion component to an aimed composition range and to disperse inclusions uniformly within a cast slab. Again, it needs to be mentioned that removal of coarse inclusions is of prime importance.

The new caster # 3 at RSP is equipped with a high reduction force bearing segment with high rigidity at the horizontal part, and by optimizing the casting condition with soft reduction, the compatible goal of reducing center segregation and center porosity with high productivity has been achieved. Furthermore, by incorporating refining approaches such as lowering sulfur to an ultra-low level and oxide metallurgy, steelmaking technologies that enable mass production of high-quality heavy plates have been established.

2.1 Steelmaking Measures

The process is characterized by the reduction of sulfur and phosphorous concentrations to the lowest possible level to obtain purity of the highest degree through desulfurization of molten iron by hot metal de-sulfurization (CaC_2/Mg based), effective dephosphorization in converter, followed by the secondary refining process at LF and RHOB. In these processes, control of inclusions (oxide metallurgy) is also conducted.

2.2 Control of Steel Sulfur

Hot metal tapped off a blast furnace contains about 0.03–0.05% of sulfur. It is desulfurized to a low level of <0.01% in the steelmaking process. In the refining process for very low-sulfur ~0.005% in steel, desulfurization is applied at two stages: (i) hot metal de-sulfurization before converter process (aim 'S': 0.005%) using co-injection of magnesium and calcium carbide reagents at 1:5 ratio and (ii) ladle steel desulfurization after converter blowing process. During stabilization of the process, most incidence of high sulfur reversal in the BOF was observed which was nullifying the impact of hot metal treatment. Sulfur reversal <0.005% was successfully established by improving slag skimming efficiency after hot metal de-sulfurization and use of good quality scrap (low S content).

Steel sulfur content is lowered in steel ladle by adopting the innovative slag engineering initiated from the tapping of steel from BOF. Modification in deoxidation practice from Si–Al killing to Al–Si killing helped to improve the slag basicity and the overall de-sulfurization efficiency. The fluidity of ladle slag is improved by using slag modifier. Trial is conducted to control the oxidation potential of the ladle top slag by the introduction of ferro-aluminum chips.

The processing of steel in ladle furnace with a strong stirring force improves molten steel cleanliness. The process is capable of securing a desulfurization ratio of ~60% and producing steel of low sulfur content <0.010% (Fig. 2). Furthermore, 0.005% of sulfur is aimed at for steels that require hot metal treatment for removal of sulfur before charging of metal to BOF. The high stirring force through argon purging during ladle treatment is applied for homogenization of steel bath and removal of inclusion.

2.3 Control of Steel Phosphorus

Most high-end applications of steel products now require much lower phosphorus levels, typically 0.015% and below. The demand for steel with lower phosphorus content is increasing day by day. The hot metal contains ~ 0.1–0.15% phosphorus. Most of the phosphorus removal takes place in BOF during oxygen blowing under the favorable thermodynamic conditions for its removal. Phosphorus gets oxidized to P_2O_5 but it is less stable in slag and therefore the risk of phosphorus reversal looms large. Improvement in BOF oxygen blowing conditions with respect to flux addition practice, lance profile has been carried out. Phosphorus holding capacity of the slag was improved by quick and fluid slag formation. The bottom flux (calcined lime and calcined dolo) addition and a soft blowing practice had been adopted for improving the flux dissolution and early slag formation. Improved slag formation with high phosphorus capacity had been observed by maintaining slag basicity ~3–3.2, FeO ~ 19–21%, MgO ~ 7% and tapping temperature ~1660 °C. The addition of iron ore has been initiated during oxygen blowing as alternate coolant and also to

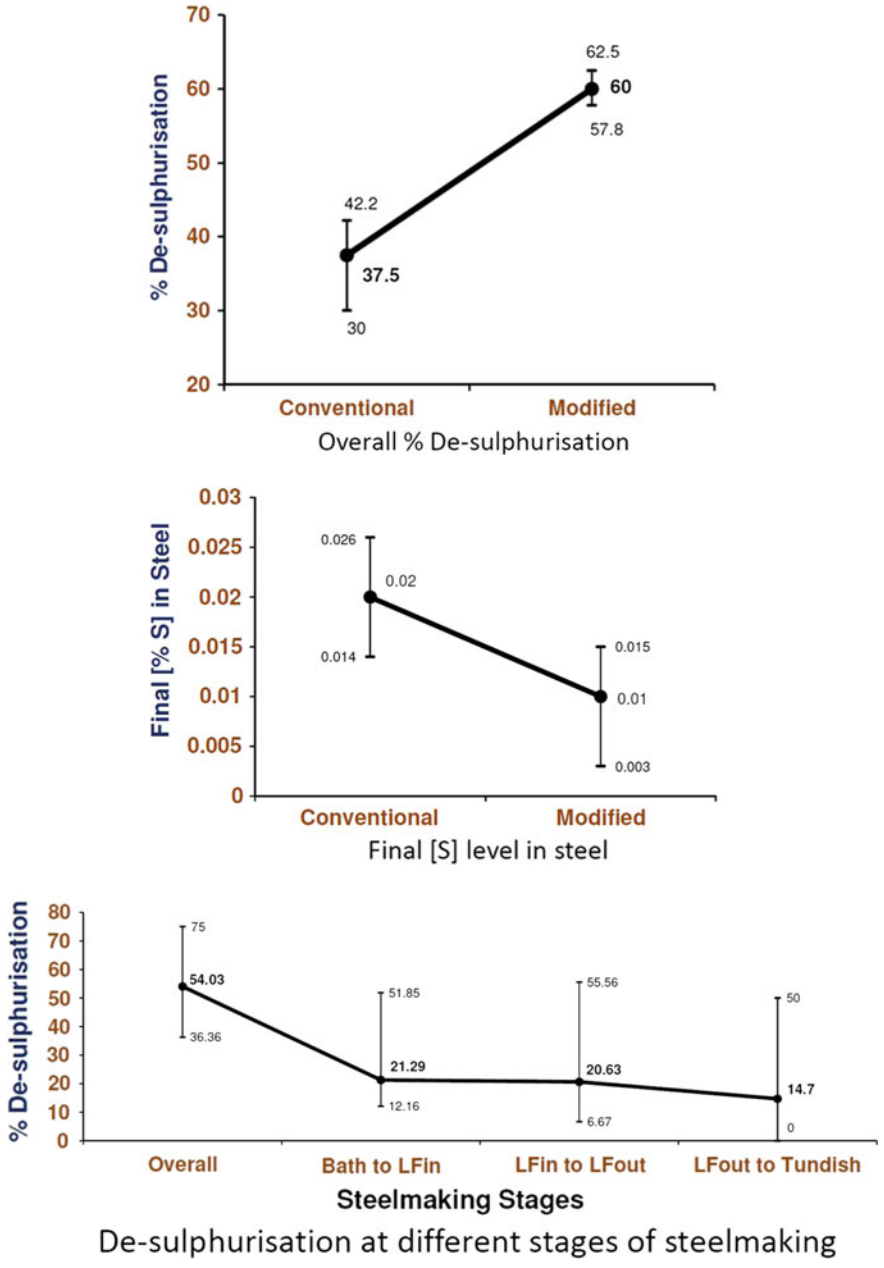

Fig. 2 Trend in de-sulfurization in steelmaking process

supply extra oxygen and FeO to the slag to maintain its fluidity. The slag formation, control of turn down temperature, and oxygen blowing lance profile are important to achieve desired kinetics for phosphorus refining of steel. The turndown phosphorus < 0.015% has been established in BOF.

2.4 Vacuum Treatment of Liquid Steel

Vacuum degassing is an efficient means of mixing and homogenization of the steel ladle. Vigorous mixing promotes agglomeration and flotation of nonmetallic inclusions, particularly alumina. When steels are tapped at higher C level from BOF, the absorbed oxygen in steel bath under vacuum promotes carbon–oxygen reaction. Carbon monoxide formation is facilitated at low pressure and is continuously removed from the system under vacuum. This facilitates simultaneous removal of carbon and oxygen. Lower initial level of oxygen in the liquid steel promotes better yield of microalloying elements and fewer nonmetallic inclusions are formed in steel. Hydrogen from the bath is removed by diffusion. Therefore, hydrogen removal is facilitated at low partial pressure of steel bath. Steel bath circulation under vacuum facilitates homogenization of steel in very quick time.

2.5 Continuous Casting of Steel

The new slab caster −3 (in SMS-II) has been installed to produce a thick as well as wide slab (width up to 2500 mm) which is one of the widest in the country. The new caster is mainly installed to make quality slabs to feed to 4.2 m wide plate mill. The handling capacity of slab has also been enhanced up to 30 t, while the old slab casters have the capacity of 16–17 t. The specification of slab caster package includes latest design and state-of-the-art technology such as ladle to tundish slag detection system, vertical high speed mould with automatic width adjustment, hydraulic mould oscillator, automatic mould level controller, breakout prediction system, air mist spray cooling system, dynamic spray cooling system, continuous straightening, automatic torch cutting machine, slab pusher cum piler arrangement, transverse torch cutting machines, and computerized process control system (Level II). The modern design and technology selected ensures achievement of benchmarks in technical, technological, operating parameters, environment norms, at par with International Standards. The slab casting shop is capable to cast superior quality steels such as API—5L, up to X 70, DD, EDD, medium carbon, SAILMA, IS 2002, IS 2062, IS 6240, IS 5986, IS 3589, CRNO grades, etc.

It has been made clear by many researchers [3, 4] that center segregation in continuously cast slab is attributable to the flow of molten steel which is caused by various mechanical factors and solidification shrinkage. Ishiguro et al. [5]. reported that soft reduction in the final stage of solidification is effective for the suppression of the flow of molten steel due to solidification shrinkage, thermal shrinking, and inter-roll bulging. It is employed to reduce the size of center segregation particles. This suppresses the molten steel flow resulted by solidification shrinkage by reducing the roll gap by an amount equivalent to the amount of the shrinkage (offsetting the solidification shrinkage with roll gap reduction). It can be utilized effectively by decreasing the roll diameter and roll pitch in a casting machine, together with the selection of optimum roll reduction amount meeting the casting condition such as cast slab thickness and casting speed. Ogibayash et al. [6] considered necessary to optimize the reduction timing and to suppress uneven reduction due to mechanical factors such as roll bending for the improvement of center segregation. The application of soft reduction technology becomes harder because the solidified shell strength increases as the strength of the steel grade is increased. Soft reduction is successfully applied to the slabs with the thickness of 300 mm. The macrostructure of thick slab (300 mm) is shown in Fig. 3. Furthermore, as the demand of heavier plates having a thickness of >60 mm is increasing, crimping of center porosity by rolling is becoming difficult; thus, countermeasures for the reduction of cast slab center porosity have also become very important.

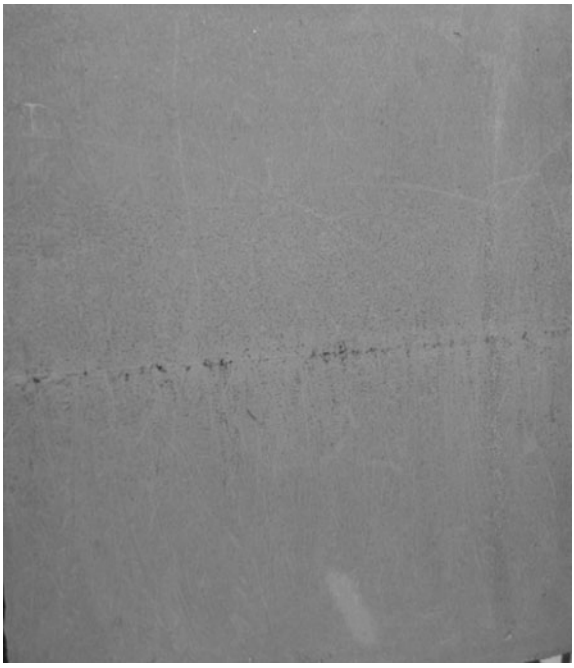

Fig. 3 Macrostructure of thick slab (300 mm) with soft reduction

2.6 Rolling at New Plate Mill

The new plate mill employs various technological upgrades. The schematic layout of the mill is shown in Fig. 1 and rolling specification is given in Table 4. The major technological upgrades are as follows:

(a) Hydraulic Automatic Gauge Control (HAGC) system for faster roll gap adjustment, uniform gauge control across the roll length, i.e., plate width and gauge correction between passes based on feedback.
(b) Plan View Rolling: This facility allows for correction of the plate ends from defects like barrel edge or tongue and optimizes the crop ends.
(c) Roll bending facility for achieving uniform gauge.
(d) Roll Shifting facility: This facility is provided to compensate for the work roll barrel wear by shifting the rolls on either side of the mill centerline, so that the roll gap across the length of the barrel can be maintained.

The finishing equipment has been commissioned recently. With the commissioning of finishing equipment, production of new plate has ramped up. The production has increased significantly and presently producing more than 50,000 t per month. Further the production of special steel such as IS 2062 E350/E410/E450 has also been successfully established in new plate mill. The ultrasonic test (UST) rejection of thicker plates is one of the concerns at new plate mill. Trials were conducted for rolling of thick plates with UST to optimize the reduction schedule for rolling 300 mm slabs, so that higher reduction percentage can be given in initial 4–5 passes to avoid UST failure. The production of special steel is increased by more than 25% of the total production.

2.7 Heats Routed Through RHOB

RHOB has been commissioned at SMS-II, RSP. Comparison of percentage of plates failed in UST from heat processed through RHOB and heat without processing in RHOB is shown in Fig. 4. From the figure, it is evident that UST failure

Table 4 Rolling specification for new plate mill

Input slab		Output
Width	1200–2400 mm	As rolled plate length: 42 m (Max)
Length	2200–4100 mm	Finished plate thickness: 6–100 mm
Thickness	210–300 mm	Width: 1500–4100 mm Length: 6000–15000 mm Sheared plate thickness: 6–50 mm Cold leveling: 40 mm (Max)

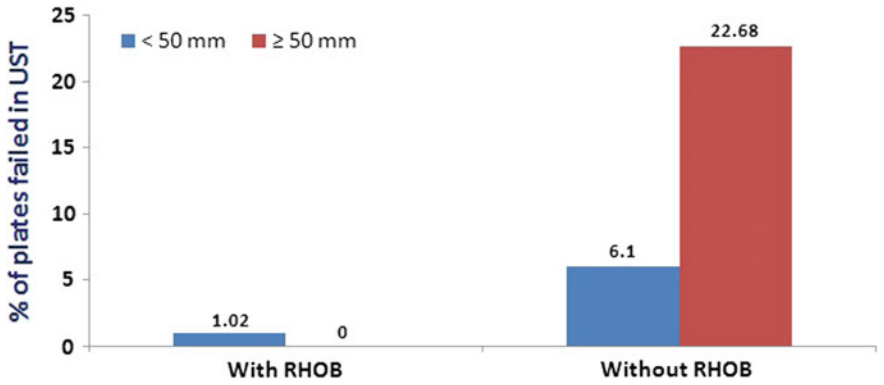

Fig. 4 Comparison of UST failures in heats with RHOB and without RHOB

is negligible in the plates processed through RHOB heat. Rejection is nil in the thicker plates processed from RHOB heat, whereas UST failure is more than 20% in thicker plates processed from heats without RHOB. Thus, ultrasonic soundness of the plates is more dependent on clean steel than % reduction given during initial passes at plate mill.

3 Conclusion

Rourkela Steel Plant has completed a massive modernization and expansion programme to double its production capacity to 4.2 mtpa by augmentation of major units which include new Blast Furnace # 5 with a useful volume of 4060 cubic meters, state-of-the-art third BOF and 4.2 m wide plate mill. Efforts are made for improvement and optimization of steelmaking and rolling practices for the production of special quality high-strength plates such as IS 2062, E350/E410/E450 and API X70, etc. The major modifications were carried out in each stage of its production, i.e., BOF steelmaking and secondary refining to optimize the quality of steel with respect to lower sulfur and phosphorus content. Reduction in UST failure of the plates has been observed for the liquid steel processed through newly commissioned RHOB at the shop. Soft reduction was successfully applied for thick slabs to eliminate the center line segregation. The rolling parameters were optimized to achieve the desired mechanical properties, however ultrasonic soundness of the plates was found to be more dependent on clean steel than the higher reduction schedule given during initial passes at plate mill.

References

1. H. Tamehiro, T. Takeda, S. Matsuda, K. Yamamoto and N. Okumura, Transaction ISIJ, 25 (1985), 982–988
2. K. Murakami, Y. Tsuchida, Y. Kobayashi, M. Nakada and S. Endo, Tetsu-to-Hagane, 85 (1999), 301–306
3. T. Kawawa, H. Satoh, S. Miyahara, K. Koyano and H. Nemoto, Tetsu-to-Hagane, 60 (1974), 486
4. K. Asano, K. Hiromoto and T. Ohashi, Tetsu-to-Hagane, 59 (1973), S82
5. M. Ishiguro. S. Miyahara and I. Sugawara, Tetsu-to-Hagane, 62 (1976), S481
6. S. Ogibayashi, M. Kobayashi, M. Yamada and T. Mukai, ISIJ International, 31 (1991), 1400–1407